

University of Windsor

Scholarship at UWindor

Electronic Theses and Dissertations

Theses, Dissertations, and Major Papers

2022

A Comparison of the Oxidative Addition Chemistry of Tetrathiocins to p- and d- Block Elements

Lara Watanabe
University of Windsor

Follow this and additional works at: <https://scholar.uwindsor.ca/etd>

 Part of the [Materials Chemistry Commons](#)

Recommended Citation

Watanabe, Lara, "A Comparison of the Oxidative Addition Chemistry of Tetrathiocins to p- and d- Block Elements" (2022). *Electronic Theses and Dissertations*. 9030.
<https://scholar.uwindsor.ca/etd/9030>

This online database contains the full-text of PhD dissertations and Masters' theses of University of Windsor students from 1954 forward. These documents are made available for personal study and research purposes only, in accordance with the Canadian Copyright Act and the Creative Commons license—CC BY-NC-ND (Attribution, Non-Commercial, No Derivative Works). Under this license, works must always be attributed to the copyright holder (original author), cannot be used for any commercial purposes, and may not be altered. Any other use would require the permission of the copyright holder. Students may inquire about withdrawing their dissertation and/or thesis from this database. For additional inquiries, please contact the repository administrator via email (scholarship@uwindsor.ca) or by telephone at 519-253-3000ext. 3208.

**A Comparison of the Oxidative Addition
Chemistry of Tetrathiocins to *p*- and *d*- block
Elements**

By

Lara K. Watanabe

A Dissertation

Submitted to the Faculty of Graduate Studies
through the Department of Chemistry and Biochemistry
in Partial Fulfillment of the Requirements for
the Degree of Doctor of Philosophy
at the University of Windsor

Windsor, Ontario, Canada 2022

© 2022 Lara K. Watanabe

**A Comparison of the Oxidative Addition Chemistry of Tetrathiocins to *p*- and *d*-
block Elements**

by

Lara K. Watanabe

APPROVED BY:

L. N. Dawe, External Examiner
Wilfrid Laurier University

R. J. Caron
Department of Mathematics and Statistics

S. A. Johnson
Department of Chemistry and Biochemistry

S. J. Loeb
Department of Chemistry and Biochemistry

J. M. Rawson, Co-advisor
Department of Chemistry and Biochemistry

C. L. B. Macdonald, Co-advisor
Department of Chemistry and Biochemistry

August 30th 2022

DECLARATION OF CO-AUTHORSHIP/PREVIOUS PUBLICATION

I. Co-Authorship

I hereby declare that this thesis incorporates material that is result of joint research, as follows:

Chapter 1 is a review that is published as a perspective piece entitled “The chemistry of dithietes, 1,2,5,6-tetrathiocins and higher oligomers” (Watanabe, L. K.; Wrixon, J. D.; Rawson, J. M., *Dalton Trans.* **2021**, 50, 13620-13633.) I prepared the manuscript incorporating the introductory chapter of Justin Wrixon’s M.Sc. thesis and updating and expanding the scope of that work to include the chemistry of dithietes. My supervisor, Dr. Jeremy Rawson provided significant edits and contributions to the article prior to submission.

The results presented in **Chapter 2** were published in a research article entitled “Oxidative addition of tetrathiocins to palladium(0) and platinum(0): a route to dithiolate coordination complexes” (Watanabe, L. K.; Wrixon, J. D.; Ahmed, Z. S.; Hayward, J. J.; Abbasi, P.; Pilkington, M.; Macdonald, C. L. B. and Rawson, J. M., *Dalton Trans.*, **2020**, 49, 9086-9093.) I synthesized and characterized all 10 platinum derivatives for this project including crystallographic studies, while Justin D. Wrixon, Zeinab S. Ahmed and Mary El-Rayes prepared the Pd derivatives and tetrathiocin starting materials. Dr. Parissa Abbasi (Pilkington group, Brock University) undertook all the electrochemical studies included in the manuscript. Dr. Jeremy M. Rawson performed the crystallographic studies on the Pd derivatives, all of the computational studies and wrote the computational and electrochemical sections of this manuscript. I prepared the first draft of the manuscript, with some assistance from Dr. John J. Hayward and finally edits by Dr. Jeremy M. Rawson prior to submission.

The results presented in **Chapter 3** comprise an initial proof-of-concept reactivity study performed by Dr. John J. Hayward who also grew crystals of $[\text{CpCo}(\text{dmobdt})]_2$. I prepared and characterized all other complexes reported in **Chapter 3** and undertook the single crystal and powder X-ray diffraction studies. The Chapter was written by me and edited by Dr. Jeremy M. Rawson.

Chapter 4 contains results published in the journal article “Oxidative addition of 1,2,5,6-tetrathiocins to Co(I): A re-examination of crown ether functionalized benzene dithiolate cobalt(III) complexes” (Watanabe, L. K.; Ahmed, Z. S.; Hayward, J. J.; Heyer, E.; Macdonald, C. L. B. and Rawson, J. M., *Organomet.*, **2022**, 41, 226-234.). Crystals of $\text{CpCo}(\text{b-15-c-5-dt})$ were grown by Dr. John Hayward and crystals of the $[\text{M}(\text{CpCo}(\text{b-15-c-5-dt}))_2][\text{BPh}_4]$ complexes were grown by Zeinab S. Ahmed. I re-prepared all complexes and completed remaining characterization required for publication including recrystallization of complexes and structure re-determination to increase the quality of the crystallographic data for selected complexes. I prepared and characterized complexes derived through oxidation. I also performed all the electrochemical studies and prepared the initial version of the manuscript. DFT calculations were performed by Jeremy M. Rawson who provided final edits to this work prior to and after submission.

The complexes reported in **Chapter 5** are unpublished. Initial reactivity studies were performed by Nadia Fendi and Nabila Hamidouche with crystallographic experiments performed by Dr. Yassine Beljoudi. I re-prepared and re-crystallized all complexes to complete all necessary spectroscopic characterization for publication. In addition, I prepared and fully characterized the complex $\text{Ni}(\text{dmobdt})(\text{bpy})$ including its crystal structure determination. Molecular hyperpolarizability measurements were made using the EFISH technique and were undertaken by Prof. Francesca Tessore at the University of Milan, while DFT studies were undertaken by Dr Jeremy M. Rawson. Chapter 5 was drafted by me and edited by Dr. Jeremy M. Rawson.

I was the sole researcher for the unpublished work presented in **Chapter 6**. I drafted the Chapter which was subsequently edited by Dr. Jeremy M. Rawson.

I am aware of the University of Windsor Senate Policy on Authorship and I certify that I have properly acknowledged the contribution of other researchers to my thesis, and have obtained written permission from each of the co-author(s) to include the above material(s) in my thesis.

I certify that, with the above qualification, this thesis, and the research to which it refers, is the product of my own work.

II. Previous Publications

This thesis includes 3 original papers that have been previously published/submitted for publication in peer reviewed journals, as follows:

Thesis Chapter	Publication Title/ Full Citation	Publication status*
Chapter 1	“The chemistry of dithietes, 1,2,5,6-tetrathiocins and higher oligomers” Watanabe, L. K.; Wrixon, J. D. and Rawson, J. M., <i>Dalton Trans.</i> , 2021 , <i>50</i> , 13620-13633.	Published
Chapter 2	“Oxidative addition of tetrathiocins to palladium(0) and platinum(0): a route to dithiolate coordination complexes” Watanabe, L. K.; Wrixon, J. D.; Ahmed, Z. S.; Hayward, J. J.; Abbasi, P.; Pilkington, M.; Macdonald, C. L. B. and Rawson, J. M., <i>Dalton Trans.</i> , 2020 , <i>49</i> , 9086-9093.	Published
Chapter 4	“Oxidative addition of 1,2,5,6-Tetrathiocins to Co(I): A Re-Examination of Crown Ether Functionalized Benzene Dithiolate Cobalt(III) Complexes” Watanabe, L. K.; Ahmed, Z. S.; Hayward, J. J.; Heyer, E.; Macdonald, C. L. B. and Rawson, J. M., <i>Organomet.</i> , 2022 , <i>41</i> , 226-234.	Published

I certify that I have obtained written permission from the copyright owner(s) to include the above published material(s) in my thesis. I certify that the above material describes work completed during my registration as a graduate student at the University of Windsor.

III. General

I declare that, to the best of my knowledge, my thesis does not infringe upon anyone's copyright nor violate any proprietary rights and that any ideas, techniques, quotations, or any other material from the work of other people included in my thesis, published or otherwise, are fully acknowledged in accordance with standard referencing practices. Furthermore, to the extent that I have included copyrighted material that surpasses the bounds of fair dealing within the meaning of the Canada Copyright Act, I certify that I have obtained a written permission from the copyright owner(s) to include such material(s) in my thesis.

I declare that this is a true copy of my thesis, including any final revisions, as approved by my thesis committee and the Graduate Studies office, and that this thesis has not been submitted for a higher degree to any other University or Institution.

ABSTRACT

This thesis describes the oxidative addition of 1,2,5,6-tetrathiocins to low valent transition metals and *p*-block elements. Chapter 1 provides a literature review of tetrathiocin reactivity and the related dithiete chemistry for both the *p*- and *d*-block elements. Chapter 2 describes the synthesis of a library of tetrathiocins used extensively through the rest of this thesis alongside the synthesis of a series of group 10 dithiolate complexes through the oxidative addition of tetrathiocins to M_2dba_3 ($M = Pd$ or Pt) in the presence of the chelating phosphines dppe and dppf to generate complexes of general formula $M(dt)(dppe)$ and $M(dt)(dppf)$ [$M = Pd, Pt, dt =$ benzenedithiolate derivatives]. The coordination chemistry of complexes bearing benzo-15-crown-5-dithiolate ligands, $M(15-c-5-bdt)(dppe)$ and $M(15-c-5-bdt)(dppf)$ with Na^+ ions was probed through UV-Vis spectroscopy, X-ray diffraction and electrochemical studies. These revealed formation of 1:1 complexes $[M(Na-15-c-5-bdt)(dppe)][BPh_4]$ and $[M(Na-15-c-5-bdt)(dppf)][BPh_4]$ ($M = Pd, Pt$). Chapter 3 describes the oxidative addition of tetrathiocins to the Co(I) complex, $CpCo(CO)_2$, generating the $16e^-$ Co(III) complexes, $CpCo(dt)$ and/or the $18e^-$ complexes $[CpCo(dt)]_2$, depending on the nature of the tetrathiocin. In the case of the dimethoxybenzene dithiolate ($dmobdt^{2-}$) derivative, both monomeric $CpCo(dmobdt)$ and dimeric $[CpCo(dmobdt)]_2$ species could be isolated in the solid state depending upon crystal growth conditions. $CpCo(dmobdt)$ was found to undergo an unusual mechanochemical solid state transformation to the denser $[CpCo(dmobdt)]_2$ phase upon grinding. Chapter 4 describes the synthesis of the benzo-15-crown-5 and benzo-18-crown-6 dithiolate complexes $CpCo(15-c-5-bdt)$ and $CpCo(18-c-6-bdt)$. In contrast to the group 10 chemistry described in Chapter 2, spectroscopic studies in solution and crystallographic studies in the solid state indicated that $CpCo(15-c-5-bdt)$ was found to coordinate to the alkali metal ions Na^+, K^+, Rb^+ and Cs^+ to form 2:1 complexes $[A\{CpCo(15-c-5-bdt)\}_2][BPh_4]$ ($A = Na, K, Rb, Cs$). Chapter 5 describes the one-pot synthesis of a series of substituted nickel(II)dithiolate bipyridine ‘push-pull’ complexes, $Ni(bdt)(bpy)$, via oxidative addition chemistry of tetrathiocins to $Ni(COD)_2$ in the presence of chelating bipyridine ligands. The spectroscopic properties of the visible absorption maxima were sensitive to solvent and substituent effects. Empirical correlations were identified for both

the solvatochromic effect and the electronic properties of the functional group attached to the bipyridine ligand. EFISH measurements revealed large molecular hyperpolarizabilities, comparable with previously reported Ni(II) dithiolate/diimine complexes. Chapter 6 examines the oxidative addition chemistry of tetrathiocins to Ge(II) in the form of GeCl₂-dioxane to afford Ge(bdt)₂ derivatives. The dimethoxybenzenedithiolato complex, Ge(dmobdt)₂ was found to be polymorphic and the phase stability examined through DSC and VT-PXRD studies.

DEDICATION

I would like to dedicate this thesis to my parents, Ron and Sue and my sister, Lori for their endless support.

ACKNOWLEDGEMENTS

I applied to the University of Windsor for my graduate studies initially to Dr. Charles Macdonald, who has my gratitude for not only taking me on as a student, but for setting up a co-supervised project with Dr. Jeremy Rawson. I have had the pleasure of working under both of their supervision for the past five years, and what years they have been! Therefore, I would first like to acknowledge both Chuck and Jeremy for their continued support, advice, and patience in everything I have done, both in the lab and as extra-curricular in their own ways. They have both been wonderful research advisors, teachers, and mentors.

Thank you to my committee members, Dr. Richard Caron, Dr. Steve Loeb and Dr. Sam Johnson for your feedback and questions throughout the years, even if I had to give my transfer talk twice! As well, thank you to Dr. Louise Dawe for being my external examiner, and although you are new to my already very full committee, I would like to extend my gratitude to you for teaching me so much about crystallography at the CCCW in Montreal. It is truly my favourite instrument to run and has brought me so much joy (and frustration at times) throughout my degree.

Although the Rawson and Macdonald groups have changed throughout my years here, they have always consisted of amazing and wonderful people who have been there for support, chats, advice about chemistry and life and became some of my closest friends. Thank you to everyone who helped me get acquainted with the new labs, moving the Rawson lab, cleaning out the Macdonald lab and everything in between! To start, I would like to thank Dr. Elodie Heyer and Dr. John Hayward for showing me around Windsor on my first visit and always being up for a chat and the encouragement you have given me when I got stuck with my projects. Thank you to Mitchell Nascimento for the life advice, constant laughs, memories and support you have given me when you were here, and since leaving for Victoria. I always love when we have a chance to catch up even if its just a quick coffee run to Tim's on your way to or from an airport! I know that you are right behind in finishing your PhD degree at Victoria and cannot wait to celebrate that with you.

To Dr. Konstantina Pringouri, Dr. Aisha Alsaleh, Dr. Justin Binder, Dr. Stephanie Kosnik, Dr. Ala'Aeddeen Swidan, Dr. Fawzia Elnajjar, Dr. Bin Zhang, Brad Jacobs, Emily Omahen, Alina Secara, Zeinab Ahmed, Louae Abdullah, Blake St. Onge and Max Nascimento who were all part of the groups and left over the years, I'm thankful for all of your encouragement and support. To my fellow grad students that I started with, Nadia Stephaniuk and Dominique DeSantis, thank you for all of the memories we have shared from the many conference seasons, to playing softball and packing up the lab for the big CORE move. Nadia, I have not known Windsor without you until the past few months, but even so I know that we will be life-long friends. Thank you for all of the late nights, weekends, early mornings in the lab really any time of the day and making sure I remembered to eat meals. You have been my rock in and out of the lab, and I have watched you succeed after graduating I have no doubts you will find success in whatever you do. Finally, to the current group, Mary and Asli, thank you for laughs and conversations over the past year, but mostly being patient with me when I was too busy for my own good. I know you will both do well in finishing up your degrees and wish you all the best in your future endeavours.

I would also like to thank my family and friends who have always encouraged me to pursue my education and aided me along the way to get to where I am now. Thank you to my parents and family for your never ending belief in me and patience with me throughout the years even through all of my stresses and lack of communication because I had a deadline to meet.

This department is unlike any other, so I would also like to thank many of other past and present graduate students and post-docs in the department, Dr. Ben Wilson, Dr. Ayan Dhara, Dr. Jennifer Murphy, Dr. Kenson Ambrose, Jacob Rothera, Adam Cassar, Junyang Liu, Joey Zurakowski, Adit Nyayachavadi, Maddison Mooney, Rahaf Hussein, the volunteers for all the WinChem events and all of the past and present members of the 'Topes softball team. Thanks for all the memories; from going to Barrell House after games, attending conferences together, grabbing a bite to eat or to having a quick chat down the hall. It has been all of these small interactions that have kept me going and sane.

To anyone I have forgotten, I am sorry and thank you for everything. It is because of the amazing support system I am surrounded by that I was able to finish this degree.

As well, to the amazing staff and faculty we have in the Department of Chemistry and Biochemistry. Thank you to Beth, Cathy, Jayne and Marlene for helping the grad students the way you do an ensuring the department runs the way it does. Thank you to Ronan and Una and Nedhal, it has been a pleasure to know you all and work with all of you over the years. Thank you to Peter Rowsell, Tina Lepine, Sharon Lavigne for my endless inquiries and sometimes strange asks of CCC. I would like to thank Janeen Auld for training me on how to run EA, a skill that has been put good use for the department. A HUGE thank Joe Lichaa for everything that he does from the many flood alarms going off to fixing pumps and for coming running at every call I gave even if it happened to be a holiday when there was a problem with the X-ray. This department truly wouldn't be functional without you, Joe. Thank you to the department for the Chem Proms the Christmas parties and informal after seminar gatherings and making this a wonderful place to work for the last five years. I am grateful for the opportunities I have had within our department to and have cherished my time at the University of Windsor. Thank you for everything.

TABLE OF CONTENTS

DECLARATION OF CO-AUTHORSHIP/PREVIOUS PUBLICATION.....	iii
ABSTRACT.....	vii
DEDICATION.....	ix
ACKNOWLEDGEMENTS	x
LIST OF TABLES	xx
LIST OF FIGURES	xxiii
LIST OF CHARTS	xxix
LIST OF SCHEMES	xxx
LIST OF ABBREVIATIONS AND SYMBOLS	xxxii
CHAPTER 1: INTRODUCTION.....	1
1.1 Introduction to dithietes and higher oligomers	1
1.2 Dithietes	2
1.2.1. Preparation	2
1.2.2. Structural studies of dithietes	4
1.2.3. Computational studies on dithietes	5
1.2.4. Reactivity	5
1.2.6. Ring interconversion reactions	13
1.3 Introduction to 1,2,5,6-tetrathiocins	14
1.3.1. Preparation	14
1.3.2. Structural studies of 1,2,5,6-tetrathiocins	17
1.3.3. Computational studies on 1,2,5,6-tetrathiocins	17
1.3.4. Reactivity of 1,2,5,6-tetrathiocins	18

1.3.5. Biological studies	24
1.4 Trimeric and tetrameric dithietes	25
1.4.1. Preparation	25
1.4.2. Structural studies	27
1.4.3. Computational studies	27
1.4.4. Reactivity studies	28
1.5 Overview of this thesis	28
1.6 References	30

**CHAPTER 2: SYNTHESIS AND REACTIVITY OF PLATINUM AND
PALLADIUM DITHIOLATE PHOSPHINE COMPLEXES37**

2.1 Introduction	37
2.2 Results and Discussion	39
2.2.1. Synthesis	39
2.2.2. Structural Studies	41
2.2.3. Complexation Studies	42
2.3.4. Electrochemical Studies	44
2.3 Conclusion & Future Work	48
2.4. Experimental	49
2.4.1. General Procedures	49
2.4.2. Physical Measurements	49
2.4.3. X-Ray Crystallography	50
2.4.4. Computational Methods	50
2.4.5. Synthesis of benzo-18-crown-6-1,2,5,6-tetrathiocins (1h)	51
2.4.5. Synthesis of 1,1-dimethyldioxolobenzene-1,2,5,6-tetrathiocin (1i)	51
2.4.5. Synthesis of (deobdt)Pd(dppe) (2b)	52
2.3.6. Synthesis of (doxlbdt)Pd(dppe) (2c)	52
2.4.7. Synthesis of (doxbdt)Pd(dppe) (2d)	53
2.4.8. Synthesis of (doxebdt)Pd(dppe) (2e)	54
2.4.9. Synthesis of (dmbimdt)Pd(dppe) (2f)	54

2.4.10. Synthesis of (b-15-c-5-dt)Pd(dppe) (2g)	55
2.4.11. Synthesis of (dmdoxlbdtd)Pd(dppe) (2i)	56
2.4.12. Synthesis of [(b-15-c-5-Na-dt)Pd(dppe)][BPh ₄] ([Na(2g)(MeOH) ₂][BPh ₄)	56
2.4.13. Synthesis of (deobdt)Pt(dppe) (3b)	57
2.4.14. Synthesis of (doxlbdt)Pt(dppe) (3c)	58
2.4.15. Synthesis of (doxbdt)Pt(dppe) (3d)	59
2.4.16. Synthesis of (doxebdt)Pt(dppe) (3e)	60
2.4.17. Synthesis of (dmbimdt)Pt(dppe) (3f)	60
2.4.18. Synthesis of (b-15-c-5-dt)Pt(dppe) (3g)	61
2.4.19. Synthesis of [(b-15-c-5-Na-dt)Pt(dppe)][BPh ₄] ([Na(3g)][BPh ₄)	62
2.4.20. Synthesis of (b-15-c-5-dt)Pd(dppf), (4g)	63
2.4.21. Synthesis of [(b-15-c-5-Na-dt)Pd(dppf)][BPh ₄] ([Na(4g)][BPh ₄)	64
2.4.22. Synthesis of [(b-15-c-5-dt)Pt(dppf)][BPh ₄] (5g)	64
2.4.23. Synthesis of [(b-15-c-5-Na-dt)Pt(dppe)][BPh ₄], ([Na(5g)][BPh ₄)	65
2.5 References	66

3. TRANSFORMATION BETWEEN MONOMER AND DIMER FORMS OF COBALT(III) DITHIOLATE SPECIES70

3.1 Introduction	70
3.2 Results and Discussion	75
3.2.1. Synthesis	75
3.2.2. Crystal Growth of Complexes	76
3.2.3. Structures of 6 and (6) ₂	77
3.2.4. Structures of 7, 8 and 10	78
3.2.5. Phase behaviour of 6	81
3.3 Conclusions & Future Work	88
3.4 Experimental	88
3.4.1. General Procedures	88
3.4.2. Physical Measurements	88

3.4.3. X-Ray Crystallography	89
3.4.4. Synthesis of CpCo(dmobdt) (6) ₂	89
3.4.5. Synthesis of CpCo(dmobdt) (6)	90
3.4.6. Synthesis of CpCo(deobdt) (7) ₂ ·2(7)	90
3.4.7. Synthesis of CpCo(doxlbd) (8)	91
3.4.8. Synthesis of CpCo(doxbd) (9)	92
3.4.9. Synthesis of CpCo(doxebdt) (10)	92
3.5 References	93

4. OXIDATIVE ADDITION OF 1,2,5,6-TETRATHIOCINS TO CO(I): A RE-EXAMINATION OF CROWN ETHER FUNCTIONALIZED BENZENE DITHIOLATE COBALT(III) COMPLEXES96

4.1 Introduction	96
4.2 Results and Discussion	98
4.2.1. Synthesis	98
4.2.2. Structures of 11 and 12	99
4.2.3. Solution Studies	100
4.2.4. DFT Studies	101
4.2.5. Coordination Chemistry of 11	102
4.2.6. Solution Studies of 11	103
4.2.7. X-ray Crystallography	104
4.2.8 Electrochemical Studies	107
4.2.9 Chemical Oxidation of 11	109
4.3 Conclusions	111
4.4 Experimental	111
4.4.1. General Procedures	111
4.4.2. Physical Measurements	112
4.4.3. X-Ray Crystallography	112
4.4.4. Computational Methods	113
4.4.5. Synthesis of CpCo(b-15-c-5-dt) (11)	113

4.4.6. Synthesis of CpCo(b-18-c-6-dt) (12)	114
4.4.7. Synthesis of [NaCpCo(b-15-c-5-dt)][BPh ₄] (13a)	115
4.4.8. Synthesis of [KCpCo(b-15-c-5-dt)][BPh ₄] (13b)	115
4.4.9. Synthesis of [RbCpCo(b-15-c-5-dt)][BPh ₄] (13c)	116
4.4.10. Synthesis of [CsCpCo(b-15-c-5-dt)][BPh ₄] (13d)	117
4.4.11. Synthesis of [CpCo(b-15-c-5-dt)][BF ₄] ₂ (14)	117
4.5 References	117

5. INVESTIGATION OF THE ELECTRONIC PROPERTIES OF NICKEL(DIIMINE)(DITHIOLATE) COMPLEXES121

5.1 Introduction	121
5.2 Results and Discussion	125
5.2.1. Synthesis	125
5.2.2. Structural Studies	126
5.2.3. UV-Vis Studies	129
5.2.4. EFISH measurements	135
5.3 Conclusions & Future Work	136
5.4 Experimental	137
5.4.1. General Procedures	137
5.4.2. Physical Measurements	137
5.4.3. X-ray Crystallography	137
5.4.4. Computational methods	138
5.4.5. Synthesis of (2,2'-bipyridyl)Ni(dmobdt) (15).	138
5.4.6. Synthesis of (Diethyl [2,2'-bipyridine]-4,4'-dicarboxylate)Ni(dmobdt) (16).	139
5.4.7. Synthesis of (4,4'-dimethyl-2,2'-bipyridyl)Ni(dmobdt) (17).	140
5.4.8. Synthesis of (4,4'-diphenyl-2,2'-bipyridyl)Ni(dmobdt) (18).	140
5.4.9. Synthesis of (4,4'-di- <i>tert</i> -butyl-2,2'-bipyridyl)Ni(dmobdt) (19).	141
5.4.10. Synthesis of (4,4'-di- <i>tert</i> -butyl-2,2'-bipyridyl)Ni(doxbdt) (20).	142
5.5 References	142

6. GERMANIUM DITHIOLATE CHEMISTRY	146
6.1 Introduction	146
6.2 Results and Discussion	148
6.2.1 Synthesis	148
6.2.2 Structural studies	149
6.2.3 Phase behaviour of 21-I and 21-II	151
6.3 Conclusions & Future Work	155
6.4 Experimental	156
6.4.1 General Procedures	156
6.4.2. Physical Measurements	156
6.4.3. X-Ray Crystallography	156
6.4.4 Synthesis of Ge(dmobdt) ₂ , Phase I (21-I)	157
6.4.5 Synthesis of Ge(dmobdt) ₂ , Phase II (21-II)	157
6.4.6 Synthesis of 2 Ge(deobdt) ₂ · 1b (22)	157
6.4.7 Synthesis of Ge(doxlbd _t) ₂ (23)	158
6.5 References	158
7. CONCLUSIONS AND FUTURE OUTLOOK	161
7.1 Conclusions	161
7.2 Future Outlook	163
7.3 References	165
APPENDIX A	167
APPENDIX B	177
APPENDIX C	183
APPENDIX D	186
I. Mass Spectrometry	187

II. Density Functional Theory	193
APPENDIX E	196
APPENDIX F	198
APPENDIX G.....	203
VITA AUCTORIS	206

LIST OF TABLES

Table 2.1. Reaction times and isolated yields of tetrathiocins.	39
Table 2.2. Yields of dithiolate complexes derived from the oxidative addition of tetrathiocins 1a–1i to Pd ₂ dba ₃ or Pt ₂ dba ₃ in the presence of the auxiliary chelating ligands dppe and dppf.....	40
Table 2.3. Electrochemical data for benzo-15-crown-5-dithiolate complexes of palladium and platinum with auxiliary dppe and dppf ligands (<i>qr</i> = quasi-reversible and reflects oxidation processes in which a maximum can be found in the return wave; <i>ir</i> – irreversible and show no clear maximum in the return wave).....	46
Table 3.1. Summary of crystallization conditions for 6–10	77
Table 3.2. Summary of bond lengths and angles in the monomer crystals of 6, 7, 8 and 10	81
Table 3.3. Unit cell parameters for 6 and (6) ₂	86
Table 7.1. Crystallographic data for compounds 13a–13d	106
Table 4.2. Values of θ , d and ψ , for complexes 13a–13d	106
Table 4.3. Summary of oxidation and reduction potentials for 11, 12 and complex 13a . Oxidation processes are irreversible and the peak potential is reported. Reduction processes were quasi-reversible. Half-wave reduction potentials and peak-peak separations are reported. All data referenced to Ag/AgCl.....	108
Table 5.1. Yields of dithiolate complexes derived from the oxidative addition of tetrathiocins to Ni(COD) ₂ in the presence of auxiliary bipyridine ligands..	125
Table 5.2. Unit cell parameters for 15–20	126
Table 5.3. Summary of bond lengths and measured distances in crystal structures of 15–20	128
Table 5.4. Previously observed solvent effects on the absorption maxima in the visible region (400–700 nm) for nickel bipyridine dithiolate complexes.....	129
Table 5.6. Summary of λ_{\max} data for complexes 15–19 and the corresponding Hammett parameters for the substituents in the 4,4' positions.	132

Table 5.7. Summary of λ_{\max} data and corresponding extinction coefficients for complexes 15–19 in both CH_2Cl_2 and DMF alongside the corresponding gas phase TD-DFT computed lowest energy transition (B3LYP-D3/LACV3P*) and oscillator strength.....	134
Table 5.8. Comparison between the experimental λ_{\max} and ϵ values for complex 15 in different solvents and TD-DFT calculated values taking into account solvent effects with a PCM model (COSMO).....	134
Table 5.9. Experimental molecular polarizability data for compounds 16–20	136
Table 6.1. Unit cell parameters for 21–I and 21–II	149
Table 6.2. Summary of important geometric bond lengths and angles for newly synthesized germanium compounds.	151
Table A.1. Crystal data and structure refinement for LW067_1_P21_c.....	168
Table A.2. Crystal data and structure refinement for LW070_P21_n.	169
Table A.3. Crystal data and structure refinement for LW071_2ndxtal.....	170
Table A.4. Crystal data and structure refinement for LW069_1.....	171
Table A.5. Crystal data and structure refinement for LW072_P21_n.	172
Table A.5. Crystal data and structure refinement for LW073_P21_c.....	173
Table A.5. Crystal data and structure refinement for LW088_1_P_1.	174
Table A.6. Crystal data and structure refinement for LW098_1_P_1.	175
Table A.7. Crystal data and structure refinement for LW089_3rdxtal_P21_c.	176
Table B.1. Crystal data and structure refinement for LW046_Pbca_a.	178
Table B.2. Crystal data and structure refinement for LW062_2_P_1_a.....	179
Table B.3. Crystal data and structure refinement for LW037_a.	180
Table B.4. Crystal data and structure refinement for LW059_P_1_a.....	181
Table B.5. Crystal data and structure refinement for LW060_P21_n_a.....	182
Table C.1. Crystal data and structure refinement for JMR_LW017.....	184
Table C.2. Crystal data and structure refinement for LW075.....	185
Table D.1. Comparison of crystallographically and computationally determined geometries for 11	193

Table D.2. Computed lowest energy UV-Vis transitions for 11 with oscillator strength, $f > 0.1$	194
Table D.3. Contributions to the lowest energy excitation with oscillator strength, $f > 0.1$	194
Table E.1. Crystal data and structure refinement for LW176_P21_c_done_a.	197
Table F.1. Crystal data and structure refinement for LW020_0m_a.	199
Table F.2. Crystal data and structure refinement for JMR_LW033_0m_a.	200
Table F.3. Crystal data and structure refinement for LW077_P21_c_a.	201
Table F.4. Crystal data and structure refinement for LW077_P21_c.	202

LIST OF FIGURES

- Figure 1.1.** Lone pair repulsion in planar *cis*-oid and non-planar twisted disulfides..... 1
- Figure 1.2.** Crystal structure of the hexanuclear complex Pd₆(tfd)₆.⁴² 11
- Figure 1.3.** Crystal structures of (C₆F₄S₂)₂ (**left**) and (C₆Cl₄S₂)₂ (**right**) which adopt the chair and twisted conformations respectively. 17
- Figure 1.4.** Optimized local energy minima for (*Z,Z*), (*E,Z*) and (*E,E*) conformations of the parent tetrathiocin, H₄C₄S₄. [Figure reproduced from reference 83 with permission]..... 18
- Figure 1.5.** Crystal structure of the cyclic tetramer, (H₂C₂S₂)₄, highlighting the *Z* configuration at each double bond (**left**) and folding of the ring (**right**)..... 27
- Figure 1.6.** Tetrathiocin ligands used to create metal dithiolate complexes. 29
- Figure 2.1.** Tetrathiocin ligands used to prepare metal dithiolate complexes..... 38
- Figure 2.2.** Crystal structures of **2g** (left) and **4g** (right) with thermal ellipsoids of the non-H atoms drawn at the 50% probability level. Minor components of disorder (**2g**) and lattice solvent molecules (**4g**) omitted for clarity. 42
- Figure 2.3.** Solution UV-Vis data for **2g** in the presence of increasing numbers of equivalents of Na⁺ ions (left) and change in λ_{max} for **2g** with equivalents of NaBPh₄ added (right) (solvent = 1:1 CH₂Cl₂:MeCN). 43
- Figure 2.4.** Crystal structure of (left) [Na(**2g**)(MeOH)₂][BPh₄] and (right) [Na(**4g**)][BPh₄]. Thermal ellipsoids for non-H atoms are drawn at 50% probability while lattice solvent and BPh₄⁻ anions are removed for clarity. 44
- Figure 2.5.** Cyclic voltammograms of complexes **2g–5g** using a 0.10 M [ⁿBu₄N][PF₆] supporting electrolyte in CH₂Cl₂ with scan rate of 100 mV/s. 45
- Figure 2.6.** DFT computed orbital energies (B3LYP/6-31G* with LACV3P* for Pd and Na) for **2g**, **2g**⁺ and [Na(**2g**)]⁺ For cationic **2g**⁺ the energies of the one-electron orbitals corresponding to “spin-up” (α) electrons and “spin-down” (β) electrons derived from the UHF calculation are presented..... 47
- Figure 2.7.** DFT computed orbital energies (B3LYP/6-31G* with LACV3P* for Pd and Fe) for **4g** and **4g**⁺. For cationic **4g**⁺ the energies of the one-electron orbitals

corresponding to “spin-up” (a) electrons and “spin-down” (b) electrons derived from the UHF calculation are presented.	47
Figure 2.8. Cyclic voltammograms of complexes 2g and 4g and their Na ⁺ complexes, [Na(2g)] ⁺ and [Na(4g)] ⁺ using a 0.10 M [nBu ₄ N][PF ₆] supporting electrolyte in CH ₂ Cl ₂ with scan rate of 100 mV/s.	48
Figure 3.1. Crystal structures of (left) dimeric [NiBr ₂ (dab)] ₂ and (right) monomeric NiBr ₂ (dab).	72
Figure 3.2. Crystal structure of (left) CpCo(bdt), highlighting centrosymmetric intermolecular Co...S contacts between the two crystallographically independent pairs of monomers; (right) dimeric structure of [CpCo(bdt)] ₂ . .	74
Figure 3.3. Novel CpCo(dt) complexes investigated in this study.	75
Figure 3.4. ¹ H NMR spectrum of 6 , in CDCl ₃ at room temperature.	76
Figure 3.5. Crystal structure of (6) ₂ with thermal ellipsoids drawn at the 50% probability level. Hydrogen atoms have been omitted for clarity.	77
Figure 3.6. Crystal structure of 6 with thermal ellipsoids drawn at the 50% probability level. Hydrogen atoms have been omitted for clarity.	78
Figure 3.7. Crystal structure of (7) ₂ ·2(7)·CH ₂ Cl ₂ with thermal ellipsoids drawn at the 50% probability level. The CH ₂ Cl ₂ solvate molecule and hydrogen atoms have been omitted for clarity.	79
Figure 3.8. Crystal structure of 7 with thermal ellipsoids drawn at the 50% probability level. Hydrogen atoms have been omitted for clarity.	79
Figure 3.9. Crystal structure of 8 with thermal ellipsoids drawn at the 50% probability level. Hydrogen atoms have been omitted for clarity.	80
Figure 3.10. Crystal structure of 10 with thermal ellipsoids drawn at the 50% probability level. Hydrogen atoms have been omitted for clarity.	80
Figure 3.11. Room temperature PXRD profile for (6) ₂ with simulation based on low temperature SC-XRD (dotted line).	83
Figure 3.12. PXRD profile for 6 at room temperature with simulation based on low temperature SC-XRD (dotted line).	83
Figure 3.13. VT-PXRD of pristine (6) ₂ from room temperature up to 150 °C.	84

Figure 3.14. DSC profile for the phase pure (a) dimeric (6) ₂ and (b) monomeric 6	84
Figure 3.15. PXRD of 6 at room temperature (solid black line) with simulation (dotted black line); the green line corresponds to a lightly ground sample of 6 while the solid red line corresponds to a sample subjected to more sustained grinding. The dotted red line corresponds to the simulated PXRD pattern based on SC-XRD studies of (6) ₂	85
Figure 3.16 Schematic relationship between molecules in 6 and the structure of (6) ₂ (one pair of molecules in the two phases are highlighted in color to emphasize the translational relationship along the <i>c</i> -axis).	87
Figure 4.1. (top) Crystal structure of 11 viewed (a) parallel to and (b) perpendicular to the C ₆ S ₂ ring plane with one of the two molecules in the asymmetric unit shown; (bottom) Crystal structure of 12 viewed (c) parallel to and (d) perpendicular to the C ₆ S ₂ plane. Thermal ellipsoids plotted at the 50% probability level. Hydrogen atoms omitted for clarity.	99
Figure 4.2. Crystal structure of (11) ₂ with thermal ellipsoids drawn at the 50% probability level with hydrogen atoms omitted for clarity.	100
Figure 4.3. DFT computed orbital energies (M06/LACV3P**+ +/COSMO(CH ₂ Cl ₂)) for 11	102
Figure 4.4. Mass spectrum of 11 after storage in a glass vial reveals 11 + NH ₄ ⁺ (<i>m/z</i> = 472, calculated isotope distribution pattern: 472 = 100, 473 = 23.1, 474 = 12.4, 475 = 2.2) and 11 + Na ⁺ (<i>m/z</i> = 477, calculated isotope distribution pattern: 477 = 100; 478 = 22.7; 479 = 12.3; 480 = 2.2). Isotopomers with less than 1% abundance are neglected.	103
Figure 4.5. The change in <i>λ</i> _{max} for 11 with of a 0.00005 mol L ⁻¹ solution with equivalents of a 0.0001 mol L ⁻¹ NaBPh ₄ solution added.	104
Figure 4.6. Crystal structure of the cations in (top) 13a and (centre) 13c with thermal ellipsoids for non-H atoms drawn at the 50% probability level. The BPh ₄ ⁻ counterions are omitted for clarity. (bottom) Illustrations of the geometric parameters <i>d</i> , <i>θ</i> and <i>ψ</i> discussed in the text.	105

Figure 4.7. Cyclic voltammograms for 11 and 13a (0.01 M [ⁿ Bu ₄ N][PF ₆] supporting electrolyte, solvent = CH ₂ Cl ₂ , scan rate 100 mV/s).....	107
Figure 4.9. Structure of the [14] ²⁺ cation in the structure of [14][BF ₄] ₂ . Thermal ellipsoids for non-H atoms presented at 50% probability. Counterions and solvent molecules omitted for clarity.	110
Figure 5.1. Schematic of the frontier orbitals (DFT, B3LYP–D3/LACV3P*) of the Ni(bpy)(dmobdt) complex highlighting the dithiolate-based HOMO (orange) and bpy-based LUMO (blue).	123
Figure 5.2. Nickel (II) complexes investigated for their NLO and near-IR potential....	125
Figure 5.3. Crystal structures of 15–20 determined by X-ray diffraction. Thermal ellipsoids for non-H atoms plotted at the 50% probability level. Solvent molecules and minor disorder in the structure of 16 omitted for clarity. For 20 only one of the two molecules in the asymmetric unit is shown.	127
Figure 5.4. Solutions of 15 in different solvents.....	130
Figure 5.5. UV-Vis of 15 in different solvents recorded at a concentration of 2.0 × 10 ⁻⁵ M.	130
Figure 5.6. Correlation of λ _{max} with solvent parameter index for 15	131
Figure 5.7. UV-Vis spectra of 15–19 in CH ₂ Cl ₂ with a concentration of 2.0 × 10 ⁻⁵ M.	132
Figure 5.8. Molecular structures of (left) Ni(bdt)(^{Me} COObpy) (μβ _o = -581 × 10 ⁻⁴⁸ esu), (center) Ni(dddt)(^{Et} COObpy) (μβ _o = -954 × 10 ⁻⁴⁸ esu) and (right) Ni(mi-5edt)(^{Et} COObpy).....	136
Figure 6.1. Crystal structures of the (left) [Tl ₂ (μ ₂ -bdt) ₂] ²⁻ anion and (right) Sn ₂ (μ ₂ -bdt){N((SiMe ₃) ₂) ₂ (H atoms omitted for clarity).....	146
Figure 6.2. Crystal structures of (left) Ge(bdt) ₂ and (right) [Ge(tdt) ₂ F] ⁻ (H atoms omitted for clarity).	147
Figure 6.3. Asymmetric unit of (a) 21-I , (b) 21-II , (c) 22 and (d) 23 shown in capped sticks.....	150
Figure 6.4. Room temperature PXRD profile for (top) 21-I and (bottom) 21-II , with simulations based on low temperature SC-XRD (dotted lines).	152

Figure 6.5. DSC profile for the phase pure 21-II (needles) at a heating rate of 5°C min ⁻¹	153
Figure 6.6. Variable temperature PXRD profile for (21-I) with simulation based on low temperature SC-XRD (dotted line line), the initial room temperature (blue line), 150 °C (green line), 175 °C (orange line), 200 °C (red line).....	154
Figure 6.7. Capillaries of 21-I at (a) room temperature (b) 175 °C and (c) 225 °C.	154
Figure 6.8. Variable temperature PXRD profile for (21-II) with simulation based on low temperature SC-XRD (dotted blue line), the initial room temperature (blue line) and room temperature PXRD after heating to 240 °C (red line).	155
Figure D.1. Mass spectrum of 1h after storage in a glass vial reveals [1h +K] ⁺ (The isotopomers at 771 correspond to [1h +Na] ⁺ and those at 766 correspond to [1h +NH ₄] ⁺). Inset: comparison of calculated and experimental isotope distribution patterns for [1h +K] ⁺	187
Figure D.2. (top) Experimental HRMS ASAP(+) mass spectrum of 12 and (bottom) simulated HRMS spectrum	188
Figure D.3. Mass spectrometry of 12 showing complexation with ions from the glass vial: 12 +NH ₄ ⁺ (<i>m/z</i> = 516; calculated isotope distribution pattern: 516 = 100, 517 = 25.4, 518 = 13.1, 519 = 2.5) 12 +Na ⁺ (<i>m/z</i> = 521; calculated isotope distribution pattern: 521 = 100, 522 = 25, 523 = 13, 524 = 2.5) and 12 +K ⁺ (<i>m/z</i> = 537; calculated isotope distribution pattern: 537 = 100, 538 = 25, 539 = 20.3, 540 = 4.3, 541 = 1.4). Isotopomers with less than 1% abundance are neglected...	189
Figure D.4. Mass spectrum of 13a showing the 2:1 ratio between the cobalt complex and Na ⁺ [(11) ₂ Na ⁺ : <i>m/z</i> = 931; calculated isotope distribution pattern: 931 = 100, 932 = 45.4, 933 = 29.7, 934 = 10.2, 935 = 3.5). The isotope distribution pattern at 947 corresponds to (11) ₂ K ⁺ (<i>m/z</i> = 947; calculated isotope distribution pattern: 947 = 100, 948 = 45.4, 949 = 36.9, 950 = 13.4, 951 = 5.6, 952 = 1.5) while the isotopomers around 926 correspond to (11) ₂ NH ₄ ⁺ (<i>m/z</i> = 926; calculated isotope distribution pattern: 926 = 100, 927 = 45.8, 928 = 29.9, 929 = 10.3, 930 = 3.5). Isotopomers less than 1% abundant are neglected.	189

Figure D.5. Mass spectrum of 13a in the low mass region, revealing the 1:1 ratio between the cobalt complex 11 and Na ⁺ , (11)Na ⁺ ($m/z = 477$, calculated isotope distribution pattern: 477 = 100; 478 = 22.7; 479 = 12.3; 480 = 2.2). Isotopomers with less than 1% abundance are neglected.	190
Figure D.6. Mass spectrum of 13b showing the 2:1 ratio between the cobalt complex 11 and K ⁺ , (11) ₂ K ⁺ ($m/z = 947$; calculated isotope distribution pattern: 947 = 100, 948 = 45.4, 949 = 36.9, 950 = 13.4, 951 = 5.6, 952 = 1.5). Isotopomers with less than 1% abundance are neglected.	191
Figure D.7. Mass spectrometry of 13b showing the 1:1 ratio between the cobalt complex and K ⁺ , (11)K ⁺ ($m/z = 493$; calculated isotope distribution pattern: 493 = 100, 494 = 22.7, 495 = 19.5, 496 = 3.8, 497 = 1.3). Isotopomers with less than 1% abundance are neglected.	191
Figure D.8. Mass spectrum of 13c in the low mass region, highlighting the (11)Rb ⁺ ion ($m/z = 539$, calculated isotope distribution pattern: 539 = 100; 540 = 22.7, 541 = 50.8, 542 = 11, 543 = 5.2). Isotopomers with less than 1% abundance are neglected.	192
Figure D.9. Mass spectrometry of 13d showing the 2:1 ratio between the cobalt complex and Cs ⁺ , (3) ₂ Cs ⁺ ($m/z = 1041$; calculated isotope distribution pattern: 1041 = 100, 1042 = 45.4, 1043 = 29.7, 1044 = 10.2, 1045 = 3.5). Isotopomers with less than 1% abundance are neglected.	192
Figure D.10. Mass spectrometry of 13d showing the 1:1 ratio between the cobalt complex and Cs ⁺ , (11)Cs ⁺ ($m/z = 587$; calculated isotope distribution pattern: 587 = 100, 588 = 22.7, 589 = 12.3, 590 = 2.2). Isotopomers with less than 1% abundance are neglected.	193
Figure D.11. Comparison of experimental and computed UV-Vis spectra for 11	194
Figure D.12. Frontier orbitals for 11 computed at the M06/LACV3P**+/COSMO(CH ₂ Cl ₂) level of theory.	195

LIST OF CHARTS

Chart 1.1. The dithiete ring (Ia) and its 1,2-dithioketone tautomer (Ib), along with the 1,2,5,6-tetrathiocin (II) and higher trimeric and tetrameric oligomers, III and IV	1
Chart 1.2. Structures of dithietes determined by X-ray diffraction.	5
Chart 1.3. Structures of natural products containing the tetrathiocin functional group. .	24

LIST OF SCHEMES

Scheme 1.1. Preparative routes to dithietes.....	3
Scheme 1.2. Formation of benzodithiete through thermal decomposition.....	4
Scheme 1.3. Cycloaddition chemistry of dithietes.	6
Scheme 1.4. Ring-opening and ring-expansion reactions of dithietes.	7
Scheme 1.5. Reactivity of group 6, 7 and 8 complexes with dithietes.....	9
Scheme 1.6. Reactivity of group 10 complexes with dithietes.....	11
Scheme 1.7. Reactivity of Group 11 complexes with dithietes.....	12
Scheme 1.8. Reaction of dithietes with phosphorus compounds.	13
Scheme 1.9. Oligomerization of dithietes.	14
Scheme 1.10. Synthetic routes to tetrathiocins.....	15
Scheme 1.11. Ring-opening reactions of tetrathiocins through oxidation and reduction processes are frequently coupled to ring-closing reactions.	19
Scheme 1.12. Photo-induced reactions of tetrathiocins.....	20
Scheme 1.13. (top) mechanistic path for the Mo(bdt)(tfd) ₂ -catalyzed reaction of dibenzo-1,2,5,6-tetrathiocin with alkenes ⁸⁸ (bottom) Mo(bdt)(tfd) ₂ catalysed cyclisation reactions.	21
Scheme 1.14. Formation of dithiolate complexes from tetrathiocins through ligand exchange.	22
Scheme 1.15. Reactivity of the tetramethoxy-dibenzo-1,2,5,6-tetrathiocin with low valent (top) transition metals and (bottom) main group P(I) compounds.	23
Scheme 1.16. Proposed mechanism for extrusion of Zn ²⁺ from zinc finger proteins [reproduced with permission from reference 62].	25
Scheme 1.17. Ring transformations between oligomers of dithietes	27
Scheme 1.18. Cycloaddition reactions of the tetramer, [(MeO ₂ C) ₂ C ₂ S ₂] ₄	28
Scheme 2.1 Synthesis of group 10 dithiolates.....	38
Scheme 2.3. Garner's route to the benzene dithiol precursors. The final steps to complex formation involve ligand deprotonation and complexation.....	41

Scheme 3.1. The [2+2] cyclization of <i>trans</i> -cinnamic acid to produce the α -truxillic acid and β -truxinic acid (H atoms omitted for clarity).....	71
Scheme 3.2. Reaction equilibrium between the monomer CpCo(bdt) and the dimer [CpCo(bdt)] ₂	73
Scheme 4.1. Transformations between the monomer CpCo(bdt) and the dimer [CpCo(bdt)] ₂	96
Scheme 4.2. Symmetric derivatives of CpCo(bdt) (X = F, Cl, Br, Ph. Y = H; X = H, Y = S ⁱ Pr).	97
Scheme 4.3. Synthesis of macrocyclic cyclopentadienyl cobalt dithiolate complexes 11 and 12 ; Route (a) – (f) taken from reference [13]; (g) – (h) this work. (a) Br ₂ , HOAc, rt; (b) Cu ⁿ Bu, quinoline, pyridine, reflux; (c) Li(s), NH ₃ (l); (d) 12 M HCl; (e) K(s), MeOH; (f) CpCo(CO)I ₂ , CH ₂ Cl ₂ ; (g) S ₂ Cl ₂ , HOAc, rt; (h) CpCo(CO) ₂ , PhMe, 150°C, μ -wave.....	98
Scheme 4.4. Alkali-metal cation binding to 11 [M = Na, K, Rb, Cs]	104
Scheme 4.8. Oxidation of the benzenedithiolate ligand to form a disulfide.	109
Scheme 6.1. Proposed ligand redistribution reaction of Ge(dmobdt)Cl ₂ to form Ge(dmobdt) ₂	148
Scheme 7.1. Outlook of <i>p</i> -block reactivity to date.....	163
Scheme 7.2. Possible reactivity of tetrathiocins with other group 6–10 <i>d</i> -block metals.....	164

LIST OF ABBREVIATIONS AND SYMBOLS

μm	micrometer
μwave	microwave
Ad	adamantyl
ASAP	atmospheric solids analysis probe (mass spectrometry)
b-15-c-5	benzo-15-crown-5, $\text{C}_{14}\text{H}_{20}\text{O}_5$
b-18-c-6	benzo-18-crown-6, $\text{C}_{16}\text{H}_{24}\text{O}_6$
bdt^{2-}	1,2-benzenedithiolate dianion, $[\text{C}_6\text{H}_4\text{S}_2]^{2-}$
bpy	bipyridine
cm^{-1}	wavenumber
COD	1,5-Cyclooctadiene, C_8H_{12}
COT	cyclo-octatetraene
Cp	cyclopentadienyl group, C_5H_5^-
Cp^*	pentamethylcyclopentadienyl group, $[\text{C}_5(\text{CH}_3)_5]^-$
CSD	crystallographic structural database
dab	N,N'- disubstituted-diazabutadiene
dba	dibenzylideneacetone, $\text{C}_{17}\text{H}_{14}\text{O}$
DCM	dichloromethane
DCM- d_2	deuterated dichloromethane
ddd^{2-}	5,6-dihydro-1,4-dithiine-2,3-dithiolate dianion, $[\text{C}_2\text{H}_4\text{S}_2\text{C}_2\text{S}_2]^{2-}$
deobdt	4,5-diethoxybenzene-1,2-dithiolato
DFT	density functional theory
dmbimdt	N,N-dimethylimidazolonebenzene-1,2-dithiolato
dmdoxlbdt	2,2-dimethoxydioxolobenzene-1,2-dithiolato
DMF	N, N'-dimethylformamide
dmobdt	4,5-dimethoxybenzene-1,2-dithiolato
DMSO	dimethyl sulfoxide
DMSO- d_6	deuterated dimethyl sulfoxide

doxlbdt	dioxolobenzene-1,2-dithiolato
doxbd	dioxanobenzene-1,2-dithiolato
doxebdt	dioxepinobenzene-1,2-dithiolato
dppb	diphenylphosphinobutane, $\text{Ph}_2\text{P}(\text{CH}_2)_4\text{PPh}_2$
dppe	diphenylphosphinoethane, $\text{Ph}_2\text{PCH}_2\text{CH}_2\text{PPh}_2$
dppf	diphenylphosphinoferrrocene, $\text{Ph}_2\text{PC}_5\text{H}_4\text{FeC}_5\text{H}_4\text{PPh}_2$
dppp	diphenylphosphinopropane $\text{Ph}_2\text{P}(\text{CH}_2)_3\text{PPh}_2$
dt	1,2-dithiolato (generic ligand)
EFISH	electric field induced second harmonic
esd	estimated standard deviation (crystallography)
ESI	electron spray ionization (mass spectrometry)
Et	ethyl
EtOH	ethanol
<i>f</i>	oscillator strength (spectroscopy)
FT	Fourier-transform
g	gram
Hz	hertz
h	hour
HOMO	highest occupied molecular orbital
HRMS	high resolution mass spectroscopy
HTT	hexathiotriphenylene anion, $[\text{C}_{18}\text{S}_6]^{6-}$
IR	Infra-red
LUMO	lowest unpaired molecular orbital
LRMS	low resolution mass spectroscopy
<i>m</i>	meta
m	multiplet
(m)	medium
M	molarity (mol L^{-1})
MALDI-TOF	matrix-assisted laser desorption/ionization–time of flight (mass spectroscopy)

mCPBA	meta-chloroperoxybenzoic acid, C ₇ H ₅ ClO ₃
Me	methyl
MeCN	acetonitrile
MeCN-d ₃	deuterated acetonitrile
MeI	methyl iodide, CH ₃ I
MeOH	methanol
MHz	megahertz
mi-5edt	1,1-(N-methylindol-5-yl)ethene-1,2-dithiolate anion, [C ₁₁ H ₉ NS ₂] ²⁻
mL	millilitre
mm	millimeter
MMLL'CT	mixed-metal ligand-to-ligand charge transfer
mmol	millimole
mnt	maleonitriledithiolate dianion, [(CN) ₂ C ₂ S ₂] ²⁻
MS	mass spectrometry
ⁿ Bu	normal-butyl
NLO	Non-linear optics
nm	nanometers
NMR	nuclear magnetic resonance
<i>o</i>	ortho
OTf	triflate anion, [CF ₃ SO ₃] ⁻
<i>p</i>	para
PCM	polarizable continuum model
Ph	phenyl
PhMe	toluene
ppm	parts per million
PXRD	powder X-ray diffraction
q	quartet
s	singlet
(s)	strong
SCE	saturated calomel electrode

SCSC	single crystal to single crystal
SC-XRD	Single crystal X-ray diffraction
T	triplet
^t Bu	<i>tert</i> -butyl
TD-DFT	Time-dependent density functional theory
tdt ²⁻	toluene dithiolate (4-methyl-benzene,1,2-dithiolato)
tfd ²⁻	1,2-bis(trifluoromethyl)ethene-1,2-dithiolate dianion, [(CF ₃) ₂ C ₂ S ₂] ²⁻
THF	tetrahydrofuran
TTF	tetrathiafulvalene
UV	ultraviolet-visible
(vs)	very strong
VT-PXRD	variable temperature powder X-ray diffraction
(vw)	very weak
(w)	weak

CHAPTER 1: INTRODUCTION

1.1 Introduction to dithietes and higher oligomers

Highly strained molecules, such as epoxides and aziridines are often used as building blocks in chemistry due to their high reactivity but well-defined chemical outcomes. For example, epoxides tend to undergo regioselective S_N2 reactions at the heterocyclic carbon atom with inversion of stereochemistry,¹ while the chemistry of the less well studied aziridine compounds have been reviewed in relation to epoxide chemistry.² The strained nature of these rings means they are often challenging to prepare and/or are extremely reactive.

Within this family, 1,2-dithietes (**Ia**, Chart 1.1) are 4-membered rings comprising a 6π aromatic core. It is well known that disulfides ($RS-SR$) prefer to adopt a *ca.* 90° torsional orientation around the S-S bond in order to minimize lone pair interactions between S atoms (Figure 1.1).³

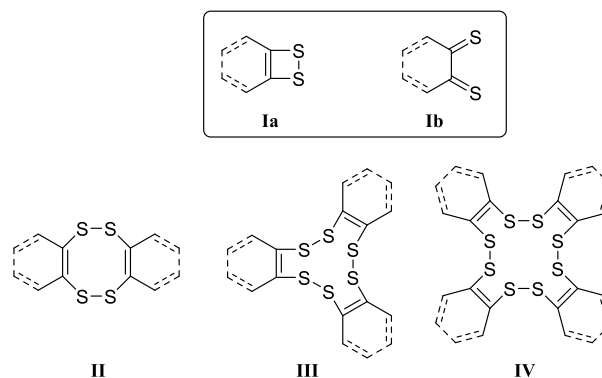


Chart 1.1. The dithiete ring (**Ia**) and its 1,2-dithioketone tautomer (**Ib**), along with the 1,2,5,6-tetrathiocin (**II**) and higher trimeric and tetrameric oligomers, **III** and **IV**.

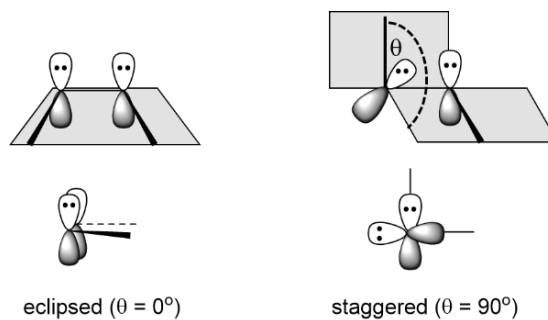


Figure 1.1. Lone pair repulsion in planar *cis*-oid and non-planar twisted disulfides.

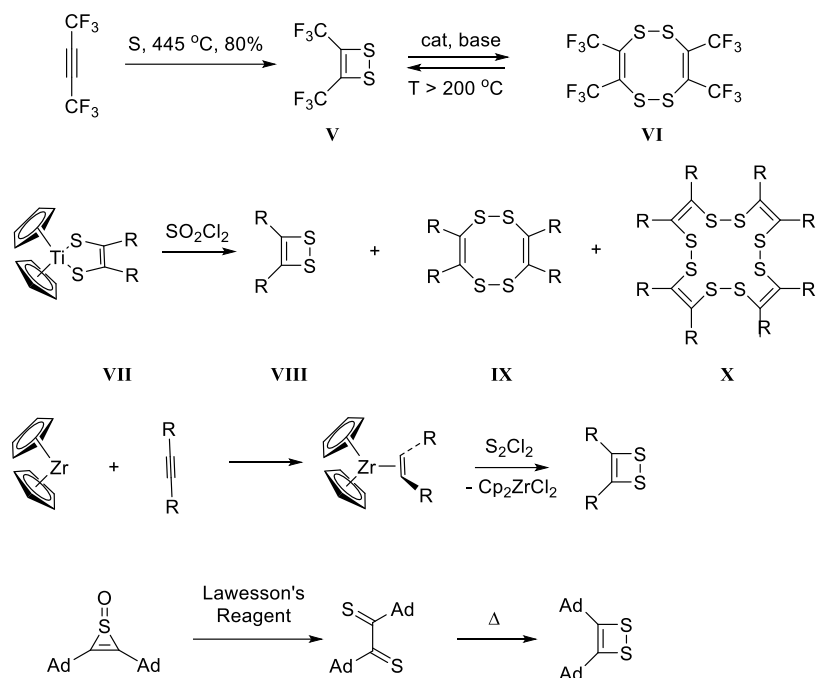
Deviation from 90° is typically associated with S–S bond weakening. When the S–S bond is a part of a dithiete ring, the *cis*-oid planar conformation is enforced, maximizing lone pair repulsions between S atoms. This weakens the S–S bond, making dithietes reactive species whose isolation can be challenging. Despite this destabilization, computational studies indicate a close energetic balance with their acyclic dithio-ketone tautomer (**Ib**).⁴ Indeed the dithio-ketone tautomer only appears prevalent when it comprises part of a strained cyclic system such as recent reports on thiosquaramides,⁵ or bulky substituents such as ^tBu and adamantyl, whereas electron-donating groups move the equilibrium towards the dithione tautomer.⁶

In this Chapter, the chemistry of dithietes, R₂C₂S₂, is reviewed and their (quasi-) reversible conversion to 1,2,5,6-tetrathiocins (R₂C₂S₂)_n (*n* = 2, **II**) and higher oligomers (*n* = 3, **III** and *n* = 4, **IV**; Chart 1.1) described. Reactivity studies on tetrathiocins are compared with the known chemistry of dithietes to show that while these unstrained tetrathiocins have long term stability, their reactivity patterns seem to largely follow those of their more reactive dithiete congeners.

1.2 Dithietes

1.2.1. Preparation

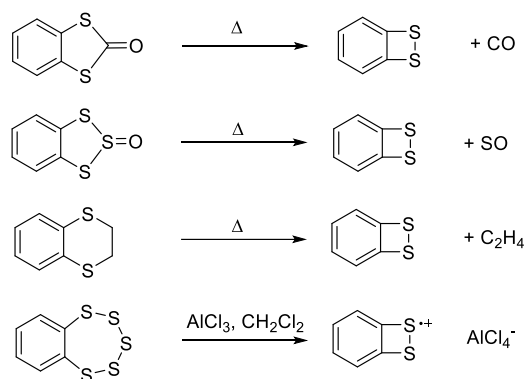
The first dithiete, (F₃C)₂C₂S₂ (**V**) was reported in 1960 from the reaction of hexafluorobut-2-yne with sulfur vapours at 445 °C in 80% yield (Scheme 1.1).⁷ Trace amounts of base facilitates S–S bond cleavage and catalyses its dimerization to form the tetrathiocin (**VI**).⁸ Notably these early studies showed that the tetrathiocin **VI** converts back to entropically favored **V** at temperatures above 200 °C.⁶ Several other fluorinated derivatives have been prepared in a similar fashion⁹ and this methodology has also been exploited to prepare dithietes from a range of both acyclic alkynes RC≡CR (R = ^tBu, Ad, Ph) and cyclic alkynes, though not all (R = COCF₃ and CO₂Me) yield the dithietes cleanly.¹⁰



Scheme 1.1. Preparative routes to dithietes.

An alternative strategy to prepare 1,2-dithietes is the reduction of transition metal dithiolate complexes. For example, the titanocene derivative **VII** reacts with SO_2Cl_2 to form the dithiete **VIII** ($\text{R} = \text{CO}_2\text{Me}$) as the major product (66%) and the larger oligomers **IX** and **X** ($\text{R} = \text{CO}_2\text{Me}$) as the minor products (Scheme 1.1).^{11,12} An alternative transition-metal mediated process is the reaction of acetylenes with zirconocene, followed by treatment with sulfur monochloride, S_2Cl_2 (Scheme 1.1), forming the dithiete and eliminating zirconocene dichloride.³ Ring expansion reactions have also been implemented with the 1-adamantyl dithiete ($\text{R} = \text{Ad}$) prepared from the dithiirane-1-oxide by treatment with Lawesson's reagent, $[(p\text{-MeOC}_6\text{H}_4)_2\text{P}_2\text{S}_4]$, initially forming the *trans*-1,2-dithione as purple crystals (Scheme 1.1).⁶ At elevated temperatures *trans/cis* isomerization and cyclization occur to form the dithiete with $\Delta H^\ddagger = 74 \text{ kJ mol}^{-1}$. Other strategies to dithietes typically involve thermal¹³ or photolytic¹⁴ entropically-driven ring contractions with elimination of volatile side products such as CO , SO or C_2H_4 (Scheme 1.2). Notably desulfurization of cyclic polysulfides in the presence of a Lewis acid such as AlCl_3 was proposed to lead to the $1e^-$ oxidized radical cation (Scheme 1.2) rather than the dithiete.¹⁵ However, studies by Passmore prepared and crystallographically characterized the

bis(trifluoromethyl)-trithiolylium radical cation, $[(F_3C)_2SSS]^{+\bullet}$ and showed its EPR spectrum was identical to $[(F_3C)_2SS]^{+\bullet}$, casting some doubt over the nature of the paramagnetic species generated during these desulfurization reactions.¹⁶ Such ring contraction reactions have been implemented to prepare benzannulated dithietes. The parent benzodithiete was first described in 1926 but analytical data were sparse.¹⁷ Subsequent spectroscopic studies indicated that the parent benzodithiete is a transient species, unstable above 180 K,¹³ and an unspecified larger oligomer was proposed based on the high melting point (185–190 °C).⁸



Scheme 1.2. Formation of benzodithiete through thermal decomposition.

1.2.2. Structural studies of dithietes

A report of the structure of **V**, determined by electron diffraction in the gas phase, revealed the dithiete ring essentially planar with C=C and S–S bond lengths of 1.40 ± 0.03 Å and 2.05 ± 0.01 Å respectively.¹⁸ The solid state structures of several dithietes and benzannulated derivatives (**XI–XIV**) have been determined by X-ray diffraction (Chart 1.2).^{9,11,19} While the benzo-fused derivatives **XI** and **XII** exhibit C–C–S bond angles (100.5 – 103.3°) comparable to the non-fused derivatives **XIII** and **XIV** (101.5 – 102°), the S–S bond lengths in **XI** and **XII** (2.12 – 2.13 Å) are a little longer than those for structurally determined acyclic derivatives **XIII** and **XIV** (2.07 – 2.09 Å) and conventional S–S bonds (2.06 Å in S_8). These geometric differences appear correlated with ring strain and the nature of the C–C bond; longer C–C bond lengths (average 1.39 Å) in the benzo-fused derivatives are accompanied by longer S–S bond lengths, whereas the shorter C=C bonds in **XIII** and

XIV (average 1.36 Å) lead to shorter S–S bonds. The average S–S distance across the series averages 2.10(2) Å.

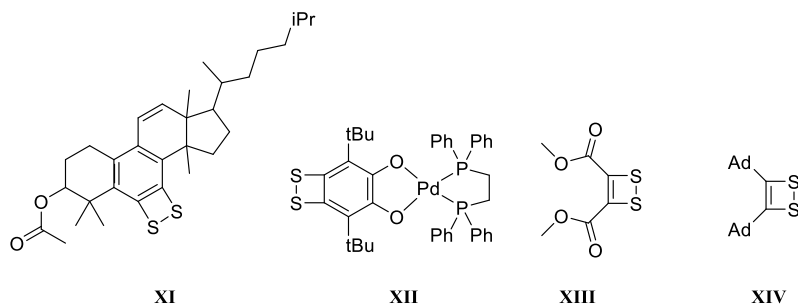


Chart 1.2. Structures of dithietes determined by X-ray diffraction.

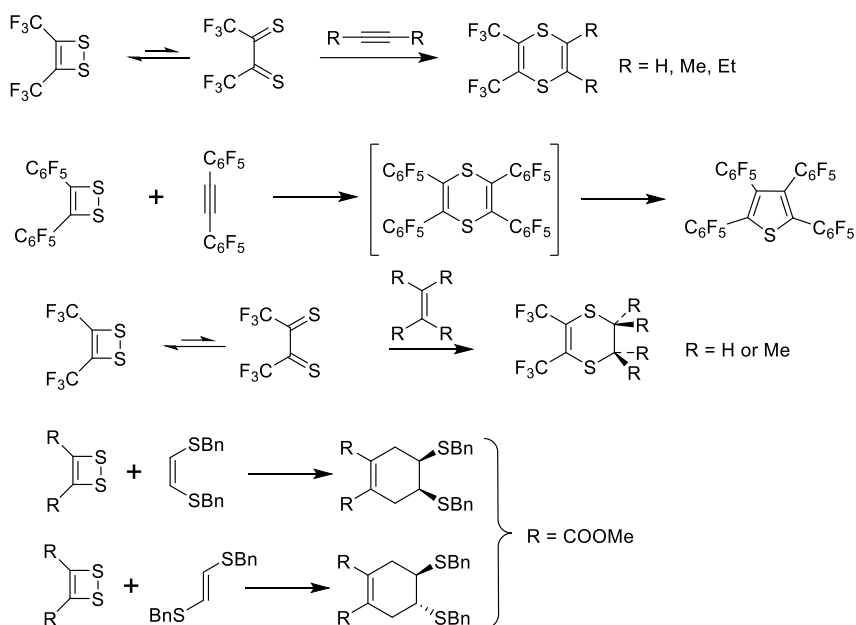
1.2.3. Computational studies on dithietes

Calculations at the Hartree–Fock, post-Hartree–Fock and Density functional levels of theory have examined the stability of the dithiete (**Ia**) in relation to the acyclic dithione (**Ib**, *cis* or *trans*). These reveal that polarization functions are essential, particularly for S, to provide a good electronic description of these molecules.²⁰ At the CCSD(T)/cc-pVTZ level of theory the dithiete H₂C₂S₂ is more stable than both the *trans*-dithione (+13 kJ mol⁻¹) and the *cis*-dithione (+33 kJ mol⁻¹) tautomers.⁴ Despite the similar thermodynamic stability of the dithiete and dithione, calculations at a range of levels reveal a substantial energy barrier to ring-opening (*ca.* 90 kJ mol⁻¹).²¹ The relative stability of the dithiete in relation to the dithione is even more pronounced for the benzo-fused derivatives; the benzodithiete is computed (MP2/6-31G*) to be substantially more stable (73 kJ mol⁻¹) than the *ortho*-benzodithioquinone while the parent H₂C₂S₂ system shows the dithiete to be more stable by just 27 kJ mol⁻¹.⁴ Such differences likely lead to significant differences in chemical reactivity between dithietes (where the dithione form appears to play an important role) and their benzannulated analogs.

1.2.4. Reactivity

Organic chemistry of dithietes. The organic reactivity of dithietes appear to largely reflect the dithione tautomer, acting as 4π dienes in Diels–Alder reactions with alkynes to form dithiins (Scheme 1.3). Substituted thiophenes are often observed as by-products of these reactions, thermally driven through elimination of sulfur and aromatization of the ring, with the thiophene favored as the dominant product at elevated temperatures.^{8,22,23}

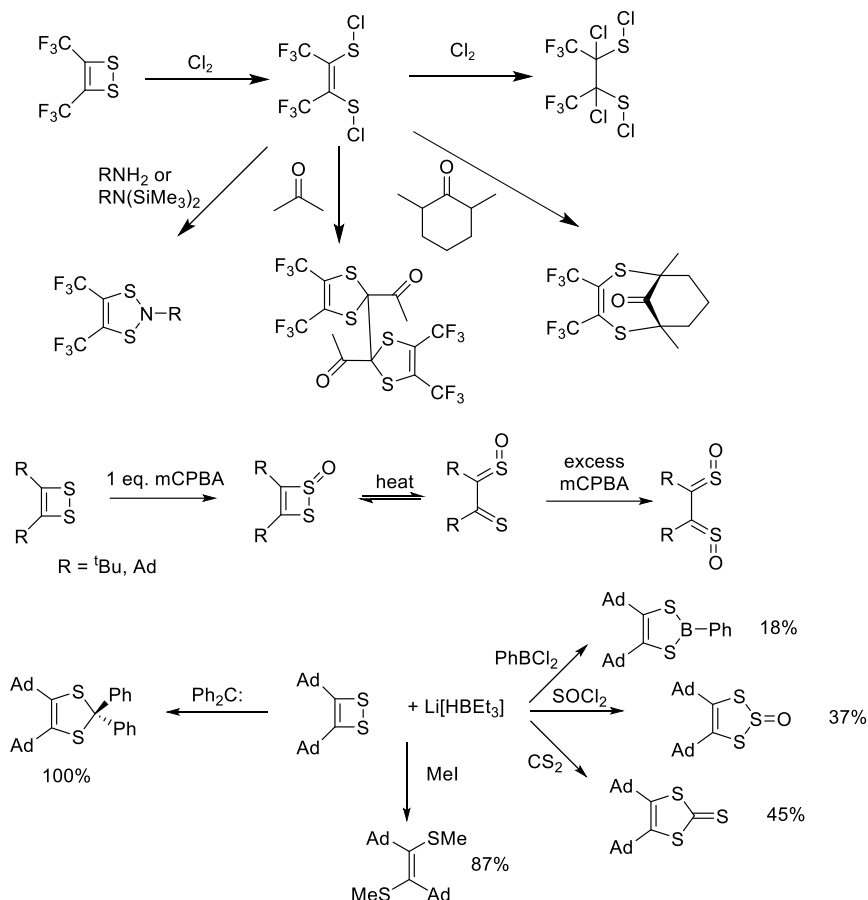
Cycloaddition reactions with alkenes have also been reported to form dihydrodithiins. Yields are typically moderate (22–72%).^{7,24,25} The cyclizations of the *Z* and *E* isomers of BnSCH=CHSBn occurred stereospecifically (Scheme 1.3), suggesting a concerted reaction pathway, consistent with a Diels–Alder cyclization mediated *via* the 1,2-dithione. Computational studies indicate that the cyclization follows a reverse electron demand process where the dominant frontier orbital interaction involves the HOMO of the alkene and the LUMO of the dithione.²⁵



Scheme 1.3. Cycloaddition chemistry of dithietes.

Chlorination of the bis(trifluoromethyl) dithiete **V** affords the bis(sulfenyl chloride) which undergoes condensation with primary amines to form dithiazoles while reaction with reactive methylene groups such as β -dicarbonyls forms dithioles.²⁶ Extended chlorination leads to chlorination of the C=C double bond. Oxidation of the bis(adamantyl)dithiete (R = Ad) with one equivalent of mCPBA affords the cyclic 1,2-dithiete *S*-oxide which undergoes a reversible ring-opening at elevated temperature (Scheme 1.4). In the presence of excess mCPBA, dithietes (R = *t*Bu, Ad, Me₂CCH₂CH₂CH₂CMe₂) form the corresponding disulfine which were identified as *E,E*, *E,Z* and *Z,Z* isomers.^{6,27} The *E,E*-isomer was crystallographically characterized but the *E,Z* and *Z,Z* isomers exist in equilibrium at room temperature. Heating the *E,E*-isomer in refluxing 1,2-dichlorobenzene

led to some isomerization to *E,Z* and *Z,Z* isomers. The disulfines are thermally robust and appear unreactive with respect to dienes, dienophiles and *o*-phenylene diamine. No evidence for further oxidation to the sulfene occurred in the presence of excess mCPBA. *In situ* generation of the carbene, R_2C , in the presence of the bis(adamantyl)dithiete leads to insertion of the R_2C group into the S–S bond in quantitative yield.²⁸



Scheme 1.4. Ring-opening and ring-expansion reactions of dithietes.

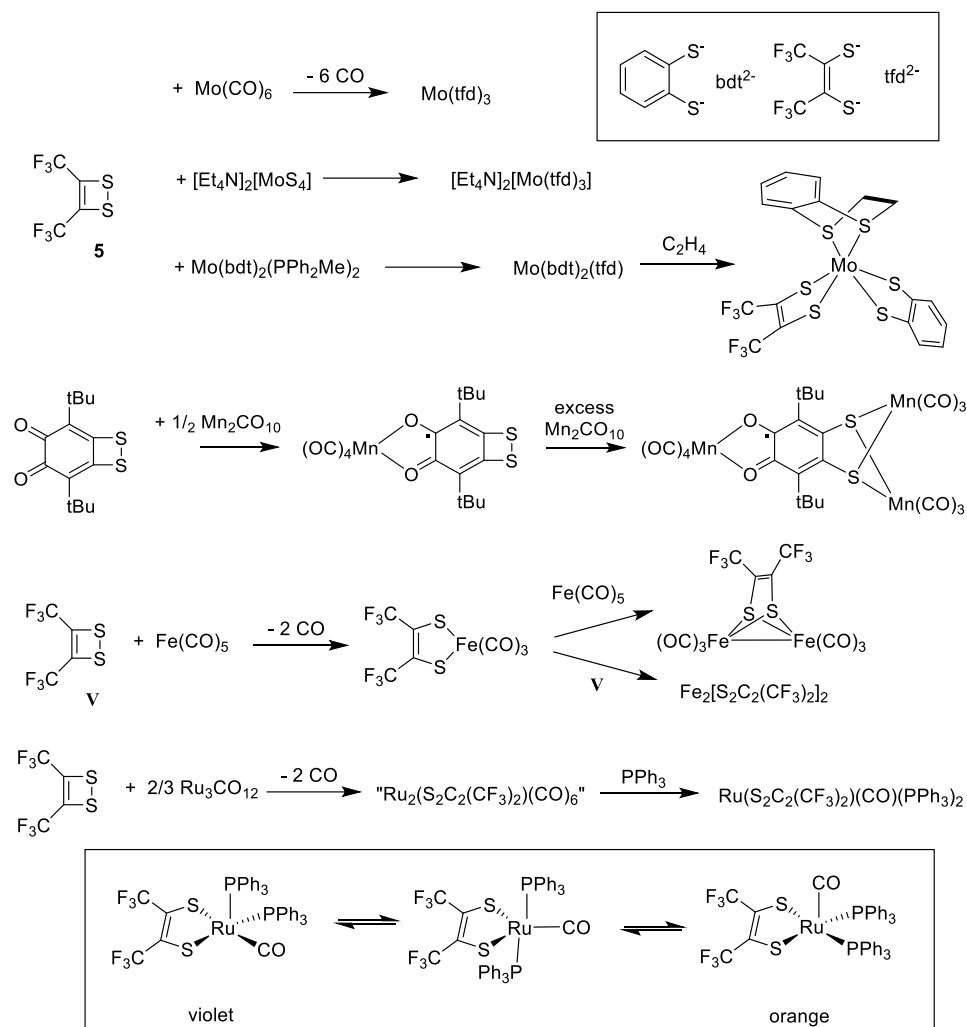
Reduction with $Li[BHET_3]$, followed by condensation with $SOCl_2$, CS_2 and $PhBCl_2$ lead to ring expansion products in modest yields while ring opening can be achieved to form the *E*-isomer upon lithiation and addition of MeI in excellent yield (Scheme 1.4).²⁸

Inorganic chemistry of dithietes. Dithietes undergo oxidative addition reactions to both main group compounds and low valent transition metal complexes. Such reactivity is comparable to the organic cycloaddition reactions where electron-flow is from the alkene to the LUMO of the dithione. The oxidative addition chemistry of dithietes to transition

metals has been examined extensively and is driven not only by the release of ring strain from the dithiete but also by the favourable chelate effect upon metal coordination.

Group 6. Reaction of the zero-valent metal carbonyl, $\text{Mo}(\text{CO})_6$ with the trifluoromethyl-functionalized dithiete **V** afforded the formal Mo(VI) species $\text{Mo}(\text{tfd})_3$ [$\text{tfd} = (\text{CF}_3)_2\text{C}_2\text{S}_2^{2-}$].²⁹ Similarly oxidative addition of **V** to the Mo(I) complex $[\text{CpMo}(\text{CO})_3]_2$ afforded the asymmetric dinuclear Mo(III) complex, $[\text{CpMo}(\text{CO})_2(\mu\text{-tfd})_2\text{MoCp}]$ which eliminates CO under irradiation to form the symmetric dimer $[\text{CpMo}(\mu\text{-tfd})_2]_2$.³⁰ Ligand exchange between **V** and $[\text{Et}_4\text{N}]_2[\text{MS}_4]$ ($\text{M} = \text{Mo}, \text{W}$) provided a route to the related Mo(IV) complexes $[\text{Et}_4\text{N}]_2[\text{M}(\text{tfd})_3]$.³¹ Similar substitution reactions include work to develop push-pull molybdenum tris(thiolene) complexes *via* reaction of $\text{Mo}(\text{bdt})_2(\text{PPh}_2\text{Me})_2$ with 3.3 equivalents of **V** to form $\text{Mo}(\text{bdt})_2(\text{tfd})$ [$\text{bdt} = \text{benzene dithiolate}, \text{C}_6\text{H}_4\text{S}_2^{2-}$].³² These asymmetric tris(dithiolene) complexes show an unconventional binding of ethene at sulfur and have been implemented as catalysts for the cycloaddition chemistry of tetrathiocins (section 1.3.4). The $2e^-$ reduction of **V** with sodium acenaphthylenide to form the dithiolate, followed by ligand exchange with $[\text{Mo}(=\text{O})\text{Cl}(\text{MeNC})_4]^+$ was used as a route to $[\text{Mo}(=\text{O})(\text{tfd})_2]$ as a model for the active site of molybdoenzymes.³³

Group 7. The quinone/dithiete ligand, $\text{O}_2\text{C}_6^t\text{Bu}_2\text{S}_2$, (Scheme 1.5) offers both hard and soft metal binding sites. Initial reaction with $\text{Mn}_2\text{CO}_{10}$ occurs at the harder quinone site, with addition to the dithiete occurring afterwards.³⁴ This should be contrasted with the reactivity of this ligand to group 10 and 11 metals (*vide infra*).



Scheme 1.5. Reactivity of group 6, 7 and 8 complexes with dithietes.

Group 8. Initial work showed that the outcome of the reaction of the trifluoromethyl-functionalized dithiete **V** with Fe(CO)_5 is sensitive to reaction stoichiometry: a 1:1 mole ratio afforded a diamagnetic violet Fe(II) dithiolate complex, Fe(tfd)(CO)_3 (Scheme 1.5, $\text{tfd} = (\text{F}_3\text{C})_2\text{C}_2\text{S}_2^{2-}$),³⁵ but formed a bridged bimetallic species when the reaction is carried out in a 1:2 ratio.³⁶ while a 2:1 ratio leads to formation of $\text{Fe}_2(\text{tfd})_2$.³⁷ Substitution of the remaining carbonyls could be achieved using Ph_3E ($\text{E} = \text{P}, \text{As}, \text{Sb}$) and related group 15 donors.³⁵ The analogous reaction with $\text{Ru}_3\text{CO}_{12}$ afforded an incompletely characterized compound of approximate composition $\text{Ru}_2(\text{tfd})(\text{CO})_6$.³⁵ Addition of PPh_3 affords $\text{Ru(tfd)(CO)(PR}_3)_2$ which exists as two different five coordinate

structural isomers.³⁸ Recent studies have examined the isomerisation of these two structural isomers and identified the intermediate in the Berry pseudo-rotation process (Scheme 1.5).³⁹

Group 10. Reaction of **V** with nickel powder in a bomb afforded the formal Ni(IV) dithiolate complex, Ni(tfd)₂.⁴⁰ This complex was found to activate ethene. In this case two possible activation processes exist; the first, an orbitally symmetry-forbidden addition, formed an isolable inter-ligand adduct, where ethene bonds across the two dithiolate ligands. Whereas, the second possibility, is the symmetry-allowed intra-ligand complex (analogous to Mo(bdt)₂(tfd), described above) was found to be unstable and led to decomposition with elimination of the dihydrodithiin. In a similar fashion, a range of Ni(IV) dithiolates (R = H, R' = CF(CF₃)₂, Scheme 1.6) were prepared from RANEY[®] nickel and the dithiete and examined as a potential *p*-dopant (a hole injection layer) for the generation of improved organic semi-conductor matrix materials.⁴¹ In terms of the heavier group 10 metals, oxidative addition of dithietes to Pt(PPh₃)₂(C₂H₄) afforded the square planar Pt(II) dithiolate complex, R₂C₂S₂Pt(PPh₃)₂.⁶ In the absence of additional coordinating ligands, reaction of the bis(trifluoromethyl)dithiete **V** with Pd₂dba₃ afforded the hexanuclear Pd(II) complex, Pd₆(tfd)₆, comprising a face-capped cube motif with bridging dithiolate ligands (Figure 1.2).⁴² The orthoquinone-dithiete, O₂C₆(^tBu)₂S₂, offers both hard and soft metal binding sites for oxidative addition. When reacted with M(PPh₃)₄ (M = Pd, Pt), the reaction occurs regioselectively at the dithiete ring.³⁴ Subsequent 1e⁻ reduction with Tl, K or Mn₂CO₁₀ led to reduction of the *ortho*-quinone to generate semiquinone radicals. Conversely, a pair of regio-isomers are formed in a *ca.* 50:50 mole ratio with Pd₂dba₃ in the presence of dppe when the reaction is undertaken in toluene,⁴³ though the composition is solvent dependent. The two regio-isomers interconvert in THF at room temperature. Computational studies support the dithiolate isomer as being more stable by *ca.* 20 kJ mol⁻¹. This chemistry appears unique to the chelating dppe ligand. When the oxidative addition is carried out in the presence of other chelating ligands such as dppp, dppb and dppf, the reactions all appear regiospecific, selectively undergoing coordination at the dithiete.⁴⁴

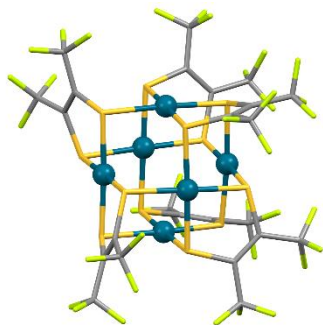
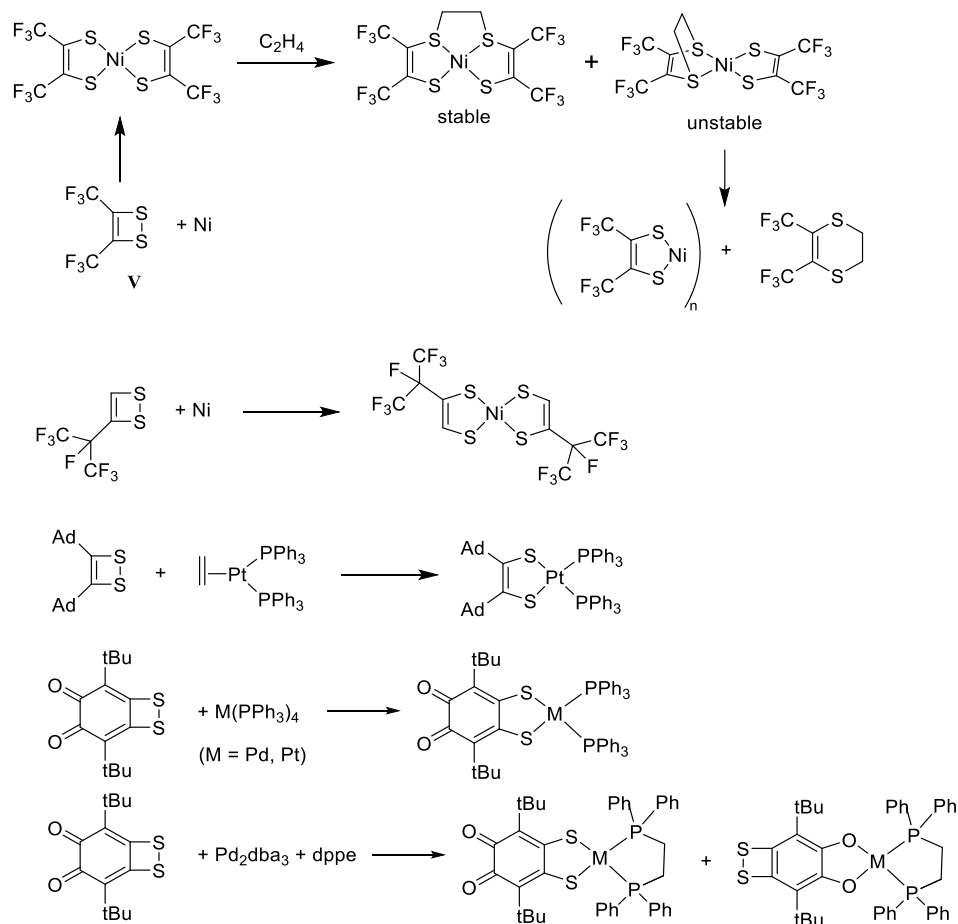


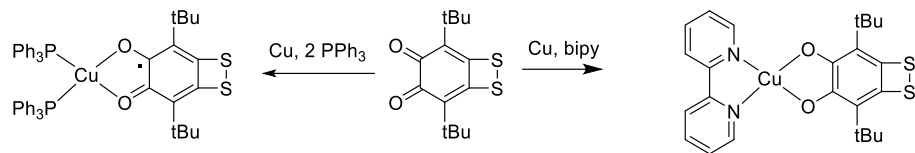
Figure 1.2. Crystal structure of the hexanuclear complex $\text{Pd}_6(\text{tfd})_6$.⁴²



Scheme 1.6. Reactivity of group 10 complexes with dithietes.

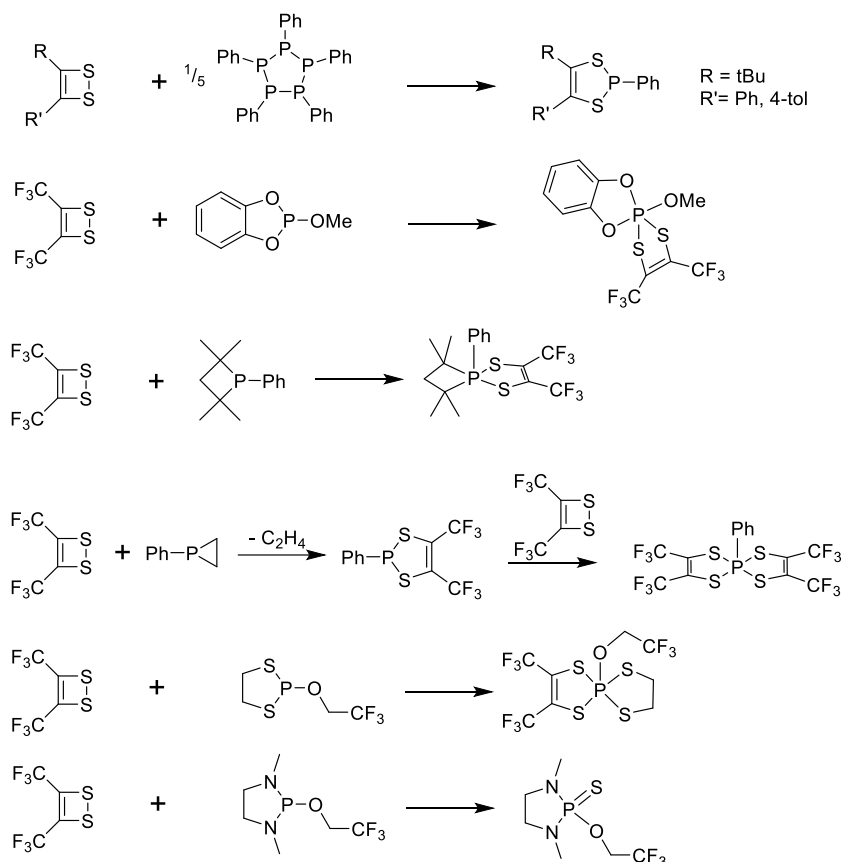
Group 11. Reaction of the quinone/dithiete ligand, $\text{O}_2\text{C}_6\text{tBu}_2\text{S}_2$, with copper metal in the presence of triphenyl phosphine leads to a Cu(I)/semiquinone complex, whereas reaction of the same ligand in the presence of bipyridine affords the Cu(II) complex

(Scheme 1.7). In both cases the Cu ion is bound at the semiquinone/catechol site, leaving the softer dithiolene ligand intact.⁴⁵



Scheme 1.7. Reactivity of Group 11 complexes with dithietes

p-Block chemistry. To date, studies of the oxidative addition chemistry of dithietes and *p*-block elements seem largely limited to phosphorus. A recent study examined the generic insertion of the P(I) species “PhP”, in the form of (PhP)₅, into S–S bonds including its reactivity with dithietes leading to the P(III) dithiaphospholes (Scheme 1.8) with recovered yields in the range 73–77%.⁴⁶ Reaction of P(III) compounds such as phosphites and phosphines with the bis(trifluoromethyl)dithiete **V** afforded a series of phosphoranes (Scheme 1.8).^{47,48} In the case of the strained cyclic phosphine, PhPC₂H₄, addition occurred with elimination of ethene and, in the presence of a further equivalent of dithiete, an additional oxidative addition reaction occurred to form the phosphorane. Similar reactivity was reported for a series of 5-membered rings containing P(III) which were shown to react with dithiete **V** to form P(V) systems.⁴⁹ In some cases, the phosphine abstracted sulfur from the dithiete (presumably forming the dithiin). The subtle balance in oxidative addition vs. S-abstraction is reflected in the comparative reactivities of C₂H₄S₂P–OCH₂CF₃ and the NMe analogue (Scheme 1.8) with the NMe derivatives favouring S-abstraction over oxidation.



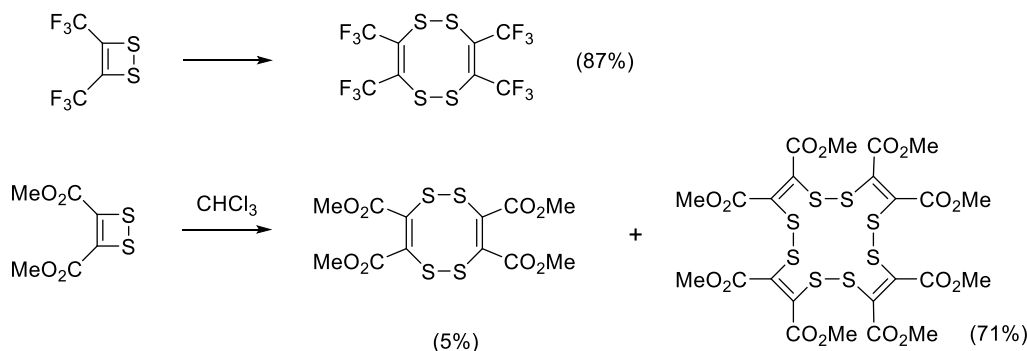
Scheme 1.8. Reaction of dithietes with phosphorus compounds.

In addition to these studies, the reaction of the bis (trifluoromethyl)dithiete **V** with CpIn(I) has been examined, leading to η^1 -CpIn(tfd). Subsequent addition of chelating bpy and phen ligands leads to 5-coordinate In(III).⁵⁰

1.2.6. Ring interconversion reactions

The dithiete **V** is a liquid (bp 93–94 °C) and undergoes slow dimerization at room temperature, depositing the tetrathiocin (mp 110–111 °C) over 2 months in 87% yield (Scheme 1.9). The addition of a drop of Et₃N catalyses this process, affording an immediate exothermic reaction with deposition of the tetrathiocin.^{7,8} Heating the tetrathiocin at 180–220 °C led to distillation of the dithiete **V**, consistent with the dithiete being entropically favoured and the tetrathiocin being the enthalpically favoured product. In contrast, dithiete **XIII** (Chart 2) forms the 16-membered tetramer (75% yield) along with a small quantity of tetrathiocin when stirred in neat CHCl₃.¹² Theoretical studies at the MP2/6-31G* level

of theory revealed the parent dithiete, $\text{H}_2\text{C}_2\text{S}_2$, was less stable than its tetrathiocin dimer, 12-membered cyclic trimer, or 16-membered cyclic tetramer with the tetramer being the most stable.¹² The interconversion between oligomers is discussed in more detail in section 1.4.



Scheme 1.9. Oligomerization of dithietes.

1.3 Introduction to 1,2,5,6-tetrathiocins

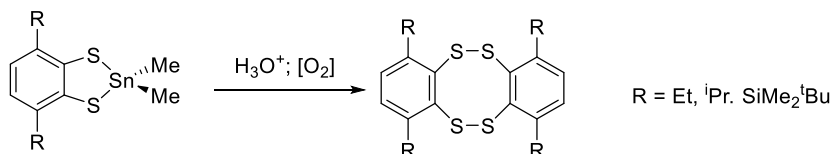
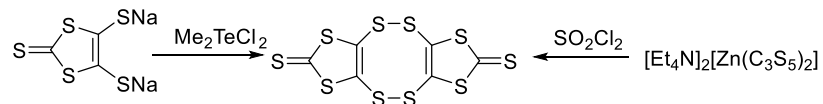
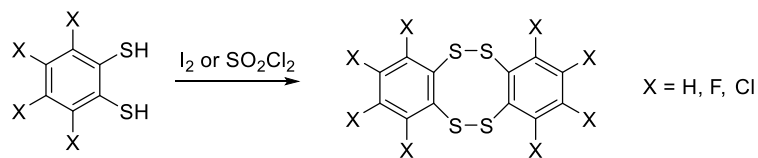
In relation to dithietes, the chemistry of their dimeric form, the 1,2,5,6-tetrathiocin, is much less explored. While examples of tetrathiocins, derived from dimerization of dithietes (section 1.2.6) are known, a large number of tetrathiocins are based on their benzannulated or other fused-ring derivatives.

1.3.1. Preparation

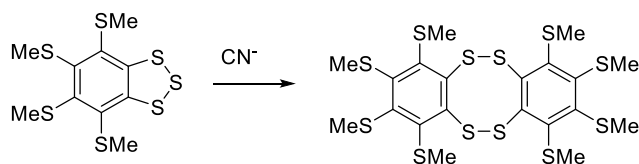
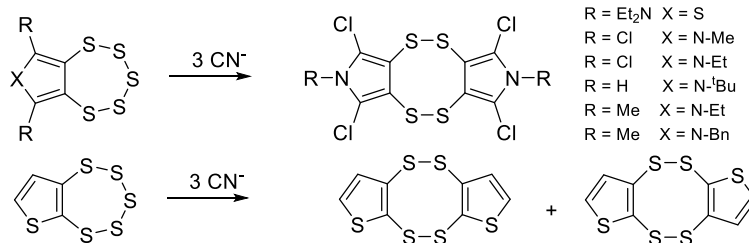
There are numerous reported routes to benzannulated tetrathiocins and other tetrathiocins with fused rings. Here we focus on methodologies which afford tetrathiocins as the major product.

Oxidation of 1,2-dithiols and dithiolates. The preparation of the parent dibenzo-1,2,5,6-tetrathiocin was reported by Field *et al.* in 1961 through oxidation of benzene dithiol with iodine as a mild oxidant (Scheme 1.10).⁵¹ In a similar fashion, Chivers *et al.* reported the oxidation of both fluorinated and chlorinated benzene dithiols $1,2\text{-C}_6\text{X}_4(\text{SH})_2$ ($\text{X} = \text{F}, \text{Cl}$) with I_2 or SO_2Cl_2 afforded the corresponding tetrathiocins with recovered yields greater than 85%.⁵² The superoxide ion has also been implemented in similar processes using benzene or toluene dithiol.⁵³

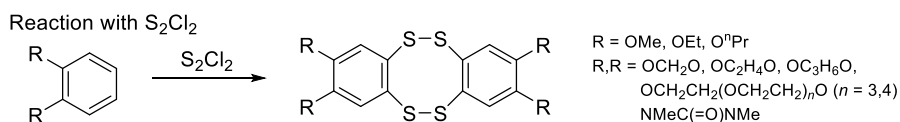
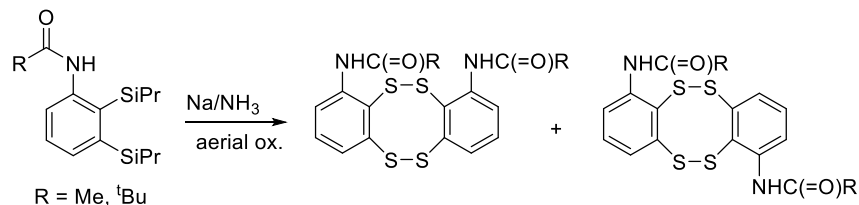
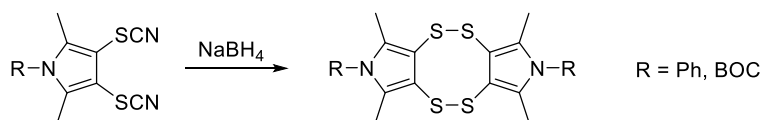
Oxidation of 1,2,-dithiols and 1,2-dithiolates



Ring contraction/dimerization



Reduction



Scheme 1.10. Synthetic routes to tetrathiocins.

A similar synthetic strategy to access 1,2,5,6-tetrathiocins is the oxidation of *s*-, *p*- and *d*-block 1,2-dithiolate complexes using mild oxidants such as I₂, SO₂Cl₂ or mCPBA. For example, oxidation of Na₂[C₃S₅] with Me₂TeCl₂ afforded C₆S₁₀ in 49% yield.⁵⁴ Similarly, oxidation of [Et₄N]₂[Zn(C₃S₅)₂] with SO₂Cl₂ affords selectively the tetrathiocin C₆S₁₀ in 46% yield.⁵⁵ Organo-tin and organo-tellurium dithiolate complexes undergo facile oxidation in high yield when treated with acid followed by aerial oxidation (Scheme 1.10).^{56,57} This methodology has also been applied to the synthesis of the heavier Se analogues in a similar manner.⁵⁷

Via reduction of thio-containing substituents (SCN, SR). Rogers and coworkers showed that reduction of organo-thiocyanates with NaBH₄ could afford tetrathiocins in a quantitative fashion.⁵⁸ This methodology has also been applied to naphthoquinone derivatives in 54% recovered yield using the mild base, NH₄OAc.⁵⁹ Birch reduction of *S*/*Pr* derivatives initially forms dithiols which readily undergo aerial oxidation to afford tetrathiocins in 45–85% recovered yield (Scheme 1.10).⁶⁰

Via ring contraction. Extrusion of sulfur from hetero-cyclic pentasulfides by treatment with Ph₃P or CN⁻ (forming Ph₃P=S or SCN⁻) can lead to tetrathiocins in 54–74% recovered yield.^{61,62} In the case of 2,3-substituted thiophenes, N-methyl indole and pyrroles, mixtures of the two possible tetrathiocin isomers are formed, typically in a 50:50 mole ratio. Benzo-fused trithioles also act as suitable precursors for tetrathiocin synthesis, using CN⁻ or NaBH₄ in good yield (84–95%).^{56,63-65}

Via reaction of S₂Cl₂ with catechol ethers. Work by Stender and co-workers⁶⁶ showed that reaction of catechol ethers with S₂Cl₂ in glacial acetic acid afforded good yields of dibenzo-1,2,5,6-tetrathiocins on a multi-gram scale (Scheme 1.10). The methodology is effective in the presence of π-donor substituents and has also been successfully applied to 1,2-dimethoxy-naphthalene and naphthalenediol with lower recovered yields (29–33%).⁶⁶ Recent exploitation of this methodology has generated a broader range of catechol ethers⁶⁷ including benzo-15-crown-5 and benzo-18-crown-6 as well as functional groups comprising π-donor N (yields: 53–88%), which will be discussed further in Chapter 2.

1.3.2. Structural studies of 1,2,5,6-tetrathiocins

A total of 22 crystal structures (excluding metal complexes and cocrystals) which contain the 1,2,5,6-tetrathiocin group were identified in the 2020 release of the Cambridge Structural Database. The majority of these structures (77%) adopt a chair geometry,^{52,55,57,58,68-80} with just 5 structures adopting a twisted geometry. Notably three of the five structures which adopt a twisted conformation comprise all the non-fused derivatives ($R_1R_2C_2S_2$)₂ ($R_1 = R_2 = CO_2Me$; $R_1 = H$, $R_2 = CO_2Me$; $R_1 = R_2 = H$),^{12,81} along with two benzo-fused derivatives, ($X_4C_6S_2$)₂ ($X = Cl$, MeS).^{52,82} The average S–S bond length for these structures is 2.06(2) Å, the same as that observed in the reported dithiete structures within 3 esd's. The structures of ($C_6F_4S_2$)₂ and ($C_6Cl_4S_2$)₂ are shown in Figure 1.3 as representative of the chair and twisted conformations respectively.⁵²

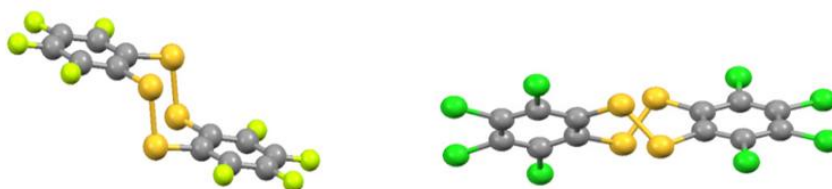


Figure 1.3. Crystal structures of ($C_6F_4S_2$)₂ (**left**) and ($C_6Cl_4S_2$)₂ (**right**) which adopt the chair and twisted conformations respectively.

1.3.3. Computational studies on 1,2,5,6-tetrathiocins

The 1,2,5,6-tetrathiocins can adopt multiple conformations, with six computationally identified local energy minima.⁸³ For annulated derivatives only the three *Z,Z* conformations need be considered and comprise twist, chair and half-chair geometries (Figure 1.4). At the MP2/6-31G* level of theory the twist conformation is more stable than the chair conformation by 22 kJ mol⁻¹,⁸³ although such a quantitative interpretation at this level of theory should be treated with some caution (see discussion of computational studies on dithietes and the importance of incorporating adequate polarization functions). The half-chair conformation is least stable and is consistent with crystallographic studies which have, to date, revealed examples of only the chair and twist conformations.

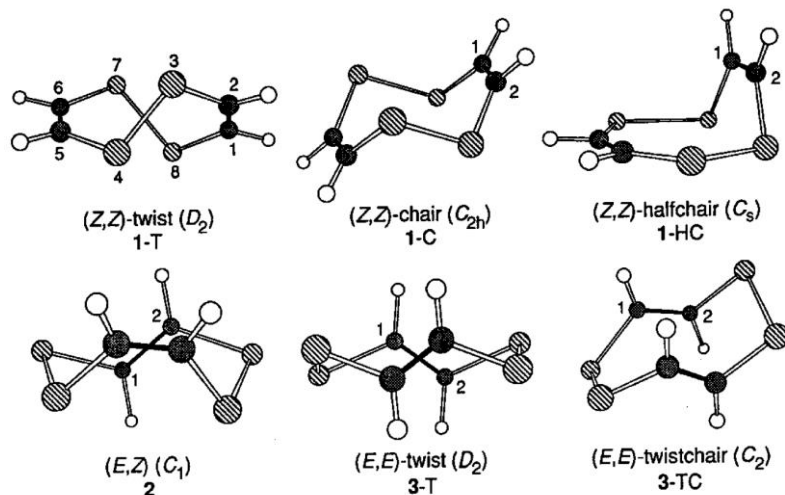


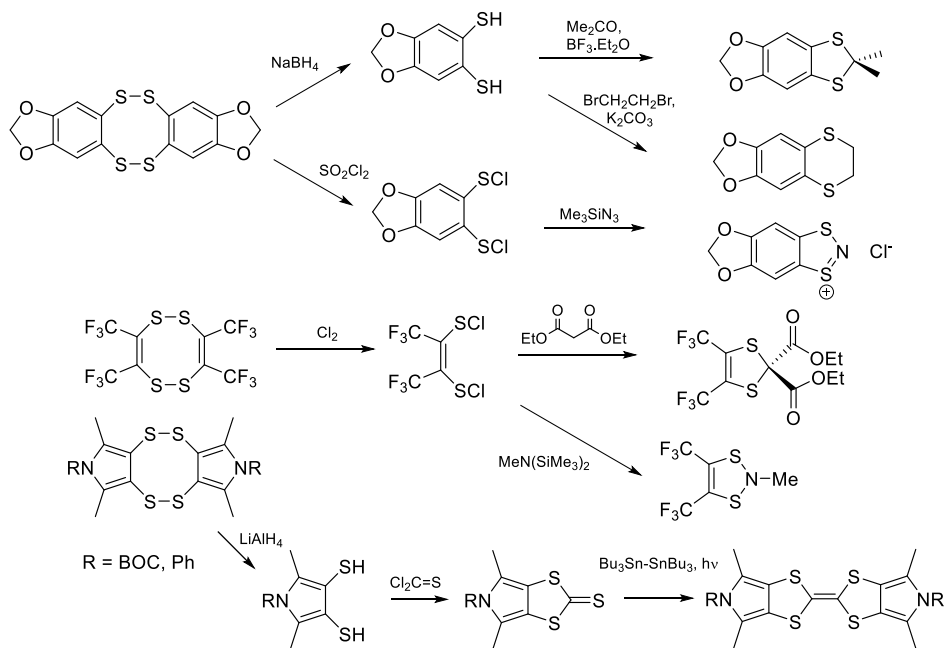
Figure 1.4. Optimized local energy minima for (Z,Z), (E,Z) and (E,E) conformations of the parent tetrathiocin, $\text{H}_4\text{C}_4\text{S}_4$. [Figure reproduced from reference 83 with permission]

1.3.4. Reactivity of 1,2,5,6-tetrathiocins

Despite the strength of the S–S bond, tetrathiocins undergo a number of reactions comparable to their dithiete monomers. Indeed, the interconversion between different oligomers, particularly at elevated temperatures, may indicate similar reactivity pathways can be expected for dithietes and tetrathiocins (1.2.6). However, for benzannulated derivatives, ring-opening of the dithiete to form the dithione is less favourable than for other dithietes (see section 1.2.4) and this may reduce some aspects of chemical reactivity where the dithione tautomer is important. Despite the greater stability of the tetrathiocins in relation to dithietes, their chemistry is rather less well explored.

Organic chemistry of tetrathiocins. Reaction of tetrathiocins with Cl_2 or with SO_2Cl_2 under reflux yields the corresponding bis(sulfonyl chloride) derivatives (Scheme 1.11).^{84,85} For example, reaction of the tetrakis(trifluoromethyl)tetrathiocin with Cl_2 affords the same bis(sulfonyl chloride) as that generated from chlorination of dithiete **V** (section 1.2.4).²⁶ Conversely, reduction of tetrathiocins with H_3PO_2 , NaBH_4 or LiAlH_4 affords the dithiol.^{58,69,86} Much of the chemistry of tetrathiocins relates to these initial chlorination or reduction steps. For example, condensation of the air-sensitive bis(sulfonyl chloride)s with one equivalent of Me_3SiN_3 affords dithiazolium salts which are precursors to stable radicals.⁸⁵ They can similarly be condensed with acidic C–H bonds to generate

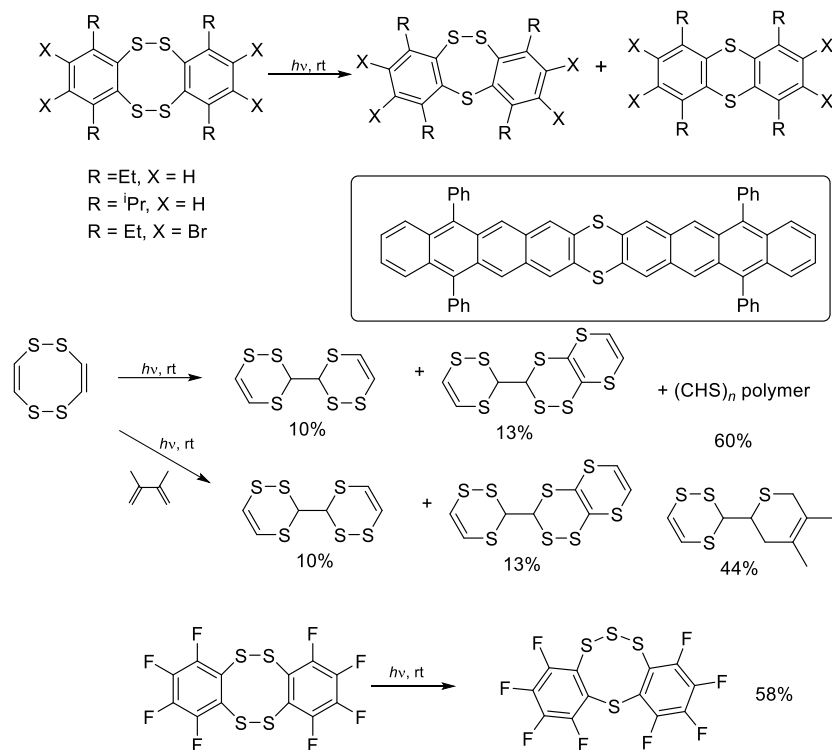
dithiols, or with amines to form dithiazoles (Scheme 1.11).²⁶ Conversely, the dithiols undergo cyclization with acetone in the presence of a Lewis acid catalyst ($\text{BF}_3 \cdot \text{Et}_2\text{O}$) to form dithiolo-substituted heterocycles or undergo ring closure with dibromoethane in the presence of base to form dithiino-fused heterocycles (Scheme 1.11). The dithiol can also be used as a precursor to tetrathiafulvalene derivatives.⁵⁸



Scheme 1.11. Ring-opening reactions of tetrathiocins through oxidation and reduction processes are frequently coupled to ring-closing reactions.

Tetrathiocins are susceptible to undergoing ring contraction reactions with stepwise elimination of sulfur under irradiation. Stirring a CH_2Cl_2 solution of the dibenzotetrathiocin derivative ($\text{R} = \text{Et}$, $\text{X} = \text{H}$) for 6 h at room temperature affords a mixture of trithiepin and thianthrene derivatives (Scheme 1.12).^{57,64} Extended reaction times (48 h) led to the thianthrene derivative in 94% yield. However, substituents appear to play an important role. For example, the tetrabromo derivative ($\text{R} = \text{Et}$, $\text{X} = \text{Br}$, Scheme 1.12) undergoes only a 7% conversion to the thianthrene,⁶⁵ whereas the related derivative ($\text{R} = \text{Et}$, $\text{X} = \text{H}$) affords 94% conversion under similar conditions. This methodology has allowed access to the polycyclic bisanthrathianthrene (Scheme 1.12) in 59%.⁶⁸ For the parent tetrathiocin,

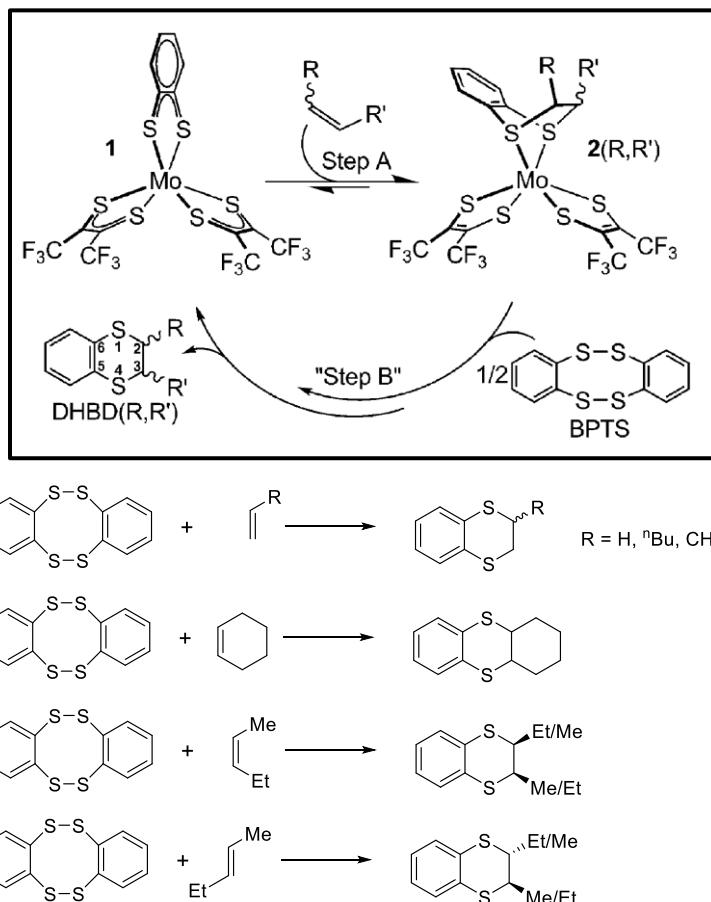
$\text{H}_4\text{C}_4\text{S}_4$, irradiation in benzene forms a $(\text{CHS})_n$ polymer as the major product and two small molecular species (Scheme 1.12) in 10% and 13% recovered yield respectively.⁸⁷ In this context, it should be noted that 1,2,5,6-tetrathiocins have also been shown to isomerize to the 1,2,3,6-tetrathiocin isomer (Scheme 1.12).⁵²



Scheme 1.12. Photo-induced reactions of tetrathiocins.

Unlike dithietes, the cycloaddition chemistry of tetrathiocins has been less studied. However, the ability of the tetrathiocin to form the dithiete on heating often leads to similar reactivity patterns. For example, reaction of the tetra-methyl-ester functionalized tetrathiocin, $(\text{MeO}_2\text{C})_4\text{C}_4\text{S}_4$ with ethyl vinyl ether yields the anticipated dihydro-dithiin (64%). Reaction with diphenylacetylene in refluxing *p*-xylene affords the thiophene derivative (49%), presumably via *S*-elimination from the expected dithiin.²⁵ Conversely, irradiation of the tetrathiocin $\text{H}_4\text{C}_4\text{S}_4$ with 2,3-dimethyl butadiene in benzene forms a mixture of compounds, derived from photodegradation of $\text{H}_4\text{C}_4\text{S}_4$, along with a cyclization product from reaction with the diene (44%) (Scheme 1.12). A major advance is the recent work by Fekl and coworkers who investigated the $[4 + 2]$ cycloaddition of dibenzo-1,2,5,6-

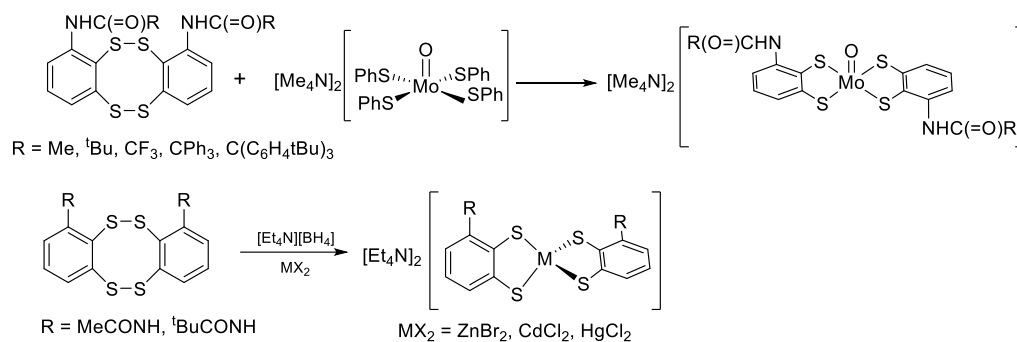
tetrathiocin (as a source of benzodithiete) with a range of alkenes in 55–96% yield (NMR) in the presence of a catalyst.⁸⁸ The catalyst (5 mol%) comprises a molybdenum tris(thiolate) complex, Mo(bdt)(tfd)₂, which has been shown to bind alkenes (section 1.2.4). The proposed mechanism is shown in Scheme 1.13. Initial turn over frequencies (TOF) were slow at *ca.* 1.2 h⁻¹ but increased to almost 10 h⁻¹ in the presence of CD₃CN. The initial step is proposed to be binding of the alkene to the catalyst, followed by cyclization and elimination of the dihydrodithiin.



Scheme 1.13. (top) mechanistic path for the Mo(bdt)(tfd)₂-catalyzed reaction of dibenzo-1,2,5,6-tetrathiocin with alkenes⁸⁸ (bottom) Mo(bdt)(tfd)₂ catalysed cyclisation reactions.

Inorganic chemistry of tetrathiocins. Tetrathiocins have been shown to generate transition metal dithiolate complexes *via* ligand exchange with transition metal complexes bearing monodentate thiolate complexes, exemplified by the Mo(IV) chemistry illustrated in Scheme 1.14.⁶⁰ These Mo(IV) complexes can also be prepared from the Mo(V)

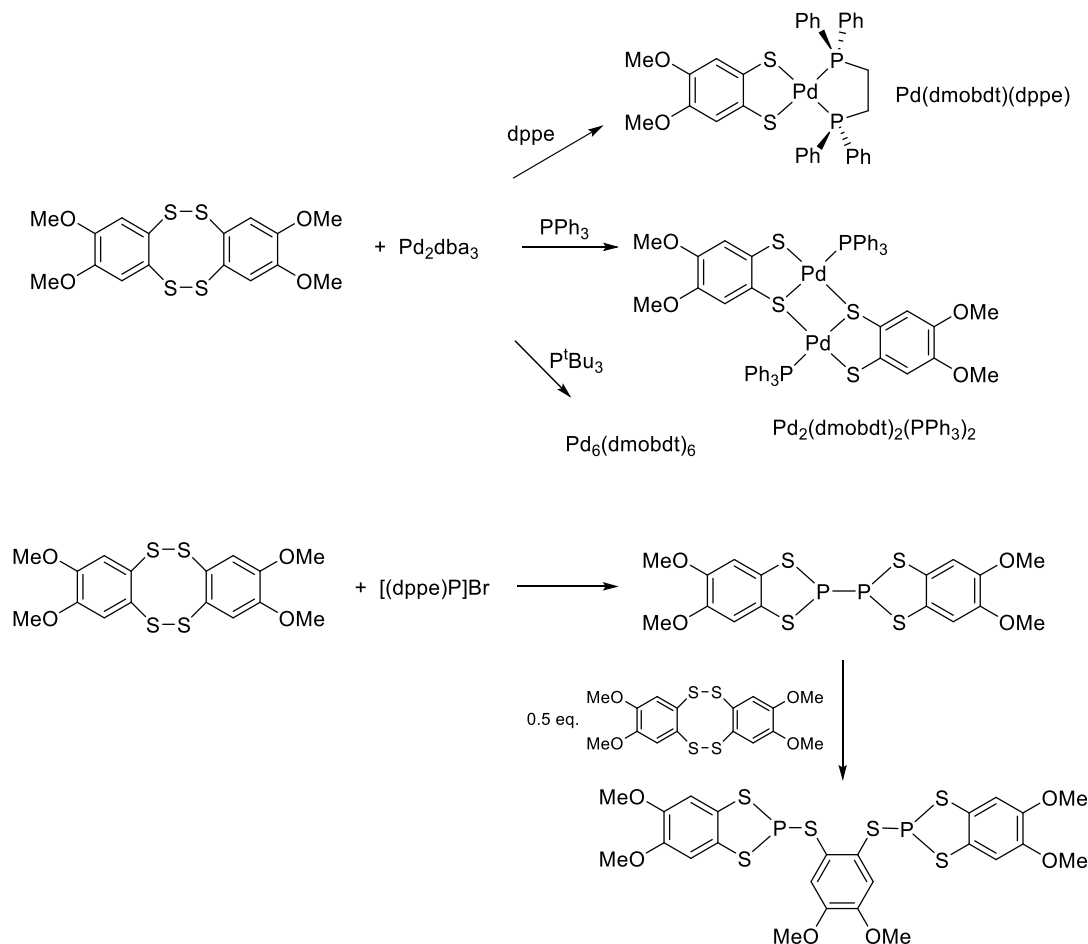
complexes, $[\text{Et}_4\text{N}][\text{MoO}(\text{SPh})_4]$ in the presence of $[\text{Et}_4\text{N}][\text{BH}_4]$.⁸⁹ For sterically less demanding groups a mixture of *cis* and *trans* isomers can be formed but sterically demanding substituents drive selective formation of the *trans* isomer.⁶⁰ Oxidation of Mo(IV) to Mo(VI) could be achieved by subsequent addition of Me_3NO . Similar reactivity patterns are observed for tungsten.⁹⁰ These molybdenum complexes are being actively pursued as models for molybdenum and tungsten oxo-transferases. Reduction of the tetrathiocin with four equivalents of $[\text{Et}_4\text{N}][\text{BH}_4]$ generates the dithiolate salt which reacts with group 12 salts MX_2 (ZnBr_2 , CdCl_2 or HgCl_2) to form the corresponding bis(dithiolate) complexes (Scheme 1.14).⁹¹



Scheme 1.14. Formation of dithiolate complexes from tetrathiocins through ligand exchange.

The reactivity of tetrathiocins with low valent transition metals appears to mimic the oxidative addition chemistry of dithietes (section 1.2.4) but is less well-established. Work by Wrixon and coworkers examined the oxidative addition of the tetramethoxy-dibenzotetrathiocin to zero-valent group 10 metals, exemplified by $\text{Ni}(\text{COD})_2$ in the presence of dppe, as well as $\text{M}(\text{dppe})_2$ ($\text{M} = \text{Pd}, \text{Pt}$) (Scheme 1.15). Under microwave heating, oxidative addition afforded a series of square-planar dithiolate complexes, $\text{M}(\text{dmobdt})(\text{dppe})$ ($\text{M} = \text{Ni}, \text{Pd}, \text{Pt}$) in 77–89% recrystallized yields (Scheme 1.15).⁹² Subsequent studies showed that the phosphine can play an important role in determining the outcome of the oxidative addition reaction to Pd_2dba_3 : chelating phosphines such as dppe, dppp and dppf favour formation of monometallic complexes, whereas Ph_3P forms $\text{M}(\text{dmobdt})(\text{PPh}_3)_2$ and the dimetallic complex $[\text{M}(\text{dmobdt})(\text{PPh}_3)]_2$ ($\text{M} = \text{Pd}, \text{Pt}$) with the

dithiolate exhibiting μ^2 -S atoms.^{70,93} Under microwave conditions, the sterically-demanding phosphine $t\text{Bu}_3\text{P}$ does not participate in the final product and a hexanuclear complex $\text{Pd}_6(\text{dmobdt})_6$ analogous to Fekl's hexamer (Figure 1.2) was isolated.⁹³ Recent studies have shown the generality of these oxidative addition reactions using a diversity of functionalized dibenzotetrathiocins.⁶⁷ Notably, the combination of Stender's synthetic methodology to access tetrathiocins, coupled with the oxidative addition reaction provides a convenient two-step route to both benzo-15-crown-5 and benzo-18-crown-6 benzene dithiolate complexes in two steps from commercial starting materials, rather than the previously reported multi-step reaction sequence.⁶⁷



Scheme 1.15. Reactivity of the tetramethoxy-dibenzo-1,2,5,6-tetrathiocin with low valent (top) transition metals and (bottom) main group P(I) compounds.

Main group reactivity. Tetrathiocins have been shown to undergo oxidative addition to the P(I) complex, [dppeP]Br, to form a mixture of P(II) and P(III) dithiaphospholes (Scheme 1.15).⁹⁴ The P(II) species appears as an intermediate *en route* to P(III), as subsequent reaction of the P–P bonded system with additional tetrathiocin has been shown to form the P(III) compound (Scheme 1.15).

1.3.5. Biological studies

The family of lissoclibadin alkaloids comprise a family of sulfur-rich natural products which have been extracted from ascidia in the southern pacific. One member of this family includes lissoclibadin 7 (Chart 1.3) which is closely related to lissoclinotoxin D.⁹⁵ In both cases the more stable ‘*trans*’ tetrathiocin isomer is proposed but the characterization is recognized as being ambiguous. Lissoclibadin 7 shows weak anti- bacterial activity against both *S. aureus* and *E. coli*, which has been tentatively assigned to the phenolic group and has also been shown to inhibit formation of colonies of Chinese Hamster V79 cells.⁹⁶

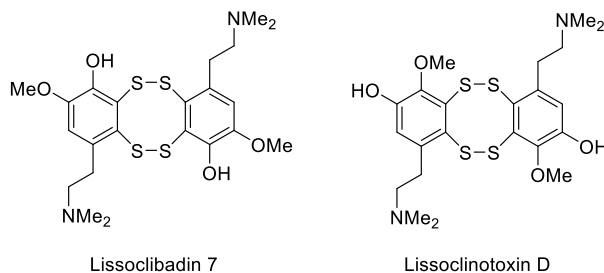
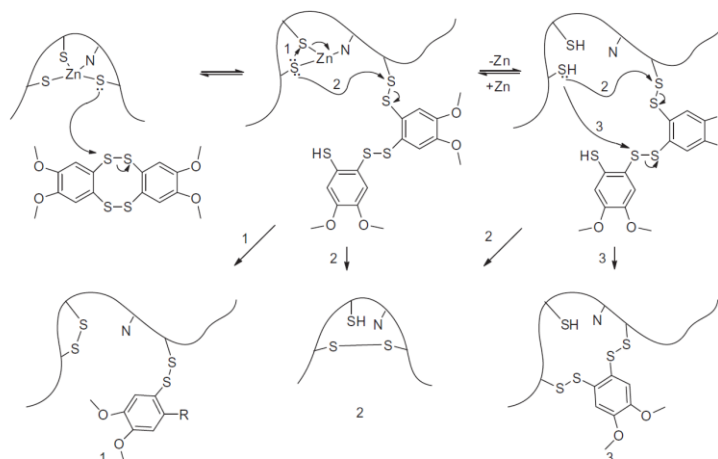


Chart 1.3. Structures of natural products containing the tetrathiocin functional group.

A series of synthetic tetrathiocins have also been examined as antiviral agents against feline immunodeficiency virus (FIV) and have been shown to have potent activity at nanomolar concentrations, yet exhibit low toxicity.⁶² The tetrathiocins are proposed to interact with the zinc finger protein, which has an S_3N coordination environment, through extrusion of the Zn^{2+} ion (Scheme 1.16). The benzo-fused tetrathiocin derivatives studied performed better than tetrathiocins with fused heterocycles.



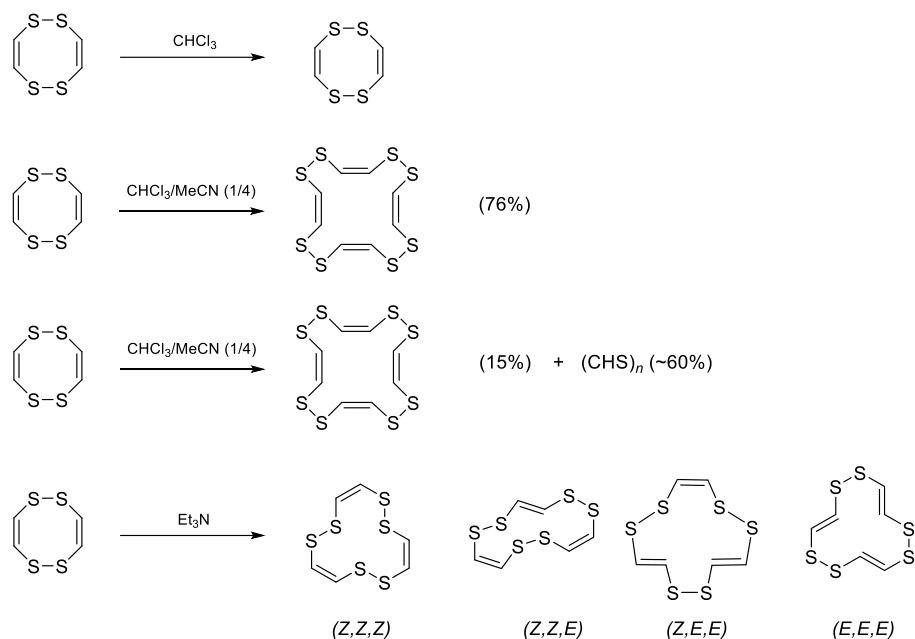
Scheme 1.16. Proposed mechanism for extrusion of Zn^{2+} from zinc finger proteins [reproduced with permission from reference 62].

1.4 Trimeric and tetrameric dithietes

1.4.1. Preparation

Early work by Krespan^{7,8} on dithietes showed that the bis(trifluoromethyl)dithiine **V** dimerized in the presence of Et_3N to selectively form the corresponding tetrathiocin but could convert back to the dithiote at elevated temperatures (section 1.2.6). Indeed, the interconversion between oligomers appears complex and sensitive to reaction conditions. For example, studies on the parent tetrathiocin, $\text{H}_4\text{C}_4\text{S}_4$, showed it was stable in CHCl_3 solution over 4.5 h but formed the tetramer in 76% yield in $\text{CHCl}_3/\text{MeCN}$ (1/4 ratio) under otherwise identical conditions, whereas the tetramer formed in just 15% yield in $\text{CHCl}_3/\text{MeOH}$ (1/4) solution (with the majority converting to $(\text{CHS})_n$ polymer).¹² The bis(methyl ester) dithiote, **XIII** (Chart 1.2), exhibits similarly complex behavior: a CHCl_3 solution of **XIII** forms the tetramer in 71% yield with a small quantity of tetrathiocin (5%) on standing for 4.5 h. Conversely, a $\text{CHCl}_3/\text{MeCN}$ (1/4) solution of **XIII** generated the dimer and tetramer in 19% and 41% respectively, whereas a CHCl_3 solution of **XIII**, stirred with silica gel, afforded the tetrathiocin as the major product (45%) while the tetramer was isolated as the minor product (24%). Time-dependent studies indicated that the tetrathiocin was formed prior to formation of the tetramer in this reaction. Notably, in pure CHCl_3 solution, both the tetrathiocin and the tetramer appear stable, with no evidence for

conversion between oligomers or back to the dithiete.¹² This indicates that both silica gel and MeCN drive these ring transformations, in an analogous fashion to Et₃N driving formation of the tetrathiocin from dithiete **V**. Supporting this argument, the different oligomers derived from dithiete **XIII** appear stable in pure CHCl₃, but form mixtures of dithiete monomer, tetrathiocin dimer and 16-membered tetrameric ring when dissolved in CHCl₃/MeCN (1/4) (Scheme 1.17).¹² While the S–S bond is strong (264 kJ mol⁻¹),⁹⁷ disulfides are well-known to be dynamic even at ambient temperature, particularly in the presence of base, and have extensive roles in supramolecular chemistry⁹⁸ and nature,⁹⁹ where disulfide reduction with thiols such as glutathione (GSH) play an important biological role. To highlight the complexity of these systems, it is notable that the trimer (H₂C₂S₂)₃ was not formed from the parent tetrathiocin in the studies above. However, the parent tetrathiocin has been shown to transform into the trimer in the presence of Et₃N.^{9b} The trimer can exist in four isomeric forms, depending on the *Z* or *E* conformation about each of the C=C bonds. Formation of isomers with *E* conformation presumably arise *via* ring-opening of a dithiete intermediate, which initially forms the *cis*-dithione but is known to convert to the more stable *trans*-dithione (section 1.2.3). While trimeric benzo-fused analogs, (C₆H₄S₂)₃, have not yet been reported, the rigidity of the structure would necessarily lead to formation of the *Z,Z,Z* isomer.



Scheme 1.17. Ring transformations between oligomers of dithietes

1.4.2. Structural studies

To date there are no known structures of the cyclic trimer, $(R_2C_2S_2)_3$, but the crystal structure of the tetrameric oligomer, $(H_2C_2S_2)_4$, has been determined by X-ray diffraction (Figure 1.5).⁸¹ The double bonds all adopt a *Z* configuration, with the arrangement of double bonds similar to that in cyclo-octatetraene (COT). The average S–S bond length in the tetramer is 2.050(2) Å, comparable to those observed in both dithietes and tetrathiocins.

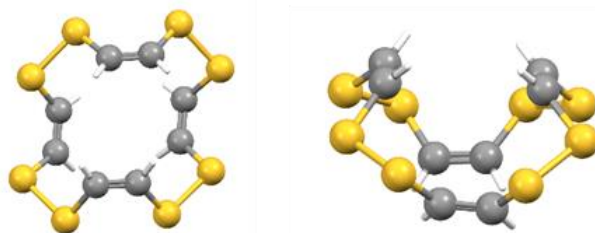


Figure 1.5. Crystal structure of the cyclic tetramer, $(H_2C_2S_2)_4$, highlighting the *Z* configuration at each double bond (**left**) and folding of the ring (**right**).

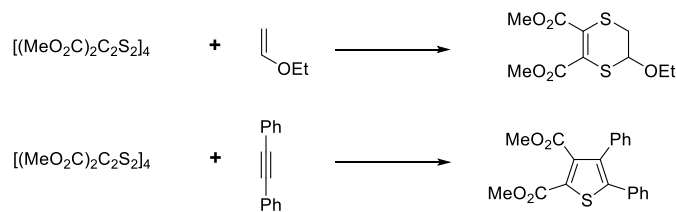
1.4.3. Computational studies

Few computational studies have been undertaken on these larger oligomers. For the parent trimer, $(H_2C_2S_2)_3$, four isomers based on the *Z* vs. *E* conformation at the double bond

are possible (Scheme 1.17). Of these, the *Z,Z,Z* conformation has been identified as the most stable trimer.^{9b} It is computed to be only slightly less stable than the tetrathiocin at the MP2/6-31G* level of theory. The scarcity of the trimer in experimental studies was proposed to arise from conformational challenges required to generate the trimer during the oligomerization process. Notably the tetramer, (H₂C₂S₂)₄, is computed to be the most stable of all the possible (H₂C₂S₂)_n oligomers (*n* = 1–4).^{9b}

1.4.4. Reactivity studies

Until recently the trimer was unknown and there are no reactivity studies reported to date. Few tetramers are known, and reactivity studies are limited. As we have seen already, conversion between different oligomers is known. While the tetramer, [(MeO₂C)₂C₂S₂]₄, is stable in pure CHCl₃, it forms both the dithiete (6%) and the tetrathiocin (12%) after 2 h in CHCl₃/MeCN.¹² Similarly, in the presence of silica gel the same tetramer forms the dithiete (10%) and tetrathiocin (40%) after 4 h. The reaction of the tetramethylester tetramer with ethyl vinyl ether at room temperature forms the dihydro-dithiin in 63% yield (Scheme 1.18), comparable with the tetrathiocin (64%) and the dithiete (65%), consistent with all reactions proceeding via the dithione.²⁵ Reaction with diphenylacetylene in refluxing *p*-xylene afforded the thiophene (Scheme 1.18), presumably proceeding *via* sulfur elimination from an intermediate dithiin, again following reactivity pathways observed for the dithiete and tetrathiocin.²⁵



Scheme 1.18. Cycloaddition reactions of the tetramer, [(MeO₂C)₂C₂S₂]₄.

1.5 Overview of this thesis

Previous studies examining the oxidative addition of tetrathiocins has been discussed in section 1.3.4, which discussed a microwave assisted synthetic methodology to obtain metal dithiolate complexes containing group 10 (M = Ni, Pd, Pt) and an auxiliary

phosphine ligand to afford $M(\text{dmobdt})(\text{dppe})$.⁹² As well, further studies investigated the role of the phosphine to promote mono-, di- or hexa-nuclear complexes.^{70,93}

In this thesis, Chapters 2–6 describe the oxidative addition reactions of the S-S bond of 1,2,5,6-tetrathiocins (Figure 1.6) to a variety of low valent *p*- and *d*- block elements to form metal dithiolate complexes. Chapter 2 extends previous studies of oxidative addition to zero-valent group 10 metals (Pd or Pt), implementing a library of tetrathiocin derivatives in the presence of an auxiliary phosphine ligand. This includes tetrathiocins with nitrogenous π -donors and benzo-15-crown-5 and benzo-18-crown-6 ether functional groups. The latter were studied as potential optical and electrochemical sensors for group 1 metals. Chapter 3 extends this synthetic methodology to the group 9 metal, cobalt, and examines the equilibrium that exists between monomeric $\text{CpCo}(\text{dmobdt})$ and dimeric $[\text{CpCo}(\text{dmobdt})]_2$. The fine balance between monomer and dimer is explored through the preparation and characterization of a series of alkoxy-functionalized $[\text{CpCo}(\text{bdt})]_n$ complexes ($n = 1, 2$). Chapter 4 describes the synthesis of the corresponding cobalt benzo-15-crown-5 and benzo-18-crown-6 derivatives and investigates their reactivity towards group 1 metals. Chapter 5 examines a series of nickel dithiolate diimine complexes that exhibit intense colours with potential applications as second order non-linear optic (NLO) materials and near-IR absorbers for solar light harvesting applications. Chapter 6 explores the reactivity of tetrathiocins towards the low oxidation state *p*-block valent Ge(II) precursor, GeCl_2 -dioxane, as an extension of previous oxidative addition to low-valent P(I) compounds. Chapter 7 provides an executive summary of the findings of this thesis, along with a perspective on possible future work.

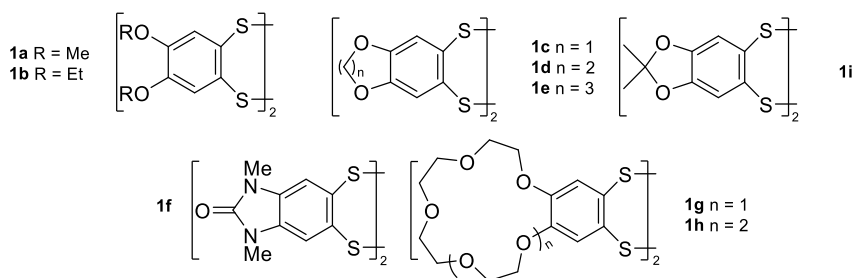


Figure 1.6. Tetrathiocin ligands used to create metal dithiolate complexes.

1.6 References

- (1) (a) S. Meninno and A. Lattanzi, *Chem. – Eur. J.*, 2016, **22**, 3632–3642; (b) C.-Y. Huang and A. G. Doyle, *Chem. Rev.*, 2014, **114**, 8153–8198.
- (2) L. Degennaro, P. Trincherà and R. Luisi, *Chem. Rev.*, 2014, **114**, 7881–7929.
- (3) J. Nakayama and A. Ishii, *Adv. Heterocycl. Chem.*, 2000, **77**, 221–284.
- (4) M. Mann and J. Fabian, *Int. J. Quantum Chem.*, 1996, **60**, 859–874.
- (5) (a) N. Busschaert, R. B. P. Elmes, D. D. Czech, X. Wu, I. L. Kirby, E. M. Peck, K. D. Hendzel, S. K. Shaw, B. Chan, B. D. Smith, K. A. Jolliffe and P. A. Gale, *Chem. Sci.*, 2014, **9**, 3617–3626; (b) M. Rombola, C. S. Sumaria, T. D. Montgomery and V. H. Rawal, *J. Am. Chem. Soc.*, 2017, **139**, 5297–5300.
- (6) Y. Ono, Y. Sugihara, A. Ishii and J. Nakayama, *J. Am. Chem. Soc.*, 2003, **125**, 12114–12115.
- (7) C. G. Krespan, B. C. McKusick and T. L. Cairns, *J. Am. Chem. Soc.*, 1960, **82**, 1515–1516.
- (8) C. G. Krespan, *J. Am. Chem. Soc.*, 1961, **83**, 3434–3437.
- (9) (a) U. Zoller, *Comp. Heterocycl. Chem. II*, 1966, **1**(35), 1113–1138; (b) T. Shimizu and N. Kamigata, *J. Organomet. Chem.*, 2000, **611**, 106–115; (c) J. Drabowicz, J. Lewkowski, W. Kudelska and A. Zajac, *Comp. Heterocycl. Chem. III*, 2008, **2**, 811–852.
- (10) S. K. Mohapatra, Y. Zhang, B. Sandhu, M. S. Fonari, T. V. Timofeeva, S. R. Marder and S. Barlow, *Polyhedron*, 2016, **116**, 88–95.
- (11) J. P. Donahue and R. H. Holm, *Acta Crystallogr., Sect. C*, 1998, **54**, 1175–1178.
- (12) T. Shimizu, H. Murakami, Y. Kobayashi, K. Iwata and N. Kamigata, *J. Org. Chem.*, 1998, **63**, 8192–8199.
- (13) M. Breitenstein, R. Schulz and A. Schweig, *J. Org. Chem.*, 1982, **47**, 1979–1980.
- (14) (a) W. Kusters and P. de Mayo, *J. Am. Chem. Soc.*, 1973, **95**, 2383–2384; (b) R. B. Boar, D. W. Hawkins, J. F. McGhie and D. H. R. Barton, *J. Chem. Soc., Perkin Trans. 1*, 1977, 515–517.

- (15) H. Bock, B. L. Chenards, P. Rittmeyer and U. Stein, *Z. Naturforsch., B*, 1988, **43**, 117–124.
- (16) T. S. Cameron, R. C. Haddon, S. M. Mattar, S. Parsons, J. Passmore and A. P. Ramirez, *J. Chem. Soc., Dalton Trans.*, 1992, 1563–1572.
- (17) P. C. Guha and M. N. Chaklader, *Q. J. Indian Chem. Soc.*, 1925, **2**, 318–335.
- (18) J. L. Hencher, Q. Shen and D. G. Tuck, *J. Am. Chem. Soc.*, 1976, **98**, 899–902.
- (19) M. F. C. Ladd and D. C. Povey, *Acta Crystallogr., Sect. B*, 1976, **32**, 1311–1317.
- (20) D. Vijay and G. N. Sastry, *J. Mol. Struct. (THEOCHEM)*, 2005, **732**, 71–78.
- (21) H. Yu, W.-T. Chan and J. D. Goddard, *J. Am. Chem. Soc.*, 1990, **112**, 7529–7537.
- (22) (a) J. Nakayama, K. S. Choi, A. Ishii and M. Hoshino, *Bull. Chem. Soc. Jpn.*, 1990, **63**, 1026–1031; (b) W. E. Parham and V. J. Traynelis, *J. Am. Chem. Soc.*, 1954, **76**, 4960–4962; (c) R. Grigg, R. Hayes and J. L. Jackson, *J. Chem. Soc. D*, 1969, 1167–1168; (d) K. Kobayashi, K. Mutai and H. Kobayashi, *Tetrahedron Lett.*, 1979, **20**, 5003–5006; (e) J. Nakayama, M. Shimomura, M. Iwamoto and M. Hoshino, *Heterocycles*, 1985, **23**, 1907–1910.
- (23) M. Arisawa, K. Sawahata, T. Ichikawa and M. Yamaguchi, *Organomet.*, 2018, **37**, 3174–3180.
- (24) K. S. Choi, I. Akiyama, M. Hoshino and J. Nakayama, *Bull. Chem. Soc. Jpn.*, 1993, **66**, 623–629.
- (25) T. Shimizu, H. Murakami and N. Kamigata, *J. Org. Chem.*, 1999, **64**, 8489–8494.
- (26) S. Reimann-Andersen, H. Pritzkow and W. Sundermeyer, *Chem. Ber.*, 1994, **127**, 533–539.
- (27) J. Nakayama, A. Mizumura, Y. Yokomori, A. Krebs and K. Schutz, *Tetrahedron Lett.*, 1995, **36**, 8583–8586.
- (28) J. Nakayama, N. Masui, Y. Sugihara and A. Ishii, *Bull. Chem. Soc. Jpn.*, 1998, **71**, 1181–1186.
- (29) A. Davison, N. Edelstein, R. H. Holm and A. H. Maki, *J. Am. Chem. Soc.*, 1964, **86**, 2799–2805.

- (30) K. Roessellet, K. E. Doan, S. D. Johnson, P. Nicholls, G. L. Miessler, R. Kroeker and S. H. Wheeler, *Organomet.*, 1987, **6**, 480–485.
- (31) K. Wang, J. M. McConnachie and E. I. Stiefel, *Inorg. Chem.*, 1999, **38**, 4334–4341.
- (32) D. J. Harrison, A. J. Lough, N. Nguyen and U. Fekl, *Angew. Chem., Int. Ed.*, 2007, **46**, 7644–7647.
- (33) J. P. Donahue, C. R. Goldsmith, U. Nadiminti and R. H. Holm, *J. Am. Chem. Soc.*, 1998, **120**, 12869–12881.
- (34) K. A. Martyanov, V. K. Cherkasov, G. A. Abakumov, M. A. Samsonov, V. V. Khrizanforova, Y. H. Budnikova and V. A. Kuropatov, *Dalton Trans.*, 2016, **45**, 7400–7405.
- (35) J. Miller and A. L. Balch, *Inorg. Chem.*, 1971, **10**, 1410–1415.
- (36) R. B. King, *J. Am. Chem. Soc.*, 1963, **85**, 1584–1587.
- (37) A. L. Balch, I. G. Dance and R. H. Holm, *J. Am. Chem. Soc.*, 1968, **90**, 1139–1145.
- (38) I. Bernal, A. Clearfield, E. F. Epstein, J. S. Ricci, A. Balch and J. S. Miller, *J. Chem. Soc., Chem. Commun.*, 1973, 39–40.
- (39) T. M. Porter, J. Wang, Y. Li, B. Xiang, C. Salsman, J. S. Miller, W. Xiong and C. P. Kubiak, *Chem. Sci.*, 2019, **10**, 113–117.
- (40) D. J. Harrison, N. Nguyen, A. J. Lough and U. Fekl, *J. Am. Chem. Soc.*, 2006, **128**, 11026–11027.
- (41) O. Zeika, A. Werner and S. Willmann, *U.S. Pat.*, 8119037 B2, 2012.
- (42) J. Moscattini, A. J. Lough and U. Fekl, *Acta Crystallogr., Sect. E*, 2017, **73**, 957–962.
- (43) K. A. Martyanov, V. K. Cherkasov, G. A. Abakumov, E. V. Baranov, A. S. Shaviyr and V. K. Kuropatov, *Dalton Trans.*, 2017, **48**, 16783–16786.
- (44) K. A. Martyanov, G. A. Abakumov, E. V. Baranov, V. V. Khrizanforova, M. N. Khrizanforov, K. V. Kholin, Y. H. Budnikova, V. A. Kuropatov and V. K. Cherkasov, *Eur. J. Inorg. Chem.*, 2020, **2020**, 4350–4357.

- (45) V. K. Cherkasov, G. A. Abakumov, G. K. Fukin, S. V. Klementyeva and V. A. Kuropatov, *Chem. – Eur. J.*, 2012, **18**, 13821–13827.
- (46) M. Arisawa, K. Sawahata, T. Yamada, D. Sarkar and M. Yamaguchi, *Org. Lett.*, 2018, **20**, 938–941.
- (47) (a) N. J. De'Ath and D. B. Denney, *J. Chem. Soc., Chem. Commun.*, 1972, 395–396;
(b) B. S. Campbell, N. J. De'Ath, D. B. Denney, D. Z. Denney, I. S. Kipnis and T. B. Min, *J. Am. Chem. Soc.*, 1976, **98**, 2924–2927.
- (48) B. C. Burros, N. J. De'Ath, D. B. Denney, D. Z. Denney and I. J. Kipnis, *J. Am. Chem. Soc.*, 1978, **100**, 7300–7304.
- (49) D. B. Denney, D. Z. Denney and L. T. Liu, *Phos., Sulf. Sil. Relat. Elem.*, 1985, **22**, 71–84.
- (50) A. F. Berniaz and D. G. Tuck, *Organomet.*, 1973, **51**, 113–118.
- (51) L. Field, W. Stephens and E. L. Lippert Jr., *J. Org. Chem.*, 1961, **26**, 4782–4783.
- (52) T. Chivers, M. Parvez, I. Vargas-Baca and G. Schatte, *Can. J. Chem.*, 1998, **76**, 1093–1101.
- (53) G. Crank and M. I. H. Makin, *Aust. J. Chem.*, 1984, **37**, 2331–2337.
- (54) S. K. Kumar, H. B. Singh, J. P. Jasinski, E. S. Paight and R. J. Butcher, *J. Chem. Soc., Perkin Trans. I*, 1991, 3341–3347.
- (55) X. Yang, T. B. Rauchfuss and S. R. Wilson, *J. Chem. Soc., Chem. Commun.*, 1990, 34–36.
- (56) T. Yamamoto, S. Ogawa, M. Sugawara, Y. Kawai and R. Sato, *Bull. Chem. Soc. Jpn.*, 2006, **79**, 460–467.
- (57) S. Ogawa, M. Sugawara, Y. Kawai, S. Niizuma, T. Kimura and R. Sato, *Tetrahedron Lett.*, 1999, **40**, 9101–9106.
- (58) K. Zong, W. Chen, M. P. Cava and R. D. Rogers, *J. Org. Chem.*, 1996, **61**, 8117–8124.
- (59) M. V. Stasevych, M. Y. Plotnikov, M. O. Platonov, S. I. Sabat, R. Y. Musyanovych and V. P. Novikov, *Heteroatom. Chem.*, 2005, **16**, 205–211.

- (60) T.-A. Okamura, Y. Ushijima, Y. Omi and K. Onitsuka, *Inorg. Chem.*, 2013, **52**, 381–394.
- (61) L. S. Konstantinova, S. A. Amelichev and O. A. Rakitin, *Russ. Chem. Bull., Int. Ed.*, 2007, **56**, 1540–1543.
- (62) C. R. M. Asquith, M. L. Meli, L. S. Konstantinova, T. Laitinen, A. Poso, O. A. Rakitin, R. Hofmann-Lehmann, K. Allenspach and S. T. Hilton, *Bioorg. Med. Chem. Lett.*, 2015, **25**, 1352–1355.
- (63) E. Fanghänel, R. Herrmann and H. Naarmann, *Tetrahedron*, 1995, **51**, 2533–2542.
- (64) T. Kimura, K. Tsujimura, S. Mizusawa, S. Ito, Y. Kawai, S. Ogawa and R. Sato, *Tetrahedron Lett.*, 2000, **41**, 1801–1805.
- (65) T. Kimura, T. Obonai, T. Nozaki, K. Matsui, T. Namauo, A. Yamakawa and Y. Takaguchi, *Heterocycles*, 2010, **80**, 183–186
- (66) K. W. Stender, N. Wolki and G. Klar, *Phos., Sulf. Sil. Relat. Elem.*, 1989, **42**, 111–114.
- (67) L. K. Watanabe, J. D. Wrixon, Z. S. Ahmed, J. J. Hayward, P. Abbasi, M. Pilkington, C. L. B. Macdonald and J. M. Rawson, *Dalton Trans.*, 2020, **49**, 9086–9093.
- (68) M. Yamashita, H. Hayashi, M. Suzuki, D. Kuzuhara, J. Yuasa, T. Kawai, N. Aratani and H. Yamada, *RSC Adv.*, 2016, **6**, 70700–70703.
- (69) M. V. Lakshmikantham, M. S. Raasch, M. P. Cava, S. G. Bott and J. L. Atwood, *J. Org. Chem.*, 1987, **52**, 1874–1877.
- (70) J. D. Wrixon, Z. S. Ahmed, M. U. Anwar, Y. Beldjoudi, N. Hamidouche, J. J. Hayward and J. M. Rawson, *Polyhedron*, 2016, **108**, 115–121.
- (71) J. Kopf, K. von Deuten, B. Nakhdjavan and G. Klar, *Z. Naturforsch. B.*, 1979, **34**, 48–51.
- (72) L. K. Jagadamma, R. G. D. Taylor, A. Kanibolotsky, M. T. Sajjad, I. A. Wright, P. N. Horton, S. J. Coles, I. D. W. Samuel and P. J. Skabara, *Sustainable Energy Fuels*, 2019, **3**, 2087–2099.

- (73) A. I. S. Neves, I. C. Santos, L. C. J. Pereira, C. Rovira, E. Ruiz, D. Belo and M. Almeida, *Eur. J. Inorg. Chem.*, 2011, 4807–4815.
- (74) T. Okamura, T. Yamada, Y. Hasenaka, S. Yamashita and K. Onitsuka, *Eur. J. Inorg. Chem.*, 2016, 2952–2961.
- (75) Y. Wang, Y. Xie, P. Wei, H. F. Schaefer and G. H. Robinson, *Dalton Trans.*, 2019, **48**, 3543–3546.
- (76) F. Bigoli, P. Deplano, F. A. Devillanova, J. R. Ferraro, V. Lippolis, P. J. Lukes, M. L. Mercuri, M. A. Pellinghelli, E. F. Trogu and J. M. Williams, *Inorg. Chem.*, 1997, **36**, 1218–1226.
- (77) T. Kimura, S. Mizusawa, A. Yoneshima, S. Ito, K. Tsujimura, T. Yamashita, Y. Kawai, S. Ogawa and R. Sato, *Bull. Chem. Soc. Jpn.*, 2002, **75**, 2647–2653.
- (78) T. Akasaka, M. Nakano, H. Tamura and G. Matsubayashi, *Bull. Chem. Soc. Jpn.*, 2002, **75**, 2621–2628.
- (79) H. Sugimoto, M. Tarumizu, K. Tanaka, M. Miyake and H. Tsukube, *Dalton Trans.*, 2005, 3558–3565.
- (80) E. J. Yearley, E. L. Lippert, D. J. Mitchell and A. A. Pinkerton, *Acta Crystallogr., Sect. C*, 2007, **63**, o576.
- (81) T. Shimizu, K. Iwata and N. Kamigata, *Angew. Chem., Int. Ed. Engl.*, 1996, **35**, 2357–2359.
- (82) E. Fanghanel, R. Herrmann, J. Bierwisch, H. Hartung, U. Baumeister, G. Maier and H. P. Reisenauer, *J. Prakt. Chem./Chem.-Ztg.*, 1994, **336**, 444–451.
- (83) T. Shimizu, K. Iwata, N. Kamigata and S. Ikuta, *J. Chem. Res., Synop.*, 1997, **2**, 38–39.
- (84) M. V. Stasevych, M. Y. Plotnikov, M. O. Platonov, S. I. Sabat, R. Y. Musyanovych and V. P. Novikov, *Heteroatom. Chem.*, 2005, **16**, 587–598.
- (85) A. Alberola, D. Eisler, R. J. Less, E. Navarro-Moratalla and J. M. Rawson, *Chem. Commun.*, 2010, **46**, 6114–6116.
- (86) P. Wessig, L. John, E. Sperlich and A. Kelling, *Eur. J. Org. Chem.*, 2021, 499–511.

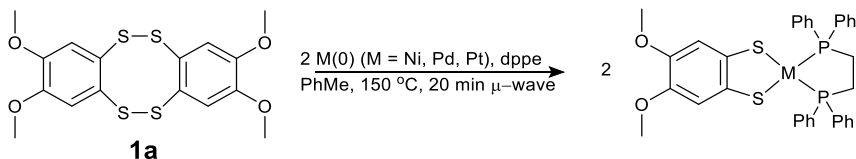
- (87) T. Shimizu, K. Iwata, H. Murakami and N. Kamagata, *Phos., Sulf. Sil. Relat. Elem.*, 1997, **120**, 457–458.
- (88) D. J. Harrison and U. Fekl, *Chem. Commun.*, 2009, 7572–7574.
- (89) K. Baba, T.-A. Okamura, C. Suzuki, H. Yamamoto, T. Yamamoto, M. Ohama and N. Ueyama, *Inorg. Chem.*, 2006, **45**, 894–901.
- (90) T.-A. Okamura, Y. Omi, Y. Hirano and K. Onitsuka, *Dalton Trans.*, 2016, **45**, 15651–15659.
- (91) K. Baba, T.-A. Okamura, H. Yamamoto, T. Yamamoto and N. Ueyama, *Inorg. Chem.*, 2008, **47**, 2837–2848.
- (92) J. D. Wrixon, J. J. Hayward, O. Raza and J. M. Rawson, *Dalton Trans.*, 2014, **43**, 2134–2139.
- (93) J. D. Wrixon, J. J. Hayward and J. M. Rawson, *Inorg. Chem.*, 2015, **54**, 9384–9386.
- (94) S. C. Kosnik, M. C. Nascimento, J. M. Rawson and C. L. B. Macdonald, *Dalton Trans.*, 2017, **46**, 9769–9776.
- (95) P. A. Searle and T. F. Molinski, *J. Org. Chem.*, 1994, **59**, 6600–6605.
- (96) T. Nakazawa, J. Xu, T. Nishikawa, T. Oda, A. Fujita, K. Ukai, R. E. P. Mangindaan, H. Rotinsulu, H. Kobayashi and M. Namikoshi, *J. Nat. Prod.*, 2007, **70**, 439–442.
- (97) J. G. Stark and H. G. Wallace, *Chemistry Data Book*, ed. S. I. Edition, J. Murray. Publ., London, 1980.
- (98) S. P. Black, J. K. M. Sanders and A. R. Stefankiewicz, *Chem. Soc. Rev.*, 2014, **43**, 1861–1872.
- (99) H. F. Gilbert, *Methods Enzymol.*, 1995, **251**, 8–28.

CHAPTER 2: SYNTHESIS AND REACTIVITY OF PLATINUM AND PALLADIUM DITHIOLATE PHOSPHINE COMPLEXES

2.1 Introduction

Transition metal dithiolene complexes have been an active area of research since the 1960s, when they were first explored by Schrauzer and Mayweg.¹ Due to the unique redox and structural properties they exhibit, these complexes can be used in such varied fields as dyes,² non-linear optics,³ catalysis,⁴ and in conducting⁵ and magnetic materials,⁶ serving as potential building blocks for many materials applications including organic light emitting diodes⁷ and solar cell technologies.⁸ In addition they have been used extensively as models for a range of metalloenzymes such as iron and nickel/iron hydrogenases.⁹ There are two main pathways typically employed to form dithiolate complexes, namely: (a) ligand exchange reactions of *s*-block metal dithiolates with *d*-block metal salts; and (b) condensation reactions of free thiols with transition metal oxo, alkoxo, and amido precursors.¹⁰ The redox behaviour of the dithiolene ligand is important in both biological and materials processes in which inter- or intra-molecular electron transfer processes play a key role.¹¹ For example intramolecular ligand-to-ligand electron transfer in nickel dithiolene complexes with N,N'-chelate ligands is sensitive to the nature of both the dithiolate and N,N'-chelate.¹² The use of π -delocalized benzene dithiolates offers the potential for both electronic and steric control of the dithiolate, yet a survey of crystallographically characterized benzene dithiolates reveals the majority derive from commercially available 1,2-benzene dithiol and 4-methyl-1,2-benzene dithiol: A search of the CSD (2019) revealed 1642 structures containing a benzo-dithiolate core. 68 % of these complexes comprised either benzene dithiolate (bdt) or toluene dithiolate (tdt) at 58 % and 10% respectively. An alternative route to dithiolene complexes involves the oxidative addition of 1,2-dithietes to low valent transition metals (see Chapter 1.2.4).¹³ In this context our recent studies indicate that benzo-fused 1,2,5,6-tetrathiocins (which can be considered as dimers of the strained dithiete ring) exhibit similar reactivity pathways to dithietes. For example, oxidative addition of tetramethoxy-dibenzo-1,2,5,6-tetrathiocin (**1a**) to zero-

valent group 10 metals [Ni(COD)₂, Pd₂dba₃ and Pt(dppe)₂] in the presence of the bidentate dppe ligand provides a convenient route to the mononuclear complexes M(dmobdt)(dppe) (M = Ni, Pd, Pt) [dmobdt = 4,5-dimethoxybenzene-1,2-dithiolato] (Scheme 2.1).¹⁴



Scheme 2.1. Synthesis of group 10 dithiolates.

Subsequent studies revealed that in the presence of monodentate phosphines, both dinuclear [M(PR₃)(dmobdt)]₂ and hexanuclear [M(dmobdt)]₆ complexes could be prepared from **1a**, with the reaction outcome largely defined by the steric demand of the phosphine.¹⁵

As an extension of these initial studies, I expanded the range of tetrathiocins available for such oxidative addition processes. Stender *et al.*¹⁶ originally reported a limited number of tetrathiocins (**1a–1d**) that were accessible *via* electrophilic aromatic substitution of activated π -donor dialkoxy-benzene derivatives. In this Chapter, this methodology has been implemented to afford a wider range of alkoxybenzenes (**1e**, **1g**, **1i**) and extended to nitrogenous π -donors (**1f**) (Figure 2.1). Their general potential to undergo oxidative addition reactions was then explored through a series of reactivity studies with zero-valent Pd and Pt forming complexes **2a–2g** and **3a–3g**, respectively with recovered yields of crystalline product ranging from 37–89%. In particular, the effectiveness of this synthetic methodology has been highlighted through the preparation of the benzo-15-crown-5 complexes **2g** and **3g** in good yield *via* this simple two-step process starting from commercial benzo-15-crown-5. This is compared to the existing literature procedure which involves a labour-intensive multi-step process.¹⁷

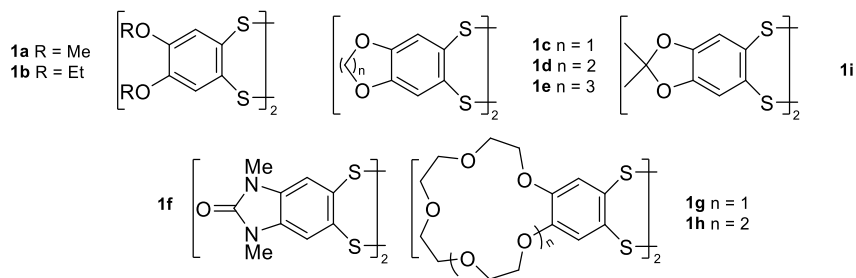


Figure 2.1. Tetrathiocin ligands used to prepare metal dithiolate complexes.

2.2 Results and Discussion

2.2.1. Synthesis

These studies commenced with the synthesis of several different tetrathiocins (**1a**–**1d** Figure 2.1) from dialkoxybenzenes using the procedure outlined by Stender *et al.*¹⁶ in which the π -donor alkoxy substituents activate the ring to electrophilic aromatic substitution by sulphur monochloride. The resultant tetrathiocins precipitated from the reaction mixture and were easily isolated by filtration. As an extension of these earlier studies, tetrathiocins **1e**, **1g**, **1h** and **1i** were also prepared using this method. Notably, the rates of substitution were slower for larger ring sizes, likely as a result of decreased π -donor ability of the O lone pair. For dioxole, a search of the Crystallographic Structural Database¹⁸ (CSD) reveals the C_{sp3} –O– C_{sp2} – C_{sp2} unit to be essentially planar, maximizing π -overlap, but increasingly deviates from planarity for dioxane and dioxepine derivatives. While the isolated yield of **1a** compared well to the literature data, yields of **1b**–**1d** were significantly improved compared to the original report by the application of extended reaction times to account for the slower reaction kinetics (Table 2.1). Based on these observations it was found that (i) π -donor N-substituents were also sufficiently activating and led to the tetrathiocin **1f** and (ii) crown ether derivatives such as benzo-15-crown-5 would also react, albeit with slow kinetics (1 week at room temperature).

Table 2.1. Reaction times and isolated yields of tetrathiocins.

Tetrathiocin	Donor type	Functionality	Time (h)	Yield
1a	–OR	–OMe	18	68% (65%) ^a
1b	–OR	–OEt	60	53% (17%) ^a
1c	–OR	1,3-dioxole	48	72% (52%) ^a
1d	–OR	1,4-dioxane	120	88% (52%) ^a
1e	–OR	1,4-dioxepin	168	78%
1f	–N(C=O)R	Urea	72	71%
1g	–OR	15-crown-5	168	61%
1h	–OR	18-crown-6	336	33%
1i	–OR	2,2-dimethyl- 1,3-dioxole	168	57%

^a Literature data in parentheses taken from reference 16.

Oxidative addition of the tetrathiocins **1a**–**1g** with $Pd_2(dba)_3$ in toluene under microwave irradiation (150 °C, 20 min) in the presence of dppe afforded derivatives **2a**–**2g**, **2i** in 48–89% recovered, recrystallized yield (Table 2.2). Using $Pt_x dba_3$ ($x = 1.9$ – 2.0) as a starting material, the corresponding Pt derivatives **3a**–**3g**, were isolated in 37–86% recrystallized

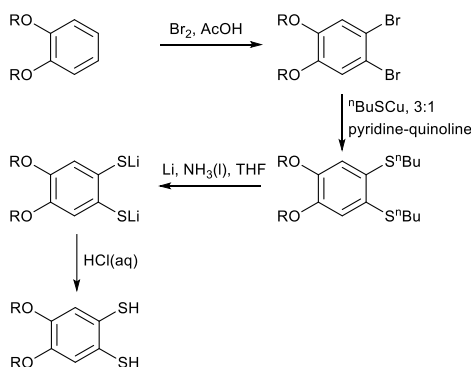
yield. The lower yields reported for **3c** and **3d** were unoptimized. Replacement of dppe by dppf permitted the ferrocene derivatives **4a**, **4g** (Pd) and **5g** (Pt) to be prepared in an analogous fashion. All complexes were characterized by ^1H and ^{31}P NMR with the coordinated dppe ligand in complexes **2b–2e** and **2g** observed as a singlet in the ^{31}P NMR with chemical shifts ranging from 51.5–51.9 ppm. The ^{31}P NMR of the corresponding Pt complexes **3a–3g** reveal the expected singlets with ^{195}Pt satellites with $^1J_{\text{Pt-P}}$ coupling ranging from 2748 to 3605 Hz, depending on the dithiolate ligand. This corresponds well with the literature data for similar complexes whose couplings correlate with their Pt–P bond lengths.^{10,19}

Table 2.2. Yields of dithiolate complexes derived from the oxidative addition of tetrathiocins **1a–1i** to Pd_2dba_3 or Pt_2dba_3 in the presence of the auxiliary chelating ligands dppe and dppf.

Complex	M	Tetrathiocin	Functionality	Phosphine	Yield
2a	Pd	1a	–OMe	dppe	85% ^a
2b	Pd	1b	–OEt	dppe	83%
2c	Pd	1c	1,3-dioxole	dppe	83%
2d	Pd	1d	1,4-dioxane	dppe	89%
2e	Pd	1e	1,4-dioxepin	dppe	78%
2f	Pd	1f	Urea	dppe	65%
2g	Pd	1g	15-crown-5	dppe	61%
2i	Pd	1i	2,2-dimethyl-1,3-dioxole	dppe	48%
3a	Pt	1a	–OMe	dppe	77% ^a
3b	Pt	1b	–OEt	dppe	57%
3c	Pt	1c	1,3-dioxole	dppe	38% ^c
3d	Pt	1d	1,4-dioxane	dppe	37% ^c
3e	Pt	1e	1,4-dioxepin	dppe	86%
3f	Pt	1f	Urea	dppe	68%
3g	Pt	1g	15-crown-5	dppe	83%
4a	Pd	1a	–OMe	dppf	50% ^b
4g	Pd	1g	15-crown-5	dppf	57%
5g	Pt	1g	15-crown-5	dppf	62%

Crystals of all complexes were grown by layering or slow diffusion. Several crystallize as solvates (see Appendix A) and once removed from the mother liquor, the crystals tend to desolvate, reflected in sub-stoichiometric quantities of solvent based on the analytical data. This synthetic methodology was successfully expanded to access the

benzo-crown ether derivatives **2g**, **3g**, **4g** and **5g** through the same two-step synthetic strategy in 57–83% recovered yield. It is noteworthy that the benzo-crown ether ligands have been prepared previously by Garner *et al.*¹⁷ However their synthetic route to the dithiol precursor requires four synthetic steps (Scheme 2.3) which must be followed by deprotonation prior to complexation. Related non-benzo-fused crown-ether dithiolate complexes were initially described by Green and more recently have been investigated by Fourmigué and co-workers.²⁰



Scheme 2.3. Garner's route to the benzene dithiol precursors. The final steps to complex formation involve ligand deprotonation and complexation.

2.2.2. Structural Studies

The structures of all new complexes were determined by X-ray diffraction. Each pair of palladium and platinum derivatives prepared from tetrathiocins **1b**, **1c**, **1d**, and **1e** were found to be isomorphous. A search of the CSD (2018 release) revealed 37 mononuclear Pd dithiolate complexes with two phosphine ligands with Pd–S bonds which revealed mean Pd–S bonds lengths of 2.30(2) Å and mean Pd–P bond lengths of 2.29(3) Å. In this context, the crystal structures of **2b–2g**, **2i** and **4g** reveal unexceptional geometric parameters with Pd–S bond lengths in the range 2.283(1)–2.310(1) Å and Pd–P bond lengths in the range 2.250(1)–2.303(1) Å. The chelate SPdS angles are almost invariant, falling in the range 88.83(3)–89.44(3)° comparable with the average bond angle derived from the CSD search (88.70(11)°), while the PPdP angles also show little variation 84.66(3)–85.97(2)°. The CSD search reveals a broader range of PPdP angles (90(7)°), but when limiting this to

chelating phosphines comprising five-membered C₂P₂Pd rings with two S donors, then a much narrower distribution of bond angles is observed at 85.5(8)°. The PdP₂S₂ centres are essentially planar with the sum of the internal angles falling in the range 356.0–360.4°. The structures of all new complexes described here are presented in Appendix A. The structures of the benzo-15-crown-5 derivatives **2g** and **4g** are presented in Figure 2.2.

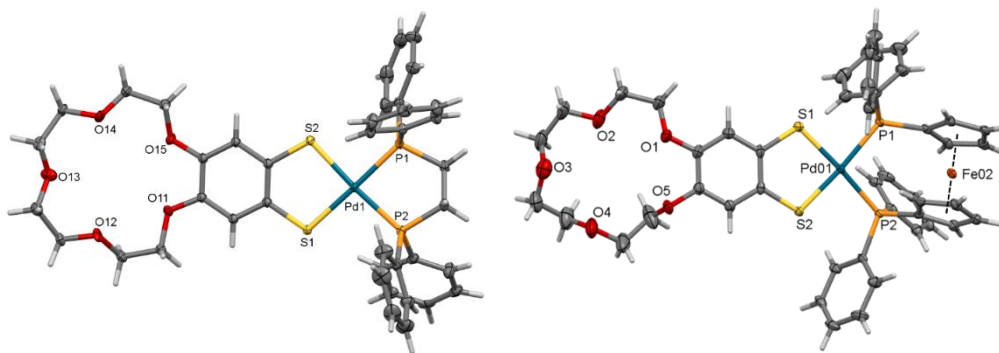


Figure 2.2. Crystal structures of **2g** (left) and **4g** (right) with thermal ellipsoids of the non-H atoms drawn at the 50% probability level. Minor components of disorder (**2g**) and lattice solvent molecules (**4g**) omitted for clarity.

2.2.3. Complexation Studies

Garner and co-workers prepared metal dithiolate complexes containing benzo-15-crown-5 dithiolate ligands with a variety of metals such as Ni, Co, W, Mo and Ti.¹⁷ They noted subtle shifts in the UV-Vis data upon coordination of alkali metals to the 15-crown-5 pocket, although no structural studies were undertaken. The cation binding properties of **2g** and **4g** with respect to Na⁺ cations, for which the benzo-15-crown-5 ligand is known to have selectivity over other alkali metals,²¹ were examined in solution and in the solid-state.

Addition of excess NaBPh₄ to a solution of **2g** led to a colour change from red to orange, reflecting a change in λ_{max} upon binding of the alkali metal. A UV-Vis spectroscopic titration (1:1 CH₂Cl₂:MeCN) revealed a plateau in λ_{max} consistent with formation of an intermediate complex [Na(**2g**)₂]⁺ (see Figure 2.3), before shifting again once the stoichiometry afforded **2g**: Na⁺ < 1:1, consistent with formation of [Na(**2g**)]⁺ as the dominant species present. MALDI-TOF mass spectrometry revealed only the presence of the 1:1 complex [Na(**2g**)]⁺ in solution, while other spectroscopic data (³¹P and ¹H NMR)

were inconclusive, revealing only subtle differences in chemical shift between free ligand and complex. The only complex which we were able to crystallize from the reaction mixture under a variety of conditions was the 1:1 complex, $[\text{Na}(\mathbf{2g})(\text{MeOH})_2][\text{BPh}_4]$, while crystals of $[\text{Na}(\mathbf{4g})][\text{BPh}_4]$ formed from solutions comprising $\mathbf{4g}$ and NaBPh_4 .

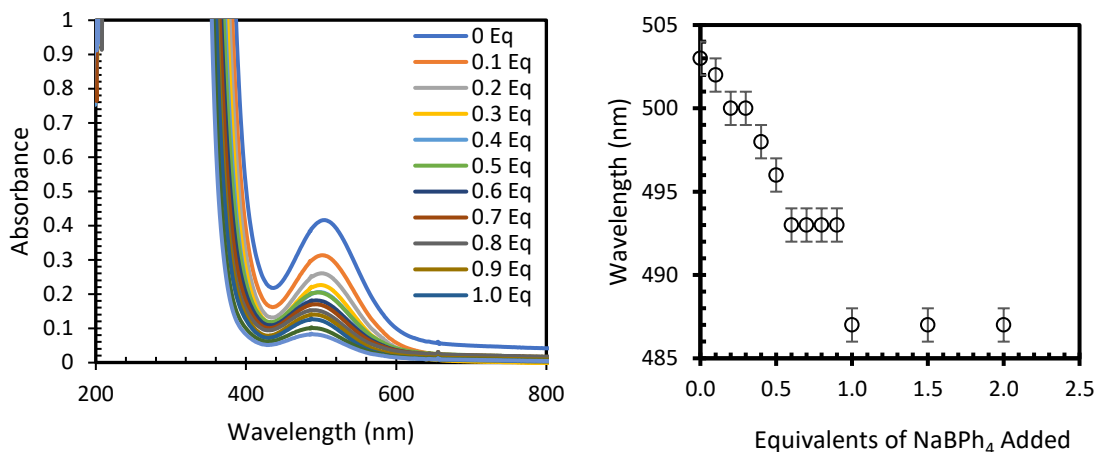


Figure 2.3. Solution UV-Vis data for $\mathbf{2g}$ in the presence of increasing numbers of equivalents of Na^+ ions (left) and change in λ_{max} for $\mathbf{2g}$ with equivalents of NaBPh_4 added (right) (solvent = 1:1 CH_2Cl_2 :MeCN).

Reaction of $\mathbf{2g}$ with one equivalent of NaBPh_4 in a 1:1 mixture of CH_2Cl_2 and MeOH afforded the crown ether complex $[\text{Na}(\mathbf{2g})(\text{MeOH})_2][\text{BPh}_4]$, which was crystallized by layering the reaction mixture with hexanes. Complexation of the macrocycle $\mathbf{2g}$ to the Na^+ cation leads to a small increase in the Pd–S bond lengths from an average of 2.300(1) Å in $\mathbf{2g}$ to 2.315(2) Å in $[\text{Na}(\mathbf{2g})(\text{MeOH})_2][\text{BPh}_4]$. However other geometric parameters including the C–S bond lengths (average 1.762(4) in $\mathbf{2g}$ and 1.768(3) Å in $[\text{Na}(\mathbf{2g})(\text{MeOH})_2][\text{BPh}_4]$) remain unchanged within error. The Na^+ cation is seven-coordinate, bound by five O-donors from the benzo-15-crown-5 macrocycle plus an additional two coordinated methanol molecules with Na–O bond lengths in the range 2.336(3)–2.559(3) Å (Figure 2.4). The geometry is highly distorted with $\text{O}\cdots\text{Na}\cdots\text{O}$ bond angles ranging from 63.53(8)–164.4(1)°, but approximates to a face-capped trigonal prism.

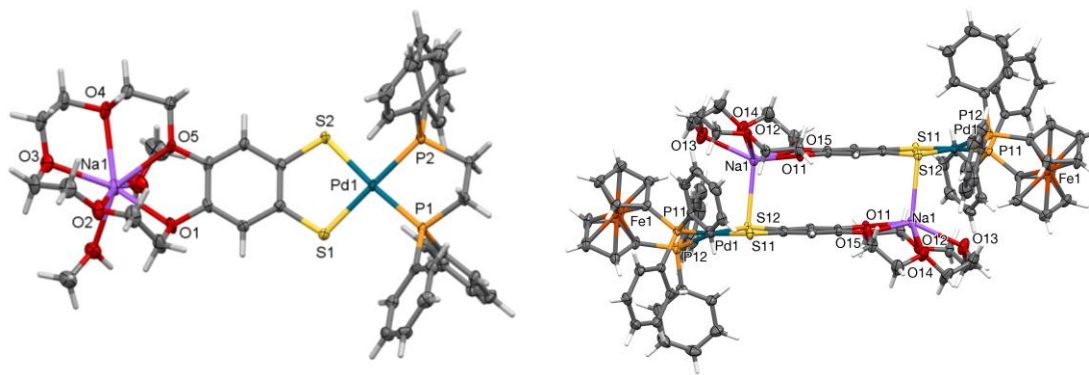


Figure 2.4. Crystal structure of (left) $[\text{Na}(\mathbf{2g})(\text{MeOH})_2][\text{BPh}_4]$ and (right) $[\text{Na}(\mathbf{4g})][\text{BPh}_4]$. Thermal ellipsoids for non-H atoms are drawn at 50% probability while lattice solvent and BPh_4^- anions are removed for clarity.

Unlike $[\text{Na}(\mathbf{2g})(\text{MeOH})_2][\text{BPh}_4]$, the crystal structure of the dppf complex, $[\text{Na}(\mathbf{4g})][\text{BPh}_4]$ reveals no solvent to complete the coordination environment of the Na^+ ion (Figure 2.4). Instead, the dimer is located about a crystallographic inversion centre generating a dimer, $[\text{Na}(\mathbf{4g})_2][\text{BPh}_4]_2$. Within the dimer the Na^+ cation adopts a six-coordinate geometry with an O_5S donor set comprising the five O donor atoms of the benzo-15-crown-5 and one of the dithiolate sulfur atoms which adopts a μ^2 -bridging mode between Pd and Na^+ ions (Figure 2.4). The Na–O bond distances to the Na^+ ion span the range 2.364(3)–2.513(4) Å. The bridging S atom (S12) forms a longer contact to Na1 (2.953(2) Å). In turn this leads to some variation in Pd–S bonding, with the bridging sulfur atom (S12) forming a longer Pd–S bond (Pd–S12 at 2.311(1) Å) than Pd1–S11 (2.290(1) Å). Overall this suggests a synergistic interplay between Na–S and Pd–S bonding within these dimers, comparable to Pd–S bond length differences observed between monodentate and bridging S atoms in dimeric $[(\text{dmobdt})\text{Pd}(\text{PPh}_3)]_2$.¹⁵

2.3.4. Electrochemical Studies

The electrochemistry of the benzo-15-crown-5 complexes **2g–5g** were studied by cyclic voltammetry (Figure 2.5) and a summary of electrochemical data presented in Table 2.3.

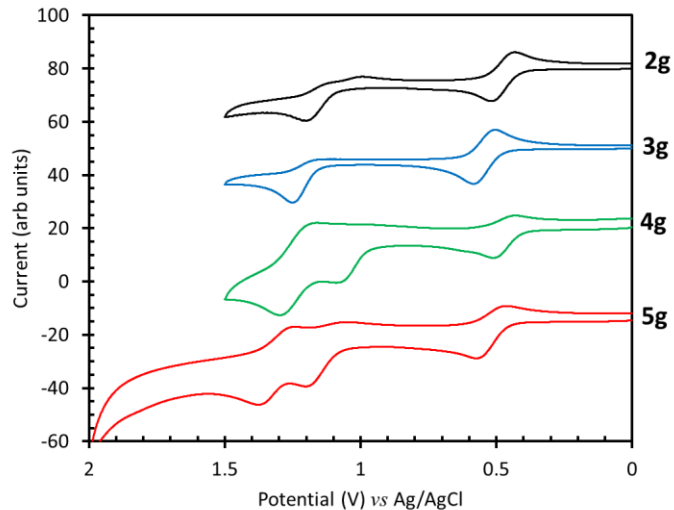


Figure 2.5. Cyclic voltammograms of complexes **2g–5g** using a 0.10 M [ⁿBu₄N][PF₆] supporting electrolyte in CH₂Cl₂ with scan rate of 100 mV/s.

All four complexes exhibit a reversible redox wave at *ca.* 0.5 V vs. Ag/AgCl, comparable with that previously reported for M(dmobdt)(dppe) (M = Pd, Pt, **2a** and **3a** respectively).¹⁴ A second oxidation is observed at higher potential (*ca.* 1.2 V) for **2g** and **3g** and two additional redox waves observed for the dppf derivatives **4g** and **5g**. The peak-to-peak separations for the first redox process ($\Delta E_{pp} = 73\text{--}110$ mV) for **2g–5g** are slightly larger than the value of 57 mV expected for an ideal Nernstian process, but more varied for subsequent oxidation processes (Table 2.3), consistent with the quasi-reversible nature of the later oxidation processes. DFT studies (B3LYP/6-31G* with an LACV3P* effective core potential for Pd) reveal that both the HOMO of **2g** and the α -HOMO of **2g**⁺ are dithiolate-based MO's supporting both oxidation processes being ligand-based (Figure 2.6).

Removal of the first electron from the complex leads to the expected orbital energy lowering upon oxidation, shifting the second redox wave to more positive potential. For the dppf derivatives **4g**, DFT studies again support the initial redox wave as being dithiolate-based (Figure 2.7) with the highest ferrocene-based MOs corresponding to the HOMO–2 and HOMO–3 (Figure 2.6). As with **2g**, oxidation lowers the orbital energies of **4g**, leading to a benzenedithiolate-based radical with a near triply degenerate set of orbitals

(HOMO–1 to HOMO–3), two of which are ferrocene-based and one dithiolate based. At this level of theory the oxidation of **4g**⁺ is expected to be dithiolate based with subsequent oxidations ferrocene based.

Table 2.3. Electrochemical data for benzo-15-crown-5-dithiolate complexes of palladium and platinum with auxiliary dppe and dppf ligands (*qr* = quasi-reversible and reflects oxidation processes in which a maximum can be found in the return wave; *ir* – irreversible and show no clear maximum in the return wave)

Compound	$E_{p,ox}, E_{p,red}$ $E_{1/2}, \Delta E_{pp}$	$E_{p,ox}, E_{p,red}$ $E_{1/2}, \Delta E_{pp}$	$E_{p,ox}, E_{p,red}$ $E_{1/2}, \Delta E_{pp}$
Pd complexes			
2g	0.517, 0.432 0.475, 0.085	1.200, 1.141 ^{qr} 1.171, 0.059	
[Na(2g)] ⁺	0.612, 0.510 0.561, 0.102	0.951 ^{ir}	1.342, 1.135 1.239, 0.207
4g	0.495, 0.422 0.459, 0.073	1.090, 0.983 ^{qr} 1.037, 0.107	1.299, 1.159 ^{qr} 1.229, 0.140
[Na(4g)] ⁺	0.599, 0.527 0.563, 0.072	0.925, ^{qir}	1.134, 1.039 1.087, 0.095
Pt complexes			
3g	0.584, 0.506 ^{qr} 0.545, 0.078	1.251 ^{ir}	
[Na(3g)] ⁺	0.655, 0.544 0.600, 0.111	0.993 ^{ir}	
5g	0.572, 0.462 0.517, 0.110	1.202, 1.068 ^{qr} 1.135, 0.134	1.372, 1.242 ^{qr} 1.307, 0.130

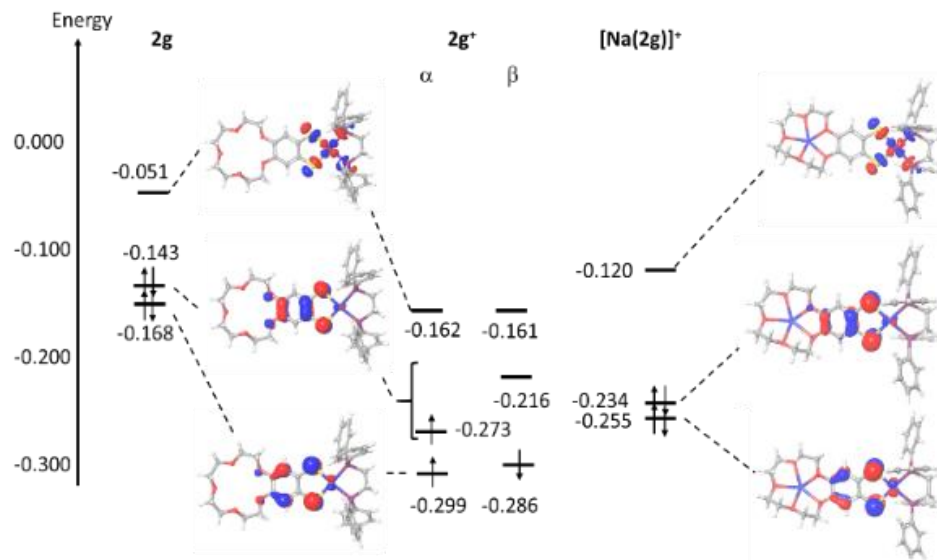


Figure 2.6. DFT computed orbital energies (B3LYP/6-31G* with LACV3P* for Pd and Na) for $2g$, $2g^+$ and $[Na(2g)]^+$. For cationic $2g^+$ the energies of the one-electron orbitals corresponding to “spin-up” (α) electrons and “spin-down” (β) electrons derived from the UHF calculation are presented.

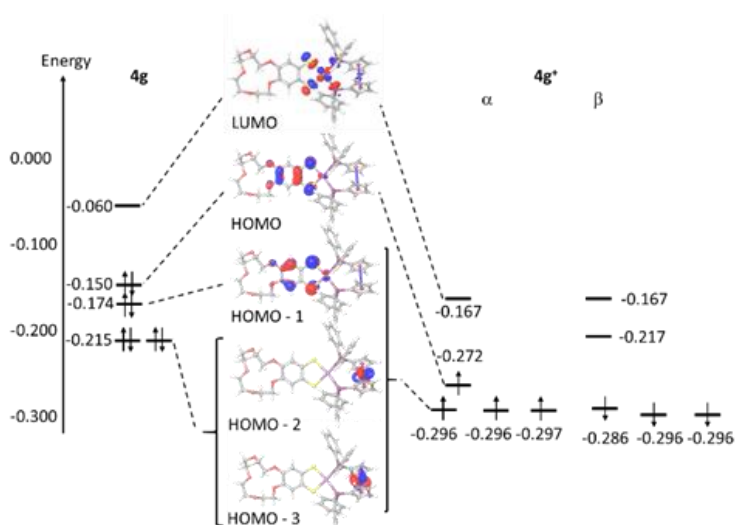


Figure 2.7. DFT computed orbital energies (B3LYP/6-31G* with LACV3P* for Pd and Fe) for $4g$ and $4g^+$. For cationic $4g^+$ the energies of the one-electron orbitals corresponding to “spin-up” (a) electrons and “spin-down” (b) electrons derived from the UHF calculation are presented.

Coordination of Na^+ to the benzo-15-crown-5 complexes (**2g**, **4g** and **5g**) leads to a shift of *ca.* +100 mV in the first oxidation potential of these complexes (Figure 2.8), as reflected in the DFT studies (Figure 2.7) which show a lowering of the frontier orbital energies of $[\text{Na}(\mathbf{2g})]^+$ in relation to **2g**. Similar positive shifts in redox potential have been observed for other redox active groups attached to crown ethers such as TTF studied by Hansen and Bryce (up to 120 mV).²² The additional oxidation process for both $[\text{Na}(\mathbf{2g})]^+$ and $[\text{Na}(\mathbf{4g})]^+$ around 0.95 V corresponds to the irreversible oxidation of the BPh_4^- counterion.

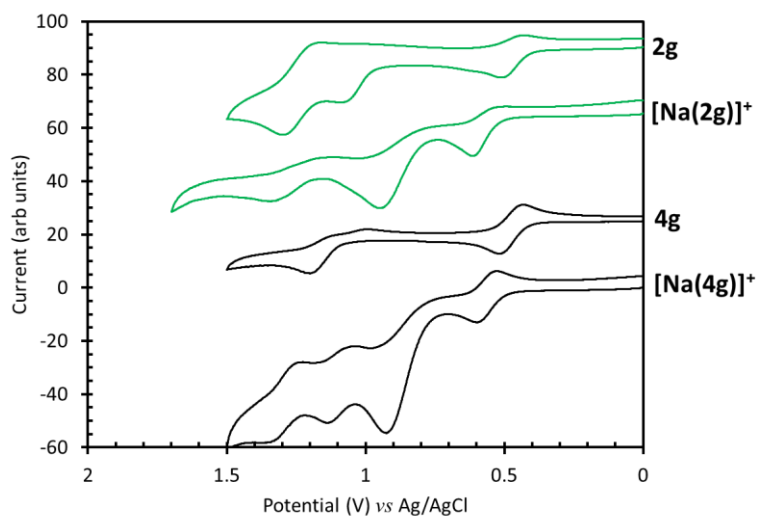


Figure 2.8. Cyclic voltammograms of complexes **2g** and **4g** and their Na^+ complexes, $[\text{Na}(\mathbf{2g})]^+$ and $[\text{Na}(\mathbf{4g})]^+$ using a 0.10 M $[\text{nBu}_4\text{N}][\text{PF}_6]$ supporting electrolyte in CH_2Cl_2 with scan rate of 100 mV/s.

2.3 Conclusion & Future Work

The current study has expanded the range of tetrathiocins available for oxidative addition chemistry to low valent metals through a convenient one-pot process. This methodology has been highlighted by incorporating a crown ether functional group into the backbone, which provides a highly flexible two-step synthetic route to metal–dithiolate complexes *via* (i) tetrathiocin synthesis and (ii) a one-pot self-assembly of the coordination complex. This should be broadly applicable to a range of transition metals. Preliminary studies indicated similar oxidative addition chemistry with low oxidation state *p*-block

elements, exemplified by P(I).²³ For the transition metal reactivity, the oxidative addition will likely support a range of other auxiliary ligands in addition to phosphines. The oxidative addition of tetrathiocins to the *d*-block metals nickel and cobalt with supporting N-donor and Cp groups is described in Chapters 3, 4, and 5, while the oxidative addition chemistry to low oxidation state *p*-block compounds is described in Chapter 6.

2.4. Experimental

2.4.1. General Procedures

Unless otherwise stated all chemicals were purchased from Sigma-Aldrich, Strem or Alfa Aesar. Tetrathiocins **1a–1d** were prepared according to a modified procedure and their analytical data matched the literature report.¹⁶ *N,N'*-Dimethylbenzimidazole was prepared from literature methods.²⁴ Pd₂dba₃·CHCl₃ and Pt_{*x*}dba₃·CH₂Cl₂ were prepared according to the literature methods.^{25,26} Pt_{*x*}dba₃·CH₂Cl₂ is known²⁶ to often be sub-stoichiometric in Pt and micro-analytical data were recorded on each batch prepared before use. In our hands the quantity of Pt persistently fell close (*x* = 1.9–2.0) to the stoichiometric value. Standard solvents were dried and deoxygenated using an Innovative Technology Solvent Purification System and manipulation of air-sensitive materials carried out under an atmosphere of dry nitrogen using standard Schlenk techniques and a dry-nitrogen glove box (MBraun Labmaster). Microwave reactions were carried out in sealed vessels using a Biotage Initiator 1 microwave.

2.4.2. Physical Measurements

Elemental compositions were determined on a PerkinElmer 2400 Series II CHNS/O Analyzer. UV-Vis spectra were measured on an Agilent 8453 spectrophotometer using *ca.* 2 × 10⁻³ M solutions in a 1:1 mixture of dichloromethane and acetonitrile in the range 200–800 nm. IR spectra were obtained using a Bruker Alpha FT-IR spectrometer equipped with a Platinum single reflection diamond ATR module. NMR spectra were recorded at room temperature on a Bruker Avance Ultrashield 300 MHz. Chemical shifts are reported in ppm relative to internal standards for ¹H using CDCl₃ (¹H δ = 7.26 ppm, s), DMSO-d₆ (¹H δ = 2.50 ppm, quintet), or MeCN-d₃ (¹H δ = 1.94 ppm, septet) as an internal reference point relative to Me₄Si (δ = 0 ppm) and external standard for ³¹P (85% H₃PO₄ = 0 ppm). Mass

spectra were recorded on a Waters XEVO G2-XS spectrometer specifically using the atmospheric solids analysis probe in positive resolution mode (ESI+) or on a Waters Micromass LCT Classic Electrospray Ionization Time of Flight (ESI-TOF) mass spectrometer operated in positive mode. Electrochemical studies were undertaken using a BAS electrochemical instrument controlled through BAS epsilon software using scan rates between 100 and 500 mV s⁻¹. Samples were measured using a degassed CH₂Cl₂ solution of 0.10 M [ⁿBu₄N][PF₆] supporting electrolyte and a 3.0 M NaCl reference electrode at room temperature.

2.4.3. X-Ray Crystallography

Crystals of the metal complexes were mounted on a cryoloop with paratone oil and examined on either a Bruker D8 Venture diffractometer equipped with Photon 100 CCD area detector or a Bruker APEX-II diffractometer with CCD detector using graphite-monochromated Mo-K α radiation ($\lambda = 0.71073 \text{ \AA}$). An Oxford Cryostream cooler was used to maintain cryogenic temperatures for these studies. Data were collected using the APEX-II software²⁷ integrated using SAINT²⁸ and corrected for absorption using a multi-scan approach (SADABS).²⁹ Final cell constants were determined from full least squares refinement of all observed reflections. The structures of **2c–2f** were solved by direct methods (SHELXS),³⁰ [Na(**2g**)(MeOH)₂][BPh₄] was solved using charge flipping methods (olex2.solve),³¹ while all other structures were solved using intrinsic phasing (SHELXT).³² All structures were refined with full least squares refinement on F^2 using either SHELXL³³ or Olex2 software.³¹ In structures **2b**, **2g**, **3b**, and **4g** there were regions of poorly resolved electron density located in voids indicative of residual lattice solvent that could not be modelled sensibly. These were treated with a solvent mask using PLATON SQUEEZE.³⁴ All hydrogen atoms were added at calculated positions and refined isotropically with a riding model.

2.4.4. Computational Methods

Geometry-optimized DFT calculations on **2g**, **2g**⁺ and [Na(**2g**)]⁺ as well as **4g** and [Na(**4g**)]⁺ were made within Jaguar and visualized using the Maestro GUI.³⁵ Geometry optimization used the B3LYP functional and 6-31G* basis set for all non-metals and the

LACV3P* basis set for Na, Pd and Fe. The crystallographic geometry was implemented as an initial starting point for these calculations. The extent of solvation of the Na⁺ ion in [Na(**2g**)⁺] and [Na(**4g**)⁺] in solution is unknown and likely solvent dependent. For these qualitative studies the methanol solvate molecules in the cation [Na(**2g**)(MeOH)₂]⁺ were omitted and the donor S-atom making up the coordination environment of the sodium ion in [Na(**4g**)⁺] was similarly omitted. For the paramagnetic species **2g**⁺ and **4g**⁺ an unrestricted Hartree Fock approach was implemented.

2.4.5. Synthesis of benzo-18-crown-6-1,2,5,6-tetrathiocins (**1h**)

Benzo-18-crown-6 (1.40 g, 4.46 mmol) was added to 10 mL of degassed glacial acetic acid under a nitrogen atmosphere. S₂Cl₂ (0.37 mL, 4.5 mmol) was added dropwise to the solution, and the solution was stirred for 14 days, undergoing a color change from yellow to green and finally forming a yellow precipitate in solution. The solution was vacuum filtered and washed with Et₂O (2 × 10 mL). The yellow solid was dried *in vacuo* (1.67 g, 34%). A sample was redissolved in CH₂Cl₂ (15 mL), washed with H₂O (3 × 20 mL) to remove trace HOAc, dried over MgSO₄, and dried was used for characterization.

HRMS (ESI+) *m/z*: [M]⁺ calc. for C₃₂H₄₄O₁₂S₄⁺ 748.1716. Found 748.1703.

MS (ESI+) *m/z*: [M + K]⁺ calc. for C₃₂H₄₄O₁₂S₄K⁺ 787.1. Found: 787.1.

Elemental Analysis calc. for C₃₂H₄₄O₁₂S₄·CH₂Cl₂: C 47.53; H 5.56. Found: C 47.32; H 5.47.

IR ν_{\max} (cm⁻¹): 2861 (br, m), 1633 (w), 1571 (m), 1554 (m), 1488 (s), 1448 (s), 1352 (s), 1351 (s), 1312 (m), 1256 (vs), 1203 (vs), 1090 (vs), 1046 (vs), 968 (s), 954 (s), 942 (s), 912 (m), 881 (m), 868 (s), 839 (m), 803 (s), 678 (w), 645 (w), 611 (w), 552 (w), 510 (w), 462 (w), 446 (w).

2.4.5. Synthesis of 1,1-dimethyldioxolobenzene-1,2,5,6-tetrathiocin (**1i**)

2,2-dimethyl-1,3-benzodioxole, (1.00 g, 6.60 mmol) was added to 20 mL of degassed glacial acetic acid under a nitrogen atmosphere. S₂Cl₂ (0.53 mL, 6.6 mmol) was added dropwise to the solution, and the solution was stirred for 7 days, undergoing a color change from yellow to green and finally forming a yellow precipitate in solution. The solution was vacuum filtered and washed with Et₂O (2 × 10 mL). The yellow solid was dried *in vacuo* (0.591 g, 42%).

Elemental Analysis calc. for C₁₈H₁₆O₄S₄: C 47.53; H 5.56. Found: C 47.31; H 3.60.

2.4.5. Synthesis of (deobdt)Pd(dppe) (2b)

Pd₂dba₃·CHCl₃ (0.100 g, 0.109 mmol), dppe (0.087 g, 0.218 mmol) and tetrathiocin **1b** (0.050 g, 0.109 mmol) were combined in an oven-dried 5 mL microwave vial in the glove box. Dry toluene (5 mL) was added, and the suspension was heated in the microwave for 20 min at 150 °C. The resultant pink solid was isolated from a pale-yellow solution by filtration. The precipitate was washed with hexanes and dried in air (0.133 g, 83% yield). The solid was recrystallized from a saturated CH₂Cl₂ solution layered with hexanes to produce red needles suitable for X-ray diffraction.

¹H NMR (300 MHz, ppm, CDCl₃) δ_H = 7.88–7.81 (8H, m, phosphine *m*-H), 7.51–7.44 (12H, m, phosphine *o,p*-H), 6.93 (2H, s, benzo C–H), 3.97 (4H, q, *J* = 6.9 Hz, O–CH₂), 2.51 (4H, d, ²*J*_{P–H} = 20.7 Hz, PCH₂), 1.36 (6H, t, *J* = 6.9 Hz CH₃).

³¹P NMR (121 MHz, ppm, CDCl₃) δ_P{¹H} = 51.73.

HRMS (ESI-TOF) *m/z*: [M + H]⁺ calc. for C₃₆H₃₇O₂P₂S₂Pd⁺ 733.0757; found 733.0767.

Elemental Analysis calc. for C₃₆H₃₆O₂P₂S₂Pd: C 58.98, H 4.95%; found: C 58.92, H 4.87%.

IR (ν_{max}, cm⁻¹): 3050(w), 2974(m), 2901(w), 1583(w), 1463(s), 1434(vs), 1389(m), 1337(m), 1235(vs), 1148(s), 1101(s), 1046(s), 998(w), 877(m), 820(m), 745(m), 690(vs), 528(vs), 483(m).

2.3.6. Synthesis of (doxlbdt)Pd(dppe) (2c)

Pd₂dba₃·CHCl₃ (0.100 g, 0.109 mmol), dppe (0.087 g, 0.218 mmol) and tetrathiocin **1c** (0.040 g 0.109 mmol) were combined in an oven-dried 5 mL microwave vial in the glove box. Dry toluene (5 mL) was added, and the suspension was heated in the microwave for 20 min at 150 °C. The resultant dark red solid was isolated from a pale-yellow solution by filtration. The precipitate was washed with hexanes and dried in air (0.125 g, 83% yield). The solid was recrystallized from a saturated CH₂Cl₂ solution layered with hexanes to produce red-orange needles suitable for X-ray diffraction.

¹H NMR (300 MHz, ppm, CDCl₃) δ_H = 7.87–7.81 (8H, m, phosphine *m*-H), 7.51–7.44 (12H, m, phosphine *o,p*-H), 6.85 (2H, s, benzo C–H), 5.82 (2H, s, O–CH₂–O), 2.51 (4H, d, ²J_{P–H} = 20.7 Hz, PCH₂).

³¹P NMR (121 MHz, ppm, CDCl₃) δ_P{¹H} = 51.52.

HRMS (ESI-TOF) *m/z*: [M + H]⁺ calc. for C₃₃H₂₉O₂P₂S₂Pd⁺ 689.0131; found 689.0153.

Elemental Analysis calc. for C₃₃H₂₈O₂P₂S₂Pd·1/8CH₂Cl₂: C 56.87, H 4.05%; found: C 57.07, H 3.82%.

IR (ν_{max}, cm⁻¹): 3052(w), 2888(w), 1498(w), 1454(vs), 1435(s), 1309(w), 1216(vs), 1102(m), 1036(m), 998(w), 928(m), 819(m), 745(m), 690(s), 662(m), 527(s), 480(m).

2.4.7. Synthesis of (doxbd)Pd(dppe) (2d)

Pd₂dba₃·CHCl₃ (0.100 g, 0.109 mmol), dppe (0.087 g, 0.218 mmol) and tetrathiocin **1d** (0.043 g, 0.109 mmol) were combined in an oven-dried 5 mL microwave vial in the glove box. Dry toluene (5 mL) was added and the suspension was heated in the microwave for 20 min at 150 °C. The resultant red-orange solid was isolated from a pale-yellow solution by filtration. The precipitate was washed with hexanes and dried in air (0.137 g, 89% yield). The solid was recrystallized from a saturated CH₂Cl₂ solution layered with hexanes to produce red-orange needles suitable for X-ray diffraction.

¹H NMR (300 MHz, ppm, CDCl₃): δ_H = 7.87–7.81 (8H, m, phosphine *m*-H), 7.49–7.43 (12H, m, phosphine *o,p*-H), 6.89 (2H, s, benzo C–H), 4.13 (4H, s, O–CH₂–CH₂–O), 2.50 (4H, d, ²J_{P–H} = 20.7 Hz, PCH₂).

³¹P NMR (121 MHz, ppm, CDCl₃) δ_P{¹H} = 51.63.

HRMS (ESI-TOF) *m/z*: [M + H]⁺ calc. for C₃₄H₃₁O₂P₂S₂Pd⁺ 703.0287; found 703.0265.

Elemental Analysis calc. for C₃₄H₃₀O₂P₂S₂Pd·1/5CH₂Cl₂: C 57.05, H 4.26%; found: C 57.07, H 4.13%.

IR (ν_{max}, cm⁻¹): 3052(w), 2972(w), 2917(w), 2869(w), 1556(m), 1458(vs), 1435(vs), 1289(vs), 1246(vs), 1093(s), 1067(s), 894(m), 749(m), 690(vs), 529(vs), 483(m).

2.4.8. Synthesis of (doxebdt)Pd(dppe) (2e)

Pd₂dba₃·CHCl₃ (0.100 g, 0.109 mmol), dppe (0.087 g, 0.218 mmol) and tetrathiocin **1e** (0.046 g, 0.109 mmol) were combined in an oven-dried 5 mL microwave vial in the glove box. Dry toluene (5 mL) was added and the suspension was heated in the microwave for 20 min at 150 °C. The resultant dark red-brown solid was isolated from a pale-yellow solution by filtration. The precipitate was washed with hexanes and dried in air (0.122 g, 78% yield). The solid was recrystallized from a saturated CH₂Cl₂ solution layered with hexanes to produce orange needles suitable for X-ray diffraction.

¹H NMR (300 MHz, ppm, CDCl₃): δ_H = 7.86–7.80 (8H, m, phosphine *m*-H), 7.50–7.45 (12H, m, phosphine *o,p*-H), 7.03 (2H, s, benzo C–H), 3.99 (4H, t, *J* = 5.1 Hz, O–CH₂–CH₂–O), 2.50 (4H, d, ²*J*_{P–H} = 21.0 Hz, PCH₂), 2.06 (2H, apparent triplet, *J* = 5.1 Hz, O–CH₂–CH₂–CH₂–O).

³¹P NMR (121 MHz, ppm, CDCl₃) δ_P{¹H} = 51.96.

HRMS (ESI-TOF) *m/z*: [M + H]⁺ calc. for C₃₅H₃₃O₂P₂S₂Pd⁺ 717.0444; found 717.0462.

Elemental Analysis calc. for C₃₅H₃₂O₂P₂S₂Pd·1/4CH₂Cl₂: C 57.34, H 4.44%; found: C 57.17, H 4.30%.

IR (ν_{max}, cm⁻¹): 3072(w), 2953(w), 2865(w), 1467(vs), 1450(vs), 1435(vs), 1382(m), 1296(m), 1264(vs), 1250(s), 1096(s), 1046(s), 874(m), 690(vs), 528(vs), 482(m).

2.4.9. Synthesis of (dmbimdt)Pd(dppe) (2f)

Pd₂dba₃·CHCl₃ (0.100 g, 0.109 mmol), dppe (0.087 g, 0.218 mmol) and tetrathiocin **1f** (0.049 g, 0.109 mmol) were combined in an oven-dried 5 mL microwave vial in the glove box. Dry toluene (5 mL) was added and the suspension was heated in the microwave for 20 mins at 150 °C. The resultant dark purple solid was isolated from a pale solution by filtration. The precipitate was washed with hexanes and dried in air (0.104 g, 65% yield). The solid was recrystallized from a saturated CH₂Cl₂ solution layered with hexanes to produce red needles suitable for X-ray diffraction.

¹H NMR (300 MHz, ppm, CDCl₃): δ_H = 7.90–7.80 (8H, m, phosphine *m*-H), 7.48–7.45 (12H, m, phosphine *o,p*-H), 7.00 (2H, s, benzo C–H), 3.28 (6H, s, NCH₃), 2.52 (4H, d, ²*J*_{PH} = 20.7 Hz, PCH₂).

^{31}P NMR (121 MHz, ppm, CDCl_3) $\delta_{\text{P}}\{^1\text{H}\} = 51.66$.

HRMS (ASAP) m/z : $[\text{M} + \text{H}]^+$ calc. for $\text{C}_{35}\text{H}_{33}\text{N}_2\text{OP}_2\text{S}_2\text{Pd}^+$ 729.0556; found 729.0561.

Elemental Analysis calc. for $\text{C}_{35}\text{H}_{32}\text{N}_2\text{O}_2\text{P}_2\text{S}_2\text{Pd}$: C 57.65, H 4.42, N 3.84%; found: C 57.62, H 4.38, N 3.47%.

IR (ν_{max} , cm^{-1}): 3048(w), 2960(w), 2915(w), 1690(C=O, vs), 1580(m), 1496(m), 1483(m), 1435(s), 1398(m), 1378(m), 1319(w), 1261(s), 1187(w), 1101(s), 1081(m), 1027(m), 998(m), 941(w), 876(w), 820(m), 730(s), 691(s), 650(s), 617(m), 582(m), 530(s), 482(m).

2.4.10. Synthesis of (b-15-c-5-dt)Pd(dppe) (2g)

$\text{Pd}_2\text{dba}_3 \cdot \text{CHCl}_3$ (0.100 g, 0.109 mmol), dppe (0.087 g, 0.218 mmol) and tetrathiocin **1g** (0.073 g 0.109 mmol) were combined in an oven-dried 5 mL microwave vial in the glove box. Dry toluene (5 mL) was added and the suspension was heated in the microwave for 20 mins at 150 °C. The resultant pink microcrystalline solid was isolated from a pale yellow solution by filtration. The precipitate was washed with hexanes and dried in air (0.172 g, 94% yield). The solid was recrystallized from the slow diffusion of Et_2O into a saturated MeCN solution to produce bright red needles of **2g** suitable for X-ray diffraction (61% yield for recrystallized material).

^1H NMR (300 MHz, ppm, CDCl_3): $\delta_{\text{H}} = 7.87\text{--}7.79$ (8H, m, phosphine *m*-H), 7.51–7.42 (12H, m, phosphine *o,p*-H), 6.93 (2 H, s, benzo C–H), 4.06–4.01 (4H, m, crown C–H), 3.86–3.81 (4H, m, crown C–H), 3.75–3.71 (8H, m, crown C–H), 2.51 (4H, d, $^2J_{\text{PH}} = 20.8$ Hz, PCH_2); (300 MHz, DMSO- d_6): $\delta_{\text{H}} = 7.86\text{--}7.77$ (8H, m, phosphine *m*-H), 7.62–7.57 (12H, m, phosphine *o,p*-H), 6.72 (2H, s, benzo C–H), 3.92–3.85 (4H, m, crown C–H), 3.74–3.69 (4H, m, crown C–H), 3.62–3.59 (8H, m, crown C–H), 2.64 (4H, d, $^2J_{\text{PH}} = 20.2$ Hz, PCH_2); (300 MHz, ppm, MeCN- d_3) $\delta_{\text{H}} = 7.85\text{--}7.76$ (8H, m, phosphine *m*-H), 7.57–7.47 (12H, m, phosphine *o,p*-H), 6.72 (2 H, s, benzo C–H), 3.96–3.91 (4H, m, crown C–H), 3.75–3.70 (4H, m, crown C–H), 3.61–3.56 (8H, m, crown C–H), 2.63 (4H, d, $^2J_{\text{PH}} = 20.5$ Hz, PCH_2).

^{31}P NMR (121 MHz, ppm, DMSO- d_6) $\delta_{\text{P}}\{^1\text{H}\} = 53.52$; (121 MHz, ppm, MeCN- d_3) $\delta_{\text{P}}\{^1\text{H}\} = 52.89$.

HRMS (ESI-TOF) m/z : $[M + H]^+$ calc. for $C_{40}H_{42}O_5P_2S_2Pd^+$ 835.1076; found 835.1097.

Elemental Analysis calc. for $C_{40}H_{42}O_5P_2S_2Pd \cdot 12CH_2Cl_2$: C 55.42, H 4.95%; found: C 55.36, H 5.14%.

IR (ν_{max} cm^{-1}): 2923(m), 2862(m), 1474(s), 1450(s), 1435(vs), 1244(s), 1134(m), 1102(vs), 1064(m), 876(w), 713(m), 703(s), 691(vs), 528(s), 481(m).

2.4.11. Synthesis of (dmdoxlbdtd)Pd(dppe) (2i)

$Pd_2dba_3 \cdot CHCl_3$ (0.100 g, 0.109 mmol), dppe (0.087 g, 0.218 mmol) and tetrathiocin **1i** (0.046 g, 0.109 mmol) were combined in an oven-dried 5 mL microwave vial in the glove box. Dry toluene (5 mL) was added and the suspension was heated in the microwave for 20 mins at 150 °C. The resultant dark purple solid was isolated from a pale solution by filtration. The precipitate was washed with hexanes and dried in air (0.104 g, 65% yield). The solid was recrystallized from a saturated CH_2Cl_2 solution layered with hexanes to produce red needles suitable for X-ray diffraction.

1H NMR (300 MHz, ppm, $CDCl_3$) $\delta_H = 7.87-7.84$ (8H, m, phosphine *m*-H), 7.54–7.41 (12H, m, phosphine *o,p*-H), 6.88 (2H, s, benzo C–H), 2.45 (4H, d, $^2J_{P-H} = 22.9$ Hz, PCH_2), 1.70 (6H, s, $O-C(CH_3)_2-O$).

^{31}P NMR (121 MHz, ppm, $CDCl_3$) $\delta_P\{^1H\} = 51.40$.

Elemental Analysis calc. for $C_{33}H_{28}O_2P_2S_2Pd$: C 57.52, H 4.15%; found: C 57.07, H 3.82%.

IR (ν_{max} cm^{-1}): 3053(w), 2983(w), 1466(m), 1377(w), 1217 (s), 1098(m), 1093(s), 843(m), 744(w), 691(s), 521(vs), 477(m), 432(w).

2.4.12. Synthesis of [(b-15-c-5-Na-dt)Pd(dppe)][BPh₄] ([Na(2g)(MeOH)₂][BPh₄])

$Pd_2dba_3 \cdot CHCl_3$ (0.100 g, 0.109 mmol), dppe (0.087 g, 0.218 mmol) and tetrathiocin **1g** (0.073 g 0.109 mmol) were combined in an oven-dried 5 mL microwave vial in the glove box. Dry toluene (5 mL) was added and the suspension was heated in the microwave for 20 mins at 150 °C. The resultant pink microcrystalline solid was isolated from a pale yellow solution by filtration. The precipitate was washed with hexanes and dried in air (0.172 g, 94% yield). The solid was recrystallized from the slow diffusion of Et_2O into a saturated MeCN solution to produce bright red needles of **2i** suitable for X-ray diffraction

¹H NMR (300 MHz, ppm, DMSO-d₆): δ_H = 7.82-7.79 (8H, m, phosphine *m*-H), 7.55-7.53 (12H, m, phosphine *o,p*-H), 7.17-7.15 (8H, m, borate C-H), 6.94-6.89 (8H, m, borate C-H), 6.81-6.76 (4H, m, borate *p*-C-H), 6.71 (2H, s, benzo C-H), 3.93-3.90 (4H, m, crown C-H), 3.70 (4H, m, crown C-H), 3.59 (8H, br s, crown C-H), 2.73 (4H, d, ²J_{PH} = 21.1 Hz, PCH₂); (300 MHz, ppm, MeCN-d₃) δ_H = 7.77 – 7.75 (8H, m, *m*-H), 7.56-750 (12H, m, *o,p*-H), 7.26 (8H, br s, borate C-H), 6.99 (8H, t, *J* = 7.2 Hz, borate C-H), 6.85-6.83 (4H, br d, *J* = 3.3 Hz, borate C-H), 5.45 (2H, s, benzo C-H), 4.03 (4H, s, crown C-H), 3.76 (4H, s, crown C-H), 3.66 (8H, s, crown C-H), 2.62 (4H, 2.66-2.59, d, ²J_{PH} = 21.3 Hz, PCH₂).

³¹P NMR (121 MHz, ppm, DMSO-d₆) δ_P{¹H} = 53.59; (121 MHz, ppm, MeCN-d₃); δ_P{¹H} = 54.12.

HRMS (MALDI-MS) *m/z*: [M]⁺ calc. for C₄₀H₄₂O₅P₂S₂PdNa⁺ found: 857.0895; found: 857.0896.

Elemental Analysis calc. for C₆₄H₆₂BNaO₅P₂S₂Pd·MeOH C 64.55, H 5.50%; found: C 64.78, H 5.21%.

IR (ν_{max} cm⁻¹): 3053(w), 2911(w), 2876(w), 1585(w), 1480(m), 1455(m), 1433(m), 1383(w), 1357(w), 1348(w), 1307(w), 1244(s), 1184(m), 1118(m), 1101(s), 1093(s), 1051(m), 1030(m), 998(w), 972(w), 927(m), 876(m), 858(w), 849(w), 840(m), 821(m), 747(s), 733(s), 704(vs), 690(vs), 623(w), 610(s), 530(s), 523(s), 482(s), 430(w).

2.4.13. Synthesis of (deobdt)Pt(dppe) (3b)

Pt₂dba₃·CH₂Cl₂ (0.133 g, 0.109 mmol), dppe (0.087 g, 0.218 mmol) and tetrathiocin **1b** (0.050 g, 0.109 mmol) were combined in an oven-dried 5 mL microwave vial in the glove box. Dry toluene (5 mL) was added and the suspension was heated in the microwave for 60 min at 150 °C. The resultant solution was stirred overnight and a yellow-brown solid was isolated from a pale orange solution by filtration. The precipitate was washed with hexanes and dried in air (0.103 g, 57% yield). The solid was recrystallized from a saturated CH₂Cl₂ solution layered with hexanes to produce clear yellow plate-shaped crystals suitable for X-ray diffraction.

¹H NMR (300 MHz, ppm, CDCl₃): δ_H 7.825 (8H, 7.84-7.81, m, phosphine *m*-H), 7.46 (12H, 7.51-7.40, m, phosphine *o,p*-H), 7.09 (2H, s, benzo C-H), 3.97 (4H, q, *J* = 8.4 Hz, CH₂), 2.47 (4H, d, ²*J*_{PH} = 20.4 Hz, PCH₂), 1.36 (6H, t, *J* = 6.3 Hz, CH₃).

³¹P NMR (121 MHz, CDCl₃) δ_P{¹H} = 45.30 with satellites at 56.86 and 33.74 (¹*J*_{Pt-P} = 2816 Hz).

HRMS (ESI-TOF) *m/z*: [M + H]⁺ calc. for C₃₆H₃₇O₂P₂S₂Pt⁺ 822.1358; found 822.1306.

Elemental Analysis calc. for C₃₆H₃₆O₂P₂S₂Pt: C 52.61; H 4.42%; found: C 52.47; H 4.37%.

IR (ν_{max}, cm⁻¹): 3049(w), 2969(w), 2954(w), 2915(w), 2848(w), 1585(w), 1572(m), 1463(m), 1433(s), 1402(m), 1388(m), 1338(m), 1237(s), 1182(m) 1156(m), 1152(m), 1099(s), 1043(m), 998(m), 917(m), 877(m), 847(m), 815(m), 746(s), 714(s), 693(vs), 654(s), 532(vs), 792(s), 463(m), 438(m).

2.4.14. Synthesis of (doxlbdt)Pt(dppe) (3c)

Pt₂dba₃·CH₂Cl₂ (0.128 g, 0.109 mmol), dppe (0.087 g, 0.218 mmol) and tetrathiocin **1c** (0.040 g, 0.109 mmol) were combined in an oven-dried 5 mL microwave vial in the glove box. Dry toluene (5 mL) was added and the suspension was heated in the microwave for 60 min at 150 °C. The resultant solution was stirred overnight and a yellow-brown solid was isolated from a pale orange solution by filtration. The precipitate was washed with hexanes and dried in air (0.064 g, 38% yield). The solid was recrystallized from a saturated CH₂Cl₂ solution layered with hexanes to produce clear yellow plate-shaped crystals suitable for X-ray diffraction.

¹H NMR (300 MHz, ppm, CDCl₃): δ_H = 7.845 (8H, 7.87-7.82, m, phosphine, *m*-H), 7.47 (12H, 7.51-7.44, m, phosphine *o,p*-H), 6.99 (2H, s, benzo C-H), 5.84 (2H, s, O-CH₂-O), 2.45 (4H, d, ²*J*_{PH} = 17.4 Hz, PCH₂).

³¹P NMR (121 MHz, ppm, CDCl₃): δ_P{¹H} = 41.60 with satellites at 56.46 and 26.70 (¹*J*_{Pt-P} = 3622 Hz).

HRMS (ESI-TOF) *m/z*: [M + H]⁺ calc. for C₃₃H₂₉O₂P₂S₂Pt⁺ 778.0732; found 778.0695.

Elemental Analysis calc. for $C_{33}H_{28}O_2P_2S_2Pt \cdot \frac{1}{2} CH_2Cl_2$: C 48.33; H 3.44%; found: C 48.11; H 3.60%.

IR (ν_{max} , cm^{-1}): 3050(w), 2860(w), 1494(w), 1472(m), 1455(s), 1435(s), 1405(m), 1350(w), 1310(w), 1220(s), 1102(m), 1064(m), 1035 (m), 998(w), 949(w), 933(m), 877 (m), 842(m), 820(m), 745(m), 688(s), 655(m), 527(s), 495(m), 439(m).

2.4.15. Synthesis of (doxbd)Pt(dppe) (3d)

$Pt_2dba_3 \cdot CH_2Cl_2$ (0.138 g, 0.109 mmol), dppe (0.087 g, 0.218 mmol) and tetrathiocin **1d** (0.043 g, 0.109 mmol) were combined in an oven-dried 5 mL microwave vial in the glove box. Dry toluene (5 mL) was added and the suspension was heated in the microwave for 60 min at 150 °C. The resultant solution was stirred overnight and a brown-orange solid was isolated from a pale yellow solution by filtration. The precipitate was washed with hexanes and dried in air (0.0632 g, 37% yield). The solid was recrystallized from a saturated CH_2Cl_2 solution layered with hexanes to produce clear yellow plate-shaped crystals suitable for X-ray diffraction.

1H NMR (300 MHz, ppm, $CDCl_3$): $\delta_H = 7.82$ (8H, 7.83-7.81, m, phosphine *m*-H), 7.45 (12H, 7.46-7.44, m, phosphine *o,p*-H), 7.04 (2H, s, benzo C-H), 4.13 (4H, s, O-CH₂-CH₂-O), 2.45 (4H, d, $^2J_{PH} = 18.3$ Hz, PCH₂).

^{31}P NMR (121 MHz, ppm, $CDCl_3$): $\delta_P\{^1H\} = 41.60$ with satellites at 56.50 and 26.71 ($^1J_{Pt-P} = 3622$ Hz).

HRMS (ESI-TOF) *m/z*: $[M + H]^+$ calc. for $C_{34}H_{31}O_2P_2S_2Pt^+$ 703.0287; found 703.0265.

Elemental Analysis calc. for $C_{34}H_{30}O_2P_2S_2Pt \cdot \frac{1}{4}CH_2Cl_2$: C 50.23; H 3.72%; found: C 50.50; H 3.49%.

IR (ν_{max} , cm^{-1}): 3045(w), 2912(w), 2865(w), 1554(m), 1458(m), 1449(m), 1433(s), 1376(w), 1349(w), 1287(s), 1245(s), 1186(w), 1169(w), 1101(m), 1091(s), 1062(s), 1027(m), 998(m), 910(m), 893(m), 880(m), 854(m), 749(m), 742(m), 714(s), 703(s), 688(vs), 528(vs), 483(s).

2.4.16. Synthesis of (doxebdt)Pt(dppe) (3e)

Pt₂dba₃·CH₂Cl₂ (0.128 g, 0.056 mmol), dppe (0.087 g, 0.104 mmol) and tetrathiocin **1e** (0.024 g, 0.056 mmol) were combined in an oven-dried 5 mL microwave vial in the glove box. Dry toluene (5 mL) was added and the suspension was heated in the microwave for 60 min at 150 °C. The resultant solution was stirred overnight and a yellow-brown solid was isolated from a pale orange solution by filtration. The precipitate was washed with hexanes and dried in air (0.079 g, 86% yield). The solid was recrystallized from a saturated CH₂Cl₂ solution layered with hexanes to produce clear yellow plate-shaped crystals suitable for X-ray diffraction.

¹H NMR (300 MHz, ppm, CDCl₃): δ_H = 7.845 (8H, 7.88-7.81, m, phosphine *m*-H), 7.455 (12H, 7.47-7.44, m, phosphine *o,p*-H), 7.12 (2H, s, benzo C-H), 4.00 (4H, 4.02-3.98, t, *J* = 5.4 Hz, O-CH₂-CH₂-CH₂-O), 2.46 (4H, d, ²J_{PH} = 18.3 Hz, PCH₂), 2.07 (2H, 2.087-2.053, apparent t, *J* = 5.1 Hz, O-CH₂-CH₂-CH₂-O).

³¹P NMR (121 MHz, ppm, CDCl₃): δ_P{¹H} = 41.53 with satellites at 56.40 and 26.63 (¹J_{Pt-P} = 3618 Hz).

HRMS (ESI-TOF) *m/z*: [M + H]⁺ calc. for C₃₄H₃₁O₂P₂S₂Pt⁺ 806.1045; found 806.1049.

Elemental Analysis calc. for C₃₄H₃₀O₂P₂S₂Pt·1½CH₂Cl₂: C 45.05; H 3.46%; found: C 44.93; H 3.56%.

IR (ν_{max}, cm⁻¹): 3048(w), 2953(w), 2860(w), 1585(vw), 1572(vw), 1537(vw), 1483(m), 1468(m), 1449(s), 1409(m), 1381(m), 1335(w), 1296(m), 1252(s), 1184(m), 1160(w), 1097(s), 1043(s), 983(m), 948(w), 878(m), 820(w), 746(m), 688(vs), 654(s), 634(m), 528(vs), 489(m), 480(m), 447(m).

2.4.17. Synthesis of (dmbimdt)Pt(dppe) (3f)

Pt₂dba₃·CH₂Cl₂ (0.138 g, 0.109 mmol), dppe (0.087 g, 0.218 mmol) and tetrathiocin **1f** (0.046 g, 0.109 mmol) were combined in an oven-dried 5 mL microwave vial in the glove box. Dry toluene (5 mL) was added and the suspension was heated in the microwave for 60 min at 150 °C. The resultant solution was stirred overnight and a yellow-brown solid was isolated from a yellow solution by filtration. The precipitate was washed with hexanes and dried in air (0.121 g, 68% yield). The solid was recrystallized from a saturated CH₂Cl₂

solution layered with hexanes to produce clear yellow plate-shaped crystals suitable for X-ray diffraction.

¹H NMR (300 MHz, ppm, CDCl₃): δ_H = 7.85 (8H, 7.887-7.802, m, phosphine *m*-H), 7.48 (12H, 7.52- 7.45, m, phosphine *o,p*-H), 7.14 (2H, s, benzo C-H), 3.285 (6H, s, NCH₃), 2.49 (4H, d, 2.524-2.462, ²J_{PH} = 18.6 Hz, PCH₂).

³¹P NMR (121 MHz, ppm, CDCl₃): δ_P{¹H} = 41.63 with satellites at 56.47 and 26.69 (¹J_{Pt-P} = 3621 Hz).

HRMS (ESI-TOF) *m/z*: [M + H]⁺ calc. for C₃₅H₃₃N₂OP₂S₂Pt⁺ 729.0556; found 729.0561.

Elemental Analysis calc. for C₃₅H₃₂O₂P₂S₂Pt·½CH₂Cl₂: C 48.87; H 3.75%; N 3.26%; found: C 48.22; H 3.61% N 3.26%.

IR (ν_{max}, cm⁻¹): 3056(w), 3048(w), 2978(w), 2943(w), 2904(w), 1695(vs), 1582(w), 1504(s), 1481(m), 1435(s), 1398(m), 1357(w), 1320(w), 1293(w), 1262(m), 1243(m), 1137(m), 1098(s), 1079(m), 1027(m), 897(m), 851(m), 741(s), 703(s), 690(vs), 649(m), 618(s), 581(s), 531(vs), 486(s), 476(s), 455(s).

2.4.18. Synthesis of (b-15-c-5-dt)Pt(dppe) (3g)

Pt₂dba₃·CH₂Cl₂ (0.138 g, 0.109 mmol), dppe (0.087 g, 0.218 mmol) and tetrathiocin **1g** (0.066 g, 0.109 mmol) were combined in an oven-dried 5 mL microwave vial in the glove box. Dry toluene (5 mL) was added and the suspension was heated in the microwave for 60 min at 150 °C. The resultant solution was stirred overnight and a yellow-brown solid was isolated from a yellow solution by filtration. The precipitate was washed with hexanes and dried in air (0.061 g, 30% yield). The solid was recrystallized from a saturated CH₂Cl₂ solution layered with hexanes to produce clear yellow plate-shaped crystals suitable for X-ray diffraction.

¹H NMR (300 MHz, ppm, MeCN-d₃) δ_H = 7.836–7.769 (8H, m, phosphine *m*-H), 7.53–7.46 (12H, m, phosphine *o,p*-H), 6.91 (2H, s, benzo C-H), 3.98–3.95 (4H, m, crown C-H), 3.75–3.72 (4H, m, crown C-H), 3.62–3.57 (8H, m, crown C-H), 2.58 (4H, d, ²J_{PH} = 19.6 Hz, PCH₂).

³¹P NMR (121 MHz, ppm, MeCN-d₃): δ_P{¹H} = 46.44 with satellites at 57.87 and 35.09 (¹J_{Pt-P} = 2784 Hz).

HRMS (ESI-TOF) m/z : $[M + H]^+$ calc. for $C_{40}H_{42}O_5P_2S_2Pt^+$ 923.1597; found 923.1588.

Elemental Analysis calc. for $C_{40}H_{42}O_5P_2S_2Pt \cdot \frac{1}{2}CH_2Cl_2$: C 48.65; H 4.29%; found: C 49.08; H 4.11%.

IR (ν_{max} , cm^{-1}): 3048(w), 2908(w), 2862(w), 1584(w), 1483(m), 1449(m), 1434(s), 1405(m), 1356(m), 1346(m), 1308(s), 1246(m), 1193(m), 1132(vs), 1099(s), 1064(m), 1028(m), 996(m), 942(m), 928(m), 878(m), 846(m), 821(m), 750(m), 712(vs), 692(vs), 683(vs), 651(m), 526(vs), 473(s).

2.4.19. Synthesis of [(b-15-c-5-Na-dt)Pt(dppe)][BPh₄] ([Na(3g)][BPh₄])

Complex **3g** (0.020 g, 0.0218 mmol) and NaBPh₄ (0.010 g, 0.0218 mmol) were combined in a small 10 mL vial with a 1:1 mixture of CH₂Cl₂ and MeOH (8 mL) and left to stir for 1 hour under ambient conditions. Crystallization occurred by layering hexanes on a concentrated CH₂Cl₂:MeOH mixture to afford yellow crystals suitable for X-ray diffraction (0.022 g, 79% yield).

¹H NMR (300 MHz, ppm, DMSO-*d*₆): $\delta_H = 7.82$ - 7.74 (8H, m, phosphine *m*-H), 7.55 - 7.48 (12H, m, phosphine *o,p*-H), 7.18 - 7.11 (8H, m, borate C-H), 6.94 - 6.83 (8H, m, borate C-H), 6.81 - 6.76 (4H, m, borate C-H), 6.74 (2H, s, benzo C-H), 3.95 - 3.89 (4H, m, crown C-H), 3.71 (4H, m, crown C-H), 3.64 (8H, br s, crown C-H), 2.63 (4H, d, $^2J_{PH} = 19.6$ Hz, PCH₂); (300 MHz, MeCN-*d*₃) $\delta_H = 7.86$ – 7.77 (8H, m, phosphine *m*-H), 7.59 - 7.47 (12H, m, phosphine *o,p*-H), 7.31 - 7.24 (8H, m, borate C-H), 7.06 - 6.96 (8H, m, borate C-H), 6.88 - 6.82 (4H, m, borate C-H), 5.47 (2H, s, benzo C-H), 4.08 (4H, s, crown C-H), 3.80 (4H, s, crown C-H), 3.68 (8H, s, crown C-H), 2.60 (4H, d, $^2J_{PH} = 18.9$ Hz, PCH₂).

³¹P NMR (121 MHz, ppm, DMSO-*d*₆) $\delta_P\{^1H\} = 46.14$ with satellites at 57.51 and 34.80 ($^1J_{Pt-P} = 2748$ Hz); (121 MHz, ppm, MeCN-*d*₃) $\delta_P\{^1H\} = 46.23$ with satellites at 57.57 and 34.85 ($^1J_{Pt-P} = 2749$ Hz).

HRMS (ESI(+)) m/z : $[M + H]^+$ calc. for $C_{40}H_{42}O_5P_2S_2PtNa^+$ 946.1494; found: 946.1492.

Elemental Analysis calc. for $C_{64}H_{62}BO_5NaP_2S_2Pt \cdot \frac{1}{2}MeOH$: C 59.71, H 4.85 %; found: C 59.70, H 4.94%.

IR (ν_{\max} , cm^{-1}): 3052(w), 2980(w), 2917(w), 2873(w), 1684(w), 1654(w), 1602(w), 1579(w), 1535(w), 1513(w), 1482(m), 1452(m), 1435(s), 1384(w), 1350(m), 1290(w), 1245(m), 1177(m), 1120(m), 1100(vs), 1087(s), 1047(m), 1029(m), 975(w), 938(m), 923(m), 909(m), 878(m), 847(m), 825(m), 798(w), 782(w), 747(m), 733(s), 704(vs), 689(vs), 658(m), 611(s), 533(vs), 484(s), 432(w).

2.4.20. Synthesis of (b-15-c-5-dt)Pd(dppf), (4g)

$\text{Pd}_2\text{dba}_3 \cdot \text{CHCl}_3$ (0.100 g, 0.109 mmol), dppf (0.121 g, 0.218 mmol) and tetrathiocin **1g** (0.072 g 0.109 mmol) were combined in an oven-dried 5 mL microwave vial in the glove box. Dry toluene (5 mL) was added and the suspension was heated in the microwave for 20 min at 150 °C. The resultant dark solution was filtered off leaving behind a small amount of dark red solid. The filtrate was evaporated in vacuo to afford dark solid (0.062 g, 57% yield). Recrystallization of the solid was achieved by layering hexanes on a concentrated CH_2Cl_2 :MeOH mixture affording yellow crystals suitable for X-ray diffraction.

^1H NMR (300 MHz, ppm, DMSO- d_6): $\delta_{\text{H}} = 7.73$ - 7.67 (8H, m, phosphine *m*-H), 7.46-7.41 (12H, m, phosphine *o,p*-H), 6.38 (2H, s, benzo C-H), 4.55 (4H, s, Fc C-H), 4.16 (4H, s, Fc C-H), 3.84-3.82 (4H, m, crown C-H), 3.65 (4H, m, crown C-H), 3.59 (8H, s, crown C-H); (300 MHz, ppm, MeCN- d_3) $\delta_{\text{H}} = 7.75$ - 7.73 (8H, m, phosphine *m*-H), 7.44-39 (12H, m, phosphine *o,p*-H), 6.42 (2H, s, benzo C-H), 4.26 (4H, s, Fc C-H), 4.20 (4H, s, Fc C-H), 3.88-3.86 (4H, m, crown C-H), 3.71-3.69 (4H, m, crown C-H), 3.60 (8H, br s, crown C-H).

^{31}P NMR (121 MHz, ppm, DMSO- d_6) $\delta_{\text{P}}\{^1\text{H}\} = 24.97$; (121 MHz, ppm, MeCN- d_3) $\delta_{\text{P}}\{^1\text{H}\} = 25.10$.

HRMS (ESI(+)) m/z : $[\text{M} + \text{H}]^+$ calc. for $\text{C}_{48}\text{H}_{47}\text{FeO}_5\text{P}_2\text{S}_2\text{Pd}^+$ 991.0743; found: 991.0726.

Elemental Analysis calc. for $\text{C}_{48}\text{H}_{46}\text{FeO}_5\text{P}_2\text{S}_2\text{Pd} \cdot 1/4\text{CH}_2\text{Cl}_2$: C 57.24, H 4.64 %; found: C 57.42, H 5.06 %.

IR (ν_{\max} , cm^{-1}): 3053(w), 2911(m), 2865(m), 1480(s), 1450(s), 1435(vs), 1306(w), 1247(s), 1133(m), 1096(s), 1063(m), 931(w), 847(w), 824(w), 746(m), 732(m), 695(vs), 635(w), 546(s), 491(s), 466(m).

2.4.21. Synthesis of [(b-15-c-5-Na-dt)Pd(dppf)][BPh₄] ([Na(4g)][BPh₄])

Complex **2g** (0.089 g, 0.089 mmol) and NaBPh₄ (0.031 g, 0.089 mmol) were combined in a small 10 mL vial with a 1:1 mixture of CH₂Cl₂ and MeOH and left to stir for 1 hour under ambient conditions. Crystallization occurred by layering hexanes on a concentrated CH₂Cl₂:MeOH mixture to afford orange crystals suitable for X-ray diffraction. The yield for this reaction was invariably low, yielding only a few crystals per reaction attempt.

¹H NMR (300 MHz, ppm, DMSO-d₆): δ_H = 7.54 (8H, m, phosphine *m*-H), 7.43 (12H, m, phosphine *o,p*-H), 6.92 (12H, m, borate C-H), 6.78 (8H, m, borate C-H), 6.41 (2H, s, benzo C-H), 4.54 (4H, s, Fc C-H), 4.16 (4H, s, Fc C-H), 3.85 (4H, m, crown C-H), 3.65 (4H, m, crown C-H), 3.58 (12H, m, crown C-H); (300 MHz, ppm, MeCN-d₃) δ_H = 7.53 (8H, m, phosphine *m*-H), 7.27 (12H, m, phosphine *o,p*-H), 6.99 (12H, m, borate C-H), 6.84 (8H, m, borate C-H), 6.52 (2H, s, benzo C-H), 4.47 (4H, s, Fc C-H), 4.19 (4H, s, Fc C-H), 3.97 (4H, m, crown C-H), 3.64 (4H, m, crown C-H), 3.58 (12H, s, crown C-H).

³¹P NMR (121 MHz, ppm, DMSO-d₆) δ_P{¹H} = 25.49; (121 MHz, ppm, MeCN-d₃) δ_P{¹H} = 25.78.

HRMS (MALDI-MS) *m/z*: [M]⁺ calc. for C₄₈H₄₆FeO₅P₂S₂PdNa⁺ 1013.0562; found 1013.0568.

Elemental Analysis calc. for C₇₂H₆₆BFeO₅NaP₂S₂Pd C 64.85, H 4.99%; found: C 64.50, H 4.95%.

IR (ν_{max}, cm⁻¹): 3049(w), 2153(w), 1982(w), 1579(w), 1480(m), 1454(m), 1433(m), 1385(w), 1351(w), 1242(m), 1179(m), 1126(m), 1095(s), 1058(m), 1031(m), 998(w), 938(w), 927(w), 910(w), 846(m), 823(m), 744(s), 732(s), 704(vs), 693(vs), 631(w), 611(s), 544(m), 527(m), 520(s), 491(vs), 464(vs), 430(s).

2.4.22. Synthesis of [(b-15-c-5-dt)Pt(dppf)][BPh₄] (**5g**)

Pt₂dba₃ (0.119 g, 0.109 mmol), dppf (0.121 g, 0.218 mmol) and tetrathiocin **1g** (0.072 g 0.109 mmol) were combined in an oven-dried 5 mL microwave vial in the glove box. Dry toluene (5 mL) was added and the suspension was heated in the microwave for 60 min at 150 °C. The resultant dark solution was filtered off leaving behind a small amount of dark brown solid. The filtrate was evaporate in vacuo to afford dark solid (0.062 g, 57%

yield). The solid was recrystallized from DCM layered with hexanes to produce yellow plates suitable for X-ray diffraction.

¹H NMR (300 MHz, ppm, DMSO-d₆): δ_H = 7.69-7.66 (8H, m, phosphine *m*-H), 7.55-7.40 (12H, m, phosphine *o,p*-H), 6.54 (2H, s, benzo C-H), 4.52 (4H, s, Fc C-H), 4.15 (4H, s, Fc C-H), 3.862-3.830 (4H, m, crown C-H), 3.65 (4H, m, crown C-H), 3.59 (8H, s, crown C-H); (300 MHz, ppm, MeCN-d₃) δ_H = 7.77- 7.71 (8H, m, phosphine *m*-H), 7.52-7.49 (12H, m, phosphine *o,p*-H), 6.59 (2H, s, benzo C-H), 4.44 (4H, s, Fc C-H), 4.21 (4H, s, Fc C-H), 3.91-3.88 (4H, m, crown C-H), 3.72-3.69 (4H, m, crown C-H), 3.60 (8H, br s, crown C-H).

³¹P NMR (121 MHz, ppm, DMSO-d₆) δP{¹H} = 17.72 with satellites at 29.94 and 5.59 (¹J_{Pt-P} = 2946 Hz); (121 MHz, ppm, MeCN-d₃) δP{¹H} = 17.49 with satellites at 29.70 and 5.33 (¹J_{Pt-P} = 2949 Hz).

HRMS (ESI(+)) *m/z*: [M + H]⁺ calc. for C₄₈H₄₇O₅P₂S₂PtFe⁺ 1080.1338; found: 1080.1306.

Elemental Analysis calc. for C₄₈H₄₆FeO₅P₂S₂Pt: C 52.39, H 4.29 %; found: C 53.70, H 4.58 %.

IR (ν_{max}, cm⁻¹): 3071(w), 3046(w), 2920(w), 2860(w), 1647(w), 1622(w), 1579(w), 1547(w), 1472(m), 1453(m), 1433(m), 1393(w), 1344(w), 1301(m), 1251(m), 1170(m), 1131(s), 1094(m), 1061(m), 1028(m), 982(w), 868(w), 832(w), 748(s), 693(vs), 636(m), 550(m), 530(m) 511(m), 490(s), 464(vs), 436(m)

2.4.23. Synthesis of [(b-15-c-5-Na-dt)Pt(dppe)][BPh₄], ([Na(5g)][BPh₄])

Complex **5g** (0.020 g, 0.0218 mmol) and NaBPh₄ (0.010 g, 0.0218 mmol) were combined in a small 10 mL vial with a 1:1 mixture of CH₂Cl₂ and MeOH (8 mL) and left to stir for 1 hour under ambient conditions. Crystallization occurred by layering hexanes on a concentrated CH₂Cl₂:MeOH mixture to afford yellow crystals suitable for X-ray diffraction (0.022g, 79% yield).

¹H NMR (300 MHz, ppm, DMSO-d₆): δ_H = 7.73-7.64 (8H, m, phosphine *m*-H), 7.55-7.38 (12H, m, phosphine *o,p*-H), 7.18-7.11 (8H, m, borate C-H), 6.94-6.86 (8H, m, borate C-H), 6.81-6.75 (4H, m, borate C-H), 6.54 (2H, s, benzo C-H), 4.53-4.45 (4H, s, Fc C-H), 4.16-4.12 (4H, s, Fc C-H), 3.85-3.81 (4H, m, crown C-H), 3.66-3.58 (12H, m,

crown C–H); (300 MHz, MeCN-d₃) $\delta_{\text{H}} = 7.78\text{--}7.66$ (8H, m, phosphine *m*-H), 7.55–7.31 (12H, m, phosphine *o,p*-H), 7.30–7.18 (8H, m, borate C–H), 7.03–6.90 (8H, m, borate C–H), 6.88–6.77 (4H, m, borate C–H), 6.70 (2H, s, benzo C–H), 4.45–4.33 (4H, s, Fc C–H), 4.22–4.12 (4H, s, Fc C–H), 4.02–3.92 (4H, m, crown C–H), 3.68–3.53 (12H, m, crown C–H)

³¹P NMR (121 MHz, ppm, DMSO-d₆) $\delta_{\text{P}}\{^1\text{H}\} = 17.47$ with satellites at 29.58 and 5.26 ($^1J_{\text{Pt-P}} = 2943$ Hz); (121 MHz, ppm, MeCN-d₃) $\delta_{\text{P}}\{^1\text{H}\} = 17.80$ with satellites at 30.05 and 5.64 ($^1J_{\text{Pt-P}} = 2954$ Hz).

HRMS (ESI(+)) *m/z*: [M + H]⁺ calc. for C₄₈H₄₆O₅P₂S₂PtNaFe⁺ 1103.1171; found: 1103.1172.

Elemental Analysis calc. C₇₂H₆₆BF₆FeO₅NaP₂S₂Pt: C 60.81, H 4.68 %; found: C 60.50, H 4.54%.

IR (ν_{max} , cm⁻¹): 3053(w), 2036(w), 3003(w), 2902(w), 2864(w), 1578(w), 1475(m), 1451(m), 1431(m), 1381(w), 1353(w), 1293(w), 1239(m), 1166(m), 1115(m), 1093(s), 1036(m), 997(w), 975(w), 940(w), 919(m), 846(m), 822(m), 735(s), 696(vs), 636(m), 610(m), 550(s), 516(m), 490(vs), 466(vs), 436(m).

2.5 References

- (1) G. N. Schrauzer and V. Mayweg, *J. Am. Chem. Soc.*, 1962, **84**, 3221–3221.
- (2) N. Robertson and L. Cronin, *Coord. Chem. Rev.*, 2002, **227**, 93–127.
- (3) L. Pilia, M. Pizzotti, F. Tessore and N. Robertson, *Inorg. Chim. Acta.*, 2015, **430**, 114–119.
- (4) (a) A. Zarkadoulas, M. J. Field, V. Artero and C. A. Mitsopoulou, *ChemCatChem*, 2017, **9**, 2308–2317; (b) G.-G. Luo, Y.-H. Wang, J.-H. Wang, J.-H. Wu and R.-B. Wu, *Chem. Commun.*, 2017, **53**, 7007–7010.
- (5) (a) P. Cassoux, L. Valade, H. Kobayashi, A. Kobayashi, R. A. Clark and A. E. Underhill, *Coord. Chem. Rev.*, 1991, **110**, 115–160; (b) C.-P. Li, L. Ni, W.-B. Pei, L. Li, Z.-F. Tian, J.-L. Liu, X.-S. Gao and X.-M. Ren, *J. Solid State Chem.*, 2016, **243**, 38–43.

- (6) (a) W.-H. Ning, L. Zhai and X.-M. Ren, *Synth. Met.*, 2015, **199**, 255–262; (b) Y. Liu, Y.-H. Zhou, X.-L. Liao, L.-M. Man, B.-W. Wang, J.-R. Zhou and C.-L. Ni, *J. Struct. Chem.*, 2017, **58**, 1656–1662; (c) N. Venkatalakshmi, B. Varghese, S. Lalitha, R. F. X. Williams and P. T. Manoharan, *J. Am. Chem. Soc.*, 1989, **111**, 5748–5757.
- (7) L. Chen, H. You, C. Yang, D. Ma and J. Qin, *Chem. Commun.*, 2007, **13**, 1352–1354.
- (8) E. A. M. Geary, L. J. Yellowlees, L. A. Jack, I. D. H. Oswald, S. Parsons, N. Hirata, J. R. Durrant and N. Robertson, *Inorg. Chem.*, 2005, **44**, 242–250.
- (9) D. Schilter, J. M. Camara, M. T. Huynh, S. Hammes-Schiffer and T. B. Rauchfuss, *Chem. Soc. Rev.*, 2016, **116**, 8693–8749.
- (10) *Dithiolene chemistry: Synthesis, properties, and applications*, ed. E. I. Stiefel, Interscience, Hoboken, New Jersey, 2003.
- (11) G. A. Bowmaker, P. D. W. Boyd, G. K. Campbell, J. M. Hope and R. L. Martin, *Inorg. Chem.*, 1982, **21**, 1152–1159.
- (12) C. L. Linfoot, P. Richardson, K. L. McCall, J. R. Durrant, A. Morandeira and N. Robertson, *Sol. Energy*, 2011, **85**, 1195–1203.
- (13) (a) K. Roesselet, K. E. Doan, S. D. Johnson, P. Nicholls and G. L. Miessler, *Organomet.*, 1987, **6**, 480–485; (b) J. Moscattini, A. J. Lough and U. Fekl, *Acta Crystallogr., Sect. E: Crystallogr. Commun.*, 2017, **73**, 957–962; (c) K. Wang, A. O. Patil, S. Zushma and J. M. McConnachie, *J. Inorg. Biochem.*, 2007, **101**, 1883–1890.
- (14) J. D. Wrixon, J. J. Hayward, O. Raza and J. M. Rawson, *Dalton Trans.*, 2014, **43**, 2134–2139.
- (15) (a) J. D. Wrixon, J. J. Hayward and J. M. Rawson, *Inorg. Chem.*, 2015, **54**, 9384–9386; (b) J. D. Wrixon, Z. S. Ahmed, M. U. Anwar, Y. Beldjoudi, N. Hamidouche, J. J. Hayward and J. M. Rawson, *Polyhedron*, 2016, **108**, 115–121.
- (16) K. W. Stender, N. Wolki and G. Klar, *Phosphorus, Sulfur Silicon Relat. Elem.*, 1989, **42**, 111–114.
- (17) N. D. Lowe and C. D. Garner, *J. Chem. Soc., Dalton Trans.*, 1993, 2197–2207.

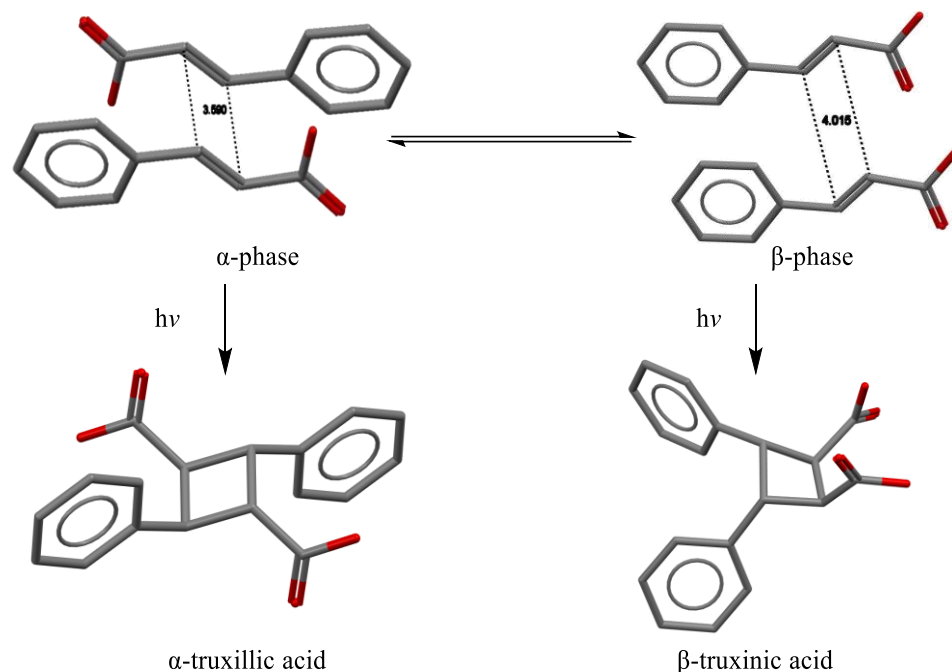
- (18) C. R. Groom, I. J. Bruno, M. P. Lightfoot and S. C. Ward, *Acta Crystallogr., Sect. B: Struct. Sci., Cryst. Eng. Mater.*, 2016, **72**, 171–179.
- (19) P. G. Waddell, A. M. Z. Slawin and J. D. Woollins, *Dalton Trans.*, 2010, **39**, 8620–8625.
- (20) (a) M. L. H. Green, W. B. Heuer and G. C. Saunders, *Dalton Trans.*, 1990, 3789–3792; (b) A. Famengo, D. Pinero, O. Jeannin, T. Guizouarn, L. Piekara-Sady and M. Fourmigué, *New J. Chem.*, 2012, **36**, 638–643.
- (21) (a) C. J. Pedersen, *J. Am. Chem. Soc.*, 1967, **89**, 2495–2496; (b) C. J. Pedersen, *J. Am. Chem. Soc.*, 1967, **89**, 7017–7036.
- (22) (a) T. K. Hansen, T. Jorgensen, P. C. Stein and J. Becher, *J. Org. Chem.*, 1992, **57**, 6403–6409; (b) A. J. Moore, L. M. Goldenberg, M. R. Bryce, M. C. Petty, J. Moloney, J. A. K. Howard, M. J. Joyce and S. N. Port, *J. Org. Chem.*, 2000, **65**, 8269–8276; (c) M. R. Bryce, A. S. Batsanov, T. Finn, T. K. Hansen, A. J. Moore, J. A. K. Howard, M. Kamenjicki, I. K. Lednev and S. A. Asher, *Eur. J. Org. Chem.*, 2001, 933–940.
- (23) S. C. Kosnik, M. C. Nascimento, J. M. Rawson and C. L. B. Macdonald, *Dalton Trans.*, 2017, **46**, 9769–9776.
- (24) S. Lin, T. Yeh, C. Kuo, J. Song, M. Cheng, Y. Chen, C. Yang, M. Wu, C. Hsieh, W. Hsiao, Y. Peng, J. Wu, L. Lin, M. Sun, Y. Chao, C. Shih, S. Wu, S. Pan, M. Hung and S. Ueng, *J. Med. Chem.*, 2016, **59**, 419–430.
- (25) Y. Ishii, *Ann. N. Y. Acad. Sci.*, 1974, **239**, 114–128.
- (26) L. N. Lewis, T. A. Krafft and J. C. Huffman, *Inorg. Chem.*, 1992, **31**, 3555–3557.
- (27) *APEX II*, Bruker AXS, Madison, WI, USA.
- (28) *SAINT*, Bruker AXS, Madison, WI, USA.
- (29) *SADABS*, Bruker AXS, Madison, WI, USA.
- (30) G. M. Sheldrick, *SHELXS-97*, A Program for Automatic Solution of Crystal Structures, University of Göttingen, 1997.

- (31) O. V. Dolomanov, L. J. Bourhis, R. Gildea, J. A. K. Howard and H. Puschmann, *J. Appl. Crystallogr.*, 2009, **42**, 339–341.
- (32) G. M. Sheldrick, *Acta Crystallogr., Sect. A: Found. Adv.*, 2015, **71**, 3–8.
- (33) SHELXTL, Bruker AXS, Madison, WI, USA, 2015.
- (34) A. L. Spek, *Acta Crystallogr., Sect. C: Struct. Chem.*, 2015, **71**, 9–18.
- (35) A. D. Bochevarov, E. Harder, T. F. Hughes, J. R. Greenwood, D. A. Braden, D. M. Philipp, D. Rinaldo, M. D. Halls, J. Zhang and R. A. Friesner, *Int. J. Quantum Chem.*, 2013, **113**, 2110–2142.

3. TRANSFORMATION BETWEEN MONOMER AND DIMER FORMS OF COBALT(III) DITHIOLATE SPECIES

3.1 Introduction

Typically, reactions occur in solution or gas phases where molecules are able to move freely to orient themselves in an appropriate orientation for a reaction to occur. Indeed, the orientation factor, along with collision frequency determine the pre-exponential term, A , in the Arrhenius equation in the collision theory of chemical reactions.^{1,2} Conversely, in the solid state, the relative orientation of molecules is determined by crystal packing forces, and it is therefore unusual for molecules to adopt molecular packing arrangements which support chemical reactions in the solid state. When such solid state chemical reactions occur, they are known as topochemical processes. One of the most well-studied solid-state reactions is the [2+2] photodimerization of alkenes. The first example to be investigated by X-ray diffraction was the dimerization of cinnamic acid by Schmidt *et al.* in 1964,³⁻⁵ although this reaction was first described over 20 years earlier by Bernstein and Quimby.⁶ These reports indicate that the α -*trans*-cinnamic acid dimerizes to α -truxillic acid, whereas β -*trans*-cinnamic acid dimerizes to β -truxinic acid (Scheme 3.1), provided that the irradiation is carried out at low temperature (< 50 °C) where the (thermal) $\beta \rightarrow \alpha$ phase transition cannot occur.⁴ These studies identified the importance of the spatial orientation of adjacent molecules in the solid state in order to support the orbital overlap required for the [2+2] cyclization, highlighted in Schmidt's rule⁷ that the double bonds should be separated by *ca* 3.5 – 4.2 Å. In this context, a range of supramolecular strategies have been implemented to generate the desired packing arrangements to promote the [2+2] cycloaddition.⁸



Scheme 3.1. The [2+2] cyclization of *trans*-cinnamic acid to produce the α -truxillic acid and β -truxinic acid (H atoms omitted for clarity).

While the [2+2] cycloaddition process is arguably one of the most well-studied topochemical processes, it is certainly not unique in solid state chemistry and, generally, solid state reactions and phase transitions are considered to occur with minimum atomic and molecular movement.⁹ Single crystal to single crystal (SCSC) transformations have become particularly topical in recent years,^{10–12} since SCSC reactions can lead to unusual products due to the geometric constraints imposed by the solid state packing.¹³ These types of transformations usually require an external stimulus such as light,¹⁴ heat,¹⁵ vapour¹⁶ or solvent,¹⁷ or in other cases applying a mechanochemical force.¹⁸ In these SCSC transformation complexes, the structural changes often lead to a change of physical property such as colour, magnetism, porosity, luminescence, chirality, etc. as well as a change in coordination number, geometry, and dimensionality.^{19,20}

Such topochemical processes are not limited to organic chemistry and examples of coordination complexes that exhibit topotactic reactions have been reported, in some cases more substantial lattice reorganization occurs. For example, Jameson and co-workers²¹ described the interconversion of $[\text{NiX}_2(\text{dab})]_2$ ($\text{X} = \text{Cl}$ or Br and $\text{dab} = \text{N,N}'$ -disubstituted-

diazabutadiene) into $\text{NiX}_2(\text{dab})$ on heating to 105 °C, whereupon “a violet reaction front can be observed advancing through the yellow crystals”. Here the dimeric yellow Ni(II) complex with trigonal bipyramidal coordination geometry converts to a violet monomeric Ni(II) complex with tetrahedral coordination (Figure 3.1). This transformation is irreversible but topotactic, i.e. the unit cell parameters of monomer and dimer phases are related. In this case the dimer adopts the monoclinic space group $C2/c$ ($a = 20.429(5)$, $b = 7.156(1)$, $c = 20.504(5)$ Å, $\beta = 98.50(2)^\circ$) whereas the monomer is monoclinic $P2_1/n$ ($a = 7.125(3)$, $b = 19.717(10)$, $c = 10.396(5)$ Å, $\beta = 90.91(2)^\circ$). Notably the displacement of the Ni atoms is reported to be over 10 Å!²¹

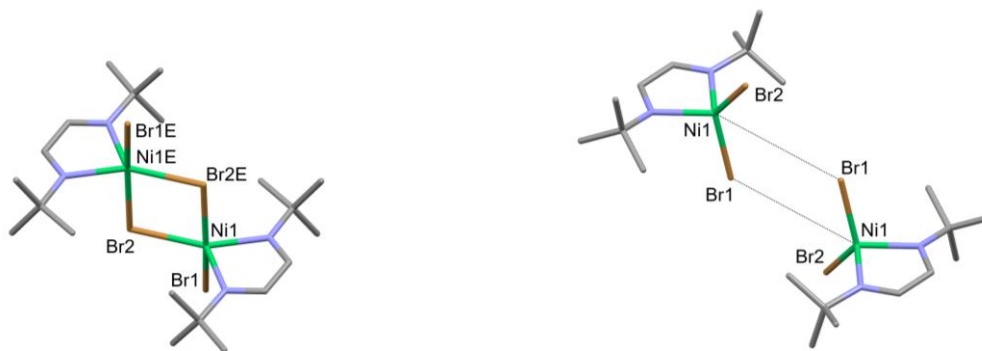
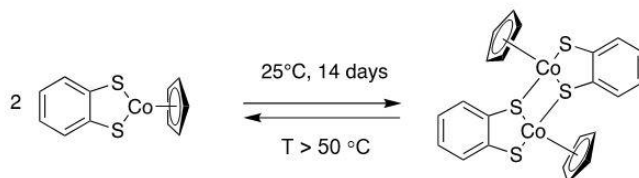


Figure 3.1. Crystal structures of (left) dimeric $[\text{NiBr}_2(\text{dab})]_2$ and (right) monomeric $\text{NiBr}_2(\text{dab})$.

In the latter example, the breakdown of the dimer into the monomer is associated with cleavage of two Lewis base/Lewis acid dative bonds between Br and Ni(II). A similar transformation has been observed for the organometallic cobalt (III) complex, $\text{CpCo}(\text{bdt})$ (bdt = benzene dithiolate, $\text{C}_6\text{H}_4\text{S}_2^{2-}$) and its dimer, $[\text{CpCo}(\text{bdt})]_2$, described by Miller and co-workers.²² The monomer is a formal $16e^-$ complex in which the Co(III) centre is Lewis acidic and is capable of reacting with strong donors such as phosphites, e.g. $\text{P}(\text{OMe})_3$.²³ Conversely the dithiolate S atom is Lewis basic and can donate its lone pair and adopt a bridging mode, forming a range of complexes with $\text{M}(\text{CO})_n$ [$\text{M} = \text{Mo}$ or W , $n = 2$; $\text{M} = \text{Fe}$, $n = 3$].²⁴⁻²⁶ In the absence of a Lewis acid or Lewis base, $\text{CpCo}(\text{bdt})$ can dimerize to form $[\text{CpCo}(\text{bdt})]_2$ through formation of two $\text{S} \rightarrow \text{Co}$ dative bonds. In this case the process is reversible: the monomer undergoes a kinetically slow solid-state conversion to the dimer

at 25 °C, while the dimer can be transformed back to the monomer by heating to temperatures in excess of 150 °C (Scheme 3.2). DSC studies reveal $\Delta H = +18.9 \text{ kJ mol}^{-1}$ for this process from which the entropy change ΔS can be estimated as *ca.* $+45 \text{ J K}^{-1} \text{ mol}^{-1}$.



Scheme 3.2. Reaction equilibrium between the monomer $\text{CpCo}(\text{bdt})$ and the dimer $[\text{CpCo}(\text{bdt})]_2$.

Structural studies on the monomeric phase indicated it crystallized in the monoclinic space group $P2_1/c$ with two molecules in the asymmetric unit ($Z' = 2$). They identified that one of the two crystallographically independent molecules forms a pair of centrosymmetric $\text{Co}\dots\text{S}$ contacts ($\text{Co1}\dots\text{S1}$ at 4.70 \AA). The second crystallographically independent molecule has a similar but even longer pair of centrosymmetric contacts ($\text{Co2}\dots\text{S3}$ at 5.06 \AA) (Figure 3.2). In contrast, the dimer phase has half a molecule in the asymmetric unit with equivalent $\text{Co1}\dots\text{S2b}$ bonds of 2.27 \AA , much shorter than the inter-molecular contacts in the monomer phase. With two molecules in the asymmetric unit of the monomer phase and just one molecule in the dimer phase, the unit cell volumes are not the same and the orientation of the crystallographic b -axis is not the same in the two forms. As a consequence, the reaction is not topotactic (i.e. the two unit cells are not directly related).

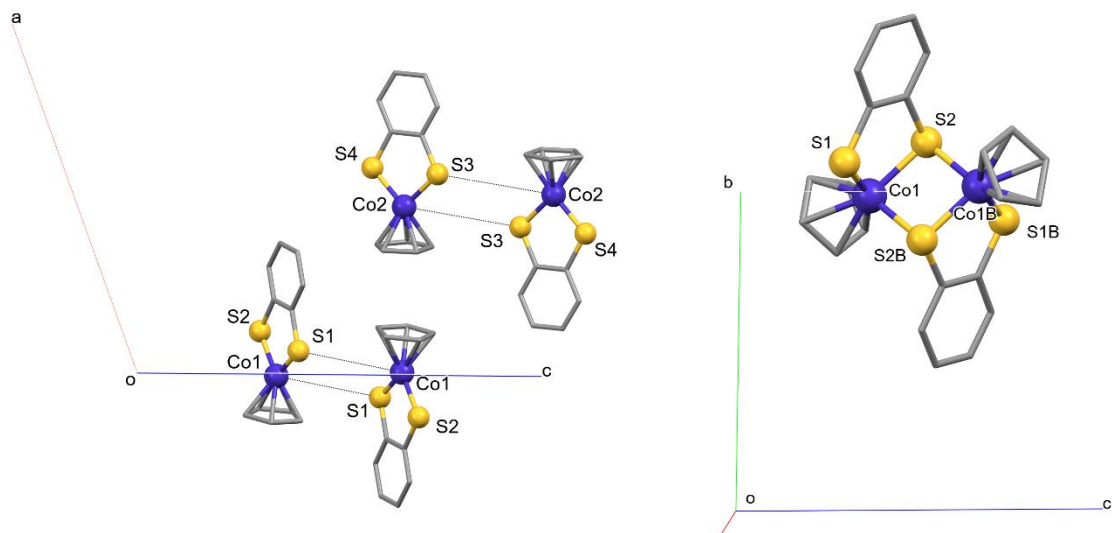


Figure 3.2. Crystal structure of (left) CpCo(bdt), highlighting centrosymmetric intermolecular Co...S contacts between the two crystallographically independent pairs of monomers; (right) dimeric structure of [CpCo(bdt)]₂.

Miller *et al.* indicated that CpCo(S₂C₂R₂) (R = CN, CF₃, H), CpCo[(NH)₂C₆H₄], CpCo[(NH)SC₆H₄] and CpCo(O₂C₆H₄) do not dimerize in the solid state and, as a consequence are unable to exhibit similar solid state transformations. Similarly the stronger electron-donating effect of the Cp* group makes the Co(III) centre a weaker Lewis acid and Cp* cobalt dithiolate complexes appear to be invariably monomeric.^{27,28,29} As a consequence, fine tuning of the dithiolate ligand, may provide insight into this process. Specifically, electron-donating groups on the benzene ring are anticipated to increase the Lewis basicity of the S, favoring dimerization. In this context, this Chapter describes the preparation and characterization of the related cobalt complexes **6–10** (Figure 3.3). We find that these derivatives exhibit a range of both monomer and dimer phases as well as mixed phases comprising both monomers and dimers. In the case of **6** a mechanochemically driven solid state phase transition is observed from monomer to dimer.

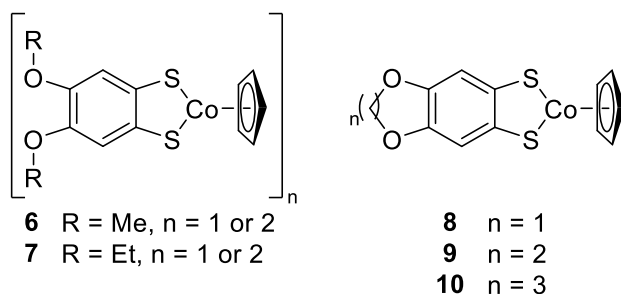


Figure 3.3. Novel CpCo(dt) complexes investigated in this study.

3.2 Results and Discussion

3.2.1. Synthesis

Reaction of tetrathiocins **1a–e** with CpCo(CO)₂ in a sealed 2–5 mL microwave reaction vial at 150 °C for 30 min in toluene under microwave irradiation afforded the corresponding complexes **6–10**. After releasing the pressure, the toluene was evaporated, and the blue residue was taken up in CHCl₃, filtered, and dried *in vacuo*. The resultant complexes were isolated as dark blue solids by dissolving in the minimum amount of CH₂Cl₂ and precipitating with hexanes in 71–75% isolated yield.

¹H NMR studies were conducted on complexes **6–10** and reveal a single resonance for the benzo protons, consistent with a symmetric monomer in solution. In this context, previous work on dimers of the form [Pt(dmobt)(PPh₃)₂]₂ reveal two distinct benzo protons reflecting benzo H atoms adjacent to chelating S and bridging S atoms.³⁰ The NMR spectrum of **6** is shown in Figure 3.4, as representative of this series and comprises a singlet for the benzo H atoms at 7.51 ppm, a singlet for the Cp ring at 5.40 ppm and a single resonance for the methoxy group at 3.85 ppm. Low temperature NMR studies in both deuterated chloroform and deuterated DCM down to *ca.* –85 °C showed no evidence for dimer formation. UV-Vis spectroscopy measurements on **6** reveals two absorptions at 291 nm and 538 nm, comparable to similar complexes.³¹

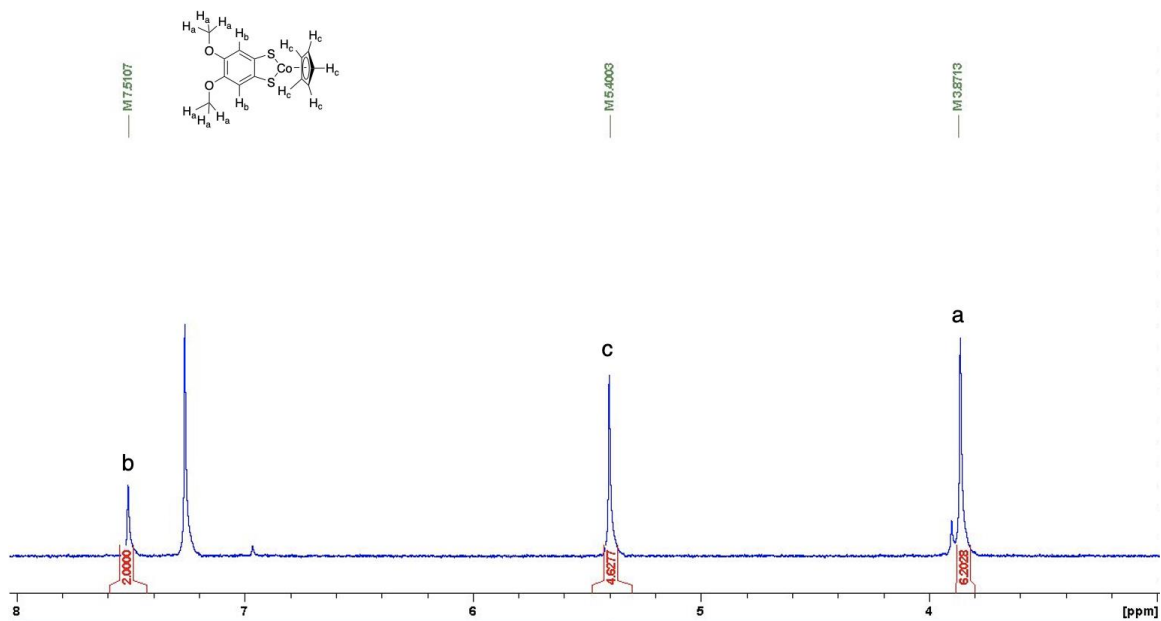


Figure 3.4. ^1H NMR spectrum of **6**, in CDCl_3 at room temperature.

3.2.2. Crystal Growth of Complexes

Based on the previous work by Miller *et al*, crystallization was attempted from both solution and vacuum sublimation. To date, multiple attempts to generate single crystals of **9** suitable for single crystal X-ray diffraction from either solution or by vacuum sublimation have proved unsuccessful, although other spectroscopic data (EA, ^1H NMR and MS) support its molecular structure. Results of these studies for complexes **6–8** and **10** are summarized in Table 3.1. Complex **6** was found to exhibit similar behaviour to the parent $\text{CpCo}(\text{bdt})$ in that crystallization from solution afforded selectively a dimer phase whereas sublimation afforded a monomeric phase. For the di-ethoxy derivative, **7**, the behaviour was more complex. Recrystallization at ambient temperature afforded a cocrystal phase containing two monomeric and two dimeric units in the asymmetric unit, whereas recrystallization at low temperature afforded a monomeric phase. Meanwhile, **8** and **10** were both found to crystallize as monomers from solution with phase purity confirmed by powder X-ray diffraction.

Table 3.1. Summary of crystallization conditions for **6–10**.

Compound	Crystallization Conditions		
	Recrystallization (Fridge temp = 18 °C)	Recrystallization (Room temp)	Vacuum Sublimation
6	–	(6)₂	6
7	7	Co-crystal: (7)₂·7	–
8	–	8	–
10	–	10	–

3.2.3. Structures of **6** and **(6)₂**

Crystals of **(6)₂** were grown by slow diffusion of hexanes into a saturated CH₂Cl₂ solution. It crystallizes in the monoclinic space group P2₁/c with half a molecule in the asymmetric unit. The structure of the 18e⁻ dimer adopts a three-legged piano stool geometry at the Co(III) centre with the two sulfur atoms and η⁵-coordinated Cp ring. The Cp ring is bent out of the C₆S₂Co plane such that the angle between the C₂S₂ and CoS₂ planes (Figure 3.5) is 22.98°. The C-S bonds are 1.779(2) and 1.760(3) Å for C11-S11 and C12-S12 respectively. The Co1-S11 and Co1-S12 bond lengths are 2.2309(8) and 2.2499(7) Å, while the bridging Co1-S11' bond length is 2.2672(7) Å, consistent with a dithiolate.³²

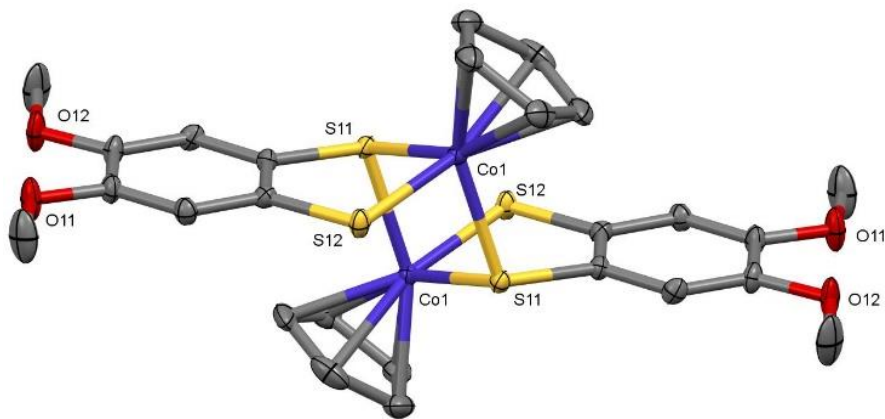


Figure 3.5. Crystal structure of **(6)₂** with thermal ellipsoids drawn at the 50% probability level. Hydrogen atoms have been omitted for clarity.

The monomeric form, **6**, was isolated through sublimation conditions (+175 °C to –3 °C) under static vacuum. Complex **6** crystallizes in the orthorhombic space group *Pbca* with one molecule per asymmetric unit. The structure of **6** (Figure 3.6) is a two-legged piano stool in which the fold angle between CoS_2 and C_2S_2 planes is just 3.23° (*c.f.* 22.98° for **(6)**₂) with the Co atom located just 0.044 Å from the $\text{C}_6\text{S}_2\text{Co}$ mean plane. The Cp ring plane is essentially perpendicular to the C_2S_2 plane, at 85.03° . The Co–S bond lengths fall in the range of 2.111(2)–2.128(2) Å, *ca.* 0.1 Å shorter than those in **(6)**₂. The C–S bond lengths are in the range of 1.726(6)–1.733(6) Å, comparable with **(6)**₂. The Cp-centroid to Co distances of 1.657 Å for **6** and is comparable with those of other $16e^-$ cyclopentadienyl cobalt(III) benzenedithiolate structures (1.640–1.656 Å) and a little shorter than the corresponding distance in **(6)**₂ (1.697 Å).^{22,28,29,33,34} A comparison of the solid state packing of **6** and **(6)**₂ is presented in section 3.2.5 and the crystallographic parameters found in Table 3.3.

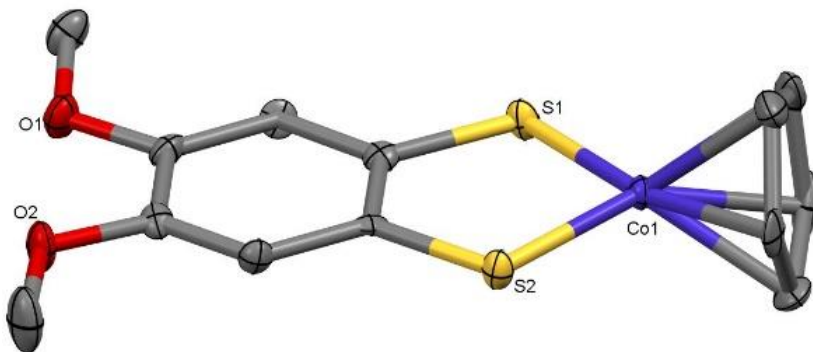


Figure 3.6. Crystal structure of **6** with thermal ellipsoids drawn at the 50% probability level. Hydrogen atoms have been omitted for clarity.

3.2.4. Structures of **7**, **8** and **10**

Recrystallization of **7** from slow diffusion of hexanes into DCM at 25 °C generates a highly unusual cocrystal comprising both **7** and **(7)**₂. The structure comprises two crystallographically independent monomers and two crystallographically independent half molecules of $[\text{CpCo}(\text{deobdt})_2]$ such that the overall composition is **(7)**₂·2**(7)**· CH_2Cl_2 . (Figure 3.7).

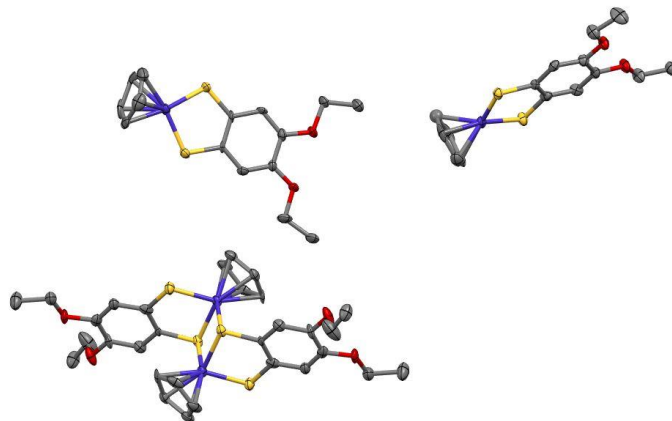


Figure 3.7. Crystal structure of $(7)_2 \cdot 2(7) \cdot \text{CH}_2\text{Cl}_2$ with thermal ellipsoids drawn at the 50% probability level. The CH_2Cl_2 solvate molecule and hydrogen atoms have been omitted for clarity.

In contrast, recrystallization of **7** at low temperature afforded the pure monomer phase, **7**, with four molecules in the asymmetric unit (Figure 3.8). Similar to **6** and $(6)_2$, the dimer exhibits a lengthening of Co–S bond lengths with the range found in the monomeric units to be 2.02(1)–2.130(2) Å vs. 2.241(3)–2.256(2) Å for the dimeric units found in the structure of $(7)_2 \cdot 2(7) \cdot \text{CH}_2\text{Cl}_2$. The $\text{Cp}_{\text{centroid}} \cdots \text{Co}$ for the two monomers are 1.646 and 1.656 Å, whereas the dimer is again, elongated to 1.706 and 1.702 Å for the crystallographically independent half molecules in the asymmetric unit.

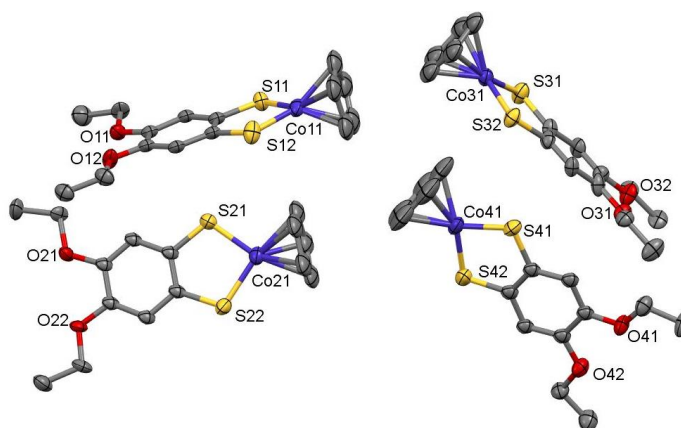


Figure 3.8. Crystal structure of **7** with thermal ellipsoids drawn at the 50% probability level. Hydrogen atoms have been omitted for clarity.

Crystallization of both **8** and **10** from slow diffusion of hexanes into a saturated DCM solution at room temperature afforded the $16e^-$ monomer phases (Figure 3.9 and 3.10) with two molecules in the asymmetric unit (**8**) and one molecule per asymmetric unit (**10**) respectively. These monomer derivatives exhibit similar geometric parameters to **6** and **7** (above) and summarized in Table 3.2.

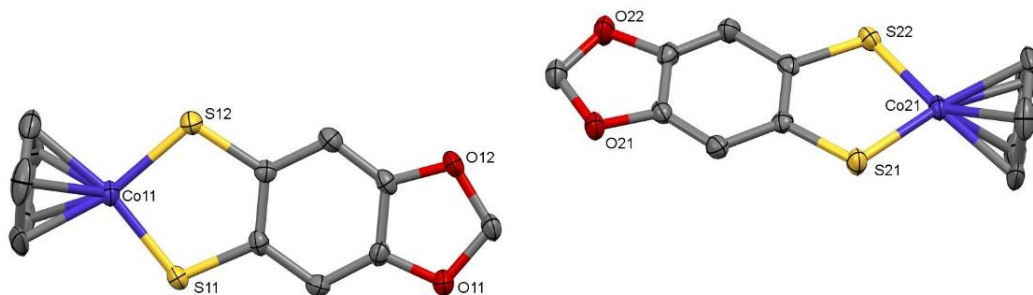


Figure 3.9. Crystal structure of **8** with thermal ellipsoids drawn at the 50% probability level. Hydrogen atoms have been omitted for clarity.

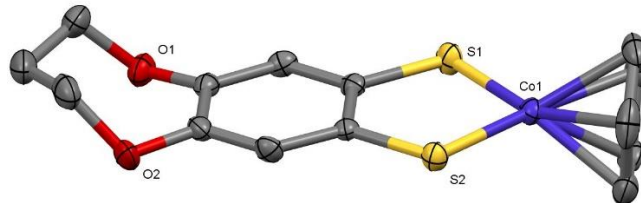


Figure 3.10. Crystal structure of **10** with thermal ellipsoids drawn at the 50% probability level. Hydrogen atoms have been omitted for clarity.

Table 3.2. Summary of bond lengths and angles in the monomer crystals of **6**, **7**, **8** and **10**.

Compound	6	7	8	10
		2.102(4)		
Co–S1 (Å)	2.111(2)	2.102(4) 2.102(4)	2.116(1)	2.116(1)
		2.108(4) 2.124(4)		
Co–S2 (Å)	2.128(2)	2.126(4) 2.128(5) 2.122(5)	2.114(1)	2.115(1)
		1.73(1)		
S1–C1 (Å)	1.726(6)	1.74(1) 1.75(1)	1.730(5)	1.737(3)
		1.73(1) 1.73(1)		
S2–C6 (Å)	1.733(6)	1.74(1) 1.73(1) 1.75(1)	1.728(5)	1.732(3)
		88.71		
Cp _(plane) ⊥ C ₂ S ₂ (_{plane}) (°)	85.03	86.10 89.08 89.87	85.84	85.65
		C102 0.037		
Maximum deviation from C ₆ S ₂ Co plane (Å)	Co1 0.044	S21 0.035 S32 0.047 C403 0.019	S12 0.028 Co2 0.023	Co1 0.035
		1.652		
Cp _{centroid} ⋯Co (Å)	1.657	1.660 1.667 1.666	1.654	1.655

3.2.5. Phase behaviour of **6**

Since complex **6** was found to form both monomer and dimer phases, analogous to CpCo(bdt), it seemed a strong candidate to explore possible phase transitions between the two phases. Initial studies commenced with confirmation of the phase purity of both (**6**)₂

(from recrystallization) and **6** (prepared by sublimation). PXRD studies on both monomeric and dimeric species revealed good agreement between the experimental PXRD pattern of the bulk sample and that predicted based on the low temperature SC-XRD structure determinations (Figure 3.11 and Figure 3.12). There is some similarity in the low angle PXRD patterns of **6** and **(6)**₂ but they are readily distinguished through high intensity reflections corresponding $2\theta = 12.2^\circ$ for **(6)**₂ and $2\theta = 18.0^\circ$ and 19.8° for **6**. These correspond to the (0 1 1) and (1 1 4) and (2 0 0) reflections for **(6)**₂ and **6** respectively.

Variable temperature PXRD on **(6)**₂ revealed no change in PXRD profile up to the upper limit of the VT-PXRD study, indicating no phase transition from **(6)**₂ to **6** up to at least 150 °C (Figure 3.13). To probe the thermal stability further, DSC studies were undertaken on both **(6)**₂ and **6**. The DSC of **(6)**₂ reveals no thermal event up to the melting point at 215 °C, consistent with the VT-PXRD studies. DSC studies on **6** shows a slightly lower melting point at 205 °C (Figure 3.14b). These observations indicate that **6** and **(6)**₂ do not interconvert up to their corresponding melting points. However, a heat/cool/re-heat cycle on **(6)**₂ revealed the emergence of a second feature around 205 °C, prior to melting of **(6)**₂ at 215 °C. The latter is consistent with formation of at least some monomer, **6**, during melting of **(6)**₂. This leads to a mixture of solid **6** and **(6)**₂, affording features associated with melting of both **6** (at 205 °C) and **(6)**₂ (at 215 °C) during the reheating cycle (Figure 3.14a).

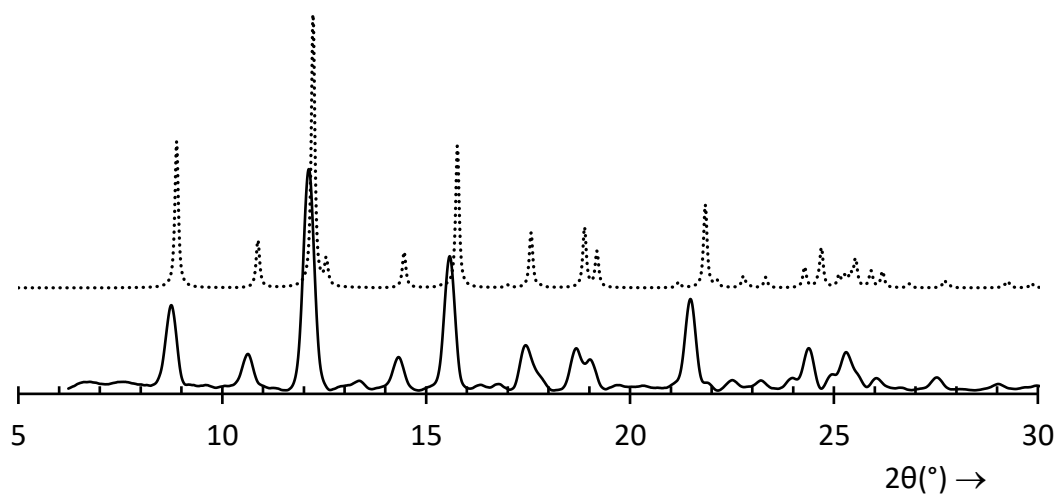


Figure 3.11. Room temperature PXRD profile for **(6)₂** with simulation based on low temperature SC-XRD (dotted line).

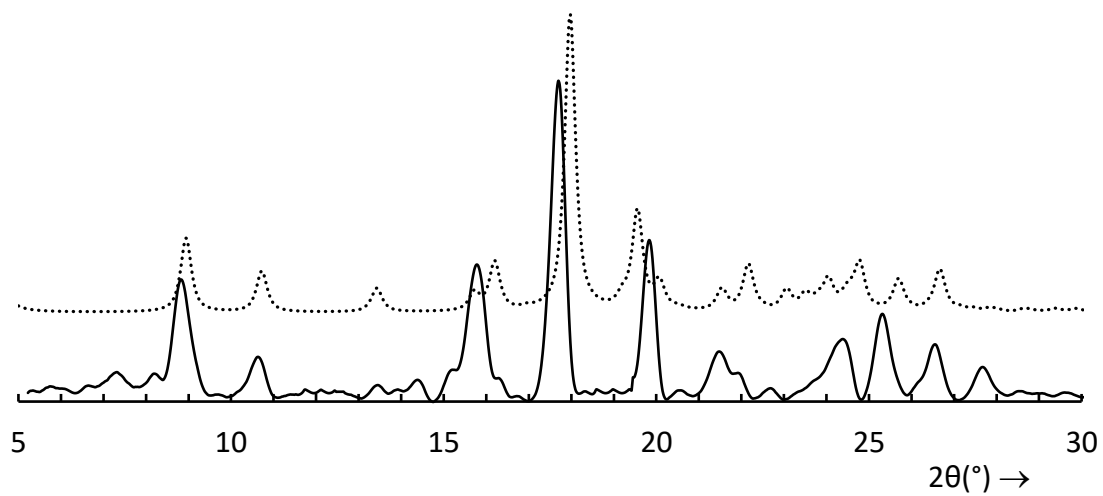


Figure 3.12. PXRD profile for **6** at room temperature with simulation based on low temperature SC-XRD (dotted line).

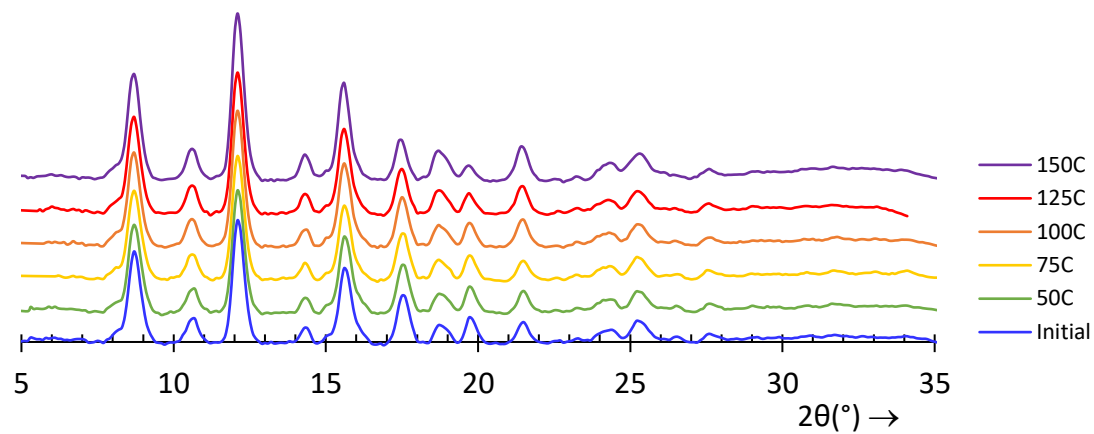


Figure 3.13. VT-PXRD of pristine **(6)**₂ from room temperature up to 150 °C

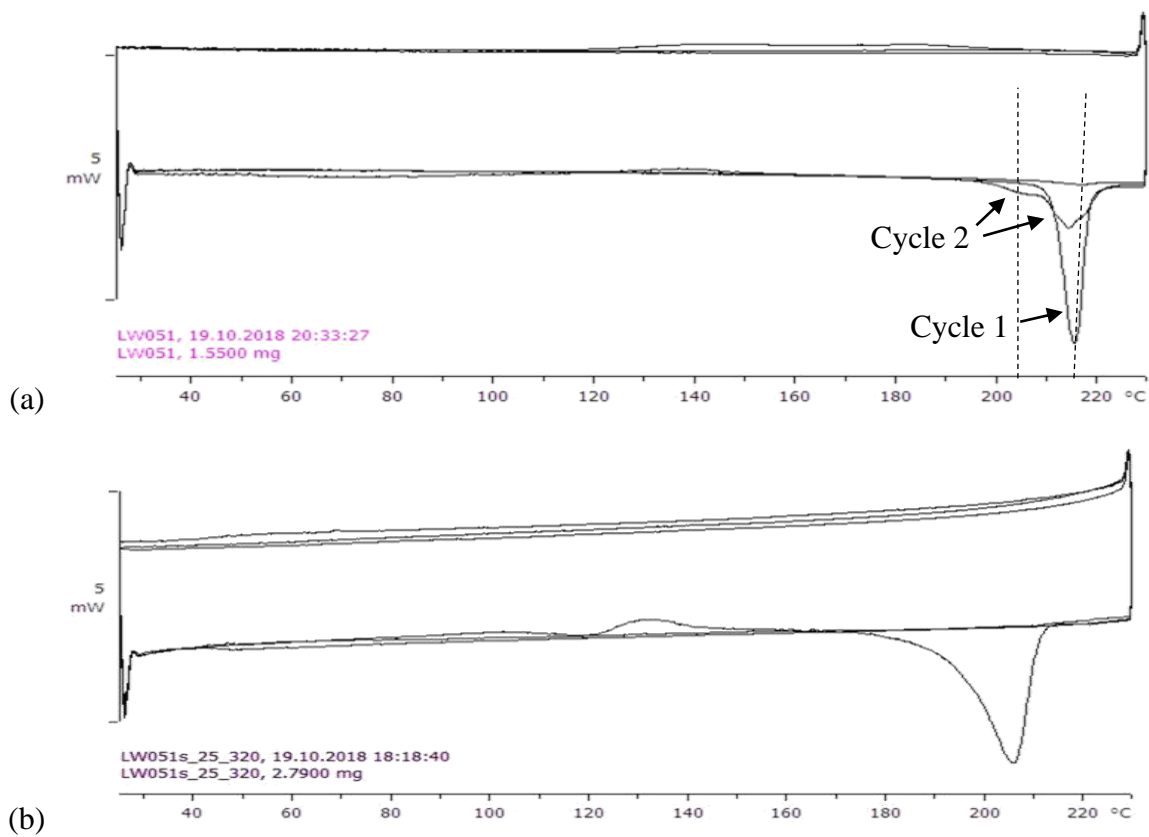


Figure 3.14. DSC profile for the phase pure (a) dimeric **(6)**₂ and (b) monomeric **6**.

In addition to these studies, both PXRD and SC-XRD studies were run concomitantly on freshly sublimed **6**, which appeared phase pure by optical microscopy. The crystalline sample was then gently ground with a pestle and mortar to facilitate mounting in capillary tubes and unexpectedly revealed a powder pattern consistent with dimeric (**6**)₂. A second sample was then prepared and carefully treated without grinding and the experimental PXRD then matched that of monomeric **6** (Figure 3.15). Additional studies indicated that samples of pristine **6**, subject to minimal grinding provided PXRD patterns comprising a mixture of both **6** and (**6**)₂ consistent with a mechanochemical transformation of **6** to (**6**)₂. The transition from **6** to (**6**)₂ upon grinding can be noted by monitoring the previously highlighted reflections at $2\theta = 18.0^\circ$ and 19.8° for **6** and $2\theta = 12.2^\circ$ for (**6**)₂.

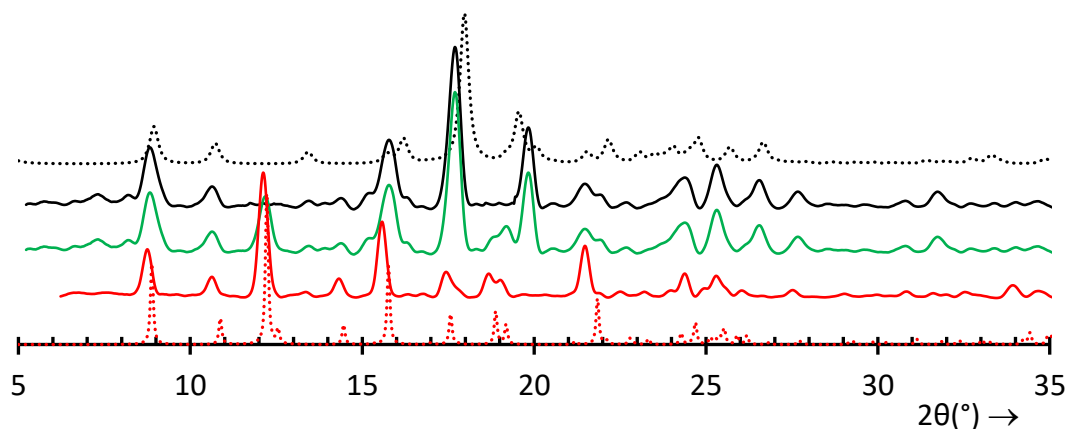


Figure 3.15. PXRD of **6** at room temperature (solid black line) with simulation (dotted black line); the green line corresponds to a lightly ground sample of **6** while the solid red line corresponds to a sample subjected to more sustained grinding. The dotted red line corresponds to the simulated PXRD pattern based on SC-XRD studies of (**6**)₂.

While there has been no evidence for (**6**)₂ to convert to **6**, the irreversible conversion of **6** to (**6**)₂ was intriguing. A comparison of the unit cell parameters for **6** and (**6**)₂ (Table 3.3) reveal a commonality of the two phases linked through an approximate halving of the

crystallographic *c*-axis, although the change in crystal system from orthorhombic to monoclinic mitigates against a true topotactic process.

Table 3.3. Unit cell parameters for **6** and (**6**)₂.

	6	(6) ₂
Crystal System	Orthorhombic	Monoclinic
Space Group	Pbca	P2 ₁ /n
<i>a</i> /Å	9.0701(4)	8.3163(4)
<i>b</i> /Å	7.3043(3)	7.7394(4)
<i>c</i> /Å	39.524(2)	20.2842(10)
α /°	90	90
β /°	90	101.737(2)
γ /°	90	90
<i>V</i> /Å ³	2618.51	1278.26
<i>D_c</i> /g cm ⁻³	1.645	1.685

Unlike the parent compound CpCo(bdt) which exhibits close Co...S intermolecular contacts (Figure 3.2) and a pre-orientation of molecules to form dimeric [CpCo(bdt)]₂, the crystal packing structure of **6** and (**6**)₂ (Figure 3.16) mitigate against a thermally-driven trivial lattice reorganization analogous to CpCo(bdt): The molecular packing of **6** indicates four monomer orientations with regard to their spatial displacement along the crystallographic *c*-axis (labelled **A** – **D** in Figure 3.16 and highlighted in orange, red, light green and dark green). While the nearest Co...S contacts (4.719(2) Å) are comparable to those in CpCo(bdt), they correspond to contacts between molecules within the same ‘stack’, i.e. of like orientation. The corresponding Co...Co separation between molecules in columns A/B (and C/D) which are related *via* the necessary inversion symmetry to generate (**6**)₂ is 14.489 Å. Formation of (**6**)₂ from **6** therefore requires substantial molecular displacements. Upon heating (required to increase molecular motion in the solid state), the conversion of **6** to (**6**)₂ is less likely since it is an entropically disfavored process. Indeed the DSC data point towards the opposite process, i.e. generation of **6** from pristine (**6**)₂,

upon melting. The thermodynamic driving force for the current transformation appears to be the application of pressure through mechanochemistry which favors the denser phase, $(\mathbf{6})_2$ (Table 3.3).

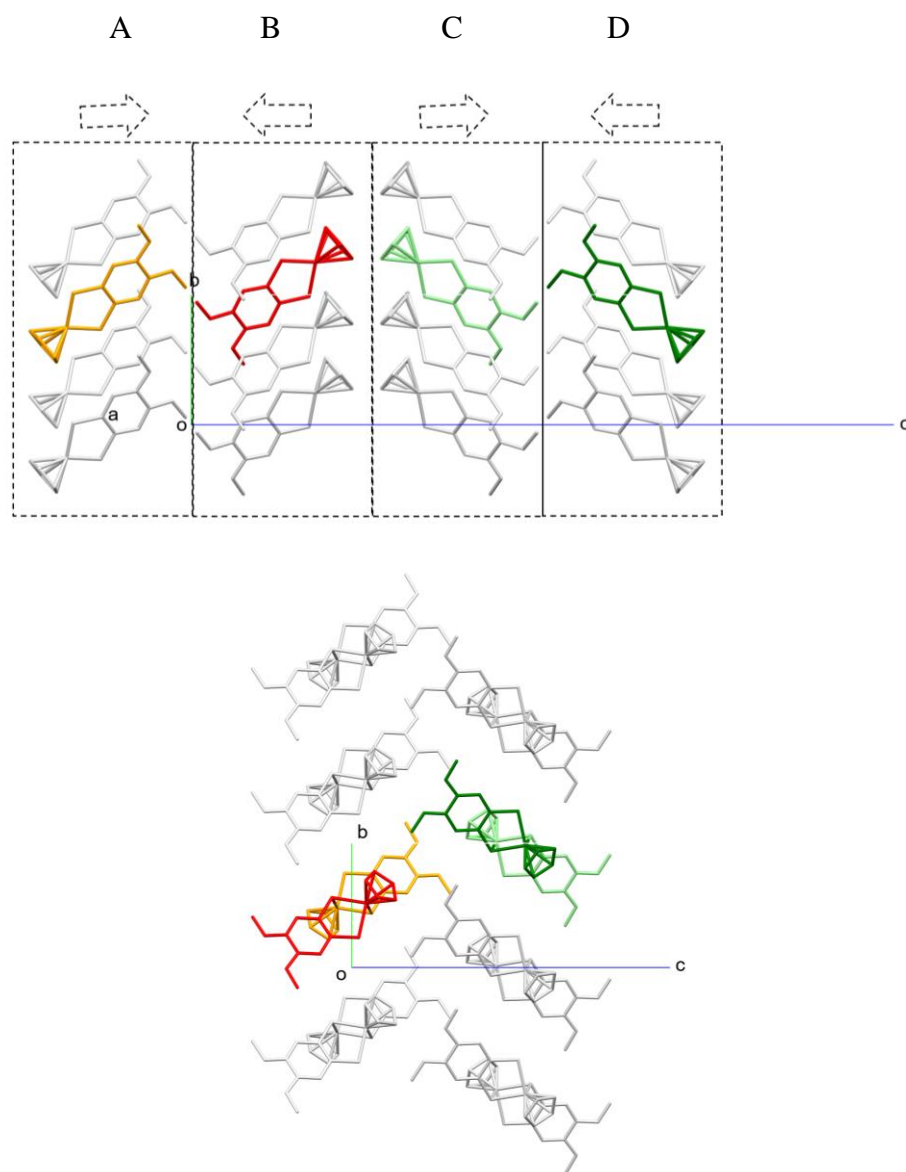


Figure 3.16 Schematic relationship between molecules in **6** and the structure of $(\mathbf{6})_2$ (one pair of molecules in the two phases are highlighted in color to emphasize the translational relationship along the *c*-axis).

Preliminary grinding studies on the monomers **7**, **8** and **10** showed no evidence for any mechanochemical phase transition.

3.3 Conclusions & Future Work

The current study describes the one pot synthesis of a series of η^5 -cyclo-pentadienyl cobalt(III) dithiolate complexes via oxidative addition of tetrathiocins to $\text{CpCo}(\text{CO})_2$. The fine energetic balance between $16e^-$ monomer and their dimeric counterparts is reflected in the polymorphic nature of **6** which crystallizes as **6** and **(6)**₂, as well as **7** which forms **7** and the cocrystal **(7)**₂·2**(7)**·CH₂Cl₂. Studies on **6** indicate that **6** does not convert to **(6)**₂ thermally but can be driven mechanochemically. Future studies will focus on examining the thermochemistry and mechanochemistry of complexes **7–10**.

3.4 Experimental

3.4.1. General Procedures

Chemicals were purchased from Millipore Sigma or Alfa Aesar. Tetrathiocins **1a–1d** were prepared according to a modified procedure and their analytical data matched the literature reports.³⁵ Standard solvents were dried and deoxygenated using an Innovative Technology Solvent Purification System and manipulation of air-sensitive materials carried out under an atmosphere of dry nitrogen using standard Schlenk techniques and a dry-nitrogen glove box (MBraun Labmaster). Microwave syntheses were carried out in sealed vessels using a Biotage Initiator 1 microwave. The microwave reactions to prepare metal complexes are carried out in a sealed glass vial evolve CO. Using a 2–5 mL microwave vial and 5 mL of solvent the final pressure was typically between 5 and 10 bar based on a 0.5 mmol reaction. The vial was cooled back to room temperature before releasing the pressure.

3.4.2. Physical Measurements

IR spectra were obtained using a Bruker Alpha FT-IR spectrometer equipped with a Platinum single reflection diamond ATR module. All NMR spectra were recorded on a Bruker DPX300 UltraShield 300 MHz spectrometer with a Broadband AX Probe using CDCl₃ (¹H δ = 7.26 ppm, s; ¹³C δ = 77.16 ppm) as an internal reference point relative to

Me₄Si ($\delta = 0$ ppm). Elemental compositions were determined on a Perkin Elmer 2400 Series II Elemental Analyzer. Mass spectra were recorded on a Waters XEVO G2-XS in either ESI(+) or ASAP(+) mode. UV-Vis spectra were measured on an Agilent 8453 spectrophotometer using *ca.* 2×10^{-4} M solutions of dichloromethane in the range 200–800 nm. Melting points were determined using a Stanford Research Systems MPA120 EZ-Melt Automated Melting Point Apparatus. DSC studies were performed on a Mettler Toledo DSC 822e or a TA Instruments DSC 2500. Samples of approximately 1.5–3.0 mg were hermetically sealed in pierced aluminium pans which were heated from 25 to 200 °C, and then cooled back to 25 °C under a nitrogen atmosphere. Heating and cooling rates were 5 °C min⁻¹.

3.4.3. X-Ray Crystallography

Crystals of the metal complexes were mounted on a cryoloop with paratone oil and examined on either a Bruker D8 Venture diffractometer equipped with Photon 100 CCD area detector or a Bruker APEX-II diffractometer with CCD detector using graphite-monochromated Mo-K α radiation ($\lambda = 0.71073$ Å) or Cu-K α radiation ($\lambda = 1.54056$ Å). An Oxford Cryostream cooler was used to maintain cryogenic temperatures for these studies. Data were collected using the APEX-II software³⁶ integrated using SAINT³⁷ and corrected for absorption using a multi-scan approach (SADABS).³⁸ Final cell constants were determined from full least squares refinement of all observed reflections. The structures of **(6)**₂, [(**7**)₂·2(**7**)·DCM], **7**, **8**, and **10** were solved by direct methods (SHELXS),³⁹ while the structure of **6** was solved using intrinsic phasing (SHELXT).⁴⁰ All structures were refined with full least squares refinement on F^2 using either SHELXL⁴⁰ or Olex2 software.³¹ All hydrogen atoms were added at calculated positions and refined isotropically with a riding model.

3.4.4. Synthesis of CpCo(dmobdt) (**6**)₂

Tetrathiocin **1a** (0.200 g, 0.5 mmol) was placed in a microwave vial under inert atmosphere to which dry toluene (5 mL) was added. The vial was sealed and CpCo(CO)₂ (0.13 mL, 1 mmol) was added via syringe. The mixture was heated in the microwave at 150 °C for 30 minutes to afford a deep blue solution. After slowly releasing pressure from the vial, the solvent was evaporated by rotary evaporation, the resultant blue solid dissolved

in CHCl₃, which was then filtered, evaporated and the dark blue-black solid washed with Et₂O and dried in air (0.262 g, 81% yield).

¹H NMR (300 MHz, ppm, CDCl₃): δ_H = 7.50 (2H, s, benzo C–H), 5.39 (5H, s, Cp C–H), 3.85 (6H, s, O–CH₃).

¹³C NMR (75 MHz, ppm, CDCl₃): δ_C = 155.87 (s, aryl O–C), 147.13 (s, aryl S–C), 111.31 (s, benzo–C), 79.35 (s, Cp–C), 56.18 (s, O–CH₃).

HRMS (ASAP) *m/z*: [M + H]⁺ calc. for C₂₆H₂₇O₄S₄Co⁺ 648.9456; found 648.9449.

Elemental Analysis calc. for C₂₆H₂₆O₄S₄Co₂: C 48.15; H 4.04%; found: C 47.95; H 4.04%.

Melting Point: 215 °C

UV-Vis (CH₂Cl₂): λ_{max} (nm), ε (mol.L⁻¹.cm⁻¹): 291(14200), 638(6720).

IR (ν_{max}, cm⁻¹): 2830(w), 1580(w), 1553(w), 1497(w), 1484(m), 1471(m), 1434(s), 1418(m), 1345(w), 1317(w), 1240(vs), 1202(s), 1179(s), 1153(w), 1105(w), 1059(w), 1037(vs), 1017(w), 1000(w), 942(w), 924(w), 852(m), 822(vs), 782(s), 682.13(m), 647(w), 583(w), 572.58(w), 445(m).

3.4.5. Synthesis of CpCo(dmobdt) (6)

The complex (6)₂ (0.262 g) was placed at the bottom of a 100 mL Schlenk tube fitted with a greased cold-finger and placed in a Buchi Kugelrohr under a static vacuum. Initial heating began at 100 °C with isopropyl alcohol circulating at *ca.*–3 °C. The temperature was increased by 15 °C each day until temperature reached 175 °C and left for 1 week total. (0.203 g) ¹H NMR, UV-Vis and IR afforded results matching those of (6)₂.

HRMS (ASAP) *m/z*: [M + H]⁺ calc. for C₁₃H₁₄O₂S₂Co⁺ 324.9767; found 324.9767.

Melting Point: 205 °C

3.4.6. Synthesis of CpCo(deobdt) (7)₂·2(7)

Tetrathiocin **1b** (0.229 g, 0.5 mmol) was placed in a microwave vial under inert atmosphere to which dry toluene (5 mL) was added. The vial was sealed and CpCo(CO)₂ (0.13 mL, 1 mmol) was added via syringe. The mixture was heated in the microwave at 150 °C for 30 minutes to afford a deep blue solution. After slowly releasing pressure from the vial, the solvent was evaporated by rotary evaporation, the resultant blue solid dissolved

in CHCl₃, which was then filtered, evaporated and the dark blue- black solid washed with Et₂O and dried in air (0.269 g, 76% yield).

¹H NMR (300 MHz, ppm, CDCl₃): δ_H = 7.50 (2H, s, benzo C–H), 5.39 (5H, s, Cp C–H), 4.05 (4H, q, ³J = 7.1 Hz, O–CH₂–CH₃), 1.47 (6H, t, ³J = 7.1 Hz, O–CH₂–CH₃)

HRMS (ASAP) m/z: [M + H]⁺ calc. for Dimer: C₃₀H₃₅O₄S₄Co⁺ 705.0082; found 705.0071 Monomer: C₁₅H₁₈O₂S₂Co⁺ 353.0080; found 353.0081

Elemental Analysis calc. for 1:2 Mixture C₃₀H₃₄O₄S₄Co₂ : C₁₅H₁₇O₂S₂Co: C 51.13; H 4.86%; found: C 50.83.68; H 4.98%.

UV-Vis (CH₂Cl₂): λ_{max} (nm), ε (mol.L⁻¹.cm⁻¹): 291(50000), 638(21100).

IR (ν_{max}, cm⁻¹): 3071(w), 2973(w), 2921(w), 2852(w), 1583(w), 1517(w), 1492(w), 1492(m), 1457(m), 1410(w), 1386(m), 1354(w), 1338(m), 1237(vs), 1195(vs), 1152(m), 1106(w), 1094(m), 1039(vs), 998(m), 919(w), 887(m), 850(m), 817(m), 692(w), 652(w), 582(w), 496(m), 448(w), 406(w).

3.4.7. Synthesis of CpCo(doxlbdt) (8)

Tetrathiocin **1c** (0.229 g, 0.5 mmol) was placed in a microwave vial under inert atmosphere to which dry toluene (5 mL) was added. The vial was sealed and CpCo(CO)₂ (0.13 mL, 1 mmol) was added via syringe. The mixture was heated in the microwave at 150 °C for 30 minutes to afford a deep blue solution. After slowly releasing pressure from the vial, the solvent was evaporated by rotary evaporation, the resultant blue solid dissolved in CHCl₃, which was then filtered, evaporated and the dark blue-black solid washed with Et₂O and dried in air (0.269 g, 76% yield).

¹H NMR (300 MHz, ppm, CDCl₃): δ_H = 7.45 (2H, s, benzo C-H), 5.87 (2H, s, O–CH₂–O), 5.38 (5H, s, Cp C-H).

Elemental Analysis calc. for C₁₂H₉O₂S₂Co·½ CHCl₃: C 43.52; H 2.76%; found: C 43.38.68; H 3.06%.

IR (ν_{max}, cm⁻¹): 3079(w), 2906(w), 2852(w), 1564(w), 1448(s), 1410(m), 1314(w), 1225(vs), 1112(m), 1019(m), 922(m), 823(m), 753(w), 662(w), 570(w).

3.4.8. Synthesis of CpCo(doxbdt) (9)

Tetrathiocin **1d** (0.229 g, 0.5 mmol) was placed in a microwave vial under inert atmosphere to which dry toluene (5 mL) was added. The vial was sealed and CpCo(CO)₂ (0.13 mL, 1 mmol) was added via syringe. The mixture was heated in the microwave at 150 °C for 30 minutes to afford a deep blue solution. After slowly releasing pressure from the vial, the solvent was evaporated by rotary evaporation, the resultant blue solid dissolved in CHCl₃, which was then filtered, evaporated and the dark blue- black solid washed with Et₂O and dried in air (0.269 g, 76% yield).

¹H NMR (300 MHz, ppm, CDCl₃): δ_H = 7.54 (2H, s, benzo C-H), 5.41 (5H, s, Cp C-H), 4.23 (4H, s, O-CH₂-CH₂-O).

Elemental Analysis calc. for C₁₃H₁₁O₂S₂Co: C 48.45; H 3.44%; found: C 47.37; H 4.07%.

IR (ν_{max}, cm⁻¹): 3095(w), 2918(vs), 2855(m), 1728(w), 1560(w), 1457(s), 1484(m), 1373(w), 1285(s), 1147(s), 1153(w), 1105(s), 1054(s), 897(m), 797(s), 695(w), 570(w), 498(w), 452(m).

3.4.9. Synthesis of CpCo(doxebdt) (10)

Tetrathiocin **1e** (0.229 g, 0.5 mmol) was placed in a microwave vial under inert atmosphere to which dry toluene (5 mL) was added. The vial was sealed and CpCo(CO)₂ (0.13 mL, 1 mmol) was added via syringe. The mixture was heated in the microwave at 150 °C for 30 minutes to afford a deep blue solution. After slowly releasing pressure from the vial, the solvent was evaporated by rotary evaporation, the resultant blue solid dissolved in CHCl₃, which was then filtered, evaporated and the dark blue- black solid washed with Et₂O and dried in air (0.269 g, 76% yield).

¹H NMR (300 MHz, ppm, CDCl₃): δ_H = 7.67 (2H, s, benzo C-H), 5.43 (5H, s, Cp C-H), 4.18 (4H, t, *J* = 5.8 Hz, O-CH₂-CH₂-CH₂-O), 2.18 (2H, apparent triplet, *J* = 5.8 Hz, O-CH₂-CH₂-CH₂-O).

Elemental Analysis calc. for C₁₄H₁₃O₂S₂Co · ¾ CH₂Cl₂: C 44.29; H 3.65%; found: C 44.70; H 3.69%.

IR (ν_{\max} , cm^{-1}): 3088(w), 2920 (w), 2860(w), 1520(w), 1485(m), 1450(m), 1381(m), 1297(m), 1242(vs), 1113(w), 1032(m), 982(m), 823(m), 730(w), 488(w), 424(w).

3.5 References

- (1) M. Trautz, *Z. Anorg. Allgem. Chem.*, 1916, **96**, 1–28.
- (2) W. C. M. Lewis, *J. Chem. Soc., Trans.*, 1918, 113, 471–492.
- (3) M. D. Cohen and G. M. J. Schmidt, *J. Chem. Soc.*, 1964, 1996–2000.
- (4) M. D. Cohen, G. M. J. Schmidt and F. I. Sonntag, *J. Chem. Soc.*, 1964, **224**, 2000–2013.
- (5) G. M. Schmidt, *J. Chem. Soc.*, 1964, **224**, 2014–2021.
- (6) H. I. Bernstein and W. C. Quimby, *J. Am. Chem. Soc.*, 1943, **65**, 1845–1846.
- (7) G. M. Schmidt, *Pure Appl. Chem.*, 1971, **27**, 647–678.
- (8) L. R. MacGillivray, J. L. Reid and J. A. Ripmeester, *J. Am. Chem. Soc.*, 2000, **122**, 7817–7818.
- (9) S. K. Kearsley, *The Prediction of Chemical Reactivity within Organic Crystals using geometric criteria in Organic solid state Chemistry* (Ed. G.R. Desiraju), Elsevier, New York, 1987, 69–115.
- (10) E. Fernandez-Bartolome, A. Martinez-Martinez, E. Resines-Urien, L. Piñeiro-Lopez and J. Sanchez Costa, *Coord. Chem. Revs.*, 2022, **52**, 214281.
- (11) A. Chaudhary, A. Mohammad and S. M. Mobin, *Crys. Growth Design.*, 2017, **17**, 2893–2910
- (12) F. Hu, X. Bi, X. Chen, Q. Pan and Y. Zhao, *Chem. Lett.*, 2021, **50**, 1015–1029.
- (13) J. B. Wright, *Molecular Crystals*, Cambridge University Press, Cambridge, 2nd edn, 1995, 120–143.
- (14) S.-L. Huang, T. S. A. Hor and G.-X. Jin, *Coord. Chem. Revs.*, 2017, **346**, 112–122.
- (15) A. Adhikary, S. Akhtar, A. Pariyar, A. S. Batsanov and R. Mondal. *ACS Omega*, 2019, **4**, 8731–8738.

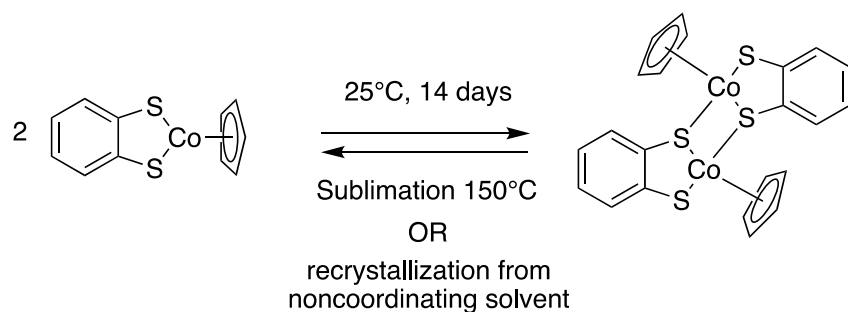
- (16) M. Jin, T. Sumitani, H. Sato, T. Seki and H. Ito, *J. Am. Chem. Soc.*, 2018, **8**, 2875–2879
- (17) L. Wen, P. Chen and W. Lin, *Chem. Commun.*, 2012, **48**, 2846–2848.
- (18) G. Liu, J. Liu, Y. Liu and X. Tao, *J. Am. Chem. Soc.*, 2014, **136**, 590–593.
- (19) J. P. Zhang, P.-Q. Liao, H.-L. Zhou, R.-B. Lin and X.-M. Chen, *Chem. Soc. Rev.*, 2014, **43**, 5789–5814.
- (20) Y. Kim, S. Das, S. Bhattacharya, S. Hong, M. G. Kim, M. Yoon, S. Natarajan and K. Kim, *Chem. Eur. J.*, 2012, **18**, 16642–16648.
- (21) G. B. Jameson, H. R. Oswald and H. R. Beer, *J. Am. Chem. Soc.*, 1984, **106**, 1669–1675.
- (22) E. J. Miller, T. B. Brill, A. L. Rheingold and W. C. A. Fultz, *J. Am. Chem. Soc.*, 1983, **105**, 7580–7584.
- (23) M. Nomura, and M. Fourmigué, *Inorg. Chem.*, 2008, **47**, 1301–1312.
- (24) S. Muratsugu, K. Sodeyama, F. Kitamura, S. Tsukada, M. Tada, S. Tsuneyuki and H. Nishihara, *Chem. Sci.*, 2011, **2**, 1960–1968.
- (25) M. Nihei, T. Nankawa, M. Kurihara and H. Nishihara, *H. Angew. Chem., Int. Ed.*, 1999, **38**, 1098–1100.
- (26) M. Murata, S. Habe, S. Araki, K. Namiki, T. Yamada, N. Nakagawa, T. Nankawa, M. Nihei, J. Mizutani, M. Kurihara and H. Nishihara, *Inorg. Chem.*, 2006, **45**, 1108–1116.
- (27) M. Nomura, and M. Fourmigué, *Inorg. Chem.*, 2008, **47**, 1301–1312.
- (28) S. Tsukada, M. Kondo, H. Sato, T. Gunji, *Polyhedron*, **2016**, 117, 265
- (29) M. Nomura, E. Tsukano, C. Fujita-Takayama, T. Sugiyama, M. Kajitani, J. *Organomet. Chem.*, **2009**, 694, 3116.
- (30) J. D. Wrixon, Z. S. Ahmed, M. U. Anwar, Y. Beldjoudi, N. Hamidouche, J. J. Hayward and J. M. Rawson, *Polyhedron*, 2016, **108**, 115–121.
- (31) R. F. Heck, *Inorg. Chem.*, 1968, **7**, 1513–1516.
- (32) H. W. Baird, B. M. White, *J. Am. Chem. Soc.*, 1966, **88**, 4744–4745.

- (33) M. Nomura, T. Sasao, T. Hashimoto, T. Sugiyama and M. Kajitani, *Inorg. Chim. Acta.*, 2010, **363**, 3647–3653
- (34) M. Nomura and M. Fourmigué, *J. Organomet. Chem.*, 2007, **692**, 2491–2499.
- (35) L. K. Watanabe, J. D. Wrixon, Z. S. Ahmed, J. J. Hayward, P. Abbasi, M. Pilkington, C. L. B. Macdonald and J. M. Rawson, *Dalton Trans.*, 2020, **49**, 9086–9093.
- (36) *APEX II*, Bruker AXS, Madison, WI, USA.
- (37) *SAINT*, Bruker AXS, Madison, WI, USA.
- (38) *SADABS*, Bruker AXS, Madison, WI, USA.
- (39) G. M. Sheldrick, *SHELXS-97*, A Program for Automatic Solution of Crystal Structures, University of Göttingen, 1997.
- (40) G. M. Sheldrick, *Acta Crystallogr., Sect. A: Found. Adv.*, 2015, **71**, 3–8.

4. OXIDATIVE ADDITION OF 1,2,5,6-TETRATHIOCINS TO CO(I): A RE-EXAMINATION OF CROWN ETHER FUNCTIONALIZED BENZENE DITHIOLATE COBALT(III) COMPLEXES

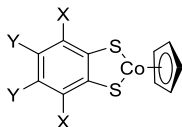
4.1 Introduction

The dithiolene ligand system, $R_2C_2S_2^{n-}$, is a well-established family of non-innocent ligands which is known in a series of oxidation states ($n = 0-2$), related by two sequential $1e^-$ redox processes.¹⁻³ The presence of multiple oxidation states for both the ligand and transition metals can make formal assignment of the metal and ligand oxidation state in transition metal dithiolene complexes challenging, and a range of computational and experimental methods have been implemented to unambiguously characterize ligand and metal oxidation states.⁴ Within the family of organometallic $16e^-$ dithiolene complexes of general formula $CpCo(S_2C_2R_2)$, the $16e^-$ Co(III) center is Lewis acidic, while the S lone pair is basic. For example, the Co(III) center forms adducts with the donor phosphite, $P(OMe)_3$,⁵ while the S lone pair is Lewis basic toward $M(CO)_n$ fragments ($M = Mo$ or W , $n = 2$; $M = Fe$, $n = 3$).⁶⁻⁸ In the absence of additional Lewis acids and bases, the complementarity of the Lewis basic S and Lewis acidic Co centers can lead to dimerization through a pair of dative $S \rightarrow Co$ bonds.^{9,10} Here there is a fine energetic balance between monomers and dimers,^{5,11,12} reflected in the solid-state conversion of the $16e^-$ monomeric $CpCo(bdt)$ complex to the $18e^-$ dimer $[CpCo(bdt)]_2$ at ambient temperature (Scheme 4.1).¹⁰



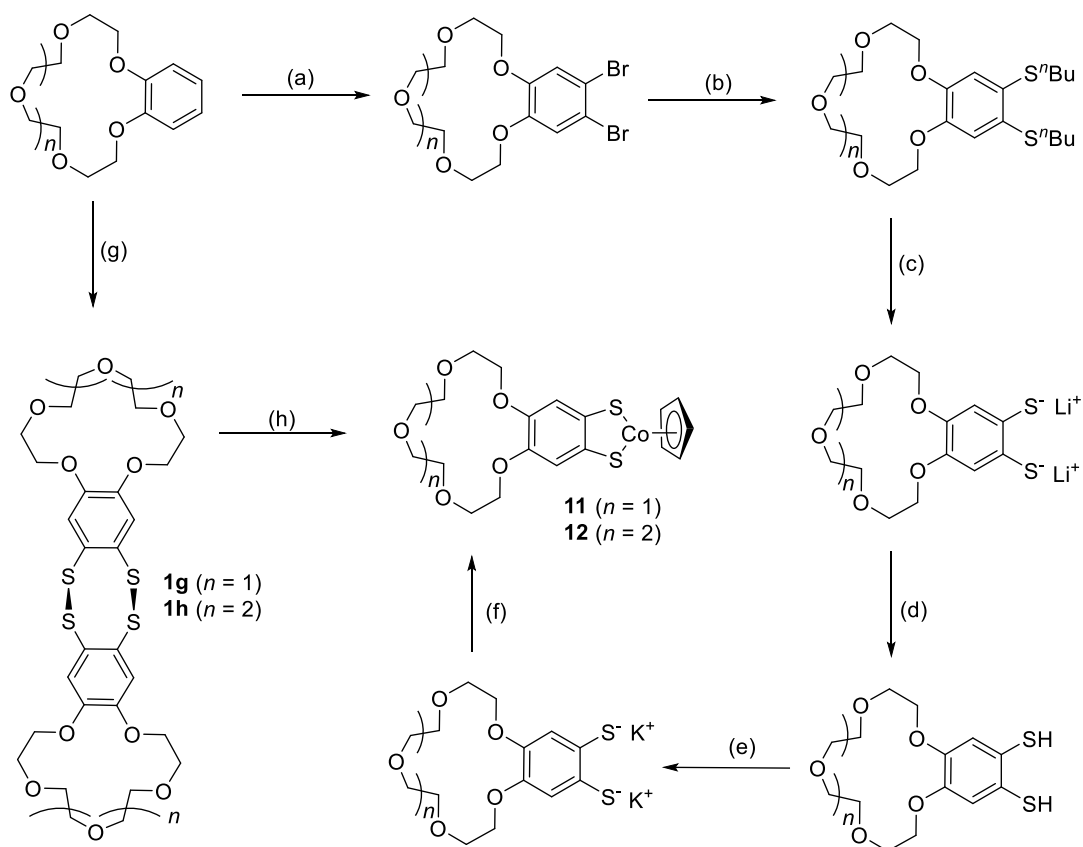
Scheme 4.1. Transformations between the monomer $CpCo(bdt)$ and the dimer $[CpCo(bdt)]_2$.

The family of $\text{CpCo}(\text{S}_2\text{C}_2\text{R}_2)$ complexes exhibits both an intense low-energy transition in the visible region and accessible redox processes within the ± 1 V window (vs Ag/AgCl) which may make them potentially suitable as probes for changes in chemical environment such as sensors for the presence of metal ions.^{13,14} A search of the CSD (release 2020.2.0) reveals that ca. 60% of structurally characterized benzene dithiolate complexes of the *d*-block metals comprise derivatives of either benzene or toluene dithiolate, primarily due to their commercial availability. While both 3,6-benzo-substituted¹¹ and 4,5-benzo-substituted ($\text{X} = \text{H}$, $\text{Y} = \text{SiPr}$) derivatives of $\text{CpCo}(\text{bdt})$ (Scheme 4.2) as well as asymmetrically substituted complexes have been described,^{13,14} $\text{CpCo}(\text{bdt})$ derivatives bearing functional groups suitable for coordination to metal ions are less well established.



Scheme 4.2. Symmetric derivatives of $\text{CpCo}(\text{bdt})$ ($\text{X} = \text{F}, \text{Cl}, \text{Br}, \text{Ph}$. $\text{Y} = \text{H}$; $\text{X} = \text{H}$, $\text{Y} = \text{Si}^i\text{Pr}$).

Notable exceptions are benzo-15-crown-5 and benzo-18-crown-6 complexes **11** and **12** reported by Garner, which were prepared from benzo-15-crown-5 and benzo-18-crown-6 in six steps (Scheme 4.3, steps a–f). Their synthetic method is lengthy, and several intermediates were incompletely characterized and/or yields not reported.^{13,14} An alternative synthetic strategy to access dithiolate complexes is the oxidative addition of dithietes to low-valent metals.¹⁵ This methodology has recently been exploited by Fekl and Kuropatov who examined oxidative addition of dithietes to $\text{Pd}(0)$.^{16,17} In this context, we have explored the related benzo-fused-1,2,5,6-tetrathiocins which can be considered as dimers of the dithiete moiety and exhibit similar reactivity to zero-valent group 10 metal complexes.^{18–23} The current study describes a simple two-step synthesis of benzo-crown functionalized derivatives **11** and **12** and explores their reactivity with selected alkali metal ions (Na^+ , K^+ , Rb^+ , and Cs^+) and 3d metal ions (Co^{2+} and Cu^{2+}), focusing on the stoichiometry of coordination and the nature of the products formed through oxidation.



Scheme 4.3. Synthesis of macrocyclic cyclopentadienyl cobalt dithiolate complexes **11** and **12**; Route (a) – (f) taken from reference [13]; (g) – (h) this work. (a) Br₂, HOAc, rt; (b) CuⁿBu, quinoline, pyridine, reflux; (c) Li(s), NH₃(l); (d) 12 M HCl; (e) K(s), MeOH; (f) CpCo(CO)₂, CH₂Cl₂; (g) S₂Cl₂, HOAc, rt; (h) CpCo(CO)₂, PhMe, 150 °C, μ -wave.

4.2 Results and Discussion

4.2.1. Synthesis

Reaction of tetrathiocins **1g** and **1h** with CpCo(CO)₂ in a sealed 2–5 mL microwave reaction vial at 150 °C for 30 min in toluene under microwave irradiation afforded the corresponding complexes **11** and **12**. After releasing the pressure, the toluene was evaporated, and the blue residue was taken up in CHCl₃, filtered, and dried *in vacuo*. Complexes **11** and **12** were isolated as dark blue solids by dissolving in the minimum amount of CH₂Cl₂ and precipitating with hexanes in 71–75% isolated yield.

4.2.2. Structures of **11** and **12**

Crystals of **11** and **12** were grown by slow diffusion of hexanes into saturated CH_2Cl_2 solutions of **11** and **12**. Complexes **11** and **12** crystallize in the space groups Cc and $P2_1/c$, each with one molecule per asymmetric unit. Both **11** and **12** have a monomeric $16e^-$ Co(III) coordination geometry (Figure 4.1) in which Co(III) adopts a “two-legged piano-stool” geometry with the cobalt, the benzene dithiolate atoms, and the Cp ring centroid essentially planar (maximum deviation from the $\text{C}_6\text{S}_2\text{Co}$ mean plane is less than 0.038 \AA for **11** and 0.023 \AA for **12**). The Cp ring plane is essentially perpendicular to the C_2S_2 plane, at 89.47° for **11** and 89.42° for **12**. For **11** and **12** the Co–S bond lengths fall in the range of $2.106(5)$ – $2.130(4) \text{ \AA}$, while the S–C bond lengths are in the range of $1.728(4)$ – $1.737(1) \text{ \AA}$ and are consistent with a dithiolate structure.²⁴ The Cp-centroid to Co distances of 1.660 and 1.651 \AA for **11** and **12** are comparable with those of other $16e^-$ cyclopentadienyl cobalt(III) benzenedithiolate structures (1.640 – 1.656 \AA).^{9–12,25}

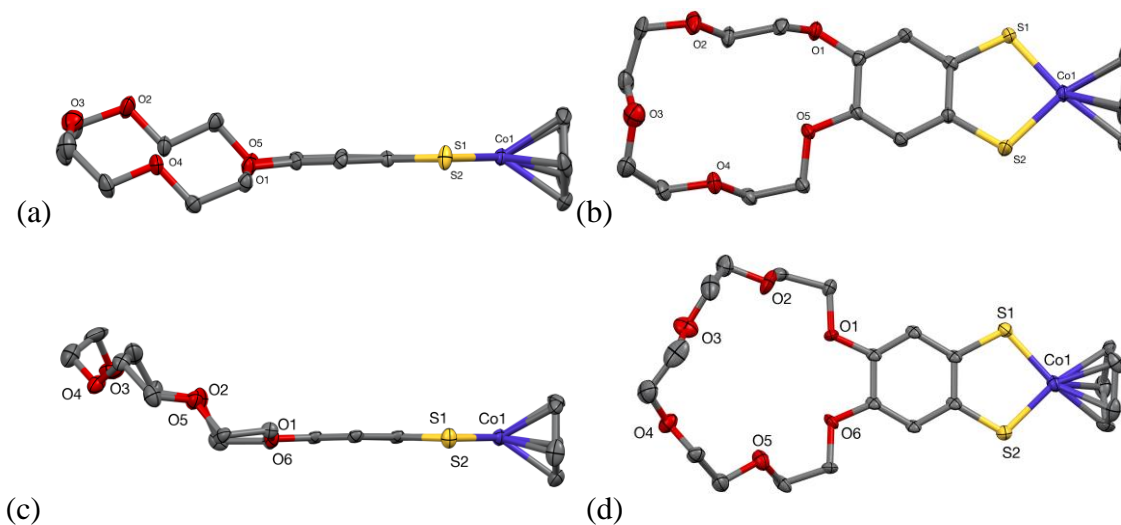


Figure 4.1. (top) Crystal structure of **11** viewed (a) parallel to and (b) perpendicular to the C_6S_2 ring plane with one of the two molecules in the asymmetric unit shown; (bottom) Crystal structure of **12** viewed (c) parallel to and (d) perpendicular to the C_6S_2 plane. Thermal ellipsoids plotted at the 50% probability level. Hydrogen atoms omitted for clarity.

During attempted coordination studies of **11** with $\text{Co}(\text{BF}_4)_2$ (*vide infra*), crystals of dimer (**11**)₂ were formed during slow diffusion of pentane into a $\text{CH}_2\text{Cl}_2/\text{MeOH}$ (1:1 v/v

ratio) of **11** in the presence of $\text{Co}(\text{BF}_4)\cdot 6\text{H}_2\text{O}$ (Figure 4.2). Under these conditions, crystallization of $(\mathbf{11})_2$ appears reproducible. Dimeric complex $(\mathbf{11})_2$ crystallizes in the monoclinic space group $C2/c$ with half a molecule in the asymmetric unit. One sulfur of each dithiolate adopts a μ_2 -bridging mode, comparable with other reported dimeric structures such as $[\text{CpCo}(\text{bdt})]_2$ (Scheme 4.1).^{9,10} The geometry at the cobalt centers now reflects a three-legged piano-stool motif with a formal $18e^-$ Co(III) center. As a result, the Co atom is pushed out of the $\text{C}_6\text{H}_2\text{S}_2$ plane and sits 0.565 \AA above the plane with the Cp ring at an angle of 129.98° to the C_6S_2 plane. Unlike $\text{CpCo}(\text{bdt})$, which undergoes a solid-state dimerization (Scheme 4.1), there was no evidence for **11** to dimerize in the solid state to form $(\mathbf{11})_2$, and the window of conditions to form $(\mathbf{11})_2$ appears narrow. Nevertheless, the identification of both monomeric **11** and dimeric $(\mathbf{11})_2$ clearly reflects a fine thermodynamic balance between the $16e^-$ monomer and $18e^-$ dimer forms. Spectroscopic studies in solution (NMR and UV-Vis) revealed that **11** and $(\mathbf{11})_2$ exhibited identical properties consistent with the complete dissociation of $(\mathbf{11})_2$ to form **11** in solution.

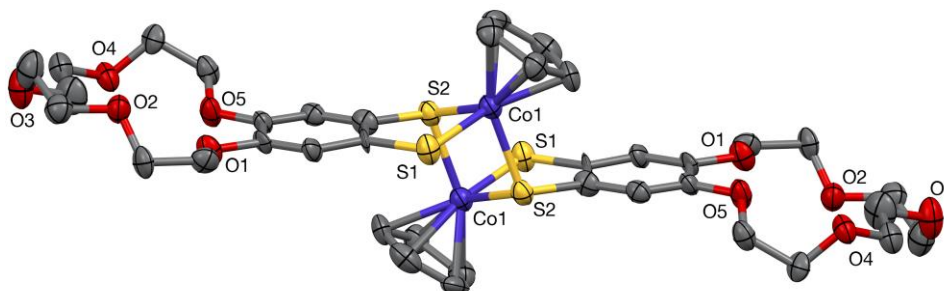


Figure 4.2. Crystal structure of $(\mathbf{11})_2$ with thermal ellipsoids drawn at the 50% probability level with hydrogen atoms omitted for clarity.

4.2.3. Solution Studies

Both **11** and **12** exhibit an intense blue color in solution reflected in one band in the visible region of the spectrum at 634 nm for **11** ($\text{CH}_2\text{Cl}_2/\text{MeCN}$ 1:1 v/v) and 649 nm for **12** (CH_2Cl_2). ^1H NMR studies on both **11** and **12** in CDCl_3 reveal the aryl protons to be equivalent, consistent with the presence of a $16e^-$ monomeric cyclopentadienyl cobalt dithiolate complex in solution rather than the $18e^-$ dimer. In this context, it is worth noting that the ^1H NMR spectra of the corresponding dimeric dithiolate-bridged group 10

complexes $[M(\text{dmobdt})(\text{PPh}_3)]_2$ ($M = \text{Pd}$ and Pt ; $\text{dmobdt}^{2-} = \text{dimethoxybenzenedithiolate}$) reveal two distinct chemical environments for the aromatic ^1H nuclei of the dmobdt^{2-} ligand.²¹

4.2.4. DFT Studies

DFT studies on **11** were undertaken using the both B3LYP-D3 and M06 functionals and the LACV3P basis set augmented with diffuse and polarization functions for all atoms. The results from the M06/LACV3P**++ are discussed here as they provided superior agreement with the UV-Vis data. The gas-phase geometry of **11** was fully optimized, and subsequent TD-DFT calculations of the UV-Vis spectra used the geometry-optimized structure, taking into account solvent effects using a conductor-like screening model.²⁶ An examination of the frontier orbitals revealed a near degenerate pair of essentially dithiolate-based ligand orbitals, whereas the LUMO is largely an antibonding orbital of π -character between the dithiolate S atoms and the CpCo fragment (Figure 4.3). The LUMO+1 is an antibonding orbital of σ -character between the S and CpCo fragments. These calculations suggest that redox processes will involve dithiolate-based oxidation and CpCoS_2^{2-} based reduction (see the Electrochemical Studies section). TD-DFT calculations on the gas-phase geometry-optimized structure (M06/LACV3P**++/COSMO (CH_2Cl_2)) revealed an intense low energy band at 622 nm (oscillator strength, $f = 0.19$), *c.f.* experimental absorption at 634 nm in 1:1 $\text{CH}_2\text{Cl}_2/\text{MeCN}$. This transition has large HOMO \rightarrow LUMO and HOMO-1 \rightarrow LUMO contributions, consistent with electron transfer between the benzenedithiolato and CpCoS₂ fragments (Figure 4.3).

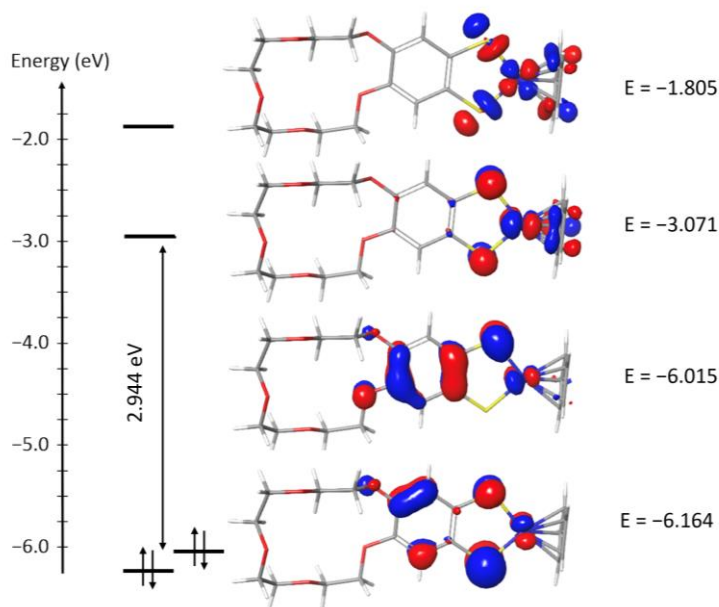


Figure 4.3. DFT computed orbital energies (M06/LACV3P**+ +/COSMO(CH₂Cl₂)) for **11**.

4.2.5. Coordination Chemistry of **11**

Crown ethers are well-known to form strong complexes with the alkali metals, underpinned by much of the pioneering work of Nobel Laureate Charles Pederson, and are known to have strong selectivity between metal ions.²⁷ Indeed, Garner reported that both the λ_{max} and redox potentials of both **11** and **12** are sensitive to the presence of Na⁺, but the composition of their *s*-block complexes were only characterized by FAB-MS data which pointed to a complex of formulation [Na(**11**)]⁺.¹³ Notably, MS studies on samples of **11** and **12** stored in glass vials revealed ions consistent with [**11** + NH₄]⁺, [**11** + Na]⁺, [**12** + NH₄]⁺, [**12** + Na]⁺, and [**12** + K]⁺, respectively, confirming their ability to bind cations (see Figures D.1–3). However, our use of softer ESI+ methods identified both the 2:1 sandwich complexes [M(**11**)₂]⁺ (M = Na, K, Rb, and Cs) as well as the corresponding 1:1 complex ion [M(**11**)]⁺. These MS studies showed the expected isotope distribution patterns (see Figures 4.4 and D.4–D.10).

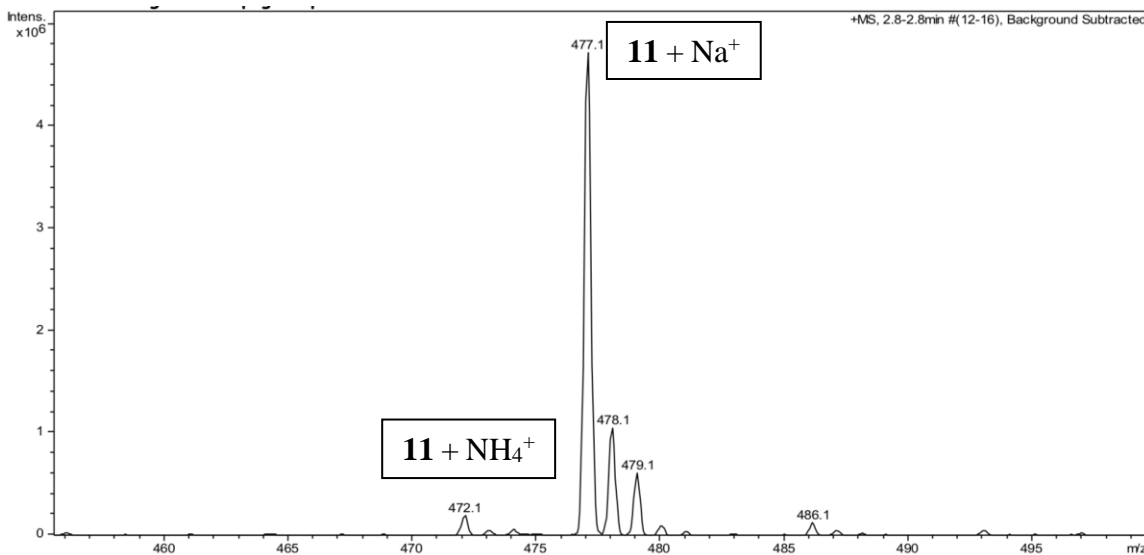


Figure 4.4. Mass spectrum of **11** after storage in a glass vial reveals **11** + NH₄⁺ ($m/z = 472$, calculated isotope distribution pattern: 472 = 100, 473 = 23.1, 474 = 12.4, 475 = 2.2) and **11** + Na⁺ ($m/z = 477$, calculated isotope distribution pattern: 477 = 100; 478 = 22.7; 479 = 12.3; 480 = 2.2). Isotopomers with less than 1% abundance are neglected.

4.2.6. Solution Studies of **11**

To probe the nature of the complex present in solution, variable-temperature ¹H NMR studies on **11** in the presence of Na⁺ were inconclusive, revealing only nuanced changes in the Cp, aryl, and crown ether regions. We therefore switched to UV-Vis spectroscopy to examine the effects of metal binding on **11**. Solution UV-Vis data on **11** (1:1 CH₂Cl₂/MeCN) in the presence of Na⁺ (as [Na][BPh₄]) shows a small dependence on the mole ratio, with the λ_{max} shifting from 634 nm (free ligand) to 616 nm in the presence of excess Na⁺ ions (Co:Na = 1:5). This replicates Garner's observations (recorded in MeCN), which showed the free ligand at 634 nm and a shift to 617 nm upon addition of Na[ClO₄]. Notably, titration of **11** with Na⁺ revealed an initial marked shift in λ_{max} on addition of Na⁺ ions up to a Co:Na ratio of 2:1, but no subsequent change in λ_{max} was observed on addition of further Na⁺ (see Figure 4.5), consistent with formation of [Na(**11**)₂]⁺ as the dominant species in solution.

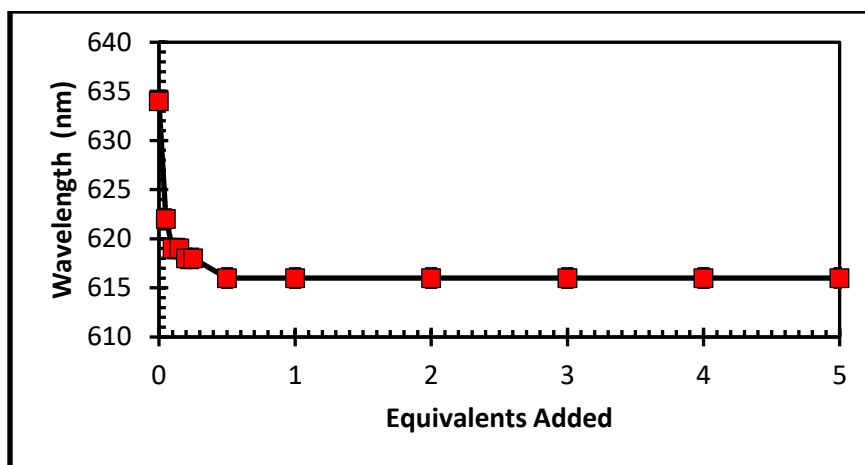
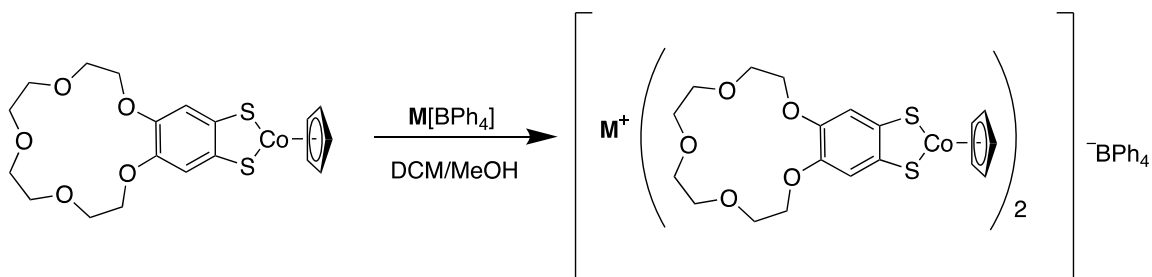


Figure 4.5. The change in λ_{max} for **11** with of a $0.00005 \text{ mol L}^{-1}$ solution with equivalents of a $0.0001 \text{ mol L}^{-1}$ NaBPh_4 solution added.

4.2.7. X-ray Crystallography

Both the MS and UV-Vis data provided evidence for formation of 2:1 complex $[\text{Na}(\mathbf{11})_2]^+$ which were confirmed by crystallographic studies. These revealed that recrystallization of **11** in the presence of $\text{M}[\text{BPh}_4]$ ($\text{M} = \text{Na}, \text{K}, \text{Rb}, \text{and Cs}$) in both 1:1 and 2:1 stoichiometric ratios invariably formed crystals of 2:1 complexes **13a–13d** in which two molecules of **11** sandwich the alkali metal (Scheme 4.4, Figure 4.6).



Scheme 4.4. Alkali-metal cation binding to **11** [$\text{M} = \text{Na}, \text{K}, \text{Rb}, \text{Cs}$]

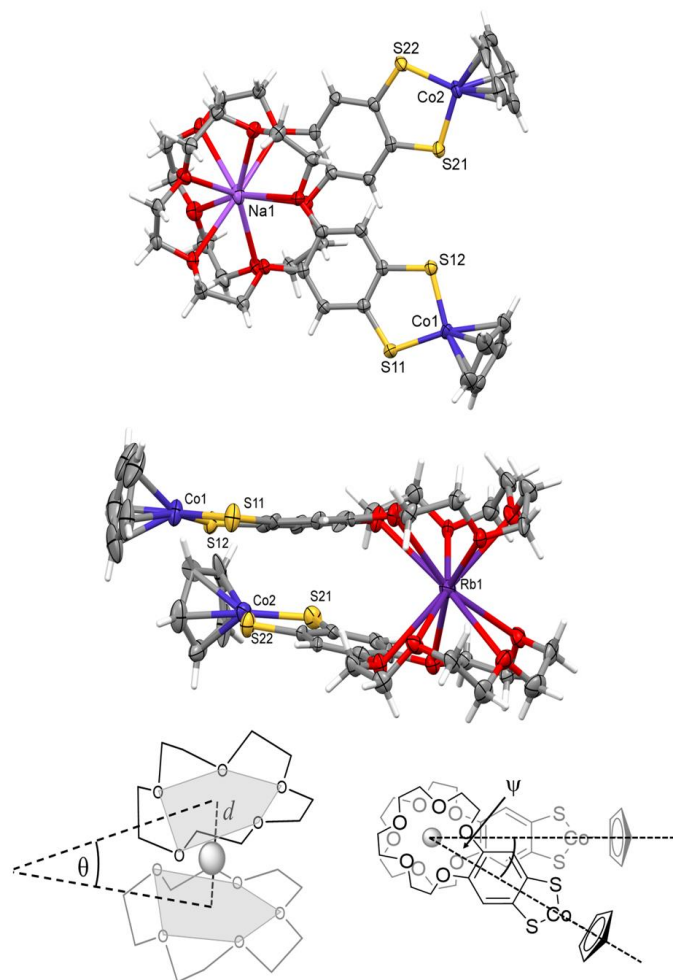


Figure 4.6. Crystal structure of the cations in (top) **13a** and (centre) **13c** with thermal ellipsoids for non-H atoms drawn at the 50% probability level. The BPh_4^- counterions are omitted for clarity. (bottom) Illustrations of the geometric parameters d , θ and ψ discussed in the text.

The structures of **13a–13d** all crystallize in the monoclinic space group $C2/c$ with Na^+ , K^+ and Rb^+ complexes being isomorphous (Table 4.1).

Table 7.1. Crystallographic data for compounds **13a–13d**

Compound	13a	13b	13c	13d
Formula	C ₆₂ H ₆₆ BCo ₂ NaO ₁₀ S ₄	C ₆₂ H ₆₆ BCo ₂ KO ₁₀ S ₄	C ₆₂ H ₆₆ BCo ₂ O ₁₀ RbS ₄	C ₆₂ H ₆₆ BCo ₂ CsO ₁₀ S ₄
FW (g mol ⁻¹)	1251.15	1266.15	1313.52	1360.96
Temp. (K)	170(2)	170(2)	170(2)	170(2)
Wavelength	0.71073	0.71073	1.54178	0.71073
Crystal System	Monoclinic	Monoclinic	Monoclinic	Monoclinic
Space Group	<i>C2/c</i>	<i>C2/c</i>	<i>C2/c</i>	<i>C2/c</i>
a	23.666(6)	23.5985(17)	23.4199(9)	17.591(6)
b	15.585(4)	15.8177(10)	16.0367(9)	22.017(7)
c	34.260(9)	34.230(2)	34.0682(14)	32.559(15)
α	90	90	90	90
β	100.904(8)	101.096(2)	100.945(3)	92.088(16)
γ	90	90	90	90
V/Å ³	12408(6)	12538.4(15)	12562.5(10)	12602(8)
Z	8	8	8	8
D _c (g cm ⁻³)	1.3394	1.343	1.389	1.435
Unique reflections	15482	10705	4973	13110
Reflections with I > 2 σ (I)	12986	8865	4049	11118
R _{int}	0.0495	0.0410	0.1133	0.0498
R ₁ (I > 2 σ (I))	0.0386	0.0319	0.0509	0.0269
wR ₂ (all)	0.0926	0.0740	0.0993	0.0560
S	1.060	1.034	1.044	1.058
$\Delta\rho_{\max}, \Delta\rho_{\min}/e^{-\text{Å}^3}$	+0.83, -0.75	+0.65, -0.67	+0.40, -0.43	+0.55, -0.78

In the case of **13a**, the Na⁺ ion is formally nine-coordinate with Na \cdots O distances ranging from 2.501(2)–2.989(2) Å and the remaining Na \cdots O contact at 3.119(2) Å, falling just beyond that expected for a formal Na–O bond. For the heavier *s*-block ions the geometries are all 10-coordinate (Figures 4.6, A2.S2, and S3). The bond distances and angles of the cobalt(III) dithiolate moiety remain relatively unchanged upon coordination to the alkali cations. There is a slight distortion of the Co center away from the C₂S₂ plane with the CoS₂ and C₂S₂ planes forming angles (φ) between 1.86 and 5.24° (Table 4.2, Figure 4.6).

Table 4.2. Values of θ , d and ψ , for complexes **13a–13d**.

Complex	Cation	θ (°)	d (Å)	ψ (°)
13a	Na ⁺	10.54	3.126	55.10(1)
13b	K ⁺	13.67	3.324	55.65(1)
13c	Rb ⁺	15.17	3.525	55.78(1)
13d	Cs ⁺	36.97	4.305	56.76(1)

As the size of the cation increases ($\text{Na}^+ < \text{K}^+ < \text{Rb}^+ < \text{Cs}^+$), the “sandwich” formed by the two $[\text{O}_5]$ planes and the s -block ion “opens up” to accommodate the larger size of the metal, highlighted in Figure 4.6. This change in geometry is manifested in (i) the angle (θ) between the two $[\text{O}_5]$ mean planes and (ii) the separation of the centroids (d) of the two $[\text{O}_5]$ planes (Table 4.2). The angle, θ , systematically increases from 10.54° in **13a** to 36.97° in **13d** to accommodate the larger cation. Similarly, the value of d increases from 3.126 \AA in **13a** to 4.305 \AA for **13d**. While the steric bulk of the CpCo fragment might be anticipated to lead to a “trans” arrangement of coordinating ligands ($\psi = 180^\circ$), the CpCo fragments are closer to an eclipsed geometry ($\psi = 0^\circ$) with ψ , corresponding to the $\text{Co}-\text{O}_{5\text{centroid}}-\text{O}_{5\text{centroid}}-\text{Co}$ torsion angle, largely invariant across the series ($55.10(1)-56.76(1)^\circ$, Table 4.2).

4.2.8 Electrochemical Studies

Electrochemical studies on **11** reveal a quasi-reversible reduction at $E_{1/2} = -0.69 \text{ V}$ and an irreversible oxidation at $E_p = +0.95 \text{ V}$ with respect to Ag/AgCl (Figure 4.7).

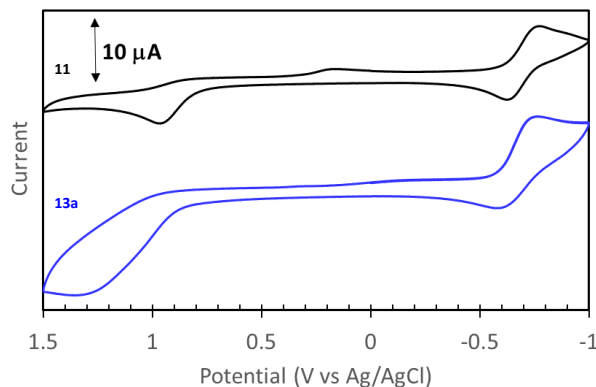


Figure 4.7. Cyclic voltammograms for **11** and **13a** (0.01 M $[\text{nBu}_4\text{N}][\text{PF}_6]$ supporting electrolyte, solvent = CH_2Cl_2 , scan rate 100 mV/s).

Under these conditions, the Fc/Fc^+ redox couple occurs at $E_{1/2} = +0.50 \text{ V}$. While the reduction potential is in good agreement with Garner’s data, the oxidation wave is shifted significantly with respect to the literature data (E_{red} at -0.65 V and E_{ox} at $+0.76 \text{ V}$ vs SCE,¹⁶ equivalent to -0.70 and $+0.72 \text{ V}$, taking into account the $+0.045 \text{ V}$ difference between SCE and Ag/AgCl reference electrodes). On the basis of the DFT calculations (Figure 4.3), the HOMO is largely dithiolate- ligand-based, yet oxidation of **11** is shifted to a considerably

more positive potential when compared to the analogous Pd(dppe) and Pt(dppe) complexes with the same 15-crown-5-benzenedithiolate ligand (+0.52 and +0.58 V vs Ag/AgCl, respectively) whose HOMO is similarly of dithiolate character²³ (See section 2.3.4). This likely arises as a consequence of the higher oxidation state of the Co(III) lowering the HOMO energy. Unlike the Pd(dppe) and Pt(dppe) derivatives, this oxidation is irreversible. The irreversible nature of this process for cobalt likely arises from the outcome of the oxidation reaction which leads to dimerization, S–S σ -bond formation and a change in metal coordination geometry (*vide infra*). Conversely, the strong geometric preference for Pt(II) and Pd(II) to adopt a square-planar geometry would appear to suppress a comparable process for the group 10 metals. For **13a**, coordination of Na⁺ into the crown ether pocket has the anticipated effect of markedly increasing the oxidation potential ($E_p = +1.32$ V) by increasing the positive charge on the complex and lowering the ligand-based HOMO energy. The DFT calculations (M06/ LACV3P**+/COSMO(CH₂Cl₂)) reveal the LUMO to be of CpCoS₂ character (Figure 4.3) and therefore expected to be relatively insensitive to the dithiolate ligand and any coordinated *s*-block cation. This is reflected in the reduction potentials of **11**, **12**, and **13a** whose potentials are almost invariant, ranging from –0.66 to –0.70 V (Table 4.3). The peak-to-peak potential for all three reduction processes is, however, significantly larger than the Nernstian value of 0.059 V expected for a 1 e^- process, suggesting these processes are better described as quasi-reversible.

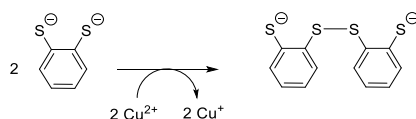
Table 4.3. Summary of oxidation and reduction potentials for **11**, **12** and complex **13a**.

Oxidation processes are irreversible and the peak potential is reported. Reduction processes were quasi-reversible. Half-wave reduction potentials and peak-peak separations are reported. All data referenced to Ag/AgCl.

Compound	Oxidation	Reduction	
	$E_{p,ox}$ (V)	$E_{1/2}$ (V)	ΔE_{pp} (V)
11	1.00	–0.70	0.15
12	1.01	–0.66	0.14
13a	1.32	–0.67	0.17

4.2.9 Chemical Oxidation of **11**

To extend our studies of the crown-ether coordination chemistry from *s*- to *d*-block metals, we made a search of the CSD which revealed a small number of benzo-15-crown-5 complexes with first row transition metals, limited to M(II) ions (M = Cu, Co, Fe, Mn, and Zn).^{28–31} We therefore commenced these studies by exploring reactivity toward M(II) salts with weakly interacting anions, exemplified by Cu(CF₃SO₃)₂ and Co(BF₄)₂·6H₂O. These did not afford coordination at the crown ether site but rather led to oxidation of **11**: The reaction of **11** with Cu(CF₃SO₃)₂ led to the fortuitous isolation of a few crystals, which were identified by X-ray diffraction as [(CpCo)₂{S₂C₆H₂O(CH₂CH₂O)₄]₂][CF₃SO₃]₂, [**14**][CF₃SO₃]₂. Crystals of [**14**][CF₃SO₃]₂ were very poor but unambiguously revealed the molecular connectivity with an S–S bond between dithiolene ligands consistent with a ligand-based oxidation (Scheme 4.8).



Scheme 4.8. Oxidation of the benzenedithiolate ligand to form a disulfide.

The structure of [**14**][CF₃SO₃]₂ can be considered to derive from the reduction of Cu(II) to Cu(I) and the oxidation of the dithiolate ligand which is accompanied by dimerization with S–S bond formation (Scheme 4.8). Similarly, reaction of **11** with Co(BF₄)₂·6H₂O over an extended period similarly generated a few crystals of [**14**][BF₄]₂·6H₂O (Figure 4.9). In both cases, NMR studies indicated the supernatant solution comprised **11** as the dominant species in solution and salts of **14**²⁺ were isolated only as a minor product.

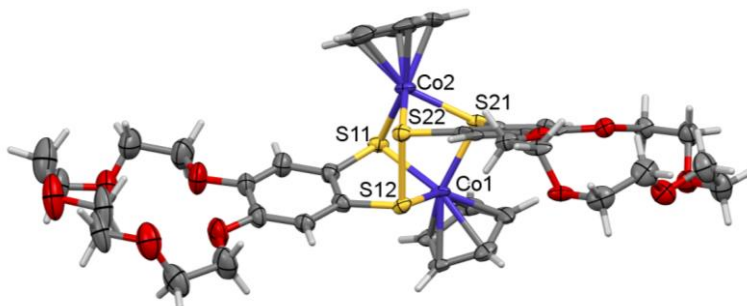


Figure 4.9. Structure of the $[14]^{2+}$ cation in the structure of $[14][BF_4]_2$. Thermal ellipsoids for non-H atoms presented at 50% probability. Counterions and solvent molecules omitted for clarity.

Here the crystal data were somewhat better (Table 4.4), though it should be noted that neither reaction was particularly reproducible, and the crystal quality was universally poor. The source of oxidant in this second reaction is less clear since Co(II) is unlikely to be reduced to Co(I) in alcoholic solution. A more likely scenario is aerial oxidation of Co(II) to Co(III),³² which then acts as an oxidizing agent for **11**, regenerating Co(II). The interplay between dithiolate and disulfide on Co(II/III) centers has been investigated experimentally and computationally.³³ The oxidation of transition metal dithiolate complexes to form disulfide complexes is not without precedent. In 2001, Liaw and co-workers reported that the manganese complex, $Mn(CO)_3(bdt)$, underwent dimerization *via* oxidation with either HBF_4 or $[Cp_2Fe][BF_4]$ to form a new S–S bond.³⁴ Another example of oxidation-induced dimerization was reported by Rosenberg *et al.* through reaction between $[M_2(CO)_{10}]$ ($M = Mn$ or Re) with triethylamine N-oxide followed by 3,4-toluenedithiol to produce $[M_2(CO)_6(tdt)_2]$.³⁵ Similarly, Leung described an iridium complex containing a 1,2-benzene dithiolate ligand that was oxidized with $Ag(OTf)$ to form a dimeric species containing a S–S bond.³⁶ In these three reported instances, the S–S bond lengths were in the range of 2.222(1)–2.317(4) Å, a little longer than that observed in $[14][BF_4]$ (2.182(3) Å), but all are comparable with 42 conventional disulfide bonds (*cf.* the S–S bond in S_8 at 2.05 Å). When the crystal structures of $(11)_2$ and $[14][BF_4]_2$ are compared, there are no significant changes in the Co–S and C–S bond lengths. For example, the Co–S bond lengths range from 2.221(3) to 2.243(2) Å in $(11)_2$ and from 2.205(3) to 2.230(2) Å in

[**14**][BF₄]₂, while the C–S bond lengths all range from 1.736(9) to 1.771(9) Å. Conversely, the S1⋯S2 distance between dithiolate ligand S atoms in (**11**)₂ is 3.164 Å, whereas the S12–S22 bond formed in [**14**][BF₄]₂ is 2.182 Å. The nonbonded S⋯S distance between C₆S₂ rings in [**14**][BF₄]₂ (3.028 Å) is comparable to the nonbonded S⋯S distance in (**11**)₂. This asymmetry in bonded and non-bonded S–S distances is manifested in the angle between the two C₆S₂ planes. The ring planes are parallel in (**11**)₂, but they intersect at an angle of 31.58° in [**14**][BF₄]₂. A change in the angle between the Cp and C₆S₂ plane shifts from 129.98° in (**11**)₂ to 118.10° and 122.15° in [**14**][BF₄]₂.

4.3 Conclusions

A simple two-step route to functionalized cyclopentadienylcobalt(III) benzene dithiolates bearing a crown ether substituent has been identified through oxidative addition of tetrathiocins to CpCo(CO)₂. This has allowed us to re-examine the coordination chemistry of these crown ether complexes. We find that although the crowns do indeed bind *s*-block metal cations, solution and solid-state measurements all point to formation of 2:1 complexes (rather than 1:1 complexes previously proposed) in which the alkali metal is sandwiched between two benzo-crown ethers. Spectroscopic studies reveal rather subtle changes in the low-energy λ_{max} (460 cm⁻¹) absorption upon *s*-block metal ion coordination, whereas electrochemical studies reveal a more marked shift in the oxidation potential (+0.32 V) associated with the increased positive charge on the complex. Preliminary complexation studies with *d*-block metals both favored oxidation processes in preference to coordination in the crown ether pocket, with no evidence for coordination of Co(II/III) or Cu(I/II) ions in the crown pocket. Crystallographic studies reveal that oxidation is associated with S–S bond formation.

4.4 Experimental

4.4.1. General Procedures

Standard solvents were dried and deoxygenated using an Innovative Technology Solvent Purification System and manipulation of air-sensitive materials carried out under an atmosphere of dry nitrogen using standard Schlenk techniques and a dry-nitrogen glove box (MBraun Labmaster). Microwave syntheses were carried out in sealed vessels using a Biotage Initiator 1 microwave. Ligand **1g** was prepared according to the literature

method.²³ **Caution!** The microwave reactions used to prepare ligands **11** and **12** are carried out in a sealed glass vial and evolve CO. Using a 2–5 mL microwave vial and 5 mL of solvent the final pressure was typically between 5 and 10 bar based on a 0.5 mmol reaction. The vial was cooled back to room temperature before releasing the pressure.

4.4.2. Physical Measurements

All NMR spectra were recorded on a Bruker DPX300 UltraShield 300 MHz spectrometer with a Broadband AX Probe using CDCl₃ (¹H δ = 7.26 ppm, s; ¹³C δ = 77.16 ppm) as an internal reference point relative to Me₄Si (δ = 0 ppm). IR spectra were obtained using a Bruker Alpha FT-IR spectrometer equipped with a Platinum single reflection diamond ATR module. Elemental compositions were determined on a Perkin Elmer 2400 Series II Elemental Analyzer. Mass spectra were recorded on a Waters XEVO G2-XS in either ESI(+) or ASAP(+) mode, a Bruker HCTplus Ion-Trap in ESI(+) mode or Thermo DFS in EI+ mode. Cyclic voltammetry measurements were made on 0.01 M solutions in CH₂Cl₂ using 0.1 M [¹⁰Bu₄N][PF₆] as the supporting electrolyte. All experiments were conducted on a CHI 760E electrochemical workstation (CHI Instruments, Texas, US) using a conventional three-electrode figuration. A silver/silver chloride (Ag/AgCl, 3 M KCl) reference electrode was used, and a Pt wire served as the counter electrode. A Pt electrode with a diameter of 1.6 mm was deployed as the working electrode. The three electrodes were positioned in the regular triangular arrangement with electrode-electrode distances of about 1.0 cm.

4.4.3. X-Ray Crystallography

Crystals were mounted on a cryoloop with paratone oil and examined on either a Bruker D8 Venture diffractometer equipped with Photon 100 CCD area detector or a Bruker APEX-II diffractometer with CCD detector using graphite-monochromated Mo-K α radiation ($\lambda = 0.71073 \text{ \AA}$) or Cu-K α radiation ($\lambda = 1.54178 \text{ \AA}$). An Oxford Cryostream cooler was used to maintain cryogenic temperatures for these studies. Data were collected using the APEX-III software,³⁷ integrated using SAINT³⁸ and corrected for absorption using a multi-scan approach (SADABS).³⁹ Final cell constants were determined from full least squares refinement of all observed reflections. All structures were solved using intrinsic phasing (SHELXT)⁴⁰ and refined with full least squares refinement on F^2 using

either SHELXL⁴¹ or Olex2 software.⁴² In structure **13d** there were regions of poorly resolved electron density located in voids indicative of residual lattice solvent. This was treated with the SQUEEZE function within PLATON.⁴³ All hydrogen atoms were added at calculated positions and refined isotropically with a riding model.

4.4.4. Computational Methods

DFT calculations on **11** were undertaken using the LACV3P**++ basis set⁴⁴ and (i) the B3LYP functional⁴⁵ with Grimme's D3 dispersion correction⁴⁶ and (ii) the M06 functional⁴⁷ within Jaguar.⁴⁸ LACV3P**++ uses a Los Alamos effective core potential for Co with triple zeta potential for valence and outermost core electrons and triple zeta 6-311G basis set for all other atoms. Diffuse and polarization functions are included for all atoms including H. A comparison of the crystallographic and computed coordination geometries are presented in Table D.1. Using the B3LYP-D3 functional, little variation was observed in the most intense low energy calculated λ_{\max} values when comparing LACV3P, LACV3P**, LACV3P++ and LACV3P**++ functionals and using a CH₂Cl₂ solvent model (PCM/COSMO) (Table D.2). Conversely the M06 functional proved more responsive to both the basis set and solvent model. The M06/LACV3P**++ functional and basis set with a polarizable continuum model (COSMO) gave good agreement with experimental (Table B.2, Figure B.11). The discrepancy between experimental and computed (M06/LACV3P**++/COSMO) values was 525 cm⁻¹. The contributions to this lowest energy transition are tabulated in Table D.3. Selected frontier orbitals (HOMO-3 to LUMO+1) are shown in Figure D.12. The two largest coefficients to the low energy transition correspond to the HOMO→LUMO and HOMO-1→LUMO transitions associated with movement of electron density from the benzene π system to the CpCoS₂ fragment.

4.4.5. Synthesis of CpCo(b-15-c-5-dt) (**11**)

Tetrathiocin **1g** (330 mg, 0.5 mmol) was placed in a microwave vial to which toluene (5 mL) was added. The vial was sealed and CpCo(CO)₂ (0.13 mL, 1 mmol) was added via syringe. The mixture was heated in the microwave at 150 °C for 30 min to afford a deep blue solution. After slowly releasing the overpressure from the vial, the solvent was evaporated by rotary evaporation, and the resultant blue solid was dissolved in CHCl₃ and

filtered. The filtrate was dried *in vacuo* to afford a dark blue solid. This was dissolved in a minimal amount of CH₂Cl₂, precipitated by the addition of excess hexanes, filtered and dried in air (320 mg, 71%).

¹H NMR (300 MHz, ppm, CDCl₃): δ_H = 7.48 (2H, s, benzo C–H), 5.39 (5H, s, Cp C–H), 4.08 (4H, 4.08–4.07, d, crown C–H, *J* = 4.2 Hz), 3.92 (4H, 3.93– 3.91, d, crown C–H, *J* = 4.2 Hz), 3.75 (8H, s, crown C–H).

¹³C NMR (75 MHz, ppm, CDCl₃): δ_C = 156.06 (s, aryl O–C), 146.93 (s, aryl S–C), 113.16 (s, benzo–C), 79.33 (s, Cp–C), 71.34 (s, crown– C), 70.46 (s, crown–C), 69.44 (s, crown–C), 68.81 (s, crown–C).

HRMS (ASAP(+)) *m/z*: [M + H]⁺ calc. for C₁₉H₂₄O₅S₂Co⁺ 455.0397. Found 455.0396.

Elemental Analysis calc. for C₁₉H₂₃O₅S₂Co·¼ C₆H₁₂: C 51.73; H 5.61. Found C 52.12; H 5.47.

UV–Vis (1:1 CH₂Cl₂/MeCN): λ_{max} (nm), ε (mol L^{–1} cm^{–1}): 634 (5100).

IR ν_{max} (cm^{–1}): 2924(w), 2864(w), 1590(w), 1516(m), 1485(m), 1475(m), 1446(s), 1411(w), 1357(m), 1334(w), 1246(vs), 1199(s), 1128(s), 1089(m), 1077(s), 1050(s), 1033(s), 999(m), 987(m), 928(m), 882(m), 847(m), 833(s), 825(s), 805(w), 692(w), 557(w), 530(w), 484(w), 425(w), 411(w), 406(w).

4.4.6. Synthesis of CpCo(b-18-c-6-dt) (12)

Ligand **1h** (43 mg, 0.05 mmol) was placed in a microwave vial to which toluene (5 mL) was added. The vial was sealed, and CpCo(CO)₂ (0.02 mL, 0.1 mmol) was added via syringe. The mixture was heated in the microwave at 150 °C for 30 min to afford a deep blue solution. After slowly releasing the overpressure in the vial, the solvent was evaporated by rotary evaporation, and the resultant blue solid was dissolved in CHCl₃ and filtered. The filtrate was evaporated to afford a dark blue solid. This was redissolved in a minimal quantity of CH₂Cl₂ and precipitated by the addition of excess hexanes, filtered, and dried in air (42 mg, 75%).

¹H NMR (300 MHz, ppm, CDCl₃): δ_H = 7.48 (2H, s, benzo C–H), 5.38 (5H, s, Cp C–H), 4.21 (4H, m, crown C–H), 4.11 (4H, m, crown C–H), 3.92 (4H, m, crown C–H), 3.77–3.67 (8H, m, crown C–H).

HRMS (ASAP(+)) m/z : $[M + H]^+$ calc. for $C_{21}H_{28}O_6S_2Co^+$ 499.0659. Found 499.0656.

Elemental Analysis calc. for $C_{21}H_{27}O_6S_2Co \cdot 2\frac{1}{4}CH_2Cl_2$: C 40.50; H 4.60. Found C 40.31; H 4.77.

UV-vis (CH_2Cl_2): λ_{max} (nm), ϵ ($mol\ L^{-1}\ cm^{-1}$): 649 (6400)

IR ν_{max} (cm^{-1}): 3097(w), 2917(w), 2856(w), 1582(w), 1518(m), 1483(m), 1470(m), 1446(s), 1415(w), 1352(m), 1338(w), 1241(vs), 1197(s), 1104(s), 1048(s), 943(m), 848(s), 795(s), 746(m), 632(w), 591(w), 583(w), 550(w) 484(w), 464(w), 419(w), 402(w).

4.4.7. Synthesis of $[NaCpCo(b-15-c-5-dt)][BPh_4]$ (**13a**)

Complex **11** (9.9 mg, 0.0218 mmol) and $Na[BPh_4]$ (5.0 mg, 0.0146 mmol) were combined in a small 20 mL vial with a 1:1 mixture of CH_2Cl_2 and MeOH (6 mL total) and left to stir for 1 h under ambient conditions. Layering hexanes onto the solution afforded blue crystals suitable for X-ray diffraction (9.2 mg, 50% yield).

1H NMR (300 MHz, ppm, $CDCl_3$): $\delta_H = 7.48$ (4H, 7.49–7.47, m, *p*-C–H BPh_4), 7.38 (8H, 7.41–7.34, m, *o*-C–H BPh_4), 6.99 (8H, 7.04–6.95, m, *m*-C–H BPh_4), 6.85 (4H, s, benzo C–H), 5.44 (10H, s, Cp C–H), 3.95 (8H, s, crown C–H), 3.76 (8H, s, crown C–H), 3.61 (16H, 3.62–3.59, m, crown C–H).

HRMS (ESI(+)) m/z : $[M]^+$ calc. for $C_{38}H_{46}O_{10}S_4Co_2Na^+$ 931.0536. Found 931.0548.

Elemental Analysis calc. for $C_{62}H_{66}O_{10}S_4BCo_2Na \cdot \frac{1}{2}CH_2Cl_2$: C 58.03; H 5.22. Found C 58.04; H 5.24.

IR ν_{max} (cm^{-1}): 3099(w), 3051(w), 2863(w), 1594(w), 1579(w), 1525(w), 1476(m), 1447(m), 1423(w), 1411(m), 1360(m), 1336(w), 1299(w), 1246(vs), 1199(s), 1150(w), 1124(m), 1096(s), 1079(s), 1046(vs), 1000(m), 929(s), 884(m), 859(s), 831(s), 750(m), 735(vs), 706(vs), 610(s), 570(m), 516(m), 470(m), 422(m), 411(m).

4.4.8. Synthesis of $[KCpCo(b-15-c-5-dt)][BPh_4]$ (**13b**)

Complex **11** (9.9 mg, 0.0218 mmol) was dissolved in CH_2Cl_2 (2 mL) and was layered with an acetone (2 mL) solution of $K[BPh_4]$ (3.9 mg, 0.0109 mmol). After 1 day, hexanes were layered onto the solution, affording blue crystals suitable for X-ray diffraction (8.9 mg, 64% yield).

¹H NMR (300 MHz, ppm, CDCl₃): δ_H = 7.43 (4H, 7.47–7.38, m, *p*-C–H BPh₄), 7.27 (8H, 7.29–7.24, m, *o*-C–H BPh₄), 7.03 (8H, 7.07–6.98, m, *m*-C–H BPh₄), 6.86 (4H, s, benzo C–H), 5.48 (10H, s, Cp C–H), 3.75 (16H, s, crown C–H), 3.61 (8H, m, crown C–H), 3.54 (8H, m, crown C–H).

HRMS (ESI(+)) *m/z*: [M]⁺ calc. for C₃₈H₄₆O₁₀S₄Co₂K⁺ 947.0275. Found 947.0275.

Elemental Analysis calc. for C₆₂H₆₆O₁₀S₄BCo₂K·½CH₂Cl₂: C 57.32; H 5.20. Found C 57.86; H 5.22.

IR ν_{max} (cm⁻¹): 3097(w), 3052(m), 2934(w), 2893(m), 2859(m), 1706(w), 1594(w), 1579(w), 1523(w), 1475(m), 1447(s), 1412(m), 1360(m), 1335(m), 1300(w), 1244(vs), 1198(s), 1149(w), 1124(s), 1105(m), 1093(s), 1078(s), 1043(s), 1002(m), 932(s), 883 (m), 856(s), 833(s), 750(m), 736(vs), 708(vs), 611(m), 568(m), 526(m), 512(m), 471(m), 424(m), 411(m).

4.4.9. Synthesis of [RbCpCo(b-15-c-5-dt)][BPh₄] (13c)

Complex **11** (9.9 mg, 0.0218 mmol) was dissolved in CH₂Cl₂ (2 mL) and was layered with an acetone (2 mL) solution of Rb[BPh₄] (4.4 mg, 0.0109 mmol). After several days, the solution was layered with hexanes, affording blue crystals suitable for X-ray diffraction (12 mg, 84% yield).

¹H NMR (300 MHz, ppm, CDCl₃): δ_H = 7.46 (4H, 7.49–7.40, m, *p*-C–H BPh₄), 7.22 (8H, 7.25–7.20, m, *o*-C–H BPh₄), 7.02 (8H, 7.04–6.99, m, *m*-C–H BPh₄), 6.84 (4H, s, benzo C–H), 5.38 (10H, s, Cp C–H), 4.04 (8H, m, crown C–H), 3.89 (8H, m, crown C–H), 3.73 (16H, s, crown C–H).

HRMS (ESI(+)) *m/z*: [M]⁺ calc. for C₃₈H₄₆O₁₀S₄Co₂Rb⁺ 992.9756. Found 992.9754.

Elemental Analysis calc. for C₆₂H₆₆O₁₀S₄BCo₂Rb·½hexanes: C 57.55; H 5.42. Found C 57.82; H 5.27.

IR ν_{max} (cm⁻¹): 3094(w), 3053 (w), 2859(w), 1706(w), 1592(w), 1579(w), 1521(w), 1475(m), 1447(m), 1413(w), 1359(m), 1334(w), 1299(w), 1244(vs), 1197(m), 1149(w), 1124(m), 1105(m), 1091(m), 1075(m), 1041(s), 1002(m), 930(s), 882(m), 854(m), 832(s), 749(m), 735(vs), 707(s), 602(m), 565(m), 524(m), 510(m), 470(m), 439(w), 423(m), 408(m).

4.4.10. Synthesis of [CsCpCo(b-15-c-5-dt)][BPh₄] (13d)

Complex **11** (9.9 mg, 0.0218 mmol) and Cs[BPh₄] (5.0 mg, 0.0109 mmol) were combined in a small 20 mL vial with a 1:1 mixture of CH₂Cl₂ and MeOH (4 mL total) and left to stir for 1 h under ambient conditions. Layering hexanes onto the solution afforded blue crystals suitable for X-ray diffraction (2.6 mg, 18% yield).

¹H NMR (300 MHz, ppm, CDCl₃): δ_H = 7.49 (8H, 7.51–7.47, m, *o*-C–H BPh₄), 7.40 (4H, 7.43–7.38, m, *p*-C–H BPh₄), 6.99 (8H, 7.03–6.97, m, *m*-C–H BPh₄), 6.84 (4H, s, benzo C–H), 5.40 (10H, s, Cp C–H), 4.06 (16H, s, crown C–H), 3.88 (8H, m, crown C–H), 3.73 (8H, m, crown C–H).

HRMS (ESI(+)) *m/z*: [M]⁺ calc. for C₃₈H₄₆O₁₀S₄Co₂Cs⁺ 1040.9693. Found 1040.9695.

Elemental Analysis calc. for C₆₂H₆₆O₁₀S₄BCo₂Cs: C 54.71; H 4.89. Found C 54.92; H 4.64.

IR ν_{max} (cm⁻¹): 3054(w), 3028(w), 3002(w), 2981(w), 2931(w), 1577(w), 1546(w), 1478(m), 1449(m), 1426(m), 1353(w), 1345(w), 1311(vw), 1246(s), 1194 (m), 1134(m), 1114(m), 1067(m), 1049(s), 1027(m), 978(m), 918(w), 872(s), 848(m), 833(m), 822(m), 738(vs), 716(vs), 707(vs), 680(m), 626(m), 600(s), 485(m), 462(m).

4.4.11. Synthesis of [CpCo(b-15-c-5-dt)][BF₄]₂ (14)

Complex **11** (9.9 mg, 0.0218 mmol) and Co(BF₄)₂·6H₂O (7.4 mg, 0.0218 mmol) were combined in a small 20 mL vial with a 1:1 mixture of CH₂Cl₂ and MeOH (4 mL total) and stirred for 1.5 h under ambient conditions. Slow diffusion of pentane into the reaction mixture afforded a small quantity of blue crystals suitable for X-ray diffraction over a period of a couple weeks. ¹H NMR, UV-Vis, and MS studies on the supernatant solution afforded results matching those of **11**, consistent with [14][BF₄]₂ being formed as a minor product with low solubility.

4.5 References

- (1) *Dithiolene chemistry: Synthesis, properties, and applications*, ed. E. I. Stiefel, Interscience, Hoboken, New Jersey, 2003.

- (2) P. J. Chirik and K. Wieghardt, *Science*, 2010, **327**, 794–795.
- (3) R. Eisenberg and H. B. Gray, *Inorg. Chem.*, 2011, **50**, 9741–9751.
- (4) S. Sproules, T. Weyhermueller, S. DeBeer and K. Wieghardt, *Inorg. Chem.*, 2010, **49**, 5241–5261.
- (5) M. Nomura, and M. Fourmigué, *Inorg. Chem.*, 2008, **47**, 1301–1312.
- (6) S. Muratsugu, K. Sodeyama, F. Kitamura, S. Tsukada, M. Tada, S. Tsuneyuki and H. Nishihara, *Chem. Sci.*, 2011, **2**, 1960–1968.
- (7) M. Nihei, T. Nankawa, M. Kurihara and H. Nishihara, *H. Angew. Chem., Int. Ed.*, 1999, **38**, 1098–1100.
- (8) M. Murata, S. Habe, S. Araki, K. Namiki, T. Yamada, N. Nakagawa, T. Nankawa, M. Nihei, J. Mizutani, M. Kurihara and H. Nishihara, *Inorg. Chem.*, 2006, **45**, 1108–1116.
- (9) M. Nomura, T. Sasao, T. Hashimoto, T. Sugiyama and M. Kajitani, *Inorg. Chim. Acta.*, 2010, **363**, 3647–3653.
- (10) E. J. Miller, T. B. Brill, A. L. Rheingold and W. C. A. Fultz, *J. Am. Chem. Soc.*, 1983, **105**, 7580–7584.
- (11) S. Tsukada, M. Kondo, H. Sato and T. Gunji, *Polyhedron*, 2016, **117**, 265–272.
- (12) M. Nomura, E. Tsukano, C. Fujita-Takayama, T. Sugiyama and M. Kajitani, *J. Organomet. Chem.*, 2009, **694**, 3116–3124.
- (13) N. D. Lowe and C. D. Garner, *J. Chem. Soc., Dalton Trans.*, 1993, 3333–3340.
- (14) N. D. Lowe and C. D. Garner, *J. Chem. Soc., Dalton Trans.*, 1993, **14**, 2197–2207.
- (15) A. Davison, R. H. Holm, R. E. Benson and W. Mahler, *Inorg. Synth.*, 2007, 8–26.
- (16) J. Moscattini, A. J. Lough and U. Fekl, *Acta Crystallogr. E*, 2017, **73**, 957–962.
- (17) K. A. Martyanov, G. A. Abakumov, E. V. Baranov, V. V. Khrizanforova, M. N. Khrizanforov, K. V. Kholin, Y. H. Budnikova, V. A. Kuropatov and V. K. Cherkasov, *Eur. J. Inorg. Chem.*, 2020, **2020**, 4350–4357.
- (18) L. K. Watanabe, J. D. Wrixon and J. M. Rawson, *Dalton Trans.*, 2021, **50**, 13620–13633.

- (19) J. D. Wrixon, J. J. Hayward, O. Raza and J. M. Rawson, *Dalton Trans.*, 2014, **43**, 2134–2139.
- (20) J. D. Wrixon, J. J. Hayward and J. M. Rawson, *Inorg. Chem.*, 2015, **54**, 9384–9386.
- (21) J. D. Wrixon, Z. S. Ahmed, M. U. Anwar, Y. Beldjoudi, N. Hamidouche, J. J. Hayward and J. M. Rawson, *Polyhedron*, 2016, **108**, 115–121.
- (22) K.-W. Stender, N. Wolki and G. Klar, *Phosphorus, Sulfur, Silicon Relat. Elem.*, 1989, **42**, 111–115.
- (23) L. K. Watanabe, J. D. Wrixon, Z. A. Ahmed, J. J. Hayward, P. Abbasi, M. Pilkington, C. L. B. Macdonald and J. M. Rawson, *Dalton Trans.*, 2020, **49**, 9086–9093.
- (24) H. W. Baird, B. M. White, *J. Am. Chem. Soc.*, 1966, **88**, 4744–4745.
- (25) M. Nomura and M. Fourmigué, *J. Organomet. Chem.*, 2007, **692**, 2491–2499.
- (26) A. Klamt and G. Schuurmann, *J. Chem. Soc., Perkin Trans. 2*, 1993, 799–805.
- (27) C. J. Pedersen, *Angew. Chem., Int. Ed.*, 1988, **27**, 1021–1027.
- (28) T. Sakurai, K. Kobayashi, S. Tsuboyama, Y. Kohno, N. Azuma and K. Ishizu, *Acta Crystallogr.*, 1983, **C39**, 206–208.
- (29) Y. Li, *Bull. Chem. Soc. Jpn.*, 1996, **69**, 2513–2523.
- (30) C. Fiolka, R. Striebinger, T. Walter, C. Walbaum and I. Pantenburg, *Z. Anorg. Allg. Chem.*, 2009, **635**, 855–861.
- (31) C. Fiolka, I. Pantenburg and G. Meyer, *Cryst. Growth. Des.*, 2011, **11**, 5159–5165.
- (32) E. Norkus, A. Vaskelis, A. Griguševičienė, G. Rozovskis, J. Reklaitis and P. Norkus, *Transition Metal Chem.*, 2001, **26**, 465–472.
- (33) F. Jiang, M. A. Siegler, X. Sun, L. Jiang, C. Fonseca Guerra and E. Bouwman, *Inorg. Chem.*, 2018, **57**, 8796–8805.
- (34) W.-F. Liaw, C.-K. Hsieh, G.-Y. Lin and G.-H. Lee, *Inorg. Chem.*, 2001, **40**, 3468–3475.
- (35) N. Begum, M. I. Hyder, S. E. Kabir, G. M. G. Hossain, E. Nordlander, D. Rokhsana and E. Rosenberg, *Inorg. Chem.*, 2005, **44**, 9887–9894.

- (36) K.-W. Chan, Y.-K. Sau, Q.-F. Zhang, W.-Y. Wong, I. D. Williams and W.-H. Leung, *Eur. J. Inorg. Chem.*, 2008, **2008**, 4353–4359.
- (37) *APEX III*, Bruker AXS, Madison, WI, USA.
- (38) *SAINT*, Bruker AXS, Madison, WI, USA.
- (39) *SADABS*, Bruker AXS, Madison, WI, USA.
- (40) G. M. Sheldrick., *Acta Cryst.*, 2015, **A71**, 3–8
- (41) G. M. Sheldrick, *Acta Cryst.*, 2015, **C71**, 3–8.
- (42) O. V. Dolomanov, L. J. Bourhis, R. Gildea, J. A. K. Howard and H. Puschmann, *J. Appl. Crystallogr.* 2009, **42**, 339–341.
- (43) A. L. Spek, *Acta Crystallogr. Sect. C: Struct. Chem.*, 2015, **71**, 9–18.
- (44) The LACV3P basis set comprises a triple-zeta version of the LACVP basis set (P. J. Hay and W. R. Wadt, *J. Chem. Phys.*, 1985, **82**, 299–310) which has been developed and tested by Schroedinger Inc.
- (45) (a) A. D. Becke, *J. Chem. Phys.*, 1998, **98**, 5648–5652; (b) C. Lee.; W. Yang and R. G. Parr, *Phys. Rev. B*, 1988, **37**, 785–789.
- (46) S. Grimme, J. Antony, S. Ehrlich, and H. Krieg, *J. Chem. Phys.*, 2010, **132**, 154104-1–154104-19.
- (47) Y. Wang, P. Verma, X. Jin, D. G. Truhlar and X. He, *Proc.Nat.Acad.Sci.*, 2018, **115**, 10257–10262
- (48) A. D. Bochevarov, E. Harder, T. F. Hughes, J. R. Greenwood, D. A. Braden, D. M. Philipp, D. Rinaldo, M. D. Halls, J. Zhang, and R. A. Friesner, *Int. J. Quantum Chem.*, 2013, **113**, 2110–2142.

5. INVESTIGATION OF THE ELECTRONIC PROPERTIES OF NICKEL(DIIMINE)(DITHIOLATE) COMPLEXES

5.1 Introduction

The interaction of light with matter is central to many fields of materials chemistry including, but certainly not limited to, non-linear optics, (solar) light-harvesting, photo-conducting materials and photo-switchable devices. At low light intensities the interaction of matter with light typically follows a linear relationship between the physical response and the light intensity or number of incoming photons. Such a linear relationship holds for the magnitude of the induced dipole (\mathbf{p}) and the light intensity (magnitude of the electric field, \mathbf{E} ; Section 5.1.1). However, in the presence of more intense light sources (such as a laser), the response may become non-linear. This Chapter explores the use of the oxidative addition chemistry of tetrathiocins to prepare nickel(II) dithiolate/bipyridine complexes and examines the second order term known as the molecular hyperpolarizability (β) which relates how the induced dipole depends upon the square of the electric field. Such higher order behaviour is important for second order non-linear optical response, or frequency doubling in which two photons are absorbed and a new photon of twice the energy is emitted. This section provides a basic introduction to non-linear optics (NLO) and provides an overview of previous work on group 10 complexes as NLO materials.

5.1.1. Non-linear optics

When a molecule is subject to an electric field, \mathbf{E} , then an induced dipole, \mathbf{p} , is generated due to the polarization of the electron cloud by the electric field. In the simplest form:

$$\mathbf{p} = \alpha\mathbf{E} \quad \text{Eq. 5.1}$$

where α is the molecular polarizability. More generally, the polarizability can be written as a power series in terms of the electric field, \mathbf{E} :

$$\mathbf{p} = \alpha\mathbf{E} + \beta\mathbf{E}^2 + \gamma\mathbf{E}^3 + \dots \quad \text{Eq. 5.2}$$

This induced polarization of the molecule by the presence of an electric field is in addition to any permanent polarization of the molecule arising from the permanent dipole. The total dipole, μ , can be written in terms of the permanent dipole in the absence of an electric field (μ^0) and induced dipole terms which can be written as a power series in \mathbf{E} :

$$\mu = \mu^0 + \alpha\mathbf{E} + \frac{1}{2}\beta\mathbf{E}^2 + \frac{1}{6}\gamma\mathbf{E}^3 + \dots \quad \text{Eq. 5.3}$$

The term β is known as the molecular hyperpolarizability. For normal, low intensity light the electric field \mathbf{E} is small and these second and third order terms (i.e. those that do not depend linearly on \mathbf{E}) can be neglected and the molecular dipole can be written in terms of the permanent dipole and the induced dipole ($\mu = \mu^0 + \alpha\mathbf{E}$). However, for high intensity light, such as a laser, then the higher order terms become significant. In second order non-linear optics (NLO), we consider the effects of the second order term, β . In the two level model (which assumes only the ground state and first excited state contribute to β):¹

$$\beta = \frac{3\hbar^2 e^2 f \Delta\mu}{2m_e \Delta E^3} \quad \text{Eq 5.4}$$

where \hbar is the reduced Planck's constant, e and m_e are the electron charge and electron mass, f is the oscillator strength ('allowedness') of the transition, $\Delta\mu$ is the difference in molecular dipole between the ground and (first) excited state and ΔE is the energy gap between the ground and excited state. Since β depends on $1/\Delta E^3$, systems with small HOMO-LUMO gaps should give rise to large values of the molecular hyperpolarizability. The β parameter can be computed using DFT calculations and measured experimentally using the electric field induced second harmonic generation (EFISH) technique.

NLO materials are important in device applications in which two photons of incident radiation with frequency ω are absorbed by the system and a single photon of energy 2ω is emitted, i.e. second harmonic generation is a frequency doubling process. Multiple other factors are also relevant to the development of second order NLO materials. These include the requirement of the material to adopt a non-centrosymmetric environment, phase matching the angle of the beam with respect to the crystal and the heat transfer properties of the material since irradiation with a high intensity laser tends to lead to localized heating.²

5.1.2. Group 10 metal complexes as non-linear optic materials

Group 10 metal complexes featuring dithiolate and bipyridine chelating ligands comprise a sub-set of a larger family of diimine-dithiolate complexes first described by Miller and Dance.³ These ‘push-pull’ complexes have been examined for a variety of applications including second order non-linear optic materials,^{4,5,6} light-harvesting devices,⁷ luminescent materials,^{8,9} as ambipolar cores for discotic liquid crystals^{10,11} and as donors in the formation of charge-transfer salts.¹² Studies have explored how they can be integrated onto silicon surfaces for device applications¹³ and have more recently been studied as light absorbers for the photo-reduction of $H^+_{(aq)}$ to H_2 .¹⁴ The optical properties of these materials are central to many of these applications and are typically reflected in an intense absorption ($\epsilon \sim 10^4 \text{ M}^{-1} \text{ cm}^{-1}$) in the visible-NIR region of the spectrum which has been assigned to a mixed-metal/ligand-to-ligand charge-transfer transition (MMLL’CT).¹⁵ This typically comprises a HOMO-LUMO transition involving a metal-dithiolate based HOMO and a diimine-based LUMO (Figure 5.1).

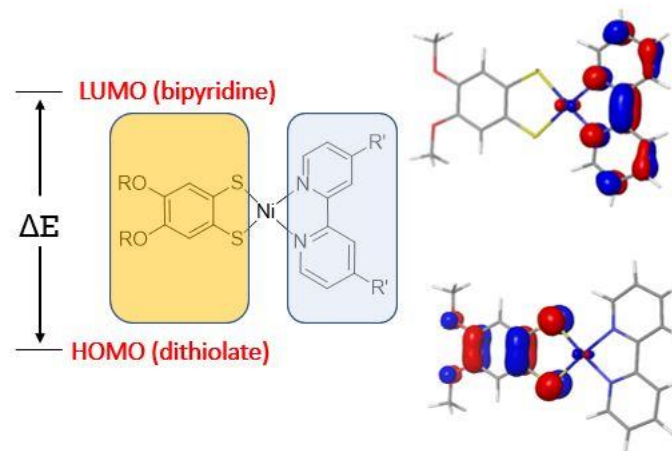


Figure 5.1. Schematic of the frontier orbitals (DFT, B3LYP–D3/LACV3P*) of the Ni(bpy)(dmobdt) complex highlighting the dithiolate-based HOMO (orange) and bpy-based LUMO (blue).

In this context, studies by Robertson and co-workers on derivatives of Ni(bpy)(dt) implemented 4,4'-ester functionalized bpy [bpy = 2,2'-bipyridine] derivatives to systematically lower the LUMO energy and increase λ_{max} .⁴ These complexes exhibited

some of the largest molecular hyperpolarizabilities (β) observed within the family of square-planar push-pull complexes. An alternative strategy to shift the NIR absorption to lower energy is to lower the HOMO-LUMO gap by raising the HOMO energy. The latter is sensitive to the nature of the dithiolate and adding donor groups to the dithiolate should raise the HOMO energy.

Nickel bipyridine-dithiolate complexes are typically prepared from Ni(bpy)Cl₂ and alkali metal salts of the dithiolate, M₂(dt) [M = Li, Na, K],^{4,5,8} although displacement of dithiolate in [M(dt)₂]²⁻ by a range of monodentate and bidentate donors including N,N'-chelate ligands has recently been described.¹⁶ Previously, fundamental studies of the microwave-assisted oxidative addition of tetrathiocins to zero-valent group 10 complexes has been undertaken in the presence of chelating phosphines as a route to dithiolate complexes.^{17,18} In this context reaction of tetrathiocins with Ni(COD)₂ in the presence of the chelating phosphine dppe afforded Ni(dmobdt)(dppe).¹⁵ Similarly, oxidative addition of the dithiete (F₃C)₂C₂S₂ to Ni(CO)₂(PPh₃)₂ has previously been described.¹⁹ Such oxidative addition reactions proved sensitive to the stereoelectronic effects of the auxiliary phosphine, variously affording mono-, di- or hexa-nuclear Pd complexes.²⁰ Work in Chapter 3 and 4 extended this methodology to the formation of cobalt (III) complexes with auxiliary cyclopentadienyl ligands. In the current contribution the oxidative addition of tetrathiocins to Ni(COD)₂ in the presence of chelating bipyridine ligands is described, affording a family (Figure 5.2) of bipyridine-dithiolate complexes of Ni(II) in good yield in a one-pot reaction. This has permitted us to undertake systematic tuning of both the dithiolate donor and the bipyridine acceptor.

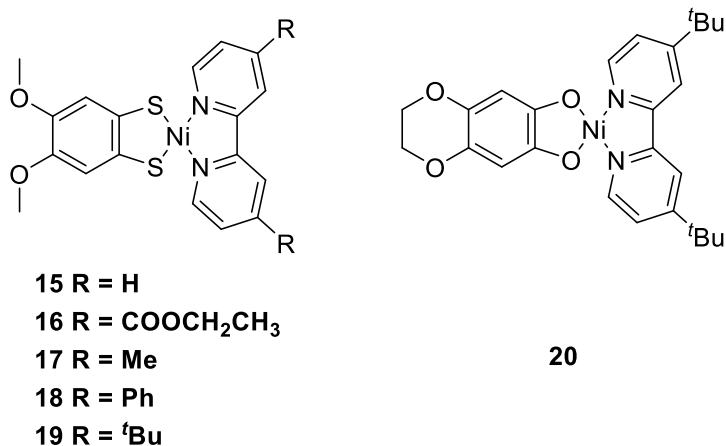


Figure 5.2. Nickel (II) complexes investigated for their NLO and near-IR potential.

5.2 Results and Discussion

5.2.1. Synthesis

Ni(II) bipyridine dithiolate complexes were prepared by adapting the synthesis of Ni(dmobdt)dppe),¹⁵ replacing the dppe ligand with a functionalized bpy ligand: Oxidative addition of the tetrathiocin to Ni(COD)₂ in toluene under microwave irradiation (150 °C, 60 min); in the presence of a series of chelating bpy derivatives afforded the derivatives **15–20** which were isolated as powders by filtration in 59–86% recovered yield (Table 5.1). Initial work was conducted by a visiting research student, Nadia Fendi, and crystals of **16–20** were grown by Nabila Hamidouche through layering a saturated CHCl₃ solution with toluene and hexanes or diethyl ether.

Table 5.1. Yields of dithiolate complexes derived from the oxidative addition of tetrathiocins to Ni(COD)₂ in the presence of auxiliary bipyridine ligands.

Complex	Dithiolate	bipyridine	Yield
15	dmobdt	bpy	75%
16	dmobdt	^{Et} COObpy	82%
17	dmobdt	^{Me} bpy	66%
18	dmobdt	^{Ph} bpy	66%
19	dmobdt	^{tBu} bpy	86%
20	doxbdt	^{tBu} bpy	59%

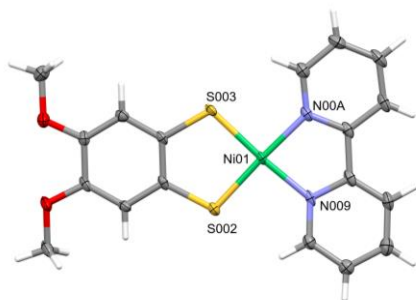
All complexes were characterized by ^1H NMR in CD_2Cl_2 as well as mass spectrometry, UV-Vis spectroscopy and X-ray diffraction (*vide infra*). These compounds were also characterized by elemental analysis. Where compounds crystallized as solvates, some residual solvent was typically required to fit the analytical data, despite extended drying *in vacuo*.

5.2.2. Structural Studies

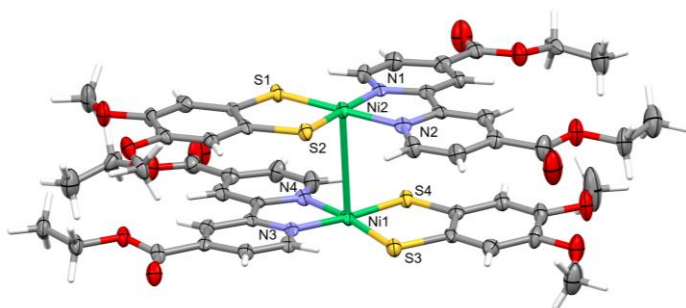
The structures of **15–20** were all determined by X-ray diffraction, with a summary of the crystallographic parameters (Table 5.2) and the molecular structures (Figure 5.3).

Table 5.2. Unit cell parameters for **15–20**.

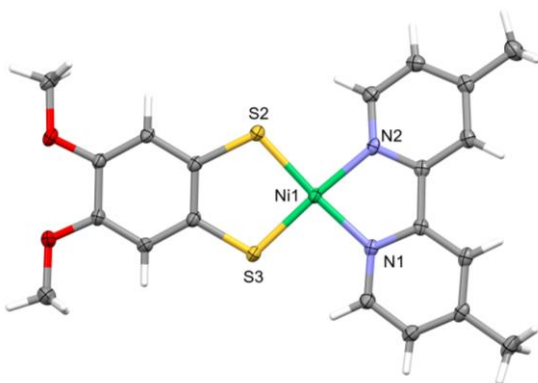
	15·CHCl₃	16·C₄H₁₀O	17	18·CHCl₃	19	20
Crystal System	Monoclinic	Triclinic	Triclinic	Monoclinic	Monoclinic	Orthorhombic
Space Group	P2 ₁ /c	P $\bar{1}$	P $\bar{1}$	P2 ₁ /n	P2 ₁ /n	P2 ₁ 2 ₁ 2 ₁
a/Å	13.248(10)	13.3519(10)	8.9511(7)	7.2720(15)	10.9877(9)	7.1757(9)
b/Å	11.843(9)	13.8437(11)	9.9971(9)	14.248(3)	16.7624(12)	19.360(2)
c/Å	14.474(10)	15.4806(12)	15.2191(13)	33.770(8)	13.9965(11)	42.861(5)
a°	90	77.575(4)	107.439(3)	90	90	90
b°	109.54(4)	88.63(5)	90.591(3)	91.95(3)	92.343(3)	90
g°	90	62.334(5)	115.402(3)	90	90	90
V/Å³	2140(3)	2465.4(4)	1158.34(18)	3496.93	2575.7(3)	5954.4(13)
D_c/g cm⁻³	1.659	1.507	1.613	1.360	1.360	1.337



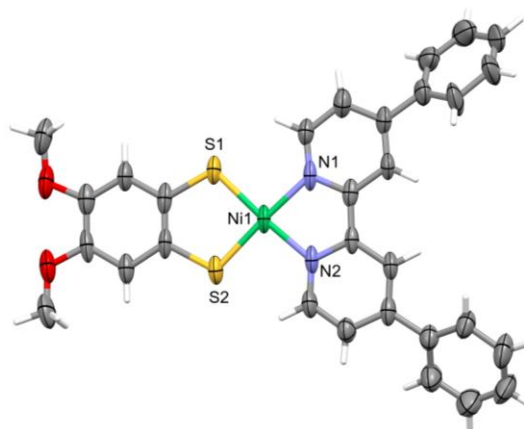
15



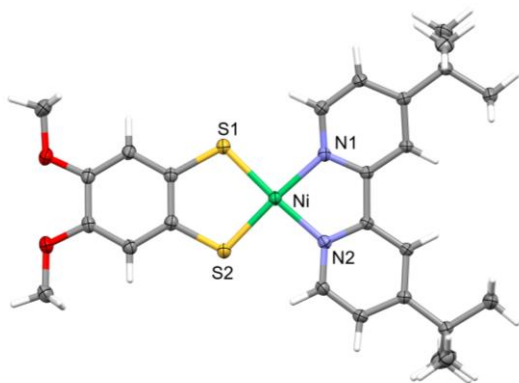
16



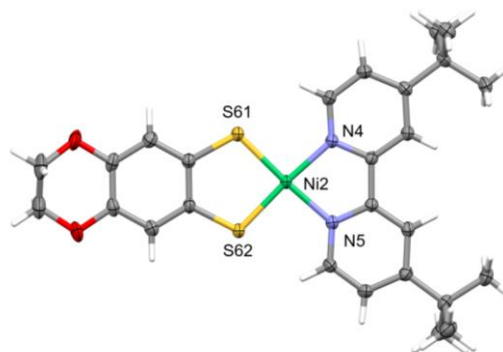
17



18



19



20

Figure 5.3. Crystal structures of **15–20** determined by X-ray diffraction. Thermal ellipsoids for non-H atoms plotted at the 50% probability level. Solvent molecules and minor disorder in the structure of **16** omitted for clarity. For **20** only one of the two molecules in the asymmetric unit is shown.

All six structures reveal square-planar coordination at the Ni(II) center with the maximum deviation from the NiN₂S₂ plane found in **17** (0.109 Å). The Ni-N and Ni-S bond lengths are tabulated in Table 5.3. A search of the CSD (2021, Nov.) revealed that there are 17 structures with Ni(II)(diimine)(dithiolate) structures with five of them bearing benzodithiolate ligands. These CSD structures reveal Ni-S bond lengths in the range 2.1339(7)–2.151(1) Å while the corresponding Ni-N bond lengths fall between 1.926(2)–1.946(5) Å.^{4,11,21,22} In this context, the coordination geometries observed for complexes **15–20** are unexceptional.

Table 5.3. Summary of bond lengths and measured distances in crystal structures of **15–20**.

	Ni–S1 (Å)	Ni–S2 (Å)	Ni–N1 (Å)	Ni–N2 (Å)	Maximum deviation from NiN ₂ S ₂ plane (Å)
15	2.150(2)	2.137(2)	1.935(3)	1.942(3)	N2 0.039
16	2.157(1)	2.146(2)	1.927(5)	1.935(4)	N1 0.028
	2.157(2)	2.138(1)	1.932(4)	1.938(5)	N3 0.091
17	2.1538(7)	2.1367(6)	1.945(2)	1.931(2)	N1 0.109
18	2.148(2)	2.143(2)	1.931(6)	1.933(6)	N1 0.004
19	2.1459(6)	2.1418(5)	1.935(1)	1.936(1)	N2 0.046
20	2.141(1)	2.139(1)	1.930(2)	1.934(2)	N2 0.026
	2.142(1)	2.131(1)	1.930(2)	1.937(2)	N3/N4 0.008

Complex **16** crystallizes with two molecules in the asymmetric unit and forms a *trans*-dimer with a weak Ni–Ni interaction of 3.385(2) Å and longer S...S contacts at 4.502–5.061 Å (Figure 5.3). This dimeric motif structure appears to only be supported in the solid state, as mass spectrometry, NMR and UV-Vis data are all consistent with a monomer in solution. All other crystals bearing the dmobdt²⁻ ligand are monomeric with

one molecule in the asymmetric unit. Complex **20** has two molecules in the asymmetric unit and crystallizes in the non-centrosymmetric space group $P2_12_12_1$.

5.2.3. UV-Vis Studies

The UV-Vis spectra were investigated to probe the HOMO-LUMO energy gap and examine how it is affected by (i) the solvent, (ii) the substituents on the 4,4' position of the bipyridine and (iii) the nature of the dithiolate ligand. Literature UV-Vis data on Ni(II) dithiolate bipyridine complexes have been recorded in a variety of solvents and found to vary significantly as a function of solvent (Table 5.4). In the current study, all complexes were measured at six concentrations across the range of 1.0×10^{-5} M to 1.0×10^{-4} M and ϵ values for each complex computed through an absorbance vs. concentration plot for each transition as well for one derivative, **15** in different solvents. This also confirmed that all transitions follow Beer-Lambert law with R^2 values in the range 0.9733–0.9926, consistent with the absence of any equilibrium process (dimerization/oligomerization/aggregation) in solution.

Table 5.4. Previously observed solvent effects on the absorption maxima in the visible region (400–700 nm) for nickel bipyridine dithiolate complexes.

Dithiolate	Bipyridine	λ_{\max} (nm)	Solvent	Ref
mnt	COOR_1bpy	520	DMF	23
		583	CHCl_3	
		559	CH_2Cl_2	
tfd	COOR_1bpy	548	DMF	24
		602	CHCl_3	
		581	CH_2Cl_2	
bdt	COOMe_1bpy	610	DMF	4
		670	CHCl_3	
		630	CH_2Cl_2	
		590	MeCN	
bdt	bpy	557	CHCl_3	22
		517	MeOH	
		520	MeCN	

Solvent effects: Compound **15** was used as a representative compound in this series to undertake to investigate the effect of solvent on λ_{\max} . Optical studies on solutions of **15** immediately reveal transitions in the visible region are sensitive to the nature of the solvent

(Figure 5.4). Spectroscopically, the corresponding λ_{max} for the transition in the visible region shifts by 118 nm as a function of solvent. Figure 5.5 reveals that the colour of complex **15** in solution is strongly solvent dependent.



Figure 5.4. Solutions of **15** in different solvents.

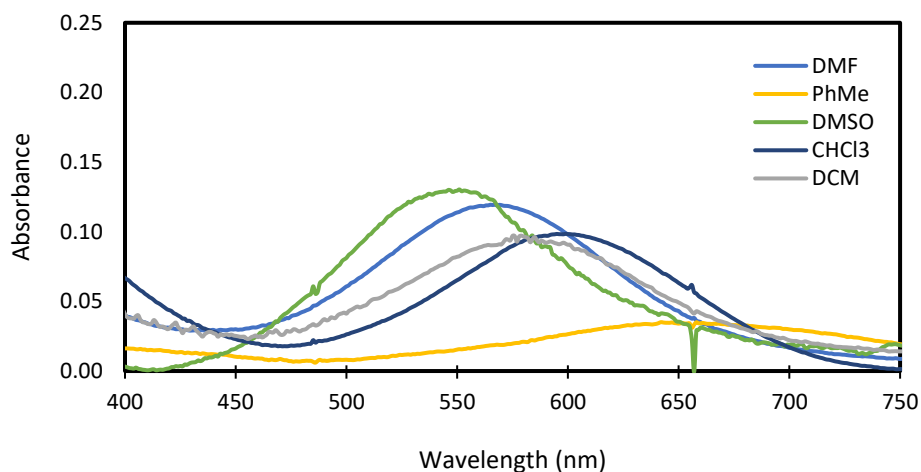


Figure 5.5. UV-Vis of **15** in different solvents recorded at a concentration of 2.0×10^{-5} M.

Previous work on related platinum dithiolate bipyridine complexes reported by Cummings *et al.* examined a range of solvent scales, but ultimately led them to develop their own empirical solvent scale covering a range of 13 different solvents.²⁵ Using their scale, an excellent linear correlation was observed between λ_{max} and their empirical solvent polarity index ($R^2 = 0.99$). Based on these data the corresponding solvent polarity index for methanol (which was not reported in their study but examined here) is 0.607. The negative slope of the plot of λ_{max} vs solvent polarity index indicates a negative solvatochromic

effect, i.e. a decrease in λ_{\max} with increasing solvent polarity (Figure 5.6). Given the strong solvent dependence of these spectra, comparative studies of **15–20** implemented a common solvent to extract meaningful information on how functional groups affect the spectroscopic properties.

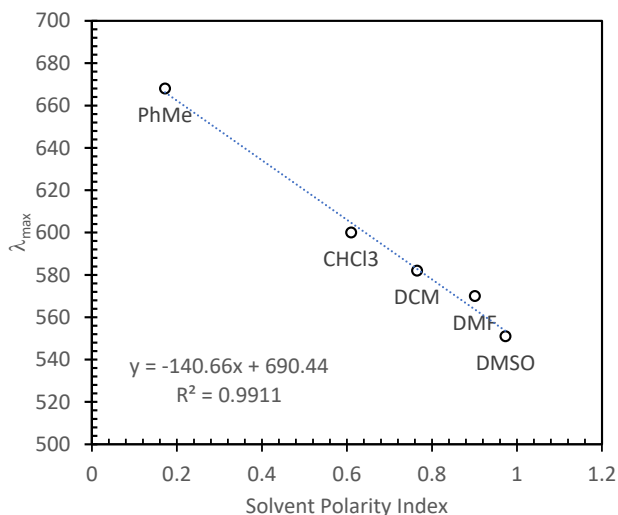


Figure 5.6. Correlation of λ_{\max} with solvent parameter index for **15**.

Effects of bipyridine substitution: For the series of complexes **15–19** the dithiolate ligand is constant and data for all complexes measured in CH_2Cl_2 reveal changes in the position of λ_{\max} in the visible region with respect to the nature of the substituents at the 4,4' position of the bipyridine ligand (Figure 5.7). The λ_{\max} values are summarized in Table 5.6 and span a range of 150 nm from 557 to 707 nm, corresponding to a change in transition energy of 3800 cm^{-1} . A plot of λ_{\max} vs σ_{para} revealed a good correlation between λ_{\max} of the absorption band *in the visible region* and the substituent permitting the λ_{\max} to be systematically tailored by tuning the functional group.

$$\lambda_{\max} = 601 + 214\sigma_p \text{ nm} \quad \text{Eq. 5.6}$$

Table 5.6. Summary of λ_{\max} data for complexes **15–19** and the corresponding Hammett parameters for the substituents in the 4,4' positions.

Complex	Substituent	σ_{para}	λ_{\max} (CH ₂ Cl ₂)/nm
15	H	0	579
17	Me	-0.17	557
18	^t Bu	-0.20	571
19	Ph	-0.01	600
16	EtCOO	+0.45	707

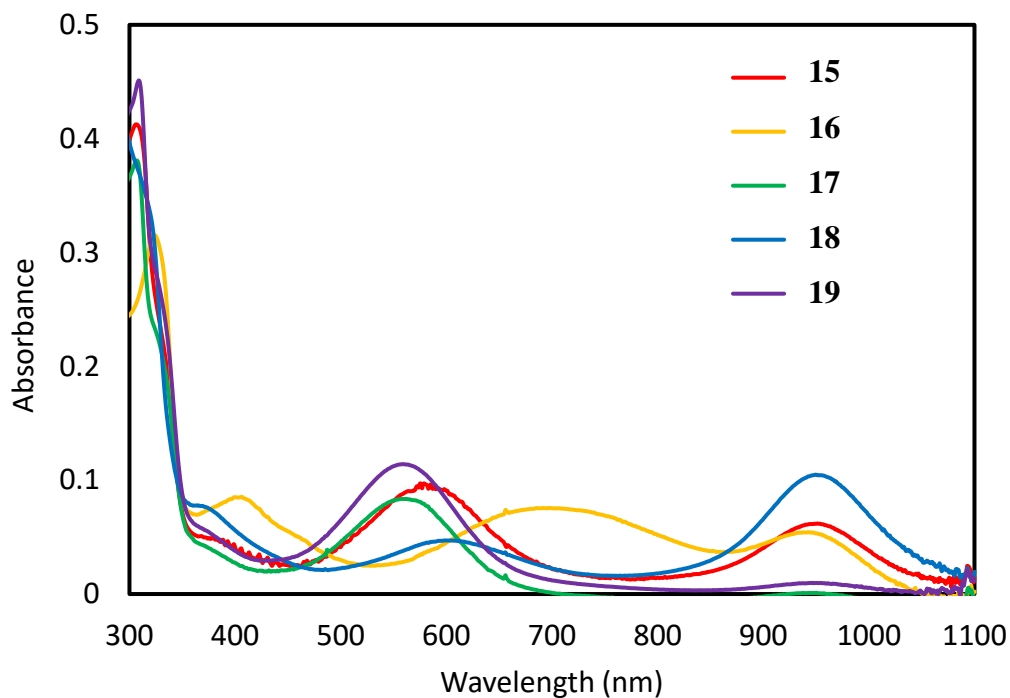


Figure 5.7. UV-Vis spectra of **15–19** in CH₂Cl₂ with a concentration of 2.0×10^{-5} M.

Effects of dithiolate substitution: The spectroscopic properties of nickel bipyridine with benzenedithiolate derivatives have not been extensively studied. In this context we note that Ni(^{Me}COObpy)(bdt) exhibits a λ_{\max} at 610 nm in DMF,³ while the closely related complex **16**, Ni(^{Et}COObpy)(dmobdt), exhibits a λ_{\max} at 667 nm in the same solvent:

Incorporation of the electron-donating methoxy groups reduces the transition energy by 1400 cm^{-1} .

Long wavelength absorption: One feature of this series of complexes is the appearance of λ_{max} values in the near infrared region (NIR) of the electromagnetic spectrum, with λ_{max} values for **15–19** occurring around 950 nm in CH_2Cl_2 (Figure 5.7). The intensity of this NIR absorption appears sensitive to both the substituent (essentially absent for **17** in CH_2Cl_2), while solvent dependent studies on **15** indicated this transition is largely suppressed in DMF and toluene (Table 5.7). Plots of absorbance vs. concentration, as indicated earlier in this section, reveal this transition follows Beer-Lambert law and is unlikely to be due to aggregation. To probe the nature of this transition preliminary TD-DFT studies were undertaken (B3LYP-D3/LACV3P*) on **15–19** in the gas phase. These calculations reveal the lowest energy transition corresponds to the HOMO-LUMO transition and occurs in the range 864 – 1069 nm. The computed transition wavelengths qualitatively agree with the experimental data measured in DMF with λ_{max} being in the order **20** < **15** < **18** < **19** but the transition energies are almost identical in CH_2Cl_2 , suggesting some considerable solvent effects. Notably the computed oscillator strengths (f) do exhibit some variation with functional group ($0.14 < f < 0.22$) but are certainly not as marked as those observed experimentally.

In order to examine solvent effects, further TD-DFT studies on **15** (B3LYP-D3/LACV3P**) were undertaken on a fully-optimized gas-phase structure, taking into account solvent effects using a conductor-like screening model (COSMO).²⁶ The results of these TD-DFT calculations in DMF, CHCl_3 and DCM are summarized in Table 5.8. These calculations clearly reveal an over-estimate of the effect of solvent in shifting the transition to higher energy in relation to the gas phase value (950 nm) but do qualitatively reflect the experimentally observed trends in extinction coefficients, with marked suppression of the transition in DMF.

Table 5.7. Summary of λ_{\max} data and corresponding extinction coefficients for complexes **15–19** in both CH_2Cl_2 and DMF alongside the corresponding gas phase TD-DFT computed lowest energy transition (B3LYP-D3/LACV3P*) and oscillator strength.

Complex	λ_{\max} (ϵ)		λ (f)
	CH_2Cl_2	DMF	TD-DFT
15	954 (2100)	983 (710)	950 (0.159)
16	944 (2650)	---	1069 (0.221)
17	941 (30)	---	991 (0.141)
18	956 (5200)	990 (3400)	957 (0.184)
19	952 (480)	1001 (1100)	1007 (0.209)
20	942 (450)	790 (800)	864 (0.179)

Table 5.8. Comparison between the experimental λ_{\max} and ϵ values for complex **15** in different solvents and TD-DFT calculated values taking into account solvent effects with a PCM model (COSMO).

Solvent	λ_{\max} (ϵ)	
	Experimental	TD-DFT
CH_2Cl_2	954 (2100)	714 (0.132)
CHCl_3	944 (4260)	751(0.162)
DMF	983 (710)	666 (0.0088)

In summary, the UV-Vis spectra of these complexes reveal a λ_{\max} in the visible region whose position is sensitive to solvent and substituent effects in a systematic manner. In addition, a long wavelength transition is observed around 950 nm which is rather invariant to substitution patterns but whose extinction coefficient appears sensitive to a lesser degree on substituent and to a greater degree on solvent effects. Correlation of these computational studies with experimental measurements in DMF solution suggest this transition is associated with the lowest energy HOMO-LUMO transition.

5.2.4. EFISH measurements

EFISH measurements on compounds **16–20** were measured by Prof. F. Tessore at the University of Milan. The experimental λ_{\max} data (Table 5.9) are in good agreement with our own observations. Their DFT-computed dipole moments (B3LYP/6-31G(TM)//COSMO(DMF)) are somewhat larger than those we computed at the B3LYP-D3/LACV3P* level of theory but are of the same magnitude. The computed values of $\mu\beta_{1.907}$ (Table 5.9) are based on the value of μ computed at the B3LYP/6-31G(TM) level of theory using a solvent continuum model for DMF and the experimental hyperpolarizability at an excitation wavelength of 1.907 μm . The values of $\mu\beta_0$ were calculated using Eq 5.7:

$$\mu\beta_0 = \mu\beta_\lambda [1 - (2\lambda_{\max}/\lambda)^2] / [1 - (\lambda_{\max}/\lambda)^2] \quad \text{Eq. 5.7}$$

where λ_{\max} is the wavelength of the absorption maximum of the charge-transfer transition and λ is the wavelength of the incident light (1907 nm). All the complexes display negative quadratic hyperpolarizability values ($\mu\beta_{1.907} < 0$). This result implies a reduction of the molecular dipole moment upon the charge-transfer excitation, so that the difference between the excited and the ground state dipole moment of the molecule is negative. This is in good agreement with the bathochromic shift of the electronic absorption band with decreasing the solvent polarity already discussed. The values of $|\mu\beta_0|$ span the range 564–895 $\times 10^{-48}$ esu and are comparable to other reported nickel/bipyridine/dithiolate complexes, which are among some of the most hyperpolarizable square planar nickel (II) complexes, e.g. Ni(bdt)(^{Me}COObpy) ($\mu\beta_0 = -581 \times 10^{-48}$ esu), Ni(dddt)(^{Et}COObpy) ($\mu\beta_0 = -954 \times 10^{-48}$ esu) and Ni(mi-5edt)(^{Et}COObpy) ($\mu\beta_0 = -618 \times 10^{-48}$ esu) (Figure 5.8).⁴

Table 5.9. Experimental molecular polarizability data for compounds **16–20**.

Compound	λ_{\max} (nm) ($\epsilon \text{ M}^{-1} \text{ cm}^{-1}$)	μ^a (D)	μ^b (D)	$\mu\beta_{1.907}^c$ ($\times 10^{-48} \text{ esu}$)	$\mu\beta_0$ ($\times 10^{-48} \text{ esu}$)
16	667 (6900)	21.03	10.53	-1280	-574
17	549 (2900)	20.06	12.00	-920	-564
18	546 (2700) 990 (3400)	21.28	12.11	-1450	-895
19	593 (5600) 1001 (1100)	21.47	11.58	-1040	-576
20	539 (7400) 790 (800)	17.31	10.87	-1250	-783

- a. Molecular dipole computed at the B3LYP/6-31G(TM) level of theory using a polarized continuum model (COSMO) for DMF.
b. Molecular dipole computed in the gas phase using the B3LYP-D3/LACV3P* level of theory.
c. Values of $\mu\beta$ are computed using the B3LYP-631G(TM) computed ground state dipole moment.

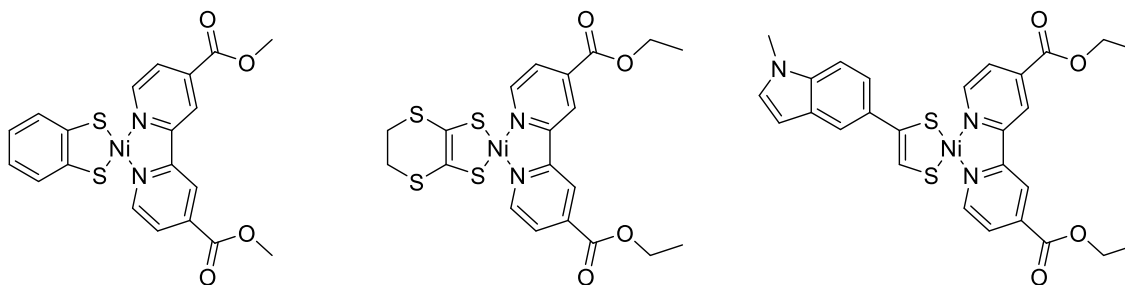


Figure 5.8. Molecular structures of (left) Ni(bdt)(^{MeCOO}bpy) ($\mu\beta_0 = -581 \times 10^{-48} \text{ esu}$), (center) Ni(dddt)(^{EtCOO}bpy) ($\mu\beta_0 = -954 \times 10^{-48} \text{ esu}$) and (right) Ni(mi-5edt)(^{EtCOO}bpy)

5.3 Conclusions & Future Work

In conclusion, we have successfully developed a one-pot reaction to generate ‘push-pull’ type nickel dithiolate/bipyridine complexes in good yield. The compounds have been structurally determined and their spectroscopic properties explored. Solvatochromic and chemical trends in λ_{\max} in the visible region have been explored and correlate extremely well with previous empirical models of solvent polarity and

substituent effects (Hammett). Preliminary data indicate these compounds offer large molecular hyperpolarizabilities and absorption maxima in the NIR region of the electromagnetic spectrum arising from a low energy HOMO-LUMO excitation.

5.4 Experimental

5.4.1. General Procedures

Tetrathiocins were prepared according to a modified procedure and their analytical data matched the literature report.²⁷ 2,2'-Bipyridine-4,4'-dicarboxylic acid²⁸ and Ni(COD)₂ were synthesized through a literature method²⁹ or purchased from Sigma Aldrich. All other bipyridines were purchased from Sigma Aldrich. Standard solvents were dried and deoxygenated using an Innovative Technology Solvent Purification System and manipulation of air-sensitive materials carried out under an atmosphere of dry nitrogen using standard Schlenk techniques and a dry-nitrogen glove box (MBraun Labmaster). Microwave syntheses were carried out in sealed vessels using a Biotage Initiator 1 microwave.

5.4.2. Physical Measurements

All NMR spectra were recorded on a Bruker DPX300 UltraShield 300 MHz spectrometer with a Broadband AX Probe using CD₂Cl₂ (¹H δ = 5.34 ppm, s) as an internal reference point relative to Me₄Si (δ = 0 ppm). IR spectra were obtained using a Bruker Alpha FT-IR spectrometer equipped with a Platinum single reflection diamond ATR module. Elemental compositions were determined on a PerkinElmer 2400 Series II Elemental Analyzer. Mass spectra were recorded on a Waters XEVO G2-XS spectrometer specifically using the atmospheric solids analysis probe in positive resolution mode (ASAP+) or Agilent 6120 Quadrupole LC/MS mass spectrometer operated in positive mode.

5.4.3. X-ray Crystallography

Crystals of the metal complexes were mounted on a cryoloop with paratone oil and examined on a Bruker D8 Venture diffractometer equipped with Photon 100 CCD area detector. An Oxford Cryostream cooler was used to maintain cryogenic temperatures for these studies. Data were collected using the APEX-II/III software,^{30,31} integrated using

SAINT³² and corrected for absorption using a multi-scan approach (SADABS).³³ Final cell constants were determined from full least squares refinement of all observed reflections. The structures of **16–20** were solved by direct methods (SHELXS),³⁴ while **15** was solved using intrinsic phasing (SHELXT).³⁵ All structures were refined with full least squares refinement on F^2 using either SHELXL³⁶ or Olex2 software.³⁷ In structures **15**, **17**, **18** and **20** residual lattice solvent molecules were identified in difference maps. All hydrogen atoms were added at calculated positions and refined isotropically with a riding model.

5.4.4. Computational methods

DFT and TD-DFT calculations on metal complexes **16–20** were performed using the B3LYP-D3 functional and LACV3P* basis set within Jaguar,³⁸ using the crystallographically determined geometry as an initial starting point for geometry refinement. Solvent effects were considered using the polarizable continuum model (PCM) employing standard parameters for each solvent for the conductor like screening model (COSMO).³⁹

5.4.5. Synthesis of (2,2'-bipyridyl)Ni(dmobdt) (**15**).

Ni(COD)₂ (0.075 g, 0.27 mmol), 2,2'-bipyridyl (0.043 g, 0.27 mmol) and **1a** (0.055 g, 0.14 mmol) was placed in an oven dried 5 mL microwave vial in the glovebox. Dry toluene (5 mL) was added and the suspension was heated in the microwave for 1 hour at 150 °C. The resultant dark blue solid was isolated from a light brown solution by filtration. The precipitate was washed with ether (30 mL) and dried in air (0.086 g, 75%). Crystals were grown from a saturated solution of CHCl₃ layered with hexanes.

¹H NMR (300 MHz, ppm, DCM-d₂) δ_{H} = 8.86 (2H, m, aryl C–H), 7.96 (4H, m, aryl C–H), 7.46 (2H, m, aryl C–H), 6.70 (2H, s, benzo C–H), 3.75 (6H, s, OCH₃).

LRMS (ESI-TOF) m/z : [M]⁺ calc. for C₁₈H₁₆O₂N₂S₂Ni⁺ 414.00; found 414.00; [M + H]⁺ calc. for C₁₈H₁₇O₂N₂S₂Ni⁺ 415.01; found 415.0.

Elemental analysis calc. for C₁₈H₁₆O₂N₂S₂Ni·¼CHCl₃: C 49.16; H 3.67; N 6.28%. Found: C 50.53; H 3.63; N, 6.40%.

UV-Vis (CH₂Cl₂): λ_{\max} (nm), ϵ (mol.L⁻¹.cm⁻¹): 247(32100), 306(18500), 579(4580), 951(2100).

IR ν_{\max} (cm⁻¹): 3053(w), 2984(w), 2933(w), 2828(w), 1602(m), 1579(w), 1482(s), 1472(s), 1463(s), 1432(vs), 1348(m), 1317(m), 1235(vs), 1199(s), 1166(m), 1108(s), 1041(s), 1021(m), 928(w), 839(s), 779(vs), 765(vs), 753(vs), 722(s), 693(m), 641(w), 458(w), 423(m).

5.4.6. Synthesis of (Diethyl [2,2'-bipyridine]-4,4'-dicarboxylate)Ni(dmobdt) (16).

Ni(COD)₂ (0.150 g, 0.545 mmol), diethyl(2,2'-bipyridine)-4,4'-dicarboxylic acid (0.164 g, 0.545 mmol) and **1a** (0.110 g, 0.273 mmol) was placed in an oven dried 5 mL microwave vial in the glovebox. Dry toluene (5 mL) was added and the suspension was heated in the microwave for 1 hour at 150 °C. The resultant dark green solid was isolated from a dark brown solution by filtration. The precipitate was washed with ether (30 mL) and dried in air (0.250 g, 82%). Crystals were grown from a saturated solution of CHCl₃ layered with hexanes.

¹H NMR (300 MHz, ppm, DCM-d₂) δ_{H} = 9.01 (2H, d, ³J = 5.8 Hz, aryl C-H), 8.46 (2H, s, aryl C-H), 7.91 (2H, d, ³J = 5.8 Hz, aryl C-H), 6.59 (2H, s, benzo), 4.46 (4H, q, ³J = 7.2 Hz, (C=O)OCH₂-CH₃), 3.75 (6H, s, OCH₃), 1.45 (6H t, ³J = 7.2 Hz, (C=O)OCH₂-CH₃).

HRMS (ASAP(+)) *m/z*: [M]⁺ calc. for C₂₄H₂₄O₆N₂S₂Ni⁺ 558.0429; found 558.0403.

Elemental analysis calc. for C₂₄H₂₄O₆N₂S₂Ni·½CHCl₃: C 47.48; H 3.98; N 4.52%. Found: C 46.48; H 3.90 N, 4.41%.

UV-Vis (CH₂Cl₂): λ_{\max} (nm), ϵ (mol.L⁻¹.cm⁻¹): 250(25900), 323(15400), 707(5150), 948(4200).

IR ν_{\max} (cm⁻¹): 3052(w), 2997(w), 2929(w), 2829(w), 1584(w), 1483(s), 1469(s), 1434(vs), 1343(m), 1244(vs), 1199(s), 1174(m), 1100(s), 1043(s), 815(m), 782(m), 746(m), 690(vs), 531(vs), 482(m).

5.4.7. Synthesis of (4,4'-dimethyl-2,2'-bipyridyl)Ni(dmobdt) (17).

Ni(COD)₂ (0.075 g, 0.27 mmol), 4,4'-dimethylbipyridine (0.054 g, 0.27 mmol) and **1a** (0.055 g, 0.14 mmol) was placed in an oven dried 5 mL microwave vial in the glovebox. Dry toluene (5 mL) was added and the suspension was heated in the microwave for 1 hour at 150 °C. The resultant dark purple solid was isolated from the brown solution by filtration. The precipitate was washed with ether (30 mL) and dried in air (0.102 g, 66% yield). Crystals were grown from a saturated solution of CHCl₃ layered with hexanes.

¹H NMR (300 MHz, ppm, DCM-d₂) δ_H = 8.63 (2H, d, ³J = 5.8 Hz, aryl C–H), 7.74 (2H, s, aryl C–H), 7.17 (2H, d, ³J = 5.8 Hz, aryl C–H), 6.70 (2H, s, benzo), 3.74 (s, 6H, OCH₃) 2.48 (6H, s, aryl-CH₃).

HRMS (ASAP(+)) *m/z*: [M]⁺ calc. for C₂₀H₂₀O₂N₂S₂Ni⁺ 442.0320; found 442.0293.

Elemental analysis calc. for C₂₀H₂₀O₂N₂S₂Ni·CHCl₃: C 44.77; H 3.76; N 4.97%. Found: C 45.22; H 3.93; N 5.16%.

UV-Vis (CH₂Cl₂): λ_{max} (nm), ε (mol·L⁻¹·cm⁻¹): 265(29700), 310(16700), 557(4390).

IR ν_{max} (cm⁻¹): 2989(w), 2950(w), 2900(w), 2831(w), 1616(s), 1583(w), 1482(m), 1437(s), 1237(vs), 1193(s), 1167(m), 1036(m), 833(s), 817(s) 742(vs), 661(w), 514(s).

5.4.8. Synthesis of (4,4'-diphenyl-2,2'-bipyridyl)Ni(dmobdt) (18).

Ni(COD)₂ (0.075 g, 0.27 mmol), 4,4'-diphenyl-bipyridine ligand (0.084 g, 0.27 mmol) and **1a** (0.055 g, 0.14 mmol) was placed in an oven dried 5 mL microwave vial in the glovebox. Dry toluene (5 mL) was added and the suspension was heated in the microwave for 1 hour at 150 °C. The resultant dark purple solid was isolated from the brown solution by filtration. The precipitate was washed with ether (30 mL) and dried in air (0.102 g, 66% yield). Crystals were grown from a saturated solution of CHCl₃ layered with toluene as a buffer layer and then hexanes.

¹H NMR (300 MHz, ppm, DCM-d₂) δ_H = 8.88 (2H, d, ³J = 5.5 Hz, aryl C–H), 7.80 (2H, s, aryl C–H), 7.70 (10H, m, Ph) 7.21 (2H, d, ³J = 5.6 Hz, aryl C–H), 6.72 (2H, s, benzo), 3.77 (6H, s, OCH₃).

LRMS (ESI+) m/z : $[M + H]^+$ calc. for $C_{30}H_{25}O_2N_2S_2Ni^+$ 567.07; found 567.2.

Elemental analysis calc. for $C_{30}H_{24}O_2N_2S_2Ni \cdot 2\frac{3}{4}CHCl_3$: C 43.88; H 3.01; N 3.12%. Found: C 44.10; H 3.05; N 2.62%.

UV-Vis (CH_2Cl_2): λ_{max} (nm), ϵ ($mol.L^{-1}.cm^{-1}$): 261(27900), 600(926), 955(2870).

IR ν_{max} (cm^{-1}): 3053(w), 2986(w), 2930(w), 2830(w), 1611(m), 1522(w), 1463(m), 1429(s), 1407(s), 1334(m), 1228(vs), 1200(m), 1157 (m), 1086(w), 1041(m), 1018(m), 925(w), 879(m), 836 (m), 762(s), 694(s), 624(m), 583(w), 512(w).

5.4.9. Synthesis of (4,4'-di-*tert*-butyl-2,2'-bipyridyl)Ni(dmobdt) (19).

Ni(COD)₂ (0.075 g, 0.27 mmol), 4,4'-di-*tert*-butyl-bipyridine (0.073 g, 0.27 mmol) and **1a** (0.055 g, 0.14 mmol) were combined in an oven-dried 5 mL glass microwave vial in the glove box. Dry toluene (5 mL) was added and the suspension was heated in the microwave for 1 hour at 150 °C. The resultant dark purple solid was isolated from a brown solution by filtration. The precipitate was washed with ether (30 mL) and dried in air (0.245 g, 86% yield). Crystals were grown from a saturated solution of $CHCl_3$ layered with toluene as a buffer layer and then hexanes.

¹H NMR (300 MHz, ppm, DCM-*d*₂) δ_H = 8.69 (2H, d, ³*J* = 5.9 Hz, aryl C–H), 7.88 (2H, s, aryl C–H), 7.46 (2H, d, ³*J* = 5.9 Hz, aryl C–H), 6.71 (2H, s, benzo), 3.75 (6H, s, OCH₃) 1.42 (18H, s, ^tBu).

HRMS (ASAP(+)) m/z : $[M]^+$ calc. for $C_{26}H_{32}O_2N_2S_2Ni^+$ 526.1258; found 526.1231.

Elemental analysis calc.: $C_{26}H_{32}O_2N_2S_2Ni \cdot \frac{1}{4}CHCl_3$: C 56.51; H 5.83; N 5.02%. Found: C 56.37; H 5.87; N 5.12%.

UV-Vis (CH_2Cl_2): λ_{max} (nm), ϵ ($mol.L^{-1}.cm^{-1}$): 253(34400), 309(21600), 571(5040), 951(350).

IR ν_{max} (cm^{-1}): 3077(w), 3009(w), 2940(w), 2869(w), 2842(w), 1616(m), 1505(s), 1482(s), 1461(s), 1435(s), 1239(vs), 1174(vs), 1046(s), 840(vs), 780(s), 695(w), 596(s).

5.4.10. Synthesis of (4,4'-di-*tert*-butyl-2,2'-bipyridyl)Ni(doxbdt) (20).

Ni(COD)₂ (0.150 g, 0.525 mmol), 4,4'-di-*tert*-butyl-bipyridine ligand (0.140 g, 0.525 mmol) and **1d** (0.108 g, 0.273 mmol) were combined in an oven-dried 5 mL microwave vial in the glove box. Dry toluene (5 mL) was added and the suspension was heated in the microwave for 1 hour at 150 °C. The resultant dark purple solid was isolated from a dark brown solution by filtration. The precipitate was washed with ether (30 mL) and dried in air (0.128 g, 89% yield). The solid was recrystallized from a saturated CHCl₃ solution layered with ether to produce dark purple (0.058 g, 59% yield) crystals suitable for X-ray diffraction. Crystals were grown from a saturated solution of CHCl₃ layered with toluene as a buffer layer and then hexanes.

¹H NMR (300 MHz, ppm, DCM-d₂) δ_H = 8.76 (2H, s, aryl C–H), 7.79 (2H, s, aryl C–H), 7.48 (2H, s, aryl H C–H), 6.63 (2H, s, benzo C–H), 4.18 (4H, s, O–CH₂–CH₂–O), 1.42 (18H, s, ^tBu)

Elemental analysis calc. for C₂₆H₃₀O₂N₂S₂Ni·2½CHCl₃: C, 41.61; H, 3.98; N, 3.41. Found: C, 41.40; H, 4.41; N, 3.36.

HRMS (ASAP(+)) *m/z*: = [M]⁺ calc. for C₂₆H₃₀O₂N₂S₂Ni⁺ 524.1102; found 524.1083.

UV-Vis (CH₂Cl₂): λ_{max} (nm), ε (mol.L⁻¹.cm⁻¹): 231(19800), 310(11000), 550(3680), 942(450).

IR ν_{max} (cm⁻¹): 2953(w), 2871(w), 1615(m), 1562(m), 1447(s), 1293(s), 1248(vs), 1105(m), 1094(m), 912(m), 836(s), 745(m), 688(m), 559(m), 420(w).

5.5 References

- (1) J. L. Oudar and D. S. Chemla, *J. Chem. Phys.*, 1977, **66**, 2664–2668
- (2) R. E. Hummel, *Electronic Properties of Materials: An Introduction for Engineers*, Springer Berlin, Heidelberg, 2nd edn. 1985, 135–208.
- (3) T. R. Miller and I. G. Dance, *J. Am. Chem. Soc.*, 1973, **95**, 6970–6979.

- (4) L. Pilia, M Pizzotti, F. Tessore and N. Robertson, *Inorg. Chem.*, 2014, **53**, 4517–4526.
- (5) A. Pintus, C. A. Aragoni, S. J. Coles, S. L. Coles, F. Isaia, V. Lippolis, A.D. Musteti, F. Telxidior, C. Vinas and A. Arca, *Dalton Trans.*, 2014, **43**, 13649–13660
- (6) C. T. Chen, T.-Y. J. Lin, C.-H. Chen and K.-J. Lin, *J. Chin. Chem. Soc.*, 2000, **47**, 197–201.
- (7) C. Browning, J. M. Huson, E. W. Reinheimer, F.-L. Kuo, R. N. McDougald Jr, H. Rabaa, H. Pan, J. Bacsa, X. Wang, K. R. Dunbar, N. D. Shepherd, and M. A. Omary, *J. Am. Chem. Soc.*, 2014, **136**, 16185–16200.
- (8) T. Biet, T. Cauchy, Q. Sun, J. Ding, A. Hauser, P. Oulevey, T. Burgi, D. Jacquemin, N. Vantuyne, J. Crassous and N. Avarari, *Chem. Commun.*, 2017, **53**, 9210–9213.
- (9) H. Sesolis, G. Gontard, A. Jutand, M. P. Gullo, E. Bandini, A. Barbieri and H. Amouri, *Eur. J. Inorg. Chem.*, 2012, **22**, 3577–3594.
- (10) F. Camerel, G. Albert, F. Barriere, C. Lagrost, M. Fourmigue and O. Jeannin, *Chem. Eur. J.*, 2019, **25**, 5719–5732.
- (11) T. M. Cocker and R. E. Bachman, *Mol. Cryst. Liq. Cryst.*, 2004, **408**, 1–19.
- (12) T. Kusamoto, K. Takada, R. Sakamoto, S. Kume and H. Nishihara, *Inorg. Chem.*, 2012, **51**, 12102–12113.
- (13) G. Yzambart, B. Fabre, T. Roisnel, V. Dorcet, S. Ababou-Girard, C. Meriadec and D. Lorcy, *Organomet.*, 2014, **33**, 4766–4776.
- (14) B. Zheng, R. P. Sabatini, W.-F. Fu, M.-S. Eum, W. W. Brennessel, L. Wang, D. W. McCamant and R. Eisenberg, *PNAS*, 2015, **112**, E3987–E3996.
- (15) J. A. Zuleta, J. M. Bevilacqua, D. M. Proserpio, P. D. Harvey and R. Eisenberg, *Inorg. Chem.*, 1992, **31**, 2396–2404.
- (16) A. Obanda, K. Martinez, R. H. Schmehl, J. T. Mague, I. V. Rubtsov, S. N. MacMillan, K. M. Lancaster, S. Sproules and J. P. Donahue, *Inorg. Chem.* 2017, **56**, 10257–10267.

- (17) J. D. Wrixon, J. J. Hayward, O. Raza and J. M. Rawson, *Dalton Trans.*, 2014, **43**, 2134–2139.
- (18) L. K. Watanabe, J. D. Wrixon, Z. S. Ahmed, J. J. Hayward, P. Abbasi, M. Pilkington, C. L. B. Macdonald and J. M. Rawson, *Dalton Trans.*, 2020, **49**, 9086–9093.
- (19) A. Davison, N. Edelstein, R. H. Holm and A. H. Maki, *Inorg. Chem.*, 1964, **3**, 814–823.
- (20) J. D. Wrixon, J. J. Hayward and J. M. Rawson, *Inorg. Chem.*, 2015, **54**, 9384–9386.
- (21) J. Kameníček, P. Herich, K. Kuča, D. Jun and M. Olšovský, *J. Coord. Chem.*, 2008, **61**, 3525–3533.
- (22) T. M. Cocker and R. E. Bachman, *Inorg. Chem.*, 2001, **40**, 1550–1556.
- (23) L. Yang, Z. Peng, S. Wang and C. Fang, *Spectrochim. Acta A Mol. Biomol. Spectrosc.*, 2004, **60**, 481–487.
- (24) C. G. Swain, and E. C. Lupton Jr, *J. Am. Chem. Soc.*, **1968**, *90*, 4328–4337.
- (25) S. D. Cummings and R. Eisenberg, *J. Am. Chem. Soc.*, 1996, **119**, 1949–1960.
- (26) A. Klamt and G. Schuurmann, *J. Chem. Soc., Perkin Trans. 2*, 1993, 799–805.
- (27) K. W. Stender, N. Wolki and G. Klar, *Phos., Sulf. Sil. Relat. Elem.*, 1989, **42**, 111–114.
- (28) K. Y. Zhang and K. K.-W. Lo, *Inorg. Chem.* 2009, **48**, 6011–6025.
- (29) D. J. Krysan and P. B. Mackenzie, *J. Org. Chem.*, 1990, **55**, 4229–4230.
- (30) APEX II, Bruker AXS, Madison, WI, USA.
- (31) APEX III, Bruker AXS, Madison, WI, USA.
- (32) SAINT, Bruker AXS, Madison, WI, USA.
- (33) SADABS, Bruker AXS, Madison, WI, USA.
- (34) G. M. Sheldrick, SHELXS-97, A Program for Automatic Solution of Crystal Structures, University of Göttingen, 1997.
- (35) G. M. Sheldrick., *Acta Cryst.*, 2015, **A71**, 3–8.
- (36) G. M. Sheldrick, *Acta Cryst.*, 2015, **C71**, 3–8.

- (37) O. V. Dolomanov, L. J. Bourhis, R. Gildea, J. A. K. Howard and H. Puschmann, *J. Appl. Crystallogr.*, 2009, **42**, 339–341.
- (38) A. D. Bochevarov, E. Harder, T. F. Hughes, J. R. Greenwood, D. A. Braden, D. M. Philipp, D. Rinaldo, M. D. Halls, J. Zhang and R. A. Friesner, *Int. J. Quantum Chem.*, 2013, **113**, 2110–2142.
- (39) A. Klamt and G. Schurmann, *J. Chem. Soc., Perkin Trans. 2*, 1993, 799–805.

6. GERMANIUM DITHIOLATE CHEMISTRY

6.1 Introduction

While the coordination chemistry of dithiolate ligands with transition metals is extensive, dithiolate complexes of the *p*-block metals are rather less studied with less than 150 examples structurally characterized across the *p*-block metals (CSD version 5.42 update #3, Sept 2021).

Group 13 complexes of benzene dithiolates are limited to the heterometallic $[\text{Cp}^*\text{Ti}(\text{bdt})_2]\text{Tl}$ where the Tl^+ acts as a counterion to the $[\text{Cp}^*\text{Ti}(\text{bdt})_2]^-$ anion,¹ the unusual dimeric Tl(I) complex $[\text{Tl}_2(\mu_2\text{-bdt})_2]^{2-}$ (Figure 6.1) and the Tl(III) complex $[\text{Tl}(\text{bdt})_2]^-$.² Particularly relevant to this work is the oxidation of dithietes to $\text{Cp}^*\text{In}(\text{I})^3$ to form $\text{Cp}^*\text{In}(\text{dt})$, described in section 1.2.4.

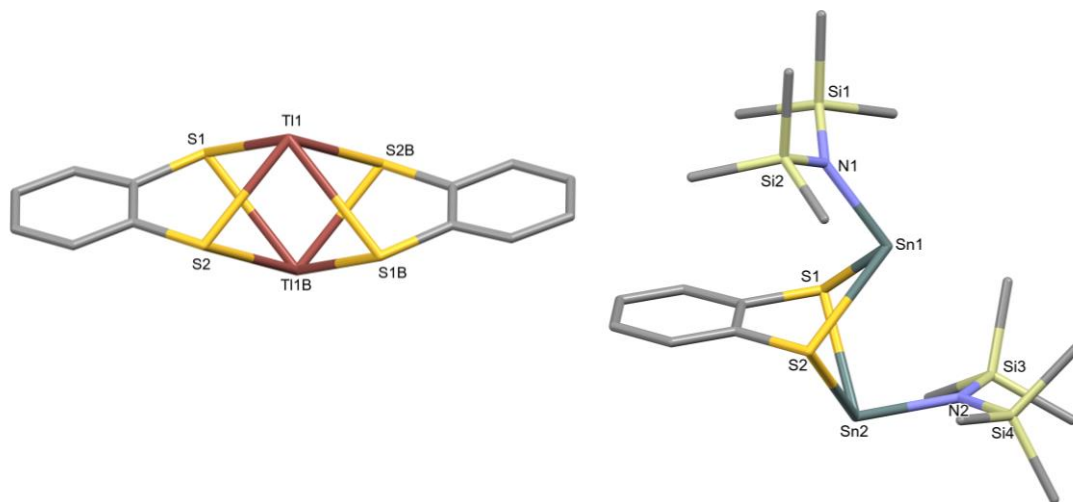


Figure 6.1. Crystal structures of the (left) $[\text{Tl}_2(\mu_2\text{-bdt})_2]^{2-}$ anion and (right) $\text{Sn}_2(\mu_2\text{-bdt})\{\text{N}((\text{SiMe}_3)_2)_2\}$ (H atoms omitted for clarity).

Examples of group 14 complexes with benzene dithiolate ligands are more expansive. Complexes in which the tetrel exists below its group oxidation state are prevalent on descending the group where the inert pair effect becomes dominant. These are exemplified by the Sn(II) dimer, $\text{Sn}_2(\mu_2\text{-bdt})(\text{N}(\text{SiMe}_3)_2)_2$ (Figure 6.1)⁴ and the Pb(II) polymers $[\text{Pb}_2(\text{S}_2\text{C}_6\text{H}_2\text{S}_2(\text{en}))_n]$ and $[\text{Pb}_3(\text{C}_6\text{S}_6)]_n$ derived from 1,2,4,5-benzenetetrathiol and 1,2,3,4,5,6-benzenehexathiol respectively, alongside the network structure $\text{Pb}_3(\text{HTT})$

where HTT is the hexathiotriphenylene anion, $[C_{18}S_6]^{6-}$.⁵ In the group valence state, examples are more plentiful and structures of general formula $M(dt)R_2$ and $M(dt)X_2$ (dt = dithiolate; R = alkyl, aryl; X = halide) abound, as well as homoleptic complexes of formula $M(dt)_2$ are known which contain tetrahedrally-coordinated tetrels, such as $Ge(bdt)_2$ (Figure 6.2).⁶ These complexes exhibit some Lewis acidity and examples of $[M(dt)R_2X]^-$, $[M(dt)X_3]^-$ and $[M(dt)_2X]^-$ have all been reported and typically adopt a hypervalent distorted square pyramidal or trigonal bipyramidal geometry.⁷ The structure of $[Ge(tdt)_2F]^-$ is shown in Figure 6.2,⁸ while the corresponding $[Ge(tdt)_2Me]^-$ anion has also been reported.⁹ Hexa-coordinate $Sn(VI)$ dithiolate complexes have also been reported, including the $[Sn(bdt)_3]^{2-}$ dianion and comprise distorted octahedral geometries.¹⁰

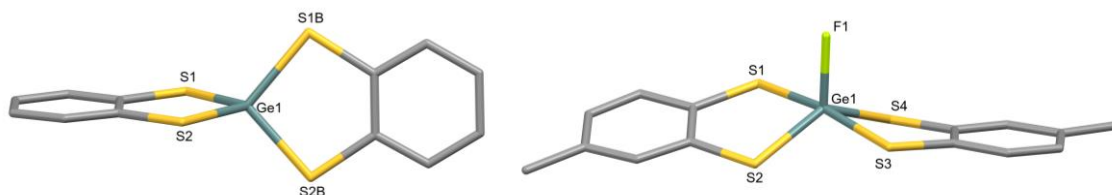


Figure 6.2. Crystal structures of (left) $Ge(bdt)_2$ and (right) $[Ge(tdt)_2F]^-$ (H atoms omitted for clarity).

For group 15, the inert pair effect leads to examples drawn from both pnictogens in the trivalent state, alongside the expected pentavalent states. This is exemplified by the Sb(III) complexes, $Sb(bdt)(SMe)$,¹¹ $Sb(bdt)Cl$,¹² $[Sb(bdt)_2]^-$,¹³ and the Sb(V) anion, $[Sb(tdt)_3]^-$.¹⁴ These are typically structurally analogous to the group 14 complexes described above.

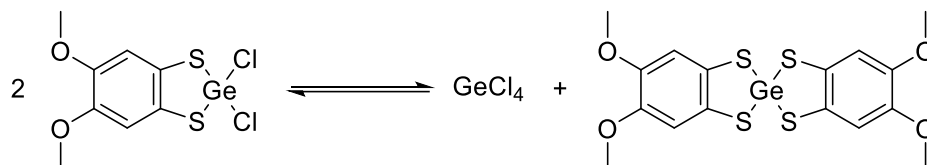
The reactivity of dithietes with main group elements is largely unexplored but reviewed in Chapter 1. Both $P(I)$ ¹⁵ and $P(III)$ ¹⁶ undergo reactions with dithietes (see Section 1.2.4). However, a preliminary foray into the oxidative addition of tetrathiocins to $P(I)$ ¹⁷ (see Section 1.3.4), afforded a mixture of formally $P(II)$ and $P(III)$ dithiolate derivatives, suggesting some divergence in reactivity between dithietes and tetrathiocins with regard to p -block chemistry. In this context the reactivity of $Ge(II)$ appeared entirely unexplored as a route towards $Ge(IV)$ dithiolate complexes. The first $Ge(IV)$ bis(dithiolate) complex was reported in 1965 by Fink *et al.* as part of a series where they prepared a series of complexes

of formula $M(\text{tdt})_2$ ($M = \text{Si}, \text{Ge}, \text{Sn}$ and Pb) to investigate their optical properties.¹⁸ In this study, the reactivity of tetrathiocins with the low-valent germanium(II) precursor, $\text{GeCl}_2 \cdot \text{dioxane}$, is explored.

6.2 Results and Discussion

6.2.1 Synthesis

The reaction of tetrathiocins **1a**, **1b** and **1c** with the low-valent Ge(II) source, $\text{GeCl}_2 \cdot \text{dioxane}$ in dry DCM under an N_2 atmosphere proceeded very quickly. This was evident by rapid formation of a clear yellow solution (whereas the tetrathiocins **1a** – **1c** are sparingly insoluble in CH_2Cl_2). The products **21**, **22**, and **23** (*vide infra*) were isolated by slow evaporation from CH_2Cl_2 with recovered yields between 33–42%. All complexes were characterized by ^1H NMR as well as mass spectrometry, X-ray diffraction and elemental analysis. The analytical data were consistent with **21** unexpectedly being the germanium bis(dithiolate) complex, $\text{Ge}(\text{dmobdt})_2$, rather than the anticipated $\text{Ge}(\text{dmobdt})\text{Cl}_2$. A likely possibility for formation of **21** is outlined in Scheme 6.1, where the initial mixed-ligand complex exhibits a Schlenk-type equilibrium (ligand redistribution reaction) with $\text{Ge}(\text{dmobdt})_2$ and GeCl_4 . However, attempts to capture GeCl_4 through complexation with solvents containing N and O donors (py and THF) were unsuccessful and this process is speculative, although ligand redistribution at Ge(IV) has been reported in mass spectrometry studies.¹⁹



Scheme 6.1. Proposed ligand redistribution reaction of $\text{Ge}(\text{dmobdt})\text{Cl}_2$ to form $\text{Ge}(\text{dmobdt})_2$.

During subsequent examination of **21** as a potential Lewis acid, a second polymorph of **21** was isolated from recrystallization of **21** in the presence of Cl^- . In subsequent discussion the two polymorphs will be referred to as **21-I** and **21-II** respectively. Similar behaviour was observed by Holmes *et al.* who found evidence for formation of a 1:1 adduct with chloride ions in solution but afforded a precipitate of the neutral bis(dithiolate) upon

cooling.⁹ It is noteworthy that a 5-coordinate chloro,-bis(dithiolato)-germanium(IV) anion has been isolated,²⁰ indicating a fine energetic balance between the 4-coordinate neutral Ge(IV) complex and the chloride adduct. The phase behaviour of **21-I** and **21-II** will be discussed in section 6.2.3.

Reaction of the related tetraethoxy tetrathiocin (**1b**) with GeCl₂-dioxane followed a slightly different reaction path. Crystals isolated from this reaction were determined to be a cocrystal comprising the expected germanium(IV) dithiolate (**22**) and unreacted **1b**. Repeated reactions using different stoichiometries persistently afforded **22·1b**. Conversely reaction of GeCl₂-dioxane with tetrathiocin **1c** afforded **23** whose structure is analogous to that of **21**.

6.2.2 Structural studies

Crystals of **21-I**, **21-II**, **22** and **23** were all grown from slow evaporation of DCM solutions under N₂ atmosphere. From the reaction mixture, **21-I** was found to crystallize as yellow blocks in the monoclinic space group P2₁/n. The second phase of Ge(dmobdt)₂, **21-II**, crystallizes in the orthorhombic space group Fdd2 as long, yellow needles. A comparison of the unit cell parameters for the two polymorphs of this complex is presented in Table 6.1.

Table 6.1. Unit cell parameters for **21-I** and **21-II**.

	21-I	21-II
Crystal System	Monoclinic	Orthorhombic
Space Group	P2 ₁ /n	Fdd2
<i>a</i> /Å	11.4460(5)	40.577(2)
<i>b</i> /Å	12.6520(7)	20.0338(12)
<i>c</i> /Å	11.7325(6)	4.5945(3)
<i>a</i> ^o	90	90
<i>b</i> ^o	92.131(2)	90
<i>g</i> ^o	90	90
<i>V</i> /Å ³	1832.06(15)	3735.2
<i>D_c</i> /g cm ⁻³	1.715	1.683

Attempts to crystallize **22** through slow evaporation of DCM from the mother liquor provided long needle-like crystals that diffracted poorly at high angles. Nevertheless, preliminary data were of sufficient quality to solve the structure which revealed that **22** forms a 1:1 cocrystal with the tetrathiocin starting material **1b**. The benzodioxole derivative, **23**, crystallized in the triclinic space group $P\bar{1}$. Crystal structures of **21** (in **21-I**) **22** (in **22-1b**) and **23** are presented in Figure 6.3.

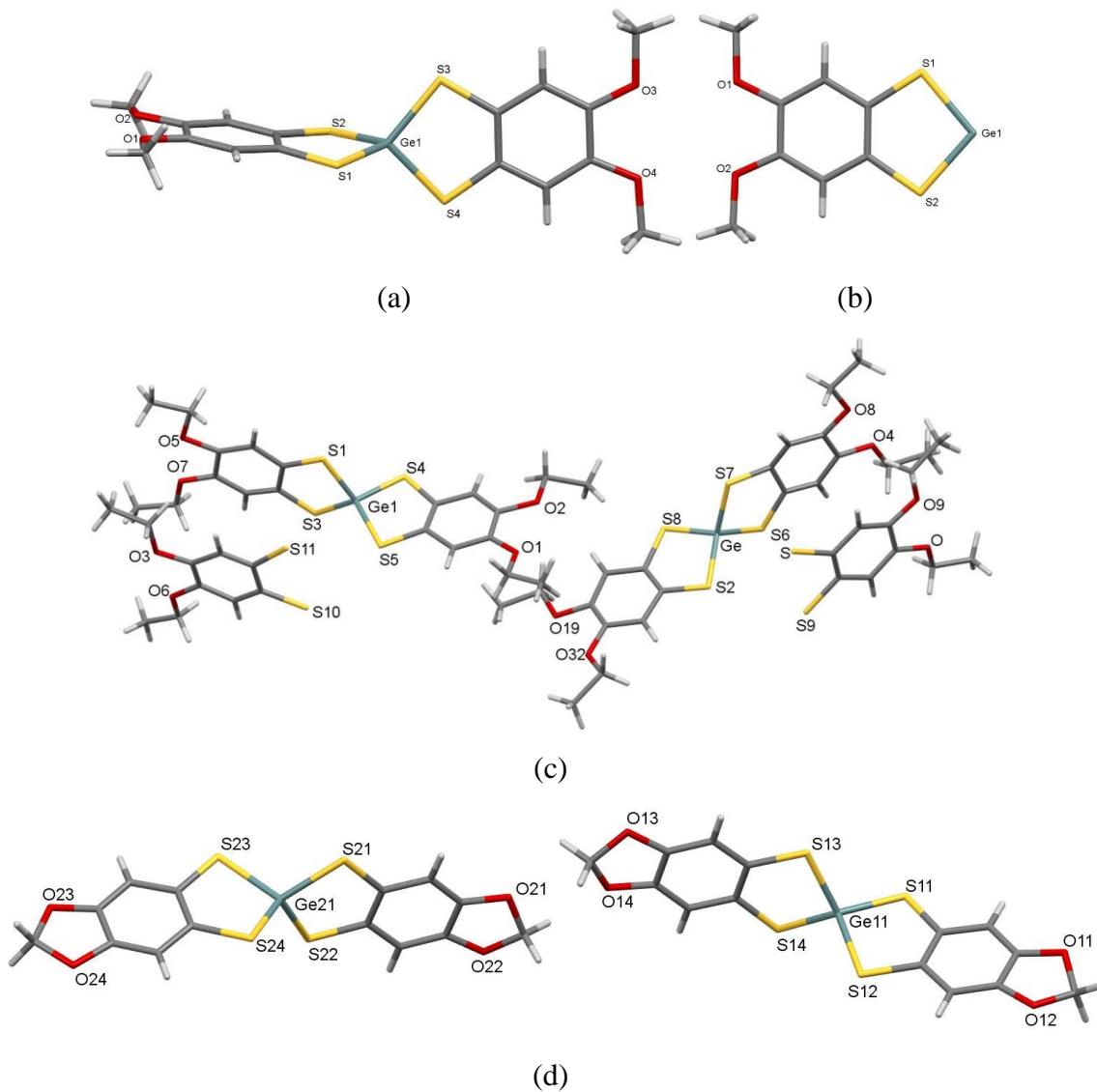


Figure 6.3. Asymmetric unit of (a) **21-I**, (b) **21-II**, (c) **22** and (d) **23** shown in capped sticks.

The Ge–S bond lengths found in these structures fall in the range 2.186(2)–2.216(1) Å and offer SGeS angles between 98.52–100.14° (Table 6.2). These parameters reflect a slightly distorted tetrahedral geometry, with angles falling between 109.15(7)–120.27(7)°, comparable with the three four-coordinate Ge(IV) dithiolate complexes previously reported.^{6,21,22} The chelating SGeS angles fall between 98.54–97.30(2) and the GeS₂ planes intersect at an angle between 77.19–88.50°.

Table 6.2. Summary of important geometric bond lengths and angles for newly synthesized germanium compounds.

	Ge–S1 (Å)	Ge–S2 (Å)	Ge–S3 (Å)	Ge–S4 (Å)	chelate ∠SGeS (°)	∠ between GeS ₂ planes (°)
21-I	2.2003(6)	2.1989(7)	2.2056(7)	2.2022(7)	98.25(2)	88.50
					98.25(2)	
21-II	2.2030(7)	2.2061(7)	–	–	98.54(2)	77.19
22	2.205(9)	2.198(8)	2.232(8)	2.184(9)	97.7(3)	88.60
					98.4(3)	
	2.213(9)	2.198(9)	2.222(9)	2.180(8)	97.7(3)	86.04
					97.7(3)	
23	2.2154(6)	2.2073(6)	2.2026(6)	2.1992(5)	97.67(2)	84.88
					97.76(2)	
	2.2163(6)	2.2007(6)	2.1970(6)	2.2051(6)	98.22(2)	87.75
					97.30(2)	

6.2.3 Phase behaviour of 21-I and 21-II

The purities of both phases of **21** (**21-I** and **21-II**) were confirmed by pXRD at room temperature (Figure 6.4).

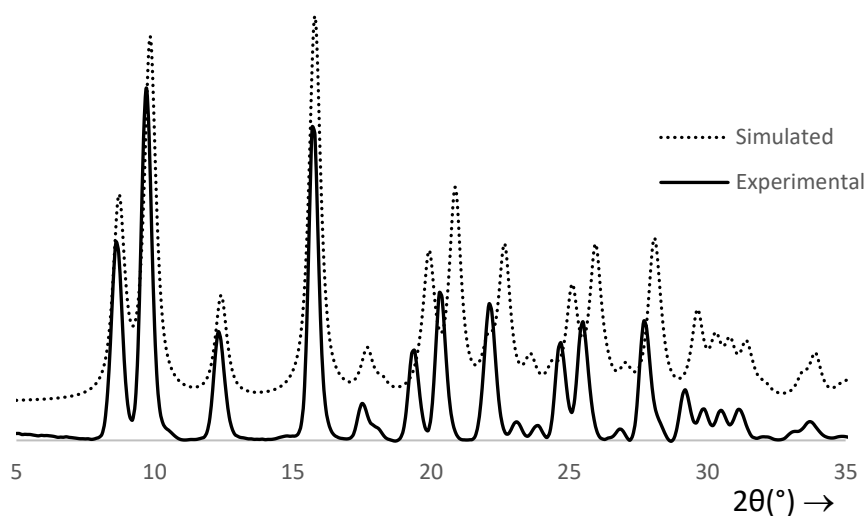
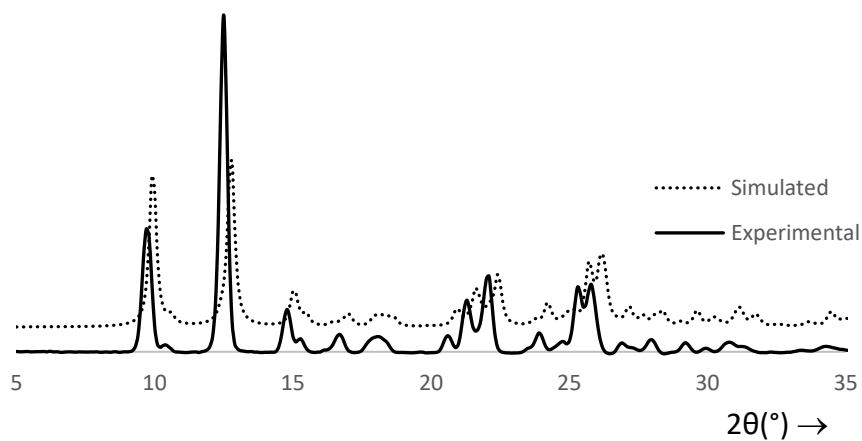


Figure 6.4. Room temperature PXRD profile for (top) **21-I** and (bottom) **21-II**, with simulations based on low temperature SC-XRD (dotted lines).

In order to understand the relationship between the two phases of **21**, DSC studies were undertaken on both the blocks (**21-I**) and needles (**21-II**). A DSC trace on pristine **21-I** showed no thermal event up to the sharp endothermic melt at 230 °C. During heating of the needle phase (**21-II**) a melt was observed at 231 °C (Figure 6.5). However, cooling and

reheating the sample revealed an exotherm (163–173 °C, $\Delta H = -4.5 \text{ kJ mol}^{-1}$) (Figure 6.5) followed by melting again at 231 °C. These observations are consistent with **21-I** melting at 230 °C and crystalizing from the melt to reform **21-I**. Conversely **21-II** appears to form a third (unidentified phase, **21-III**) from the melt. This third phase appears to undergo a transformation (163–173 °C) to reform **21-II** which exhibits the same melting point as pristine **21-II**. A third heat cycle replicates both the transition and melt observed on the previous cycle.

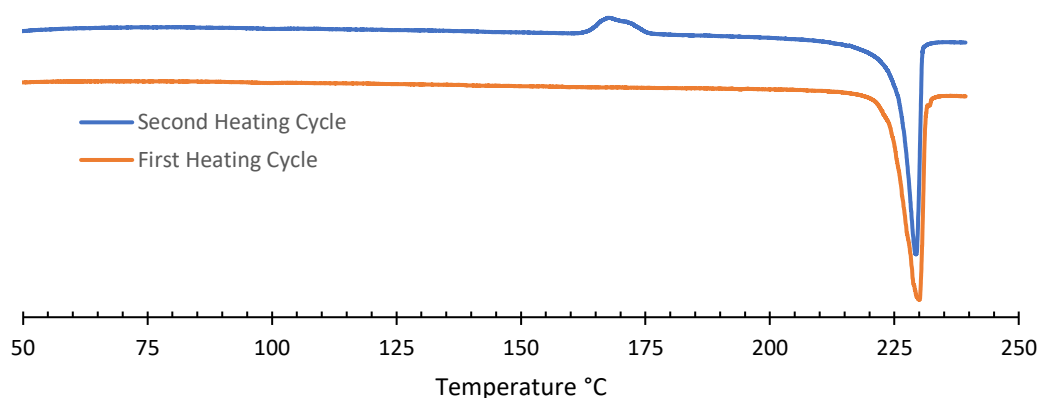


Figure 6.5. DSC profile for the phase pure **21-II** (needles) at a heating rate of 5°C min^{-1} .

VT-PXRD studies were then conducted on both phases to see if any changes to the powder pattern could be observed upon heating. VT-PXRD studies recorded on **21-I** up to 200 °C (Figure 6.6) indicated only minor changes in the peak positions and no evidence for any phase transformation across this temperature range, consistent with DSC data. However, significant discolouration of the material from yellow to orange began at approximately 175 °C (Figure 6.7). PXRD studies on the sample after cooling back to room temperature indicated it was no longer crystalline.

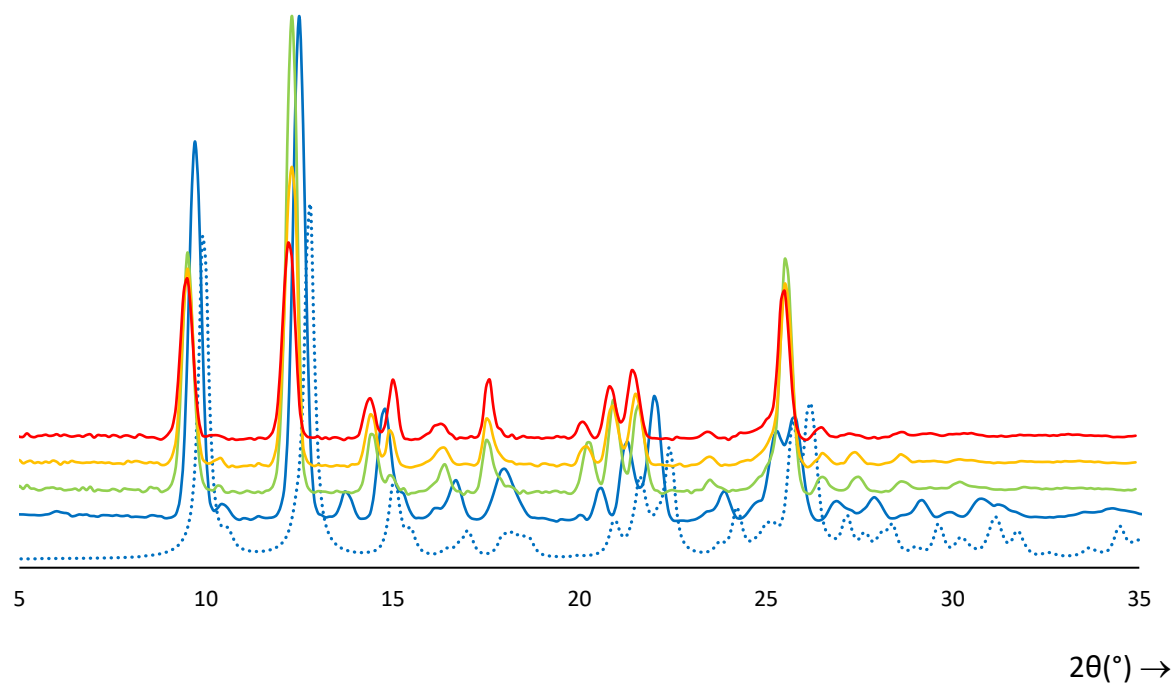


Figure 6.6. Variable temperature PXRD profile for **(21-I)** with simulation based on low temperature SC-XRD (dotted line line), the initial room temperature (blue line), 150 °C (green line), 175 °C (orange line), 200 °C (red line).

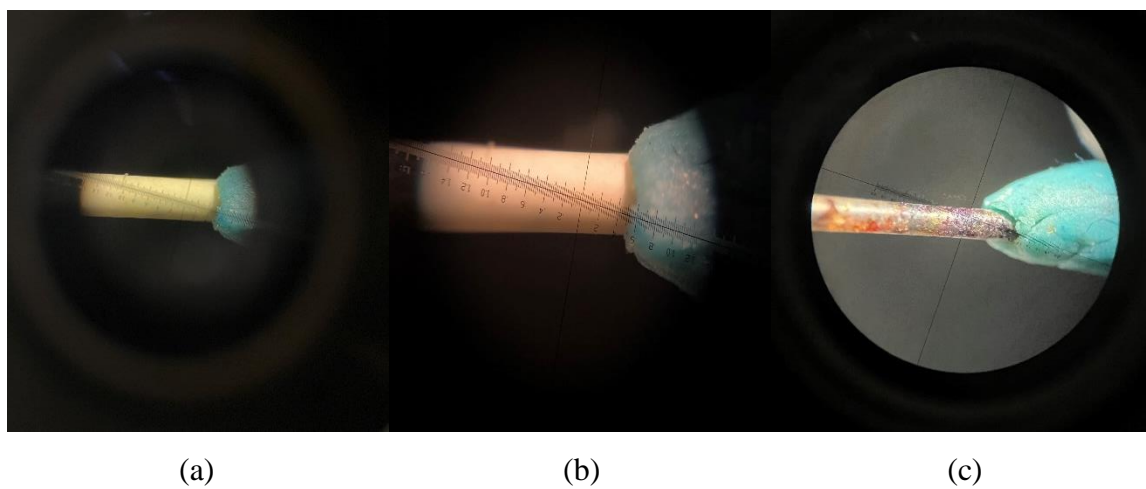


Figure 6.7. Capillaries of **21-I** at (a) room temperature (b) 175 °C and (c) 225 °C.

VT-PXRD on **21-II** indicates that the powder pattern changes on passing through the melt/cool cycle, generating a new PXRD pattern distinct from both **21-I** and **21-II**. The DSC and PXRD data are consistent provided melting of **21-II** forms a new phase (**21-III**) upon cooling the melt and **21-III** undergoes a phase transition around 163 – 173 °C to regenerate **21-II** (which melts at the same temperature as pristine **21-II**).

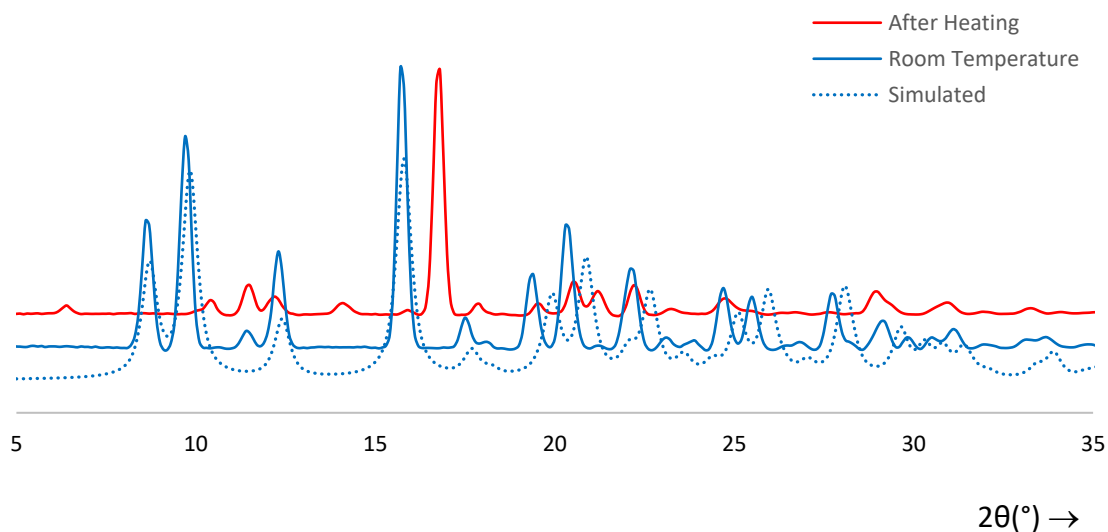


Figure 6.8. Variable temperature PXRD profile for (**21-II**) with simulation based on low temperature SC-XRD (dotted blue line), the initial room temperature (blue line) and room temperature PXRD after heating to 240 °C (red line).

6.3 Conclusions & Future Work

This chapter describes the first foray into the oxidative addition of tetrathiocins to the low valent Ge(II) precursor, GeCl₂-dioxane. Structures obtained through X-ray crystallography reveal the unexpected formation of germanium(IV) bis(dithiolato) complexes at room temperature, which may be mediated *via* a ligand redistribution reaction. The complex **21** was found to be polymorphic exhibiting two structurally determined phases and some evidence for the presence of a third phase based on DSC and PXRD data. Attempts to solve the structure of **21-III** from the PXRD data are on-going.

6.4 Experimental

6.4.1 General Procedures

All manipulations were carried out under an atmosphere of dry nitrogen using standard Schlenk techniques and a dry-nitrogen glove box (MBraun or VAC). All chemicals and reagents were purchased from Sigma-Aldrich and used without further purification. Standard solvents were dried and deoxygenated using an Innovative Technology Solvent Purification System. Tetrathiocins **1a–1c** and **1e** were prepared according to a modified procedure and their analytical data matched the literature report.²³

6.4.2. Physical Measurements

NMR spectra were recorded at room temperature on a Bruker Avance III 500 MHz or Bruker Avance Ultrashield 300 MHz spectrometer. Chemical shifts are reported in ppm relative to internal standards for ¹H and ¹³C using DCM-d₂ (¹H δ = 5.32 ppm, singlet; ¹³C δ = 53.5 ppm, quintet) as an internal reference point relative to Me₄Si (δ = 0 ppm). Elemental compositions were determined on a Perkin Elmer 2400 Series II Elemental Analyzer. Mass spectra were recorded on a Waters XEVO G2-XS spectrometer specifically using the atmospheric solids analysis probe in positive resolution mode (ESI+) or Thermo Scientific DFS (Double Focusing Sector) mass spectrometer (EI+).

6.4.3. X-Ray Crystallography

Crystals for investigation were covered in paratone oil and mounted onto a goniometer head, and then rapidly cooled under a stream of cold N₂ using the low-temperature Oxford Cryostream attached to the Bruker D8 Venture diffractometer equipped with Photon 100 CCD area detector. The data was then collected using the APEX-III software suite,²⁴ integrated using SAINT²⁵ and corrected for absorption using a multi-scan approach (SADABS)²⁶ XPREP was used to determine the space group and the structures were solved by direct methods (SHELXS)²⁷ or intrinsic phasing (SHELXT).²⁸ All structures were refined with full least squares refinement on F^2 using either SHELXL²⁹ or Olex2 software.³⁰ All hydrogen atoms were added at calculated positions and refined isotropically with a riding model.

6.4.4 Synthesis of Ge(dmobdt)₂, Phase I (21-I)

Tetrathiocin **1a** (0.145 g, 0.375 mmol) and GeCl₂·dioxane (0.184 g, 0.750 mmol) were loaded into a Schlenk flask to which dry DCM (10 mL) was added. The initial cloudy yellow solution turned clear in *ca.* 10 mins indicating the reaction was complete. The DCM was removed under reduced pressure and the resulting oil was dissolved in DCM (5 mL). The solution was left at room temperature to slowly evaporate to afford large yellow block-shaped crystals suitable for X-ray diffraction (0.060 g, 34% based on **1a**).

¹H NMR (300 MHz, ppm, DCM-d₂) δ_H = 6.96 (4H, s, benzo C–H), 3.78 (12H, s, O–CH₃)

¹³C NMR (121 MHz, ppm, DCM-d₂) δ_C = 147.8 (s, aryl O–C), 125.3 (s, aryl S–C), 109.87 (s, benzo–C), 56.2 (s, O–CH₃)

Elemental analysis calc. for C₁₆H₁₆GeO₄S₄·¼ CH₂Cl₂: C, 39.47; H, 3.36. Found: C, 39.81; H, 3.09.

HRMS (ESI(+)) *m/z*: = [M]⁺ calc. for C₁₆H₁₆GeO₄S₄⁺ 473.9142; found 473.9141.

Melting Point: 229 °C

IR ν_{max} (cm⁻¹): 2982(w), 2931(w), 2888(w), 2823(w), 1588(w), 1491(s), 1439(m), 1346(m), 1241(vs), 1149(vs), 1028(vs), 917(m), 8.26(s), 779(s), 663(,), 639(sh), 443(w).

6.4.5 Synthesis of Ge(dmobdt)₂, Phase II (21-II)

Ge(dmobdt)₂ (0.052 g, 0.109 mmol), and Ph₄PCl (0.041 g, 0.109 mmol), were loaded into a Schlenk flask to which dry DCM (10 mL) was added. The reaction was stirred for 24 h and the DCM was removed under reduced pressure. The powder was dissolved in DCM (5 mL) and left for recrystallization at room temperature for slow evaporation to afford long yellow needles as single crystals (0.23 g, 42%). Analytical data (¹H NMR, ¹³C NMR, EA, HRMS and IR) revealed this material is consistent with **21-I**, but single crystal X-ray diffraction and PXRD studies are consistent with a second phase.

Melting Point: 230 °C

6.4.6 Synthesis of 2 Ge(deobdt)₂·1b (22)

Tetrathiocin **1b** (0.171 g, 0.375 mmol) and GeCl₂·dioxane (0.184 g, 0.750 mmol) were loaded into a Schlenk flask to which dry DCM (10 mL) was added. The initial cloudy yellow solution turned clear in *ca.* 10 mins indicating the reaction was complete. The DCM

was removed under reduced pressure and the resulting oil was dissolved in DCM (5 mL). The solution was left at room temperature to slowly evaporate to afford yellow needles that could only give preliminary single crystal data (0.051 g, 30%). Note: Upon dissolving into DCM-d₂, the solution turned slightly cloudy indicating that the tetrathiocin (**1b**) was not soluble and therefore visible in the ¹H NMR.

¹H NMR (300 MHz, ppm, DCM-d₂) δ_H = 6.96 (4H, s, benzo C–H), 4.01 (8H, q, ³J = 6.8 Hz, O–CH₂CH₃), 1.39 (12H, t, ³J = 6.8 Hz, O–CH₂CH₃)

Elemental analysis calc. for 2 C₂₀H₂₄GeO₄S₄·C₂₀H₂₄O₄S₄·1½CH₂Cl₂: C, 44.90; H, 4.60. Found: C, 44.72; H, 4.21.

IR ν_{max} (cm⁻¹): 2983(w), 2932(w), 2889(w), 2823(w), 1588(w), 1492(s), 1438(m), 1346(m), 1241(vs), 1200(vs), 1119(m), 1029(vs), 916(m), 827(m), 781(m), 666(m), 634(w), 586(w).

6.4.7 Synthesis of Ge(doxlbdtd)₂(23)

Tetrathiocin **1c** (0.115 g, 0.315 mmol) and GeCl₂·dioxane (0.146 g, 0.630 mmol) were loaded into a Schlenk flask to which dry DCM (10 mL) was added. The initial cloudy yellow solution turned clear in *ca.* 10 mins indicating the reaction was complete. The DCM was removed under reduced pressure and the resulting oil was dissolved in DCM (5 mL). The solution was left at room temperature to slowly evaporate to afford yellow single crystals (0.046 g, 33%).

¹H NMR (300 MHz, ppm, DCM-d₂) δ_H = 6.94 (4H, s, benzo C–H), 5.96 (4H, s, O–CH₂–O)

Elemental analysis calc. for C₁₄H₈GeO₄S₄·1¼ CH₂Cl₂: C, 32.98; H, 1.91. Found: C, 32.88; H, 1.70.

HRMS (EI(+)) *m/z*: = [M]⁺ calc. for C₁₄H₈GeO₄S₄⁺ 441.8512; found 441.8520.

IR ν_{max} (cm⁻¹): 2964(w), 2890(w), 2776(w), 1460(vs), 1221(vs), 1124(m), 1080(m), 923(s), 835(s), 722(m), 647(m), 587(w), 549(w), 448(w).

6.5 References

- (1) M. A. Spence, G. M. Rosair and W. E. Lindsell, *J. Chem. Soc., Dalton Trans.*, 1998, 1581–1586f
- (2) B. E. Bosch, M. Eisenhawer, B. Kersting, K. Kirschbaum, B. Krebs and D. M. Giolando, *Inorg. Chem.*, 1996, **35**, 6599–6605.
- (3) A. F. Berniaz and D. G. Tuck, *Organomet.*, 1973, **51**, 113–118.
- (4) A. V. Zabula, T. Pape, F. Hupka, A. Hepp and F. E. Hahn, *Organomet.*, 2009, **28**, 4221–4224.
- (5) D. L. Turner, T. P. Vaid, P. W. Stephens, K. H. Stone, A. G. DiPasquale and Arnold L. Rheingold, *J. Am. Chem. Soc.*, 2008, **130**, 14–15.
- (6) J. Pfeiffer, M. Noltemeyer and A. Meller, *Z. Anorg. Allg. Chem.*, 1989, **572**, 145–150.
- (7) A. C. Sau, R. O. Day and R. R. Holmes, *J. Am. Chem. Soc.*, 1981, **103**, 1264–1265.
- (8) R. O. Day, J. M. Holmes, A. C. Sau and R. R. Holmes, *Inorg. Chem.*, 1982, **21**, 281–286.
- (9) R. R. Holmes, R. O. Day, A. C. Sau and J. M. Holmes, *Inorg Chem.*, 1986, **25**, 600–606.
- (10) R. L. Melen, M. McPartlin and D. S. Wright, *Dalton Trans.*, 2011, **40**, 1649–1651.
- (11) C. Burschka, *Z. Anorg. Allg. Chem.*, 1978, **446**, 185–192.
- (12) T. A. Shaikh, S. Parkin and D. A. Atwood, *J. Organomet. Chem.*, 2006, **691**, 4167–4171.
- (13) J. Wegener, K. Kirschbaum and D. M. Giolando, *J. Chem. Soc., Dalton Trans.*, 1994, 1213–1218.
- (14) J. M. Kisenyi, G. R. Willey, M. G. B. Drew and S. O. Wandiga, *J. Chem. Soc., Dalton Trans.*, 1985, 69–74.
- (15) M. Arisawa, K. Sawahata, T. Yamada, D. Sarkar and M. Yamaguchi, *Org. Lett.*, 2018, **20**, 938–941.

- (16) (a) N. J. De'Ath and D.B. Denney, *J. Chem. Soc., Chem. Commun.*, 1972, 395–396; (b) B. S. Campbell, N. J. De'Ath, D. B. Denney, D. Z. Denney, I. S. Kipnis and T. B. Min, *J. Am. Chem. Soc.*, 1976, **98**, 2924–2927.
- (17) S. C. Kosnik, M. C. Nascimento, J. M. Rawson and C. L. B. Macdonald, *Dalton Trans.*, 2017, **46**, 9769–9776.
- (18) F. H. Fink, J. A. Turner and D. A. Payne Jr., *J. Am. Chem. Soc.*, 1965, **88**, 1571–1572
- (19) C. G. R. Barrett, J. Charalambous, R. G. Copperthwaite, M. J. Frazer, *Org. Mass Spec.*, 1975, **10**, 146–154.
- (20) Y. Wang, H. Hickox, Y. Xie, P. Wei, S. A. Vlair, M. K. Johnson, H. F. Schaefer III and G. H. Robinson, *J. Am. Chem. Soc.*, 2017, **139**, 6859–6862.
- (21) V. García-Montalvo, M. Granados-Ortíz, A. A. Guevara-García, V. Lomelí, S. González-Gallardo, D. Ocampo-Gutiérrez de Velasco, R. Cea-Olivares, S. Hernández-Ortega and R. A. Toscano, *Polyhedron*, 2011, **30**, 1095–1102.
- (22) I. A. Wright, A. L. Kanibolotsky, J. Cameron, T. Tuttle, P. J. Skabara, S. J. Coles, C. T. Howells, S. A. J. Thomson, S. Gambino and I. D. W. Samuel, *Angew. Chem. Int. Ed.*, 2012, **51**, 4562–4567.
- (23) K. W. Stender, N. Wolki and G. Klar, *Phos., Sulf. Sil. Relat. Elem.*, 1989, **42**, 111–114.
- (24) *APEX III*, Bruker AXS Inc., Madison, WI, 2012.
- (25) *SAINT*, Bruker AXS, Madison, WI, USA.
- (26) *SADABS*, Bruker AXS Inc., Madison, WI, 2015.
- (27) G. M. Sheldrick, *SHELXS-97*, A Program for Automatic Solution of Crystal Structures, University of Göttingen, 1997.
- (28) G. M. Sheldrick., *Acta Cryst.*, 2015, **A71**, 3–8.
- (29) G. M. Sheldrick, *Acta Cryst.*, 2015, **C71**, 3–8.
- (30) O. V. Dolomanov, L. J. Bourhis, R. Gildea, J. A. K. Howard and H. Puschmann, *J. Appl. Crystallogr.*, 2009, **42**, 339–341.

7. CONCLUSIONS AND FUTURE OUTLOOK

7.1 Conclusions

Previous work in our group has demonstrated the oxidative addition of 1,2,5,6-tetrathiocins to zero-valent group 10 metal under microwave irradiation to yield the respective dithiolate complexes.¹ As well, the phosphine co-ligand has also been investigated in a systematic fashion that leads to a variety of mono-, di- and hexanuclear complexes with Pt and Pd centers.^{2,3} Therefore, Chapter 2 of this study looks into changing the dithiolate ligand to tune the electronic properties of the metal complex for both Pt and Pd. These complexes were able to utilize the two-step synthetic route to incorporate crown ether functional groups into the dithiolate backbone and investigate the redox potentials upon binding group 1 metal cations into the benzo-crown dithiolate ligand. Although the redox properties of the complex show shifts in oxidation waves of around 0.1 V in the presence of Na⁺ ions, further work would be required to probe the selectivity of the complexes for different alkali metals and how binding of these other ions would affect the redox and spectroscopic properties. It is also relatively subtle and comparable to other crown ether complexes attached to redox active groups.

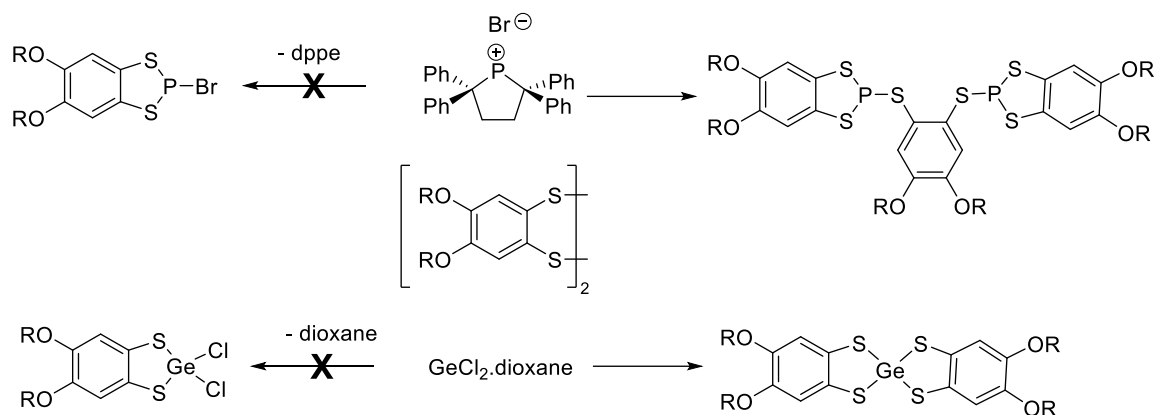
Chapter 3 successfully expands the oxidative addition of 1,2,5,6-tetrathiocins to group 9, Co. A family of compounds was synthesized through the microwave irradiation of CpCo(CO)₂ and the respective tetrathiocin derivative to isolate four novel cobalt compounds. This study investigates the energetic balance between 16e⁻ monomer and the dimeric counterpart of two CoCp(dithiolate) derivatives, **6** and (**6**)₂ as well as **7**, which forms **7** and the cocrystal (**7**)₂·2(**7**)·CH₂Cl₂. Studies on **6** indicate that **6** does not convert to (**6**)₂ thermally, which has been shown by Miller *et al.*⁴ but can be driven mechanochemically.

Chapter 4 utilizes the same synthetic methods as Chapter 3, but to generate cobalt complexes containing the benzo crown ether ligands. These compounds were initially synthesized by Garner and co-workers⁵ through a multi-step labour intensive synthetic route with a poor overall yield. This has allowed us to re-examine the coordination chemistry of these crown ether complexes. We find that although the crowns do indeed bind s-block metal cations, solution and solid-state measurements all point to formation of

2:1 complexes (rather than 1:1 complexes previously proposed) where the alkali metal is sandwiched between two benzo-crown ethers. The electronics of this complexation was probed by a nuanced change (460 cm^{-1}) in the low-energy λ_{max} absorption upon *s*-block metal ion coordination through UV-Vis, whereas electrochemical studies reveal a more pronounced shift in the oxidation potential (+0.32 V) associated with the increased positive charge on the complex. Preliminary complexation studies with *d*-block metals both favored oxidation processes in preference to coordination in the crown ether pocket, with no evidence for coordination of Co(II/III) or Cu(I/II) ions in the crown pocket, however crystallographic studies reveal that oxidation is associated with S–S bond formation.

Chapter 5 focused on synthesizing ‘push-pull’ nickel dithiolate/bipyridine complexes for non-linear optical properties. This series of compounds explored the solvatochromic and chemical trends in the λ_{max} in the visible region and correlate well with the previous empirical models of solvent polarity and substituent effects (Hammett Parameter). An initial complex to examine the effect of the role of the dithiolate ligand was also investigated with one complex. Preliminary data indicate these compounds offer large molecular hyperpolarizabilities and absorption maxima in the NIR region of the electromagnetic spectrum arising from a low energy HOMO-LUMO excitation.

The final chapter expands the reactivity with *p*-block elements through the oxidative addition with a low valent Ge(II) precursor. Synthesis pointed the initial reaction product to undergo a Schlenk equilibrium in order to obtain the germanium bis(dithiolate) species. Two derivatives were successfully crystallized and their structures were confirmed by single crystal x-ray diffraction. Furthermore, the polymorphic nature of **21** was investigated through its thermal properties monitored by DSC and pXRD, which were inconclusive but suggests a potential third phase. This initial look into the reactivity did not produce the expected complex like that which was found from the P(I) compounds.⁶ This indicates that the *p*-block chemistry is not as predictable as the *d*-block, and therefore more experiments should focus on expanding this area of chemical reactivity (Scheme 7.1).

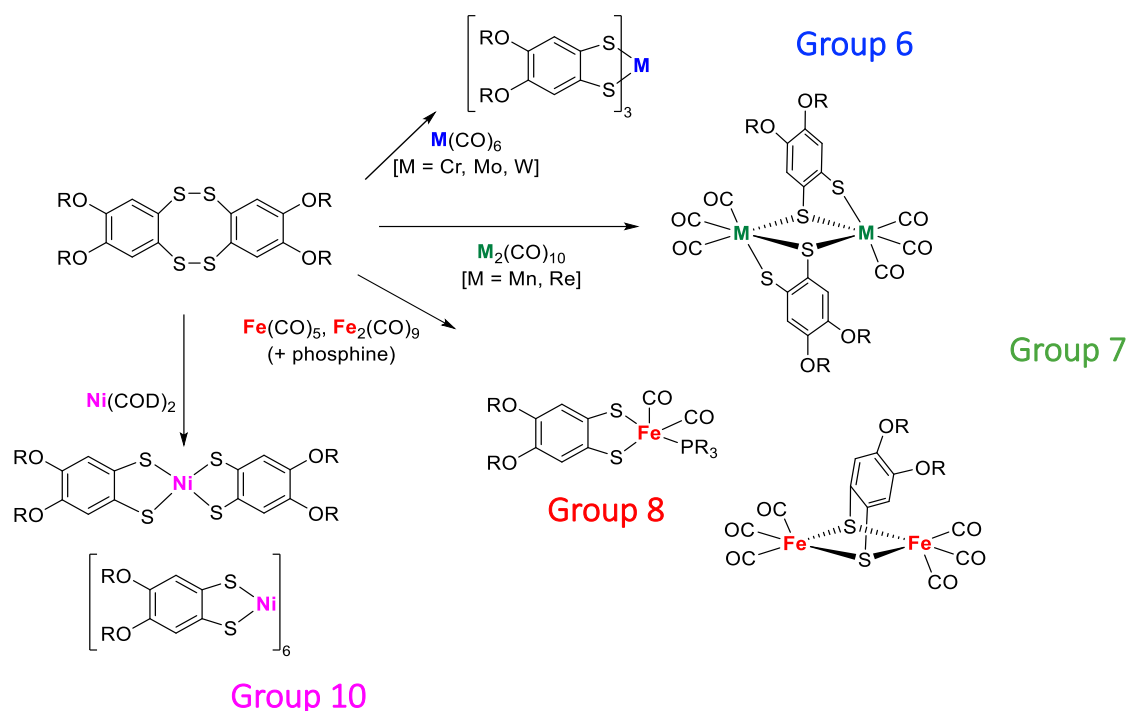


Scheme 7.1. Outlook of *p*-block reactivity to date.

Overall, this research has expanded the range of both metals and supporting ligands that can be used in such oxidative addition chemistry which now incorporates group 9 and 10 metals, Cp, phosphine and bipyridine ligands. This methodology permits a range of coordination complexes to be prepared in a one-pot synthesis. In the case of crown-ether functionalized derivatives this has led to far fewer steps in the synthetic pathway and permitted a more rigorous exploration of the solution chemistry. The latter has highlighted that crown-ether derivatives exhibit some sensitivity of the UV-Vis and electrochemical response and led to some revision of the species formed in solution on addition of alkali metals. While oxidative addition of tetrathiocins also occurs with Ge(II), the *p*-block chemistry is less predictable and further investigations are needed to develop a larger body of work to better understand the underlying themes of the reaction chemistry.

7.2 Future Outlook

The oxidative addition of tetrathiocins to CpCo(CO)₂ is a good indication for the generation of a range of *d*-block complexes derived from other low valent metal carbonyls, including group 6 carbonyls, M(CO)₆ [M = Cr, Mo, W], group 7 carbonyls such as Mn₂(CO)₁₀, and group 8 carbonyls such as Fe(CO)₅ or Fe₂(CO)₉. These reactions can be undertaken in the presence of auxiliary ligands such as phosphines (Scheme 7.2).



Scheme 7.2. Possible reactivity of tetrathiocins with other group 6–10 *d*-block metals.

The group 6 complexes generated from these reactions will be closely related to the tris(dithiolate) molybdenum complexes prepared by Fekl,⁷ which have been used to catalyse the cycloaddition chemistry of tetrathiocins with alkenes and alkynes and offer the potential to make sulfur-rich heterocycles. The iron⁸ and nickel dithiolates and mixed iron/nickel systems could be used as potential models for nickel hydrogenases or as homogeneous hydrogenation catalysts exemplified through recent work by Adams *et al.*⁹ With the extension to group 9 and promising results, future experiments may also include second row transition metals, such as Wilkinson's catalyst, RhCl(PPh₃)₃.

On the main group side, oxidative addition of 1,2,5,6-tetrathiocins has only begun in terms of possible reactivity. The germanium bis(dithiolate) species must be investigated more thoroughly to identify the potential third phase identified through PXRD and DSC studies. Furthermore, poor crystals of the diethoxy dithiolate indicated that two molecules co-crystallize with unreacted starting material. This system requires further investigation in order to unambiguously determine the reaction by obtaining the crystal structure and analytical data. Other low oxidation state *p*-block compounds could also be studied, which

might focus on readily accessible indium(I) and tin(II) precursors such as InCp or InCp* and dialkyl tin species.

Finally, metal dithiolates have been studied since their discovery in the 1960s, however their counterparts of diselenoates chemistry has not been as extensively studied. In a recent paper by Kimura *et al.*¹⁰ they prepared stable diselenetes to form Pt complexes with phosphine co-ligands. These diselenetes also showed their dimerization propensity to form the respective tetraselenocins. Similar structures have also been shown with diselenolate analogues to what is Chapter 3 and 4 of CpCo(R₂C₆H₄E₂) complexes (E = S or Se).¹¹ Work by Dr. Elodie Heyer, previously in our group has found that the corresponding tetraselenocins can be prepared in a similar fashion. Recent work by Freedman and co-workers has shown Cu and V systems offering future avenues of study for quantum computing and molecular electronics.¹²

7.3 References

- (1) J. D. Wrixon, J. J. Hayward, O. Raza and J. M. Rawson, *Dalton Trans.*, 2014, **43**, 2134–2139.
- (2) J. D. Wrixon, J. J. Hayward and J. M. Rawson, *Inorg. Chem.*, 2015, **54**, 9384–9386.
- (3) J. D. Wrixon, Z. S. Ahmed, M. U. Anwar, Y. Beldjoudi, N. Hamidouche, J. J. Hayward and J. M. Rawson, *Polyhedron*, 2016, **108**, 115–121.
- (4) E. J. Miller, T. B. Brill, A. L. Rheingold and W. C. A. Fultz, *J. Am. Chem. Soc.*, 1983, **105**, 7580–7584.
- (5) N. D. Lowe and C. D. Garner, *J. Chem. Soc., Dalton Trans.*, 1993, 2197–2207.
- (6) S. C. Kosnik, M. C. Nascimento, J. M. Rawson and C. L. B. Macdonald, *Dalton Trans.*, 2017, **46**, 9769–9776
- (7) D. J. Harrison, A. J. Lough, N. Nguyen and U. Fekl, *Angew. Chem. Int. Ed.*, 2007, **46**, 7644–7647.
- (8) W.-F. Liaw, C.-K. Hsieh, G.-Y. Lin and G.-H. Lee, *Inorg. Chem.*, 2001, **40**, 3468–3475.

- (9) H. Adams, M. J. Morris, C. C. Robertson and H. C. I. Tunnicliffe, *Organomet.*, 2019, **38**, 665–676.
- (10) T. Kimura, T. Nakahodo and H. Fujihara, *Hetero. Chem.*, 2018, **29**, e21472(1-9)
- (11) S. Habe, T. Yamada, T. Nankawa, J. Mizutani, M. Murata and H. Nishihara, *Inorg. Chem.*, 2003, **42**, 1952–1955.
- (12) M. S. Fataftah, M. D. Krzyaniak, B. Vlasisavljevich, M. R. Wasielewski, J. M. Zadrozny and D E. Freedman, *Chem. Sci.*, 2019, 10, 6707–6714.

APPENDIX A

Crystallographic Information from Chapter 2

** Note that any counterions or solvate molecules within each diagram have been removed for clarity. Where more than one molecule exists in the asymmetric unit, just one molecule is illustrated.*

Structure LW067_1_P21_c

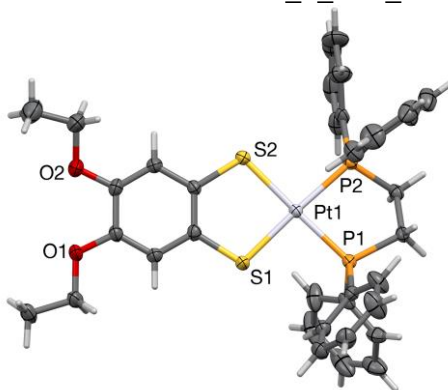


Table A.1. Crystal data and structure refinement for LW067_1_P21_c.

Identification code	LW067_1_P21_c
Empirical formula	C ₃₆ H ₃₆ O ₂ P ₂ PtS ₂
Formula weight	821.80
Temperature/K	170(2)
Crystal system	Monoclinic
Space group	P2 ₁ /c
a/Å	12.1612(5)
b/Å	13.3852(5)
c/Å	23.7430(10)
α/°	90
β/°	94.925(2)
γ/°	90
Volume/Å ³	3850.6(3)
Z	4
ρ _{calc} g/cm ³	1.418
μ/mm ⁻¹	3.863
F(000)	1632
Crystal size/mm ³	0.363 × 0.159 × 0.134
2θ range for data collection/°	2.934 to 26.447
Index ranges	-15 ≤ h ≤ 15 -16 ≤ k ≤ 16 -29 ≤ l ≤ 29
Reflections collected	85346
Independent reflections	7914 [R(int) = 0.0368]
Data/restraints/parameters	7914 / 0 / 390
Goodness-of-fit on F ²	1.029
Final R indexes [I ≥ 2σ (I)]	R ₁ =0.0200, wR ₂ =0.0424
Final R indexes [all data]	R ₁ =0.0268, wR ₂ =0.0450
Largest diff. peak/hole /e Å ⁻³	0.801 and -0.527

Structure LW070_P21_n

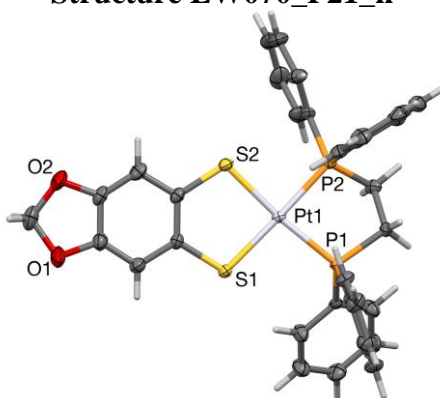


Table A.2. Crystal data and structure refinement for LW070_P21_n.

Identification code	LW070_P21_n
Empirical formula	C ₃₃ H ₂₈ O ₂ P ₂ PtS ₂
Formula weight	777.70
Temperature/K	170(2)
Crystal system	Monoclinic
Space group	P2 ₁ /n
a/Å	11.1176(4)
b/Å	12.7701(5)
c/Å	20.8750(9)
α/°	90
β/°	97.1010(10)
γ/°	90
Volume/Å ³	2941.0(2)
Z	4
ρ _{calc} g/cm ³	1.756
μ/mm ⁻¹	5.052
F(000)	1528
Crystal size/mm ³	0.386 × 0.086 × 0.016
2θ range for data collection/°	2.987 to 25.433
Index ranges	-13 ≤ h ≤ 12 -15 ≤ k ≤ 15 -25 ≤ l ≤ 25
Reflections collected	9962
Independent reflections	5420 [R(int) = 0.0650]
Data/restraints/parameters	5420 / 0 / 361
Goodness-of-fit on F ²	1.116
Final R indexes [I ≥ 2σ (I)]	R ₁ =0.0268, wR ₂ =0.0478
Final R indexes [all data]	R ₁ =0.0392, wR ₂ =0.0519
Largest diff. peak/hole /e Å ⁻³	1.227 and -0.869

Structure LW071_2ndxtal

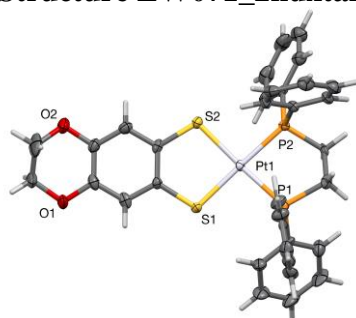


Table A.3. Crystal data and structure refinement for LW071_2ndxtal.

Identification code	LW071_2ndxtal
Empirical formula	C _{34.5} H ₃₁ ClO ₂ P ₂ PtS ₂
Formula weight	834.19
Temperature/K	170(2)
Crystal system	Monoclinic
Space group	P2 ₁ /n
a/Å	17.8196(7)
b/Å	20.1432(1)
c/Å	17.8701(9)
α/°	90
β/°	92.049
γ/°	90
Volume/Å ³	6410.3(5)
Z	8
ρ _{calc} g/cm ³	1.729
μ/mm ⁻¹	4.723
F(000)	3288
Crystal size/mm ³	0.508 × 0.278 × 0.088
2θ range for data collection/°	3.049 to 26.25
Index ranges	-19 ≤ h ≤ 22 -24 ≤ k ≤ 25 -21 ≤ l ≤ 22
Reflections collected	96564
Independent reflections	9277 [R(int) = 0.1349]
Data/restraints/parameters	9277 / 0 / 766
Goodness-of-fit on F ²	1.040
Final R indexes [I ≥ 2σ (I)]	R ₁ =0.0501, wR ₂ =0.0863
Final R indexes [all data]	R ₁ =0.0897, wR ₂ =0.1009
Largest diff. peak/hole /e Å ⁻³	2.409 and -1.733

Structure LW069_1

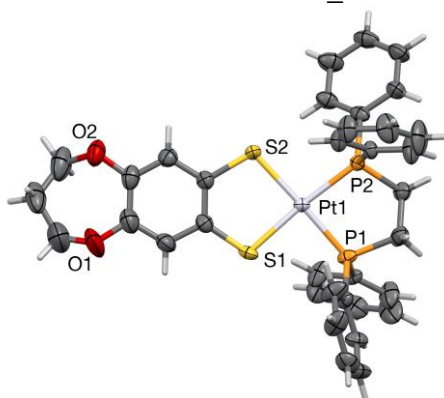


Table A.4. Crystal data and structure refinement for LW069_1.

Identification code	LW069_1
Empirical formula	C ₃₅ H ₃₂ O ₂ P ₂ PtS ₂
Formula weight	805.75
Temperature/K	170(2)
Crystal system	Orthorhombic
Space group	P 2 ₁ 2 ₁ 2 ₁
a/Å	11.4938(4)
b/Å	12.8694(4)
c/Å	21(4788(6))
α/°	90
β/°	90
γ/°	90
Volume/Å ³	3177.11(17)
Z	4
ρ _{calc} g/cm ³	1.685
μ/mm ⁻¹	4.680
F(000)	1592
Crystal size/mm ³	0.420 × 0.252 × 0.241
2θ range for data collection/°	3.040 to 27.544
Index ranges	-14 ≤ h ≤ 14 -13 ≤ k ≤ 16 -27 ≤ l ≤ 27
Reflections collected	36129
Independent reflections	7216 [R(int) = 0.0276]
Data/restraints/parameters	7216 / 60 / 409
Goodness-of-fit on F ²	1.018
Final R indexes [I ≥ 2σ (I)]	R ₁ =0.0233, wR ₂ =0.0511
Final R indexes [all data]	R ₁ =0.0263, wR ₂ =0.0524
Largest diff. peak/hole /e Å ⁻³	0.692 and -0.767

Structure LW072_P21_n

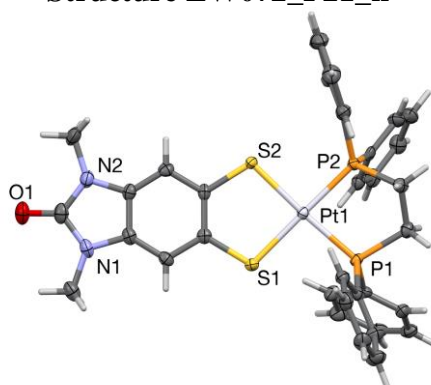


Table A.5. Crystal data and structure refinement for LW072_P21_n.

Identification code	LW072_P21_n
Empirical formula	C ₃₅ H ₃₂ O ₂ N ₂ P ₂ PtS ₂
Formula weight	817.77
Temperature/K	170(2)
Crystal system	Monoclinic
Space group	P2 ₁ /n
a/Å	10.2809(5)
b/Å	16.2519(7)
c/Å	18.8916(9)
α/°	90
β/°	95.946(2)
γ/°	90
Volume/Å ³	3139.5(3)
Z	4
ρ _{calc} g/cm ³	1.730
μ/mm ⁻¹	4.737
F(000)	1616
Crystal size/mm ³	0.269 × 0.227 × 0.138
2θ range for data collection/°	3.057 to 27.578
Index ranges	-13 ≤ h ≤ 13 -20 ≤ k ≤ 21 -24 ≤ l ≤ 24
Reflections collected	108432
Independent reflections	5755 [R(int) = 0.0901]
Data/restraints/parameters	5755 / 0 / 390
Goodness-of-fit on F ²	1.130
Final R indexes [I ≥ 2σ (I)]	R ₁ =0.0383, wR ₂ =0.0629
Final R indexes [all data]	R ₁ =0.0619, wR ₂ =0.0712
Largest diff. peak/hole /e Å ⁻³	1.502 and -0.993

Structure LW073_P21_c

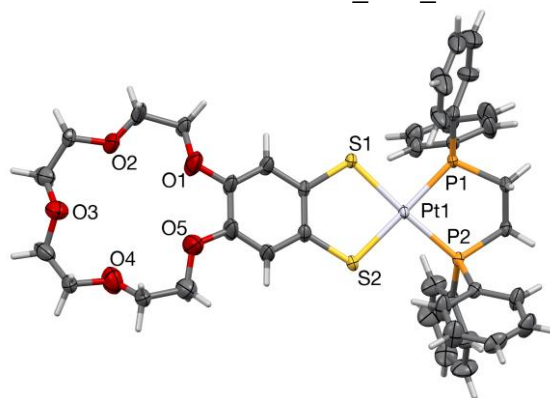


Table A.5. Crystal data and structure refinement for LW073_P21_c.

Identification code	LW073_P21_c
Empirical formula	C ₄₀ H ₄₂ O ₅ P ₂ PtS ₂
Formula weight	923.88
Temperature/K	170(2)
Crystal system	Monoclinic
Space group	P2 ₁ /c
a/Å	11.6904(5)
b/Å	13.5792(6)
c/Å	24.8680(12)
α/°	90
β/°	101.911(2)
γ/°	90
Volume/Å ³	3862.7(3)
Z	4
ρ _{calc} g/cm ³	1.589
μ/mm ⁻¹	3.866
F(000)	1848
Crystal size/mm ³	0.216 × 0.137 × 0.129
2θ range for data collection/°	2.925 to 29.206
Index ranges	-14 ≤ h ≤ 16 -18 ≤ k ≤ 18, -34 ≤ l ≤ 34
Reflections collected	158228
Independent reflections	10455 [R(int) = 0.0819]
Data/restraints/parameters	10455 / 0 / 451
Goodness-of-fit on F ²	1.051
Final R indexes [I ≥ 2σ (I)]	R ₁ =0.0478, wR ₂ =0.1012
Final R indexes [all data]	R ₁ =0.0693, wR ₂ =0.1117
Largest diff. peak/hole /e Å ⁻³	3.365 and -1.828

Structure LW088_1_P_1

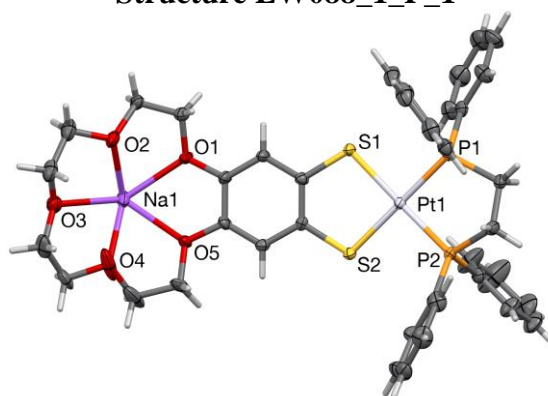


Table A.5. Crystal data and structure refinement for LW088_1_P_1.

Identification code	LW088_1_P_1
Empirical formula	C ₆₆ H ₆₆ BCl ₄ NaO ₅ P ₂ PtS ₂
Formula weight	1435.93
Temperature/K	150(2)
Crystal system	Triclinic
Space group	P $\bar{1}$
a/Å	13.0406(8)
b/Å	16.0671(16)
c/Å	16.7995(11)
α /°	80.747(4)
β /°	78.054(2)
γ /°	66.431(3)
Volume/Å ³	3144.4(4)
Z	2
ρ_{calc} g/cm ³	1.517
μ /mm ⁻¹	2.575
F(000)	1452
Crystal size/mm ³	0.237 × 0.228 × 0.118
2 θ range for data collection/°	2.941 to 27.530
Index ranges	-12 ≤ h ≤ 16 -20 ≤ k ≤ 20 -21 ≤ l ≤ 21
Reflections collected	37422
Independent reflections	14041 [R(int) = 0.0250]
Data/restraints/parameters	14041 / 29 / 762
Goodness-of-fit on F ²	1.133
Final R indexes [I ≥ 2 σ (I)]	R ₁ =0.0319 wR ₂ =0.0658
Final R indexes [all data]	R ₁ =0.0416, wR ₂ =0.0712
Largest diff. peak/hole /e Å ⁻³	2.209 and -1.181

Structure LW098

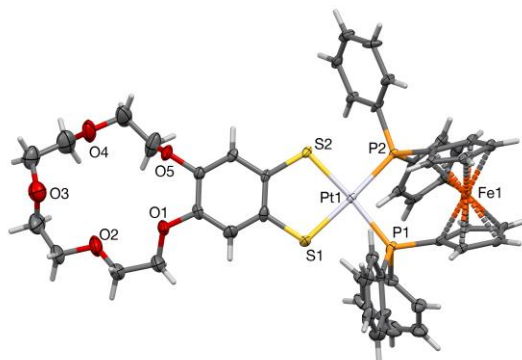


Table A.6. Crystal data and structure refinement for LW098_1_P_1.

Identification code	LW098
Empirical formula	C _{50.75} H _{51.50} Cl _{5.50} FeO ₅ P ₂ S ₂
Formula weight	1313.39
Temperature/K	150(2)
Crystal system	Monoclinic
Space group	P2 ₁ /c
a/Å	18.343(2)
b/Å	19.8358(19)
c/Å	15.1897(17)
α/°	90
β/°	102.082(4)
γ/°	90
Volume/Å ³	5404.4(10)
Z	4
ρ _{calc} g/cm ³	1.614
μ/mm ⁻¹	3.307
F(000)	2622
Crystal size/mm ³	0.388 × 0.274 × 0.149
2θ range for data collection/°	2.836 to 26.434
Index ranges	-22 ≤ h ≤ 22 -24 ≤ k ≤ 24 -18 ≤ l ≤ 19
Reflections collected	170329
Independent reflections	11090 [R(int) = 0.0965]
Data/restraints/parameters	11090 / 26 / 631
Goodness-of-fit on F ²	1.103
Final R indexes [I ≥ 2σ (I)]	R ₁ =0.0736, wR ₂ =0.1667
Final R indexes [all data]	R ₁ =0.0980, wR ₂ =0.1822
Largest diff. peak/hole /e Å ⁻³	4.480 and -2.389

Structure LW089_3rdxtal_P21_c

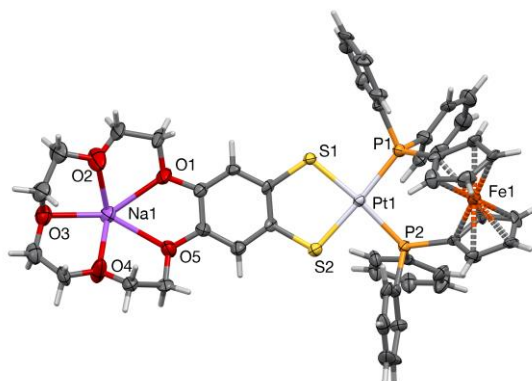


Table A.7. Crystal data and structure refinement for LW089_3rdxtal_P21_c.

Identification code	LW089_3rdxtal_P21_c
Empirical formula	C ₇₂ H ₆₆ BFeNaO ₅ P ₂ PtS ₂
Formula weight	1422.04
Temperature/K	150(2)
Crystal system	Monoclinic
Space group	P2 ₁ /c
a/Å	10.8886(6)
b/Å	33.2871(17)
c/Å	17.9102(9)
α/°	90
β/°	106.0570(10)
γ/°	90
Volume/Å ³	6238.3(6)
Z	4
ρ _{calc} g/cm ³	1.514
μ/mm ⁻¹	7.587
F(000)	2880
Crystal size/mm ³	0.176 × 0.153 × 0.109
2θ range for data collection/°	3.984 to 50.358
Index ranges	-10 ≤ h ≤ 10 -33 ≤ k ≤ 33 -17 ≤ l ≤ 17
Reflections collected	59803
Independent reflections	6471 [R(int) = 0.0534]
Data/restraints/parameters	6471 / 365 / 787
Goodness-of-fit on F ²	1.271
Final R indexes [I >= 2σ (I)]	R ₁ =0.0961, wR ₂ =0.1992
Final R indexes [all data]	R ₁ =0.1125, wR ₂ =0.2065
Largest diff. peak/hole /e Å ⁻³	1.120 and -3.703

APPENDIX B

Crystallographic Information from Chapter 3

** Note that any H atoms within each diagram have been removed for clarity.*

Structure LW046_Pbca_a

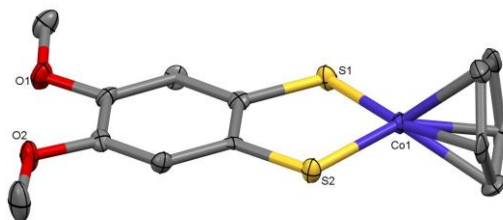


Table B.1. Crystal data and structure refinement for LW046_Pbca_a.

Identification code	LW046_Pbca_a
Empirical formula	C ₁₃ H ₁₃ CoO ₂ S ₂
Formula weight	324.28
Temperature/K	149.93
Crystal system	orthorhombic
Space group	Pbca
a/Å	9.0701(4)
b/Å	7.3043(3)
c/Å	39.5242(18)
α/°	90
β/°	90
γ/°	90
Volume/Å ³	2618.5(2)
Z	8
ρ _{calc} /cm ³	1.645
μ/mm ⁻¹	13.176
F(000)	1328.0
Crystal size/mm ³	0.365 × 0.168 × 0.161
Radiation	CuKα (λ = 1.54178)
2θ range for data collection/°	8.95 to 109.984
Index ranges	-9 ≤ h ≤ 9 -7 ≤ k ≤ 6 -41 ≤ l ≤ 41
Reflections collected	10701
Independent reflections	1633 [R _{int} = 0.0679, R _{sigma} = 0.0449]
Data/restraints/parameters	1633 / 12 / 165
Goodness-of-fit on F ²	1.286
Final R indexes [I ≥ 2σ (I)]	R ₁ = 0.0541, wR ₂ = 0.1270
Final R indexes [all data]	R ₁ = 0.0586, wR ₂ = 0.1287
Largest diff. peak/hole / e Å ⁻³	0.46/-0.52

Structure LW062_2_P_1_a

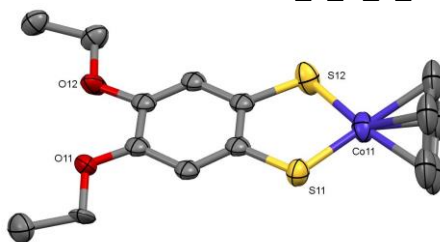


Table B.2. Crystal data and structure refinement for LW062_2_P_1_a.

Identification code	lw062_2_p_1_a
Empirical formula	C ₁₅ H ₁₇ CoO ₂ S ₂
Formula weight	352.33
Temperature/K	170(2)
Crystal system	triclinic
Space group	P-1
<i>a</i> /Å	8.6038(6)
<i>b</i> /Å	8.6688(5)
<i>c</i> /Å	41.693(3)
α/°	88.980(2)
β/°	90
γ/°	90
Volume/Å ³	3109.2(3)
Z	8
ρ _{calc} /cm ³	1.505
μ/mm ⁻¹	11.143
F(000)	1456.0
Crystal size/mm ³	0.160 × 0.052 × 0.040
Radiation	CuKα (λ = 1.54178)
2θ range for data collection/°	8.484 to 100.876
Index ranges	-8 ≤ <i>h</i> ≤ 8 -8 ≤ <i>k</i> ≤ 8 -41 ≤ <i>l</i> ≤ 41
Reflections collected	18077
Independent reflections	4343 [R _{int} = 0.0614, R _{sigma} = 0.0776]
Data/restraints/parameters	4343 / 51 / 531
Goodness-of-fit on F ²	1.053
Final R indexes [<i>I</i> ≥ 2σ (<i>I</i>)]	R ₁ = 0.0795, wR ₂ = 0.1567
Final R indexes [all data]	R ₁ = 0.1217, wR ₂ = 0.1804
Largest diff. peak/hole / e Å ⁻³	0.72 and -0.46

Structure of LW037_a

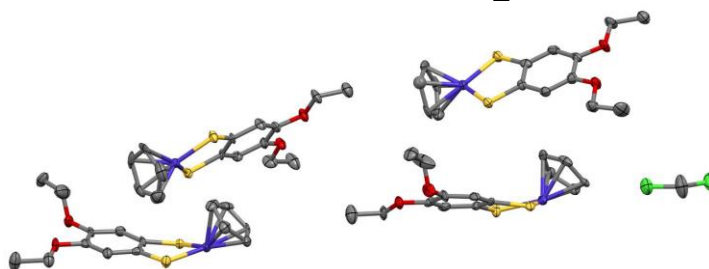


Table B.3. Crystal data and structure refinement for LW037_a.

Identification code	LW037_a
Empirical formula	$C_{15.25}H_{17}Cl_{0.5}CoO_2S_2$
Formula weight	373.06
Temperature/K	149.88
Crystal system	triclinic
Space group	P-1
a/Å	7.1883(15)
b/Å	20.081(4)
c/Å	23.291(5)
$\alpha/^\circ$	97.447(10)
$\beta/^\circ$	98.801(7)
$\gamma/^\circ$	100.016(7)
Volume/Å ³	3229.3(12)
Z	8
$\rho_{\text{calc}}/\text{cm}^3$	1.535
μ/mm^{-1}	1.403
F(000)	1536.0
Crystal size/mm ³	0.191 × 0.143 × 0.138
Radiation	MoK α ($\lambda = 0.71073$)
2 Θ range for data collection/ $^\circ$	5.802 to 51.272
Index ranges	-8 ≤ h ≤ 8 -23 ≤ k ≤ 24 -28 ≤ l ≤ 27
Reflections collected	35533
Independent reflections	11228 [$R_{\text{int}} = 0.0855$, $R_{\text{sigma}} = 0.0990$]
Data/restraints/parameters	11228 / 0 / 751
Goodness-of-fit on F ²	1.130
Final R indexes [$I \geq 2\sigma(I)$]	$R_1 = 0.0768$, $wR_2 = 0.2217$
Final R indexes [all data]	$R_1 = 0.1336$, $wR_2 = 0.2562$
Largest diff. peak/hole / e Å ⁻³	0.94/-0.89

Structure of LW059_P_1_a

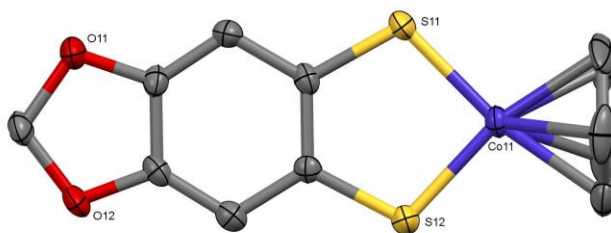


Table B.4. Crystal data and structure refinement for LW059_P_1_a.

Identification code	lw059_p_1_a
Empirical formula	C ₁₂ H ₉ CoO ₂ S ₂
Formula weight	308.24
Temperature/K	170(2)
Crystal system	triclinic
Space group	P-1
<i>a</i> /Å	6.2350(2)
<i>b</i> /Å	13.4679(4)
<i>c</i> /Å	14.6858(4)
α /°	109.1900(10)
β /°	99.8150(10)
γ /°	91.9760(10)
Volume/Å ³	1142.19(6)
<i>Z</i>	4
ρ_{calc} /cm ³	1.793
μ /mm ⁻¹	15.070
<i>F</i> (000)	624.0
Crystal size/mm ³	0.219 × 0.138 × 0.122
Radiation	CuK α (λ = 1.54178)
2 θ range for data collection/°	6.494 to 136.766
	-7 ≤ <i>h</i> ≤ 7
Index ranges	-16 ≤ <i>k</i> ≤ 16
	-17 ≤ <i>l</i> ≤ 17
Reflections collected	32545
Independent reflections	4194 [<i>R</i> _{int} = 0.0666, <i>R</i> _{sigma} = 0.0363]
Data/restraints/parameters	4194 / 0 / 307
Goodness-of-fit on <i>F</i> ²	1.059
Final <i>R</i> indexes [<i>I</i> ≥ 2 σ (<i>I</i>)]	<i>R</i> ₁ = 0.0431, <i>wR</i> ₂ = 0.0883
Final <i>R</i> indexes [all data]	<i>R</i> ₁ = 0.0571, <i>wR</i> ₂ = 0.0961
Largest diff. peak/hole / e Å ⁻³	0.65 and -0.35

Structure of LW060_P21_n_a

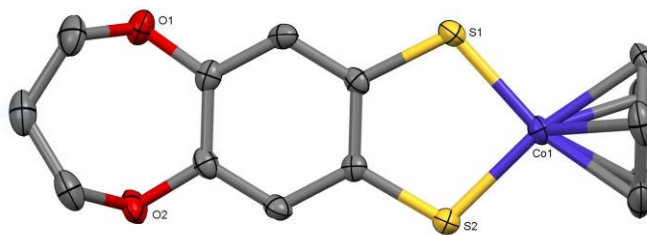


Table B.5. Crystal data and structure refinement for LW060_P21_n_a

Identification code	LW060_P21_n_a
Empirical formula	C ₁₄ H ₁₃ CoO ₂ S ₂
Formula weight	336.29
Temperature/K	170.0
Crystal system	monoclinic
Space group	P2 ₁ /n
a/Å	6.6495(2)
b/Å	7.1273(3)
c/Å	28.5224(11)
α/°	90
β/°	94.1340(10)
γ/°	90
Volume/Å ³	1348.24(9)
Z	4
ρ _{calc} /cm ³	1.657
μ/mm ⁻¹	1.575
F(000)	688.0
Crystal size/mm ³	0.214 × 0.208 × 0.184
Radiation	MoKα (λ = 0.71073)
2θ range for data collection/°	5.892 to 52.856
Index ranges	-8 ≤ h ≤ 8 -8 ≤ k ≤ 8 -35 ≤ l ≤ 35
Reflections collected	41117
Independent reflections	41117 [R _{int} = 0.0601, R _{sigma} = 0.0517]
Data/restraints/parameters	41117 / 0 / 225
Goodness-of-fit on F ²	1.068
Final R indexes [I ≥ 2σ (I)]	R ₁ = 0.0423, wR ₂ = 0.0696
Final R indexes [all data]	R ₁ = 0.0601, wR ₂ = 0.0742
Largest diff. peak/hole / e Å ⁻³	0.37 and -0.44

APPENDIX C

Crystallographic Information from Chapter 4

** Note that any H atoms within each diagram have been removed for clarity.*

Structure of JMR_LW017



Table C.1. Crystal data and structure refinement for JMR_LW017.

Identification Code	JMR_LW017
Empirical formula	C ₂₁ H ₂₇ CoO ₆ S ₂
Formula weight	498.47
Temperature/K	149.99
Crystal system	monoclinic
Space group	P2 ₁ /c
a/Å	14.5232(12)
b/Å	17.0416(11)
c/Å	8.9492(7)
α/°	90
β/°	96.345(5)
γ/°	90
Volume/Å ³	2201.3(3)
Z	4
ρ _{calc} /cm ³	1.504
μ/mm ⁻¹	1.004
F(000)	1040.0
Crystal size/mm ³	0.05 × 0.05 × 0.01
Radiation	MoKα (λ = 0.71073)
2θ range for data collection/°	3.698 to 49.35
Index ranges	-16 ≤ h ≤ 17 -19 ≤ k ≤ 19 -10 ≤ l ≤ 8
Reflections collected	21142
Independent reflections	3692 [R _{int} = 0.1491, R _{sigma} = 0.1427]
Data/restraints/parameters	3692 / 36 / 241
Goodness-of-fit on F ²	1.256
Final R indexes [I ≥ 2σ (I)]	R ₁ = 0.1350, wR ₂ = 0.2060
Final R indexes [all data]	R ₁ = 0.2071, wR ₂ = 0.2339
Largest diff. peak/hole / e Å ⁻³	0.75 and -0.81

Structure of LW075

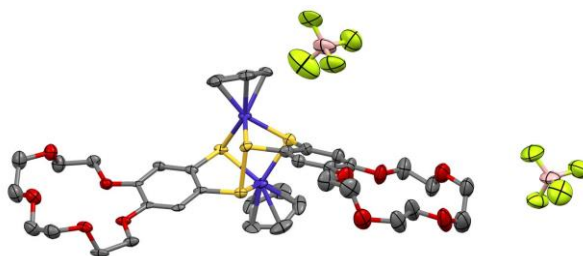


Table C.2. Crystal data and structure refinement for LW075.

Identification code	LW075
Empirical formula	C ₃₈ H ₄₆ O ₁₀ S ₄ Co ₂ B ₂ F ₈
Formula weight	1082.47
Temperature/K	170(2)
Crystal system	monoclinic
Space group	P2 ₁ /c
<i>a</i> /Å	19.2080(12)
<i>b</i> /Å	11.1691(7)
<i>c</i> /Å	25.6152(16)
α /°	90
β /°	103.133(4)
γ /°	90
Volume/Å ³	5351.6(6)
<i>Z</i>	4
ρ_{calc} /cm ³	1.343
μ /mm ⁻¹	6.969
F(000)	2216.0
Crystal size/mm ³	0.296 × 0.163 × 0.04
Radiation	CuK α (λ = 1.54178)
2 θ range for data collection/°	7.088 to 109.302
Index ranges	-20 ≤ <i>h</i> ≤ 20 -11 ≤ <i>k</i> ≤ 11 -26 ≤ <i>l</i> ≤ 26
Reflections collected	61316
Independent reflections	6592 [<i>R</i> _{int} = 0.1226, <i>R</i> _{sigma} = 0.0590]
Data/restraints/parameters	6592 / 384 / 608
Goodness-of-fit on <i>F</i> ²	1.099
Final <i>R</i> indexes [<i>I</i> >= 2 σ (<i>I</i>)]	<i>R</i> ₁ = 0.0956, <i>wR</i> ₂ = 0.2289
Final <i>R</i> indexes [all data]	<i>R</i> ₁ = 0.1094, <i>wR</i> ₂ = 0.2377
Largest diff. peak/hole / e Å ⁻³	1.30 and -0.69

APPENDIX D

Supplementary Information on Chapter 4

I. Mass Spectrometry

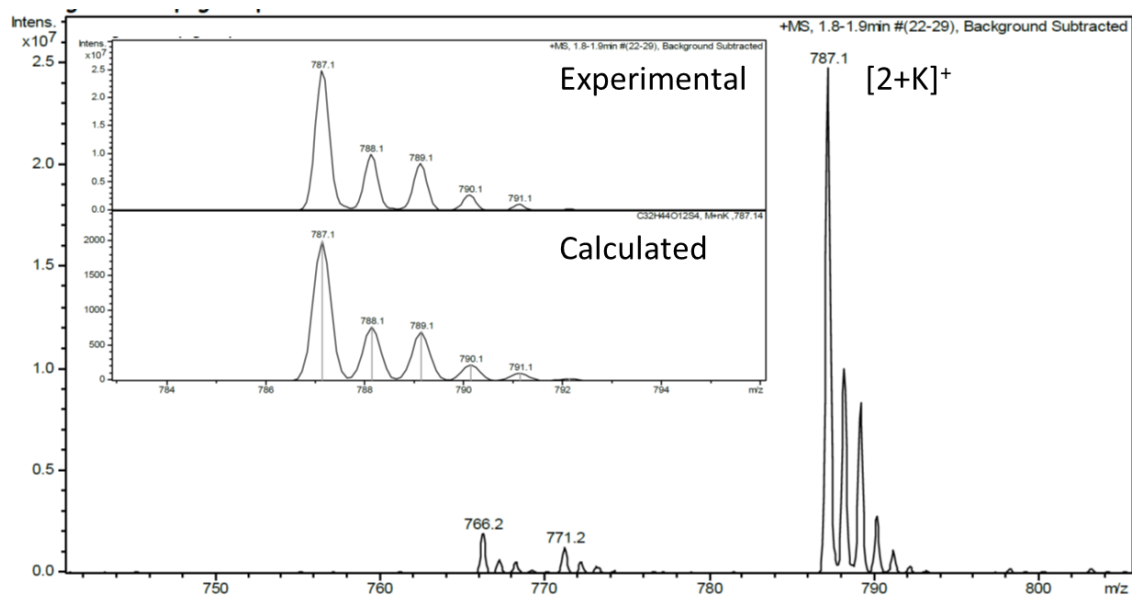


Figure D.1. Mass spectrum of **1h** after storage in a glass vial reveals **[1h+K]⁺** (The isotopomers at 771 correspond to **[1h+Na]⁺** and those at 766 correspond to **[1h+NH₄]⁺**).

Inset: comparison of calculated and experimental isotope distribution patterns for **[1h+K]⁺**.

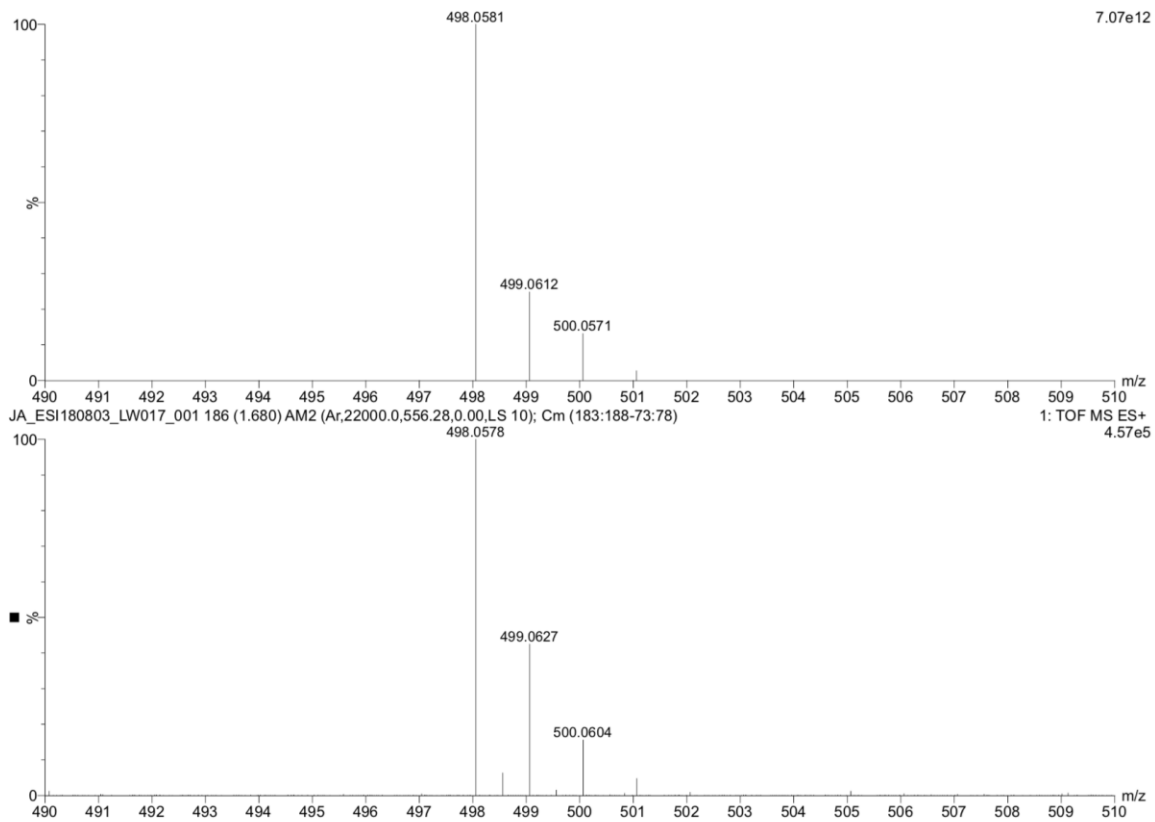


Figure D.2. (top) Experimental HRMS ASAP(+) mass spectrum of **12** and (bottom) simulated HRMS spectrum

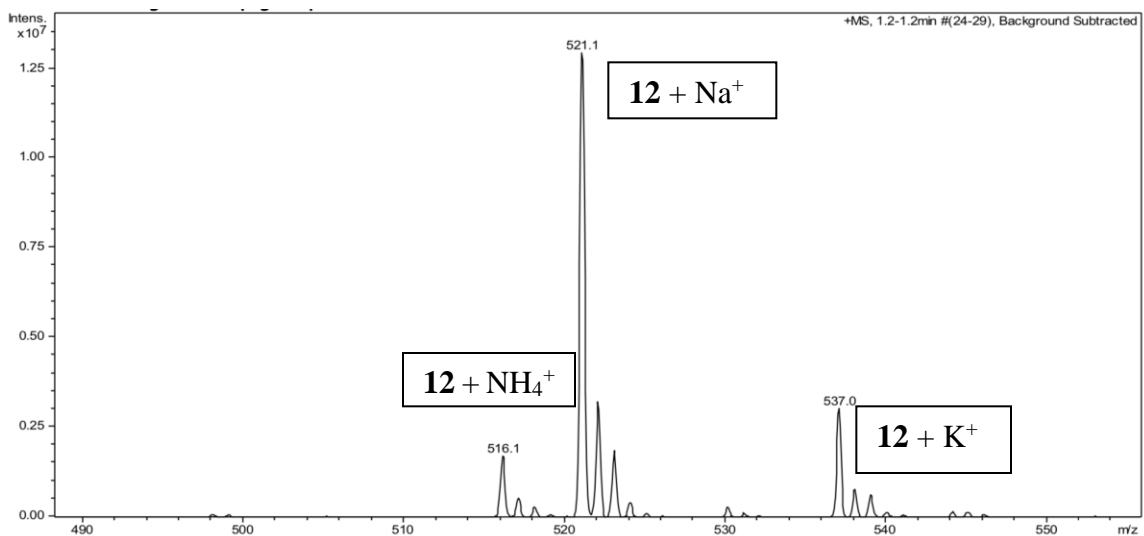


Figure D.3. Mass spectrometry of **12** showing complexation with ions from the glass vial: $12 + \text{NH}_4^+$ ($m/z = 516$; calculated isotope distribution pattern: 516 = 100, 517 = 25.4, 518 = 13.1, 519 = 2.5) $12 + \text{Na}^+$ ($m/z = 521$; calculated isotope distribution pattern: 521 = 100, 522 = 25, 523 = 13, 524 = 2.5) and $12 + \text{K}^+$ ($m/z = 537$; calculated isotope distribution pattern: 537 = 100, 538 = 25, 539 = 20.3, 540 = 4.3, 541 = 1.4). Isotopomers with less than 1% abundance are neglected.

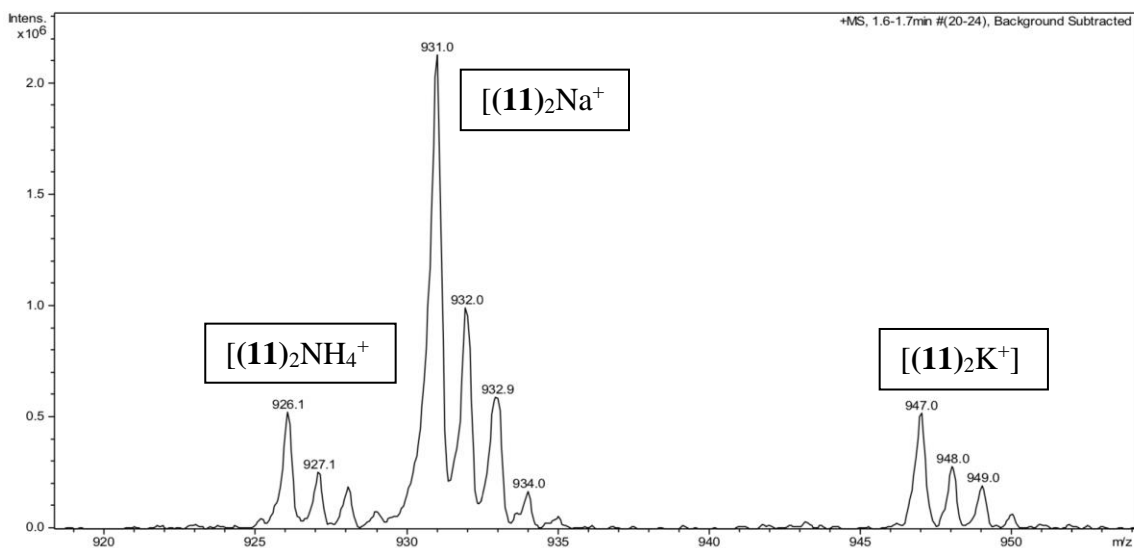


Figure D.4. Mass spectrum of **13a** showing the 2:1 ratio between the cobalt complex and Na^+ $[(11)_2\text{Na}^+]$: $m/z = 931$; calculated isotope distribution pattern: 931 = 100, 932 = 45.4,

933 = 29.7, 934 = 10.2, 935 = 3.5). The isotope distribution pattern at 947 corresponds to $(\mathbf{11})_2\text{K}^+$ ($m/z = 947$; calculated isotope distribution pattern: 947 = 100, 948 = 45.4, 949 = 36.9, 950 = 13.4, 951 = 5.6, 952 = 1.5) while the isotopomers around 926 correspond to $(\mathbf{11})_2\text{NH}_4^+$ ($m/z = 926$; calculated isotope distribution pattern: 926 = 100, 927 = 45.8, 928 = 29.9, 929 = 10.3, 930 = 3.5). Isotopomers less than 1% abundant are neglected.

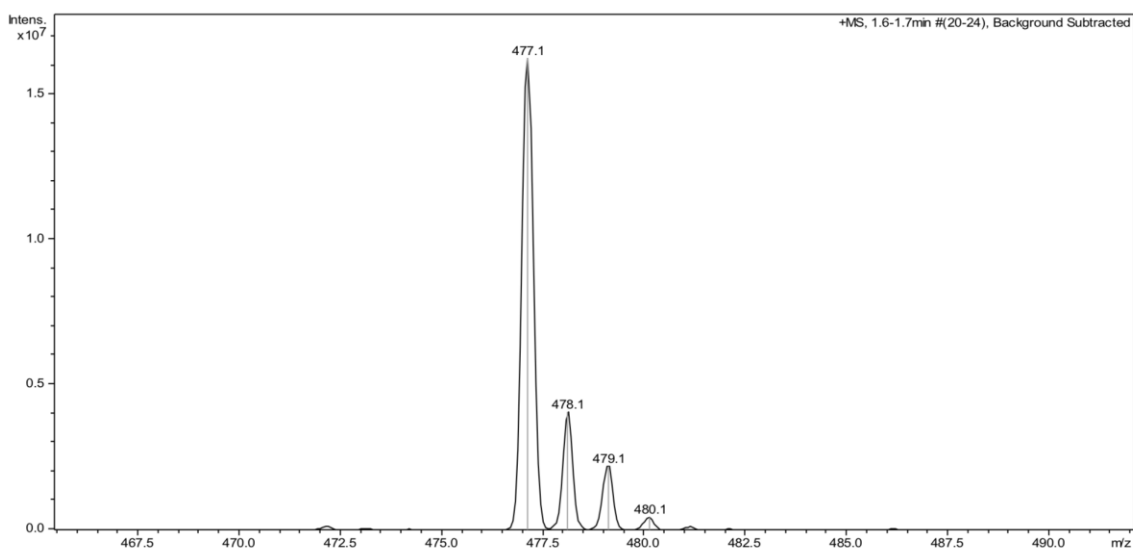


Figure D.5. Mass spectrum of **13a** in the low mass region, revealing the 1:1 ratio between the cobalt complex **11** and Na^+ , $(\mathbf{11})\text{Na}^+$ ($m/z = 477$, calculated isotope distribution pattern: 477 = 100; 478 = 22.7; 479 = 12.3; 480 = 2.2). Isotopomers with less than 1% abundance are neglected.

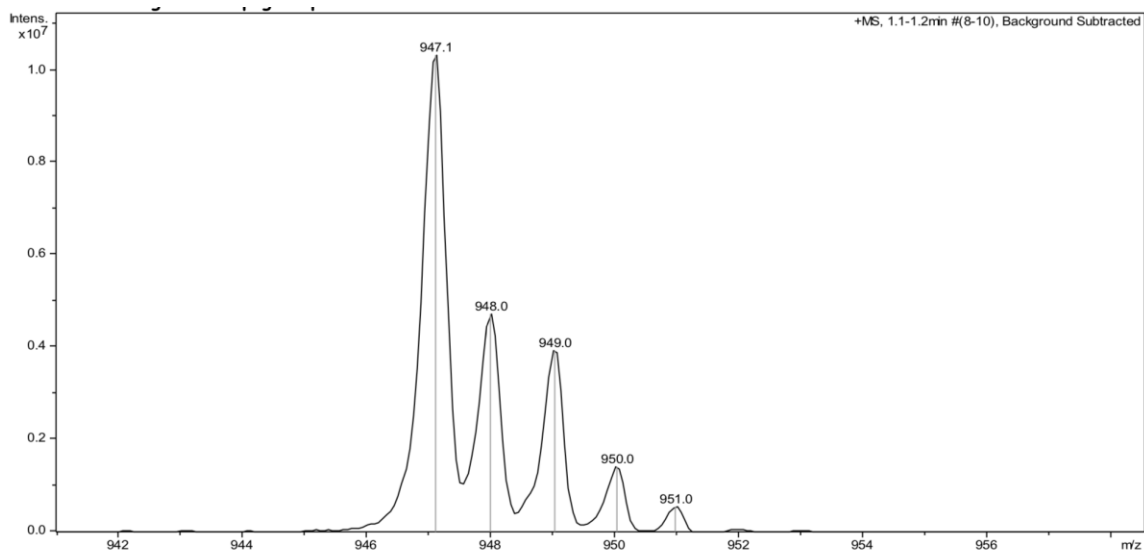


Figure D.6. Mass spectrum of **13b** showing the 2:1 ratio between the cobalt complex **11** and K^+ , $(\mathbf{11})_2\text{K}^+$ ($m/z = 947$; calculated isotope distribution pattern: 947 = 100, 948 = 45.4, 949 = 36.9, 950 = 13.4, 951 = 5.6, 952 = 1.5). Isotopomers with less than 1% abundance are neglected.

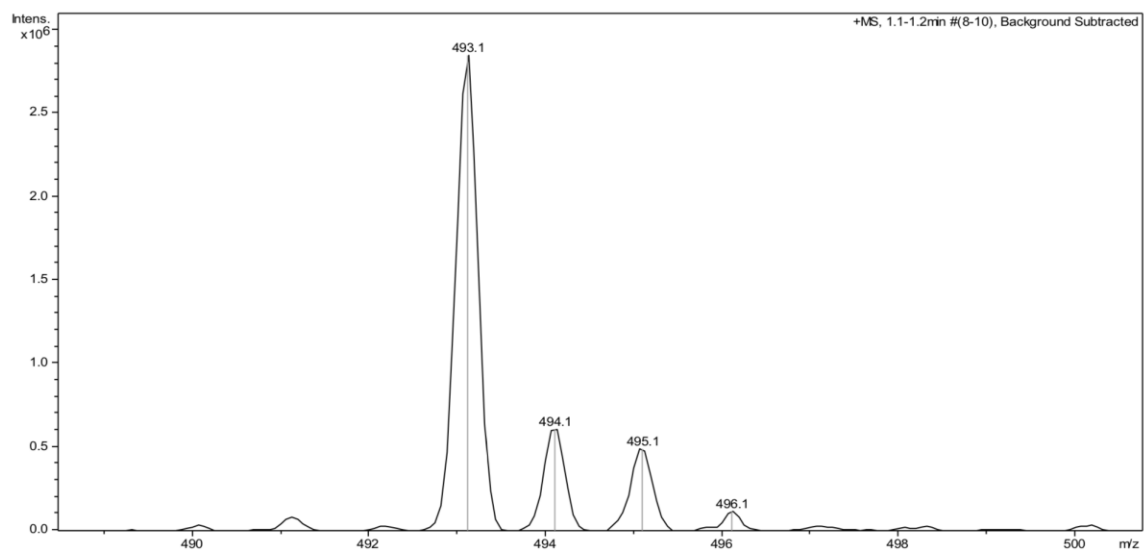


Figure D.7. Mass spectrometry of **13b** showing the 1:1 ratio between the cobalt complex and K^+ , $(\mathbf{11})\text{K}^+$ ($m/z = 493$; calculated isotope distribution pattern: 493 = 100, 494 = 22.7, 495 = 19.5, 496 = 3.8, 497 = 1.3). Isotopomers with less than 1% abundance are neglected.

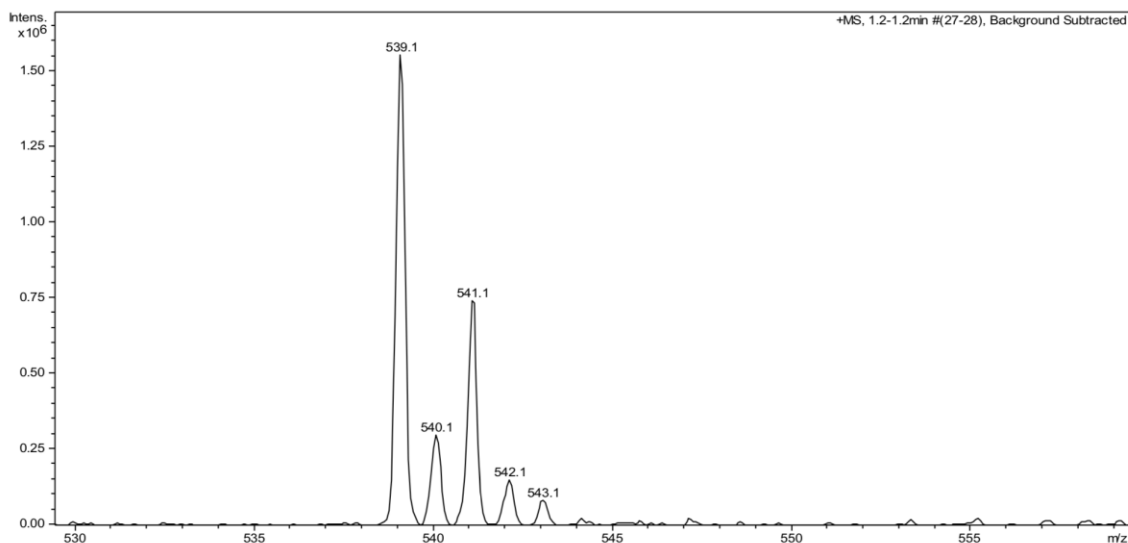


Figure D.8. Mass spectrum of **13c** in the low mass region, highlighting the $(11)\text{Rb}^+$ ion ($m/z = 539$, calculated isotope distribution pattern: $539 = 100$; $540 = 22.7$, $541 = 50.8$, $542 = 11$, $543 = 5.2$). Isotopomers with less than 1% abundance are neglected.

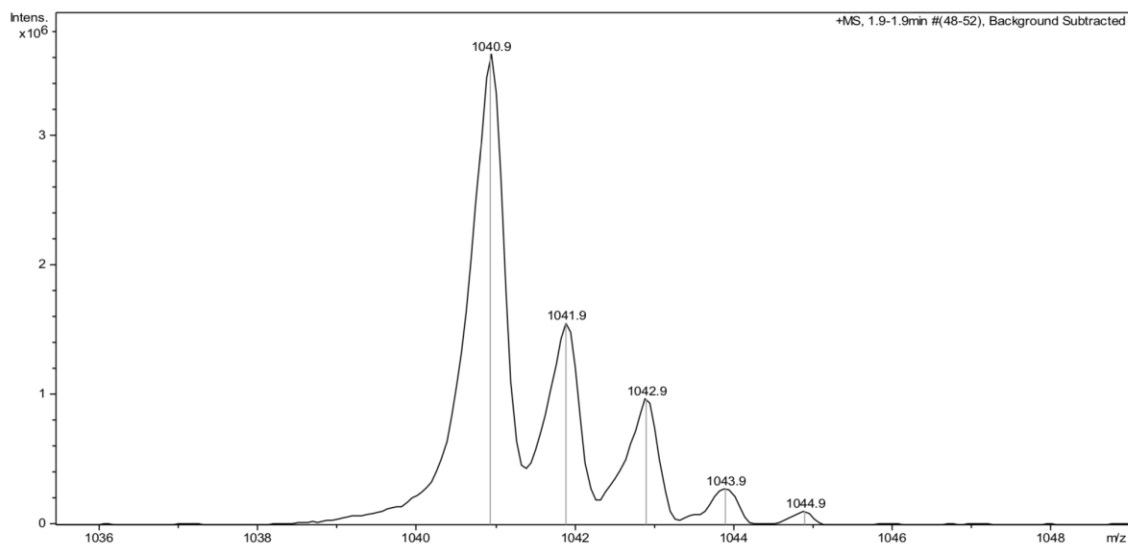


Figure D.9. Mass spectrometry of **13d** showing the 2:1 ratio between the cobalt complex and Cs^+ , $(3)_2\text{Cs}^+$ ($m/z = 1041$; calculated isotope distribution pattern: $1041 = 100$, $1042 = 45.4$, $1043 = 29.7$, $1044 = 10.2$, $1045 = 3.5$). Isotopomers with less than 1% abundance are neglected.

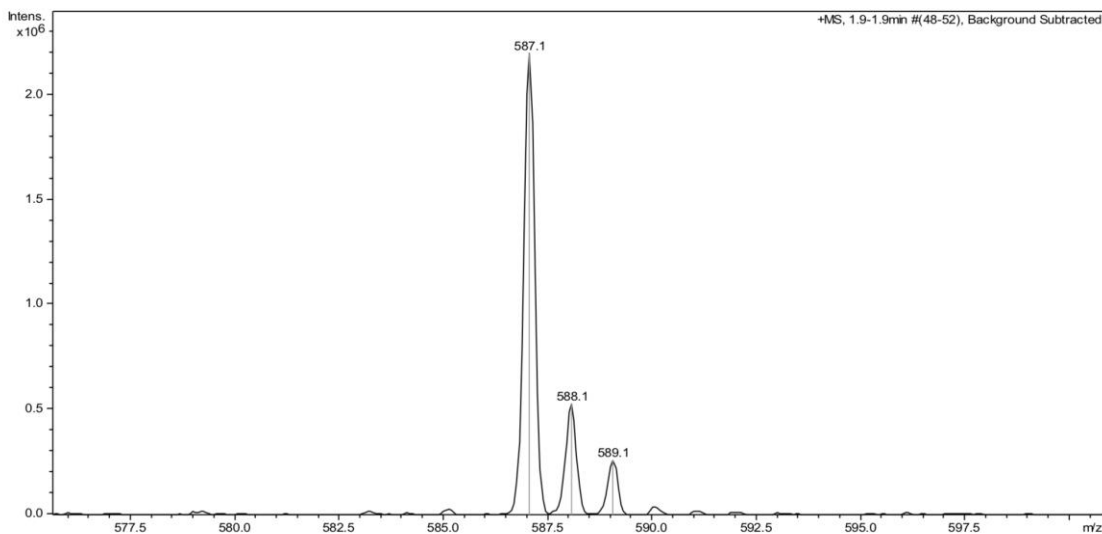


Figure D.10. Mass spectrometry of **13d** showing the 1:1 ratio between the cobalt complex and Cs^+ , $(\mathbf{11})\text{Cs}^+$ ($m/z = 587$; calculated isotope distribution pattern: $587 = 100$, $588 = 22.7$, $589 = 12.3$, $590 = 2.2$). Isotopomers with less than 1% abundance are neglected.

II. Density Functional Theory

Table D.1. Comparison of crystallographically and computationally determined geometries for **11**.

Parameter	X-ray diffraction	Computed	
		B3LYP- D3/LACV3P**++	M06/LACV3P**++
Average C-S bond length/Å	1.728	1.746	1.735
Average Co-S bond length/Å	2.117	2.149	2.132
Co-Cp-centroid distance/Å	1.660	1.689	1.726
Angle between Cp and C_6S_2 planes/ $^\circ$	89.81	88.61	86.97

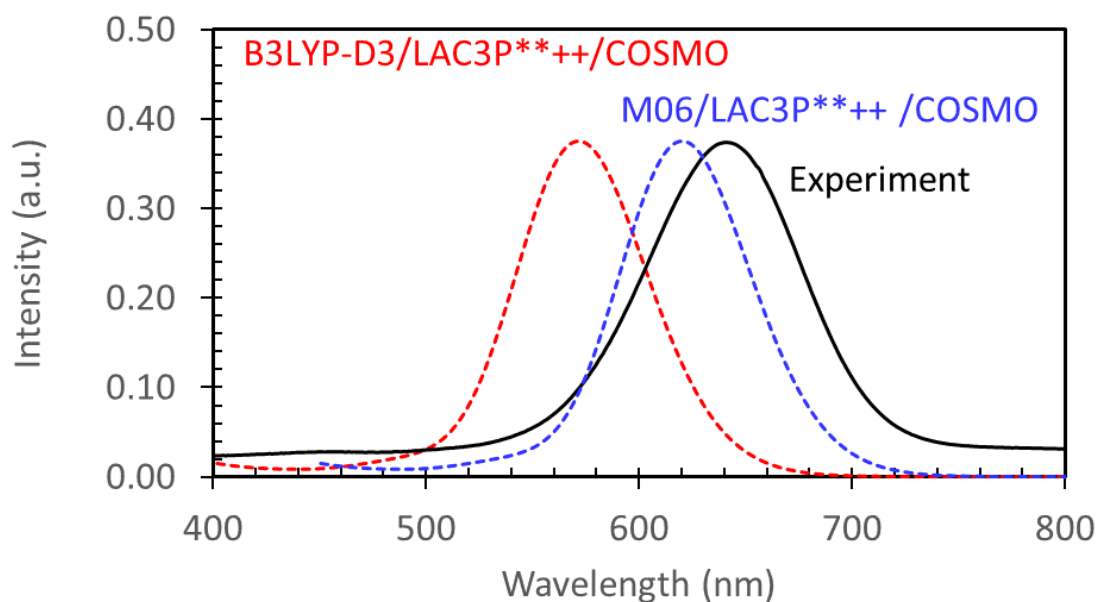


Figure D.11. Comparison of experimental and computed UV-Vis spectra for **11**.

Table D.2. Computed lowest energy UV-Vis transitions for **11** with oscillator strength, $f > 0.1$.

Basis Set	Functional	Solvent	λ_{\max}/nm
B3LYP-D3	LACV3P	gas phase	561
	LACV3P**	gas phase	565
	LACV3P***++	PCM COSMO(CH ₂ Cl ₂)	572
M06	LACV3P	gas phase	551
	LACV3P**	gas phase	583
	LACV3P***++	PCM COSMO(CH ₂ Cl ₂)	622
Experimental		CH ₂ Cl ₂	643

Table D.3. Contributions to the lowest energy excitation with oscillator strength, $f > 0.1$.

Transition number	wavelength (nm)	oscillator strength	contribution	x-coeff
5	622	0.205		

HOMO-15 → LUMO+1	0.10324
HOMO-8 → LUMO+1	0.12010
HOMO-3 → LUMO+1	-0.22127
HOMO-2 → LUMO+1	0.19946
HOMO-1 → LUMO	0.43831
HOMO → LUMO	0.82703

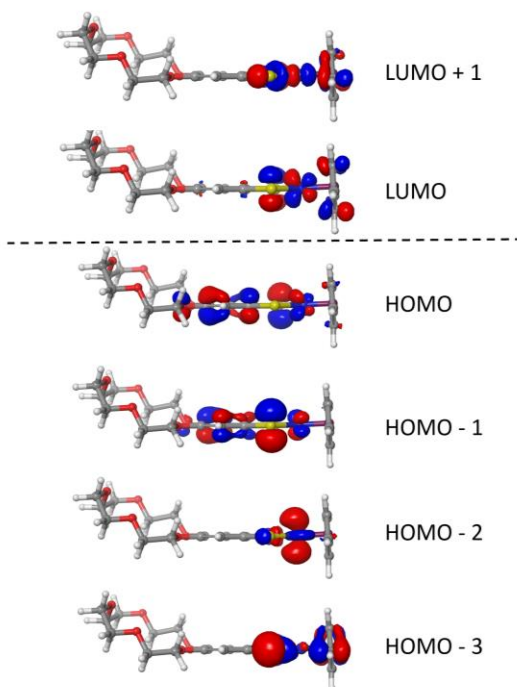


Figure D.12. Frontier orbitals for **11** computed at the M06/LACV3P**++/COSMO(CH₂Cl₂) level of theory.

APPENDIX E

Crystallographic Information from Chapter 5

** Note that any solvate molecules within each diagram have been removed for clarity. Where more than one molecule exists in the asymmetric unit, just one molecule is illustrated.*

Structure of LW176_P21_c_done_a

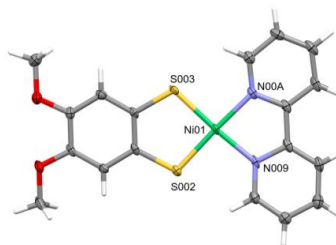


Table E.1. Crystal data and structure refinement for LW176_P21_c_done_a.

Identification code	LW176_P21_c_done_a
Empirical formula	C ₁₉ H ₁₇ Cl ₃ N ₂ NiO ₂ S ₂
Formula weight	534.52
Temperature/K	170.0
Crystal system	monoclinic
Space group	P2 ₁ /c
a/Å	13.248(10)
b/Å	11.843(9)
c/Å	14.474(10)
α/°	90
β/°	109.54(4)
γ/°	90
Volume/Å ³	2140(3)
Z	4
ρ _{calc} /cm ³	1.659
μ/mm ⁻¹	1.496
F(000)	1088.0
Crystal size/mm ³	0.86 × 0.199 × 0.033
Radiation	MoKα (λ = 0.71073)
2θ range for data collection/°	5.974 to 56.84
Index ranges	-17 ≤ h ≤ 17 -15 ≤ k ≤ 15 -19 ≤ l ≤ 19
Reflections collected	66534
Independent reflections	5340 [R _{int} = 0.1437, R _{sigma} = 0.0536]
Data/restraints/parameters	5340 / 0 / 264
Goodness-of-fit on F ²	1.130
Final R indexes [I >= 2σ (I)]	R ₁ = 0.0577, wR ₂ = 0.1104
Final R indexes [all data]	R ₁ = 0.0887, wR ₂ = 0.1267
Largest diff. peak/hole / e Å ⁻³	0.89 and -0.76

APPENDIX F

Crystallographic Information from Chapter 6

** Note that any counterions or solvate molecules within each diagram have been removed for clarity. Where more than one molecule exists in the asymmetric unit, just one molecule is illustrated.*

Structure of LW020_0m_a



Table F.1. Crystal data and structure refinement for LW020_0m_a.

Identification code	mo_LW20_0m_a
Empirical formula	C ₁₆ H ₁₆ GeO ₄ S ₄
Formula weight	473.12
Temperature/K	170.0
Crystal system	monoclinic
Space group	P2 ₁ /n
a/Å	11.4460(5)
b/Å	13.6520(7)
c/Å	11.7325(6)
α/°	90
β/°	92.131(2)
γ/°	90
Volume/Å ³	1832.06(15)
Z	4
ρ _{calc} /cm ³	1.715
μ/mm ⁻¹	2.147
F(000)	960.0
Crystal size/mm ³	0.68 × 0.35 × 0.165
Radiation	MoKα (λ = 0.71073)
2θ range for data collection/°	5.722 to 56.724
	-15 ≤ h ≤ 14
Index ranges	-18 ≤ k ≤ 18
	-15 ≤ l ≤ 15
Reflections collected	36449
Independent reflections	4583 [R _{int} = 0.0430, R _{sigma} = 0.0224]
Data/restraints/parameters	4583 / 0 / 230
Goodness-of-fit on F ²	1.190
Final R indexes [I ≥ 2σ (I)]	R ₁ = 0.0313, wR ₂ = 0.0607
Final R indexes [all data]	R ₁ = 0.0478, wR ₂ = 0.0696
Largest diff. peak/hole / e Å ⁻³	0.44 and -0.53

Structure of JMR_LW033_0m_a



Table F.2. Crystal data and structure refinement for JMR_LW033_0m_a.

Identification code	JMR_LW033_0m_a
Empirical formula	C ₁₆ H ₁₆ GeO ₄ S ₄
Formula weight	473.12
Temperature/K	150.15
Crystal system	orthorhombic
Space group	Fdd2
a/Å	40.577(2)
b/Å	20.0338(12)
c/Å	4.5949(3)
α/°	90
β/°	90
γ/°	90
Volume/Å ³	3735.2(4)
Z	8
ρ _{calc} /cm ³	1.683
μ/mm ⁻¹	2.106
F(000)	1920.0
Crystal size/mm ³	0.18 × 0.07 × 0.04
Radiation	MoKα (λ = 0.71073)
2θ range for data collection/°	4.016 to 57.774
Index ranges	-54 ≤ h ≤ 53 -26 ≤ k ≤ 26 -6 ≤ l ≤ 6
Reflections collected	30148
Independent reflections	2396 [R _{int} = 0.0451, R _{sigma} = 0.0246]
Data/restraints/parameters	2396 / 1 / 117
Goodness-of-fit on F ²	1.081
Final R indexes [I ≥ 2σ (I)]	R ₁ = 0.0225, wR ₂ = 0.0487
Final R indexes [all data]	R ₁ = 0.0243, wR ₂ = 0.0494
Largest diff. peak/hole / e Å ⁻³	0.40 and -0.28
Flack parameter	0.081(11)

Structure of LW077_P21_c_a

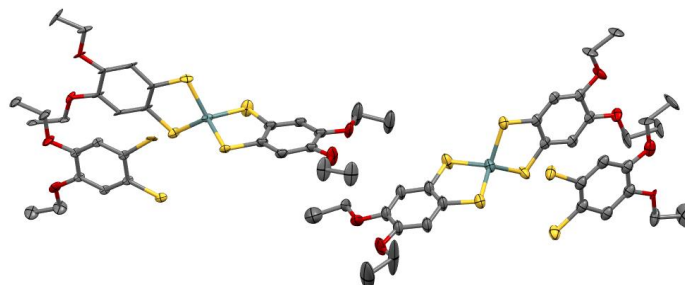


Table F.3. Crystal data and structure refinement for LW077_P21_c_a.

Identification code	LW077_P21_c_a
Empirical formula	C ₂₀ Ge _{0.67} O ₄ S ₄
Formula weight	480.83
Temperature/K	170.0
Crystal system	monoclinic
Space group	P2 ₁ /c
a/Å	37.4730(12)
b/Å	12.1737(4)
c/Å	15.6474(5)
α/°	90
β/°	102.079(2)
γ/°	90
Volume/Å ³	6980.1(4)
Z	12
ρ _{calc} /cm ³	1.373
μ/mm ⁻¹	4.875
F(000)	2848.0
Crystal size/mm ³	0.221 × 0.040 × 0.012
Radiation	CuKα (λ = 1.54178)
2θ range for data collection/°	5.774 to 90
Index ranges	-34 ≤ h ≤ 34, -11 ≤ k ≤ 11, -14 ≤ l ≤ 14
Reflections collected	44301
Independent reflections	5634 [R _{int} = 0.0985, R _{sigma} = 0.0520]
Data/restraints/parameters	5634/216/542
Goodness-of-fit on F ²	1.132
Final R indexes [I ≥ 2σ (I)]	R ₁ = 0.0739, wR ₂ = 0.1828
Final R indexes [all data]	R ₁ = 0.0821, wR ₂ = 0.1890
Largest diff. peak/hole / e Å ⁻³	1.81/-0.48

Structure of LW078_P_1



Table F.4. Crystal data and structure refinement for LW077_P21_c.

Identification code	LW078_P_1_a
Empirical formula	C ₁₄ H ₈ GeO ₄ S ₄
Formula weight	441.03
Temperature/K	150.0
Crystal system	triclinic
Space group	P-1
<i>a</i> /Å	7.1721(4)
<i>b</i> /Å	13.9502(7)
<i>c</i> /Å	16.6551(8)
α /°	99.319(2)
β /°	90.285(2)
γ /°	90.634(2)
Volume/Å ³	1644.25(15)
<i>Z</i>	4
ρ_{calc} /cm ³	1.782
μ /mm ⁻¹	2.385
<i>F</i> (000)	880.0
Crystal size/mm ³	0.222 × 0.164 × 0.064
Radiation	MoK α (λ = 0.71073)
2 Θ range for data collection/°	5.92 to 55.17
	-9 ≤ <i>h</i> ≤ 9
Index ranges	-18 ≤ <i>k</i> ≤ 18
	-21 ≤ <i>l</i> ≤ 21
Reflections collected	96110
Independent reflections	7617 [<i>R</i> _{int} = 0.0263, <i>R</i> _{sigma} = 0.0113]
Data/restraints/parameters	7617 / 0 / 415
Goodness-of-fit on <i>F</i> ²	1.143
Final <i>R</i> indexes [<i>I</i> >= 2 σ (<i>I</i>)]	<i>R</i> ₁ = 0.0246, <i>wR</i> ₂ = 0.0687
Final <i>R</i> indexes [all data]	<i>R</i> ₁ = 0.0281, <i>wR</i> ₂ = 0.0711
Largest diff. peak/hole / e Å ⁻³	0.42 and -0.79

APPENDIX G

Rights and Permissions

I. Copyright Permissions

4/8/22, 1:08 PM

Rightslink® by Copyright Clearance Center



Home ? Live Chat Lara Watanabe



Novel fused tetrathiocines as antivirals that target the nucleocapsid zinc finger containing protein of the feline immunodeficiency virus (FIV) as a model of HIV infection

Author: Christopher R.M. Asquith, Marina L. Meli, Lidia S. Konstantinova, Tuomo Laitinen, Antti Poso, Oleg A. Rakitin, Regina Hofmann-Lehmann, Karin Allenspach, Stephen T. Hilton
Publication: Bioorganic & Medicinal Chemistry Letters
Publisher: Elsevier
Date: 15 March 2015

Crown copyright © 2014 Published by Elsevier Ltd. All rights reserved.

Order Completed

Thank you for your order.

This Agreement between University of Windsor – Lara Watanabe ("You") and Elsevier ("Elsevier") consists of your license details and the terms and conditions provided by Elsevier and Copyright Clearance Center.

Your confirmation email will contain your order number for future reference.

License Number 5284310458076

[Printable Details](#)

License date Apr 08, 2022

<https://s100.copyright.com/AppDispatchServlet>

1/2



Oxidative addition of 1,2,5,6-Tetrathiocins to Co(I): A Re-Examination of Crown Ether Functionalized Benzene Dithiolate Cobalt(III) Complexes



Author: Lara K. Watanabe, Zeinab S. Ahmed, John J. Hayward, et al

Publication: Organometallics

Publisher: American Chemical Society

Date: Feb 1, 2022

Copyright © 2022, American Chemical Society

PERMISSION/LICENSE IS GRANTED FOR YOUR ORDER AT NO CHARGE

This type of permission/license, instead of the standard Terms and Conditions, is sent to you because no fee is being charged for your order. Please note the following:

- Permission is granted for your request in both print and electronic formats, and translations.
- If figures and/or tables were requested, they may be adapted or used in part.
- Please print this page for your records and send a copy of it to your publisher/graduate school.
- Appropriate credit for the requested material should be given as follows: "Reprinted (adapted) with permission from {COMPLETE REFERENCE CITATION}. Copyright {YEAR} American Chemical Society." Insert appropriate information in place of the capitalized words.
- One-time permission is granted only for the use specified in your RightsLink request. No additional uses are granted (such as derivative works or other editions). For any uses, please submit a new request.

If credit is given to another source for the material you requested from RightsLink, permission must be obtained from that source.

[BACK](#)

[CLOSE WINDOW](#)

VITA AUCTORIS

NAME: Lara Keiko Watanabe
PLACE OF BIRTH: Taizhou, China
YEAR OF BIRTH: 1995
EDUCATION: Cole Harbour District High School,
Dartmouth, NS, 2013
Mount Allison University, B.Sc.,
Sackville, NB, 2017
University of Windsor, Ph.D.,
Windsor, ON, 2022

Publications:

1. **Watanabe, L. K.**; Wrixon, J. D.; Ahmed, Z.; Hayward, J. J.; Abbasi, P.; Pilkington, M.; Macdonald, C. L. B. and Rawson, J. M. Oxidative Addition of Tetrathiocins to Palladium(0) and Platinum(0): A Route to Dithiolate Coordination Complexes, *Dalton Trans.*, **2020**, 49, 9086-9093.

2. Geier, S. J.; Binder, J. F.; Vogels, C. M.; **Watanabe, L. K.**; Macdonald, C. L. B. and Westcott, S. A. The hydroboration of α -diimines, *New J. Chem.* **2021**, 45, 14908-14912.

3. **Watanabe, L. K.**; Wrixon, J. D. and Rawson, J. M. The chemistry of dithietes, 1,2,5,6-tetrathiocins and higher oligomers, *Dalton Trans.*, **2021**, 50, 13620-13633.

4. **Watanabe, L. K.**; Ahmed, Z. S.; Hayward, J. J.; Heyer, E.; Macdonald, C. L. B. and Rawson, J. M. Oxidative addition of 1,2,5,6-tetrathiocins to Co(I): A re-examination of crown ether functionalized benzene dithiolate cobalt(III) complexes, *Organomet.*, **2022**, 41, 226-234.

5. Stephaniuk, N. T.; Nascimento, M. A.; Nikko, S.; Heyer, E.; **Watanabe, L. K.** and Rawson, J. M. A Robust S₄···O Supramolecular synthon: Structures of radical-radical cocrystals: [*p*-XC₆F₄CNEEN]₂[TEMPO] (X = F, Cl, Br, I, CN), *Chem. Eur. J.*, **2022**, 28, e202103846 (1–12).

6. Vojvodin, C. S.; Holmes, S. T.; **Watanabe, L. K.**; Rawson, J. M.; Schurko, R. Multi-Component Crystals Containing Urea: Mechanochemical Synthesis and Characterization by ³⁵Cl Solid-State NMR Spectroscopy and DFT Calculations, *CrystEngComm*, **2022**, 24, 2626-264.

7. Baird, S. R.; Vogels, C. M.; Geier, S. J.; **Watanabe, L. K.**; Binder, J. F.; Macdonald, C. L. B. and Westcott, S. A. The phosphinoboration of thiosemicarazones (Accepted Article).